A thesis submitted in partial fulfilment of the requirements for the degree of
Doctor of Philosophy

Residual stresses in large sizes forgings

By:

Jakub Sroka

Supervisors:

Professor Jesus Talamantes-Silva

Professor W. Mark Rainforth

Professor Michael Krzyzanowski

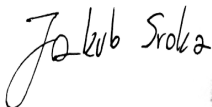Department of Materials Science and Engineering

Faculty of Engineering

The University of Sheffield
Sheffield, 2021
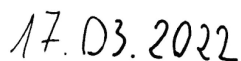
DECLARATION OF AUTHORSHIP

I, Jakub Sroka, declare that this thesis titled, Residual stresses in large size forgings, and the work presented in it are my own. I confirm that:

- This work was done wholly or mainly while in candidature for research degree at this University.
- Where any part of this thesis has previously been submitted for a degree or any other qualification at this University or any other institution, this has been clearly stated.
- Where I have consulted the published work of others, this is always clearly attributed.
- Where I have quoted from the work of others, the source is always given. With the exception of such quotations, this thesis is entirely my own work.
- I have acknowledged all main sources of help.
- Where the thesis is based on work done by myself jointly with others, I have made clear exactly what was done by others and what I have contributed myself.

Signed:

Jakub Sroka

_____

Date:

17.03.2022

_____

I dedicate this work to my dear family, my beloved wife Paulina, son Hieronim and all my future children.

ACKNOWLEDGMENTS

ABSTRACT

The presented research project attempts to improve the understanding of the residual stresses arising from both thermal and phase transformations during the heat treatment of large forgings. Particular attention is given to the accurate representation of the cooling stages. The methodology which combines both experimental and simulation techniques was developed and included finding the best practice for CCT/TTT implementation, dilatometric and hardness testing, microstructure observations and full integration of material data into finite element models. In the thesis the overall numerical investigations of stress management during heat treatment of large-size forgings was performed. Modelling of transient temperature field and a new kinetics approach to calculating the phase transformation for large-size forgings was presented. To study the residual stress that arise in the large size forging the author of the project performed complex investigations that included:

1. Determination of the occurrence and duration of influence of different factors and their possible interactions that may affect generation of stresses in the elements from the selected material (SA508 gr.3 steel) during heat treatment after deformation;

2. Analysis of the heating and cooling conditions of the final products during production, causing uneven heating and cooling of different layers of material;

3. Analysis of heterogeneity of microstructure of the chosen material (SA508 gr.3 steel) after heat treatment and phase transformation, which is a source of high internal stresses related to the heterogeneity of deformation in the volume of the processed element;

4. Analysis of residual stress caused by uneven heating and cooling of the different areas of the part leading to dimensional changes;

5. Analysis of residual stresses caused by phase transformations of the structural components of the material, occurring at different temperatures, due to the change of the specific volume that is accompanying the phase change. The analyses were supported with dilatometric and hardness tests, followed by microstructural observations on the optical microscope.

The model was validated using the industrial case provided by the company Sheffield Forgemasters Ltd. (Sheffield, United Kingdom). In this case, the cooling of the forged 95-tonne disc shaped ingot was performed. In the applied model, the relative geometry, reflecting the rectilinear 2D profile machined out of the forging before the heat treatment, was used. The model was used to calculate the cooling rates at the quarter thickness location and in the mid-

wall of the geometry. The calculated cooling rates were about two times higher inside the part than those presented in literature. The calculated transient temperature field allowed for estimation of the cooling rate at every node in the model at every time step during the process. These data were used in the last part of the work to assign thermal expansion/contraction coefficients obtained from the dilatometric test to the model. It allowed for prediction of the stress distribution within the forging. The results were presented as the changes in the dimensions of the angles between cylindrical and flat surfaces in the rectilinear model geometry and were compared to the values registered during the industry process. The stress and strain intensity values within the model during the cooling process were also presented. Although minor concerns are present, such as the possibility of insufficient FE accuracy in defining the growth sign of the angles, the obtained results were satisfying.

The developed model could be applied as a sub-function in wider investigations. To demonstrate this, in the final part of the work the sub-function was implemented in the set of simplified welding models, which represent its approach in the exemplary practical calculations. The set consists of the six models: three, where the temperature field due to the thermal exchange under different conditions were calculated, and further three models, which used such calculated fields to determine the stress/strain respond of the material. The stresses, which arose due to the thermal expansion and phase transformation and which caused the local volume change, were predicted in the characteristic locations of the geometry of the weld and within the steel table, upon which they were placed on. The models, generally geometry and condition dependent, mostly localised high tensile stresses within the lower parts of the weld at the centre and at the weld contact surfaces, while the compressive stresses were identified between the weld beads. Although the tensile stresses were identified in steel table at the bottom and in the centre of the bulk, the compressive stresses, highest at the contact surfaces, were mostly present.

The obtained results were in good correlation with the result from the literature. Besides, the author believes that the implementation of more dilatometric data could significantly improve the predictive abilities of the developed numerical tool. The aim of the work is to broaden the knowledge of the thermomechanical processes and improve the stress management during manufacturing the large-size ingots using the commercial FE modelling programs.

CONTENTS

x

1. Introduction

1.1. Thesis outline

The dynamically developing nuclear industry offers more and more modern solutions in new nuclear power plant projects. A characteristic feature of each of the next generation of these type of facilities is the use of systems of highly reliable elements for which the requirement of long-term reliability during operation in very difficult conditions is crucial. In the early 1960s it was shown that replacing small connected elements with a larger one goes hand in hand with improving the performance of the whole system, as well as extending its working life. This allows the differences between melts of the same material to be disregarded, as well as the elimination of the welding process, which in itself introduces residual stresses and requires additional expensive inspections. The use of forgings of large masses, used for work in demanding conditions requires very precise control of the course of each stage of its thermomechanical manufacturing.

The doctoral dissertation is focused on the numerical investigations of the heat treatment of a material using by manufacturers for production of large-scale elements for the nuclear industry. During designing the final product of such large dimensions to give the required properties and shape, the use of numerical methods is necessary. The numerical analysis models able to assist in predicting the impact of process parameters on the formation of self-stress, play a key role. The formation of internal stresses in such forgings, balancing in areas of varying sizes, is influenced by a number of interrelated factors. The generation of the type I stresses, the so-called macro-stress, is affected above all by heterogeneous heating or cooling, plastic working, phase changes and additional mechanical treatment of surface layers, such as turning or milling. Control of macro-stress, elimination of undesirable stress states and creation of conditions favourable for the appropriate product life cycle is of great practical importance. In addition, on the meso- (micro) scale, type II stresses arise, the so-called micro-stresses, balancing themselves in areas of the order of several grain sizes, most often caused by anisotropy of crystallites, degradation of supersaturated solutions and local structural changes, e.g., with heterogeneous chemical composition in different forgings. Type III stresses operate over several atomic distances and come from crystal lattice defects. Stresses of the first type

have the greatest practical significance. The important fact for this project is that the influence of the stresses of various kind, as well as the interactions between them, can have a different impact on the final product in the case of large dimensions used in the nuclear industry than in the case of usual smaller elements.

The causes of self-stresses are divided into mechanical, thermal and structural. Mechanical internal stresses arise during plastic forming due to the heterogeneity of the plastic deformation in the product area. This translates into heterogeneity of the macro and microstructure after deformation, which is the cause of the occurrence of macro- and micro-stresses. The heterogeneity of structure and texture occurs especially during deformation of two-phase alloys. Internal thermal stress is caused by uneven cooling (or heating) of individual layers of large-size products or their fragments, leading to expansion joints. On the other hand, structural internal stresses are caused by phase changes of the structural components of the forged material being processed, occurring in different temperature ranges. The change in specific volume accompanying the phase transformation causes the formation of self-stress. Specific volume changes due to structural changes are greater than due to thermal expansion. Therefore, thermal shrinkage and phase transitions are the main causes of self-stress. The stress values are relatively high, so that in large-size forged products, cracking or explosive destruction of the element may occur as a result of exceeding the strength limit.

The subjects covered in the work include comprehensive numerical analysis, supported with mechanical tests and microscopic observations, to determine the reasons for the occurrence of internal stresses in forged large-size steel products SA508 gr. 3, determining the impact of both process and material parameters. It is assumed that the development of a number of relevant numerical models and including them in an integration model, useful for a suitable range of materials, will allow for more focused design and effective control of product manufacture. The scope of research included a number of detailed numerical analysis, mainly based on the finite element method (FEM), supported by the experimental studies, which included dilatometric and microstructure tests using light microscopy (LM) and hardness tests. In order to eliminate numerical effects, mathematical modelling was based on the use of commercial packages, like MSC and ABAQUS.

The final output of this work is the model, which proposes the new approach of the numerical interpretation of the CCT diagram. The dilatometric tests of various cooling rates were performed in order to extract the sets of the thermal expansion/contraction coefficients.

These values were implemented into the phase transformation model, which predicts the stress values during the cooling stage, by calculating the expansion/contraction of the local volume of the material by referring to the transient temperature field and the cooling rate within the cross section.

The author of this thesis was embedded into the research and development department of Sheffield Forgemasters R&D26 team to facilitate rapid knowledge transfer in both directions. In addition, R&D26 has extensive expertise in the use and application of computational methods of modelling large forgings and castings and thus is capable of providing invaluable advice and high quality data. The developed numerical approaches were validated through solution of the real problem provided by the industry and used in prediction of the temperature field and related mechanical response in the case of welding of the SA508 gr. 3 steel, based on the literature.

1.2. Historical overview

The era of the use of nuclear energy by humanity began with a series of important discoveries in the field of particle physics in the late nineteenth and early twentieth century. An important milestone was recorded in 1934, when the Italian physicist Enrico Fermi discovered that atomic nucleus bombarded by neutrons, slowed by water or paraffin, splits, and the products are the nuclei of lighter atoms [1]–[5]. In 1938, these results enabled Otto Hahn, Fritz Strassman, Lisa Meitner and Otto R. Frisch to conduct research that led to the construction of the theory of fission and to prove the most famous equation developed by Albert Einstein [1], [2], [6]:

$$E_0 = Mc^2 \qquad\qquad (1)$$

where E_0 – the rest energy of free body, M – its mass and c = 2.99792×10^8 m/s – the speed of light in vacuum. Accordingly, the change in energy is equal to the change in mass multiplied by the velocity of light squared [7]. It proposes that mass and energy are equivalent and are two forms of the same matter, where the term 'total energy' of an object includes the rest energy, the mass. This approach is called relativistic to conventional, Newtonian and the difference between the mass of the object at rest and the mass of the object in motion begins to be seen,

when the change in energy corresponding to a unit of mass is extremely large, like during radioactive decays, where the mass of the neutron at rest is $1.67492749804(95) \times 10^{-27}$ kg [8], [9].

Figure 1 Enrico Fermi, the leader of the team, which build the Chicago Pile-1 - the world's first self-sustained nuclear reactor at the University of Chicago Metallurgical Laboratory (USA) in 1942 [10].

The particles inside the nuclei are bonded with each other through the weak interactions, one of the four elementary forces in nature. Despite the size they are containers for huge amount of energy, which is emitted as heat, together with the rest of the products of radioactive decay. The decay occurs when the bond is broken, either by itself, or through a particle shot into the nuclei. Such process is called fission [1], [2], [6], [10], where unstable nuclei change their structure together with the release of energy. Instability is associated with the unbalanced energy, ratio of protons and neutrons inside the nucleon. As can be seen in Figure 2 the probability of fission is greater in heavy nuclei, because it is related to the number of particles in the nucleus, although the spontaneous fission is not favoured [9]. Inducing fission can be done by capture of a shot neutron, which increases the energy inside the nucleus, breaking the bonds between the nucleons. In terms of profitable nuclear reaction to split the nucleus the broken by the neutron bonds have to release the greater energy than that needed for the fragmentation of atom, called the nuclear binding energy [11].
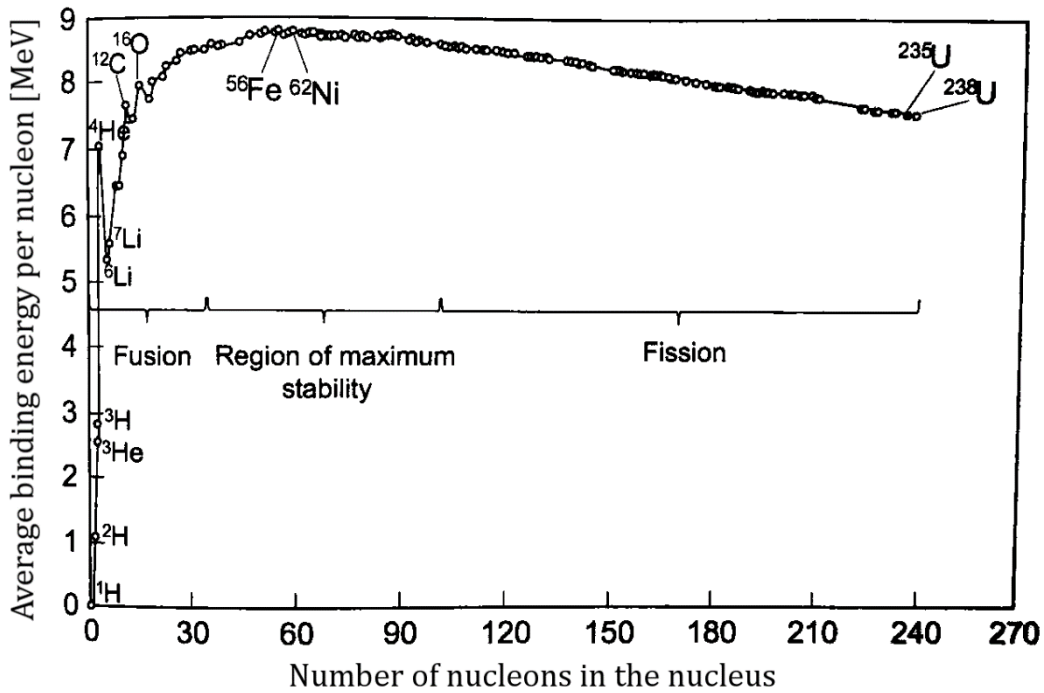
Figure 2 Average binding energy per nucleon related to the mass number A [9].

In 1942 Enrico Fermi built the world's first self-sustained nuclear reactor in the Metallurgical Laboratory at the University of Chicago, which was named the Chicago Pile-1 (CP1). The term 'pile' was chosen for a way it was built and it is worth mentioning that the name 'reactor' was not used until 1952 [11]. The system worked based on the phenomenon called 'chain reaction'. In simplified terms it means that the energy was released from fission, which occurred in uranium after reaching the sufficient mass (critical mass). One of the products of this reaction were neutrons, which were bombarding atoms of uranium nearby, initiating fission in them. The process was controlled by the cadmium rods, which were used to capture free neutrons [6], [11], [12].

The historical conditions led the researchers to construction of the atomic bomb, used in airstrikes on Hiroshima and on Nagasaki, Japan, in August, 1945 [12]. It opened a discussion on the purpose of use of the atomic energy after the war and directed the gained knowledge more and more towards the energy industry [11]. To regulate the use of nuclear power many countries created specific institutions. The Atomic Energy Commission (AEC) was established in 1946 in the United States, which in 1974 was changed into Nuclear Regulatory Commission (NRC), operating until today. Within the scope of its responsibilities there are such issues as

radiation protection, reactor safety, regulations of nuclear materials and also management of nuclear waste or licensing the new types of reactors [2], [13].

1.3. Nuclear Reactors

The most widely used type of nuclear reactors are Pressurized Water Reactor (PWR), presented schematically in Figure *3*. The ongoing fission of the atoms inside the fuel rods heats the water in the primary circuit. The energy emitted depends on the amount of the fission. The water in the primary circuit serves also as moderator; it absorbs the neutrons, and as a coolant, it transfers heat to the secondary circuit, where clean water boils into a steam. The steam then drives a turbine and the generator produces the electricity. Used steam runs further to the condensers, where its temperature drops and steam turns back into a water, which can be used as heat exchanger between the turbine and heat source again. The surplus heat from the condensers is useless in industrial terms and is released in cooling towers as clean water steam. [2], [9]. The types of the nuclear reactors can be very different due to the technical solutions in such aspects as fuel supply, choice of moderator and type of coolant [11].
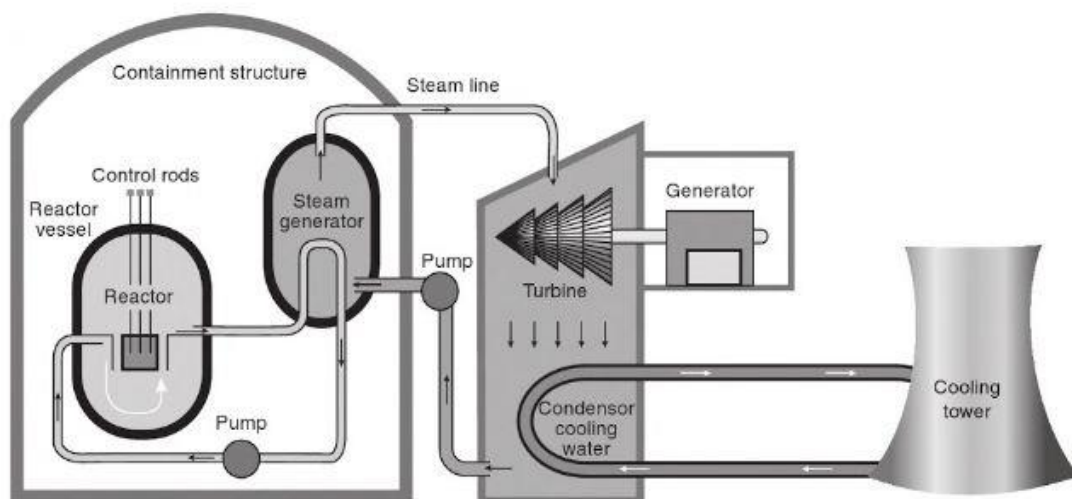
Figure 3 The scheme of a typical nuclear reactor with the pressure vessel [14].

The different reactors can be divided historically into various generations. Each generation presents specific solutions and developments, which were typically used over that time [15]. The most widely used types nowadays are reactors from 2nd Generation, although these series of nuclear reactor were designed in the 1970s and 1980s of twentieth century. The main two representatives are the Boiling Water Reactors (BWR) and the Pressurized Water Reactors (PWR), among others. Their electrical capacity is from 800 to 1500 MW(e), increasing over years together with the market's demands. The life spans of these designs were estimated as 30 – 40 years, but constant research on materials subjected to high temperatures and neutron irradiation introduced developments that allowed the extension of this period by 20 years. The most modern solutions of reactors design are grouped under the term IVth Generation (*Figure 4*) [9], [15].
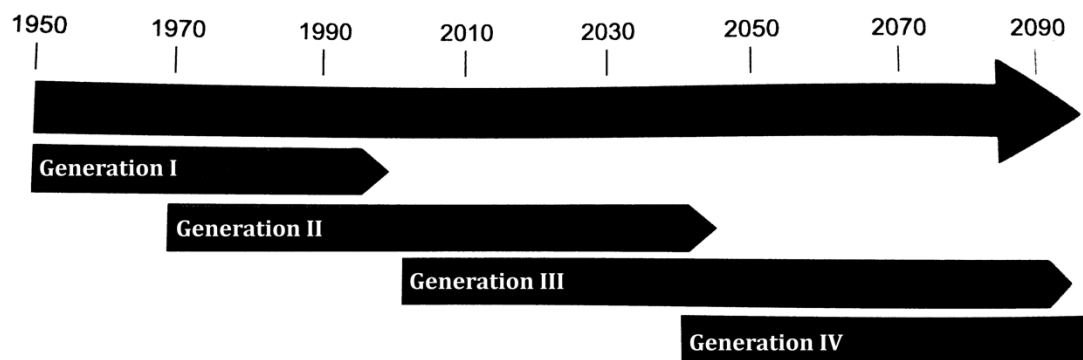
Figure 4 The evolution of the nuclear reactors in civilian sector in years 1950 – 2090 [15].

Although the nuclear power is seen as a clean and very effective method for acquisition the energy for the increasing demands, the expectations of its future popularity from the 2000s were higher. Historically there have been three serious accidents connected with high level of radioactive pollution of the environment: Three Mile Island, Chernobyl and Fukushima. The aftermaths of each incident in terms of design issues was substantial, such as increasing licensing times for new plants, higher design costs, installation of additional power and cooling systems for the units at work to satisfy the sense of security of the panicked public. Also, the rising popularity of the unconventional energy production methods and the bankruptcy of the biggest companies on the market created the unfavourable situation, where the investment risk of the large projects of new nuclear plants is too high for investors [16].

Despite this pessimistic view, the promising constant growth can be noticed from the data presented in Figure 5. There is number of reactors operating currently and capacity of the nuclear worldwide net as can be seen on the chart. The highest growth was recorded from 1958 to 1989. It is worth mentioning that the Chernobyl catastrophe was in 1986. There is a small decrease in the number of reactors in 2011, when the Fukushima accident happened, which is related to the changes applied to the Japanese nuclear economy after the incident. However, in the last years the clear upward trend in building the new nuclear installations can be undoubtedly noticed [9].
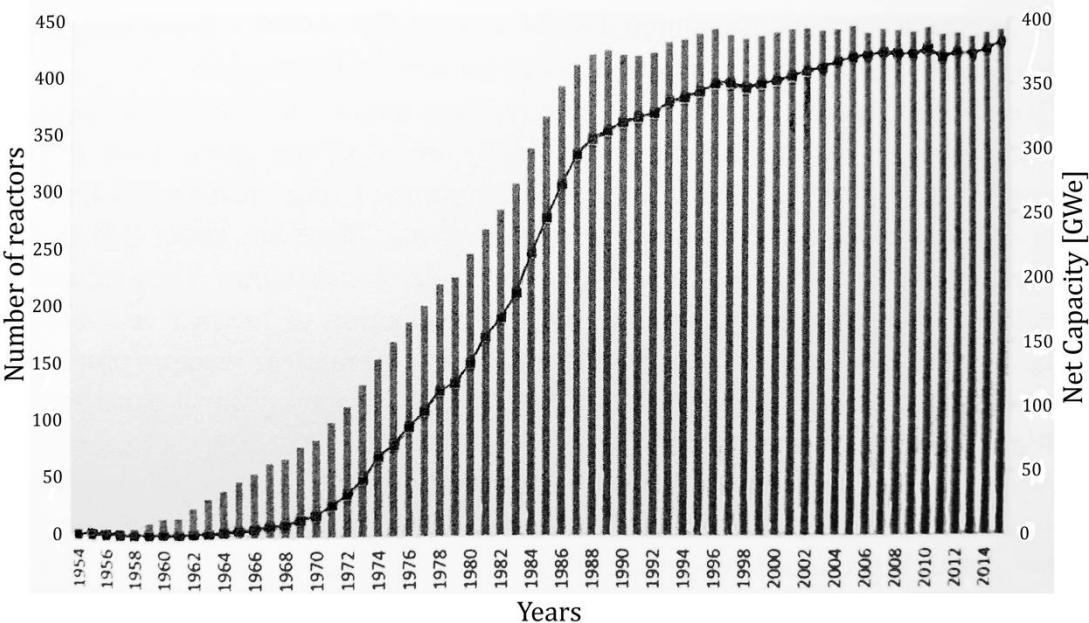
Figure 5 The capability of energy production by nuclear reactors in world (bars and scale on the right) compared to the number of reactors (line and scale on the left) in years 1954 to 2014 [9].

In 2018 the ~ 450 nuclear power plants provided over 10% of the world's energy demand according to the World Nuclear Association. Currently about 50 reactors are under construction and more are planned to be build. Also, the maintenance and upgrading of the existing units are still provided, which aims to prolonging their lifetime, improving safety systems, and ensuring the high economical profits through increasing capacity [9], [17]–[19].

About 67% of the world's nuclear reactor capacity is currently made up of PWRs, which together with BWRs provide about 20% of the world's nuclear energy. It is an important note that the accidents in water-based reactors (PWR and BWR) have never been the direct cause of death [11].

The rapid development of the industry was associated with the unprecedented increase in the need for energy. The old technologies based on the oxidation of fossil fuels have well known problems of finite resources and combustion caused serious problems of environment pollution in comparison with nuclear power. Nowadays the increased popularity can be noticed in alternative ways of generating energy from the forces of nature, like from wind, geothermal heat, sea or river water although theses may not be sufficient enough to satisfy the market demands [11].

1.4. Summary

1.4.1. Aims

The main aim of the work was to develop a new approach of the numerical modelling of the heat treatment during manufacturing of the large-size forgings, for the residual stress prediction purpose. As the expected result, the model able to map the residual stress within the cross section due to the transient temperature field and the phase transformation, based on the dilatometric curves obtained from mechanical tests, was developed. The involvement of the numerical methods was especially enhanced as the fast and economic way of the implementing the model in the industrial conditions. The particular emphasis was put upon the representation of the cooling stage during the heat treatment.

The secondary aim of the work was to perform the overall investigations of the origins of the residual stresses, which arise due to the thermal contraction and phase transformation in the cooled part. The implemented parameters represent the SA508 gr. 3 steel – the material widely used for the construction of the reactor pressure vessels (RPV). Broadening the knowledge of the area was achieved by the development of the set of the numerical models,

created on the way to the final model, together with the support of mechanical testing and microscopic observations.

1.4.2. Application

Thanks to the developed approach of the final model, which is based on mapping the transient temperature field and calculating the cooling rate within the part, and then combining the results with dilatometric curves obtained during mechanical tests, the model can be widely used in numerical modelling of residual stresses during heat treatment of steels. The implementation of the set of dilatometric tests results allows for calibrating the model to the particular material, when the numerical approach allows for adjustment of the precise boundary conditions. In this work, the model was created for the elements for nuclear reactor pressure vessels. During manufacturing parts of such large-size dimensions, stresses arise due to the mismatch between the local volumes within the part. Such mismatch is caused by the difference in thermal expansion/contraction coefficients, related to transient temperature field and the given microstructural phase. The model is able to calculate the local expansion/contraction during the heat treatment of the part to predict the residual stress, which leads to control their final values at the end of the process.

1.4.3. Importance

As the concerns of the using of the conventional fuels are arising and the renewable sources of energy are still not satisfying the increasing with every year demands of the global market the investigations towards efficiency and safety of the nuclear energy production became of significant importance. Achieving the numerical control over the arising residual stress during the manufacturing of RPVs, which are key elements of the nuclear power plants, is one of the main goal. Also, it has to be mentioned that broadening the knowledge about the overall rules of the residual stress control in nuclear materials will bring profits in the other material manufacturing branches. A major contribution of this work is to extend and systematise the

knowledge of the genesis of residual stresses arising in large-size forgings used for RPV elements.

2. Literature review

2.1. Theoretical background

2.1.1. Nuclear reactor pressure vessels materials

The nuclear reactor pressure vessel is a stainless steel or concrete container, which surrounds the fuel installations, the control rods and the coolant circuit. Its essential purposes are to prevent the radiation generated in the core of the nuclear reactor from leaking outside and to maintain the high pressure of the coolant in water based reactors (PRW, BRW). Such a process has a positive effect on the plant efficiency. The shape and the size of the nuclear reactor pressure vessel is related to the given power plant, its construction, solutions and the amount of heat generated by the core. In *Table 1*, *Table 2* and *Table 3* some of the parameters and dimensions of typical reactors used worldwide are presented.

Table 1 Materials and wall thickness of various reactor pressure vessels [17]:

Reactor type	AGR	HTGR	PWR	BWR	CANDU	LMFBR
Wall thickness [mm]	~5800	~4700	~225	~150	~30	~25
Material	Concrete	Concrete	Steel	Steel	Steel	Steel

As it can be seen from *Table 1* and *Table 2*, the wall thickness of the Reactor Pressure Vessels can vary greatly, depending on many factors. These parameters give one overall insight of the amount of the material needed for manufacturing the Reactor Pressure Vessels to ensure the safety and soundness to withstand high pressure during operation at high temperature.

Table 2 Dimensions of various Reactor Pressure Vessels [17]:

Reactor Type	Pressure Vessel Height [m]	Pressure Vessel Width or Diameter [m]	Wall Thickness [mm]	Composition	Other Features
PWR	13.4	4.83	224	SS clad carbon steel	N/A
BWR	21.6	6.05	152	SS clad carbon steel	N/A
CANDU	4.0	7.6	28.6	Stainless steel	Pressure tubs
HTGR	14.4	11.3	4720	Reinforced concrete	Steel liners
AGR	21.9	20.3	5800	Reinforced concrete	Steel liners
LMFBR	19.5	21.0	25	Stainless steel	Pool type

From *Table 2* it can be seen that there is no simple correlation between the dimensions of the Nuclear Reactor Pressure Vessels and the wall thickness. Concrete reinforced with steel liners is used, when the construction and its wall thickness are relatively large, as in the case of AGR (Advanced Gas-cooled Reactors). The PWR and BWR use low carbon steel with a stainless steel liner, as the construction must be strengthened in case of brittleness due to the long-time exposure for radiation [17].

Table 3 Common Reactor Pressure Vessels wall thicknesses and operating pressures [17]:

Reactor Type	Operating Pressure [MPa]	Operating Pressure [PSI]	Wall Thickness [mm]	Wall Thickness [in.]
PWR	15.5	2250	225	8.86
BWR	7.15	1050	150	5.90
CANDU	10.0	1450	30	1.20
HTGR	5.0	725	25	1.00
AGR	4.3	625	4700	158.05
LMFBR	~0.1	15.0	5800	228.35

It can be seen from *Table 3* that the operating pressure of the Pressurized Water Reactors is much higher that for the Boiling Water Reactors, although the dimensions of the BWR are larger. It is compensated with the thicker steel walls, which indicates that the wall thickness is related to the operating pressure of the reactor [17].

Reactor pressure vessels wall thickness is directly related to the resilience and safety of the nuclear power plant. The concept of Defence-in-Depth is presented in *Table 4*. Its scheme is briefly shown in *Figure 6*. It is an approach used worldwide for designing the power plant, which ensures the safety for workers every day and in case of accidents. Typically, it consists of five levels, which can be described as: 1th – prevention of failures, 2nd – detection and control of failures, 3rd – control of design basis accidents, 4th - control of severe accidents, 5th – emergency plans.

Table 4 Defence-in-depth scheme [9] :

Levels of defence-in-depth	Objective	Essential means
Level 1	Prevention of abnormal operation and failures	Conservative design and high quality in construction and operation
Level 2	Control of abnormal operation and detection of failures	Control, limiting and protection systems and other surveillance features
Level 3	Control of accidents within the design basis	Engineered safety features and accident procedures
Level 4	Control of severe plant conditions, including prevention of accident progression and mitigation of the consequences of severe accidents	Appropriate containment, complementary measures and accident management
Level 5	Mitigation of radiological consequences of significant releases of radioactive materials	On-site and off-site emergency response

Every level describes operations, tools and methods, which helps stopping spread of the damage to the next level and reduce the adverse effects from the previous levels.
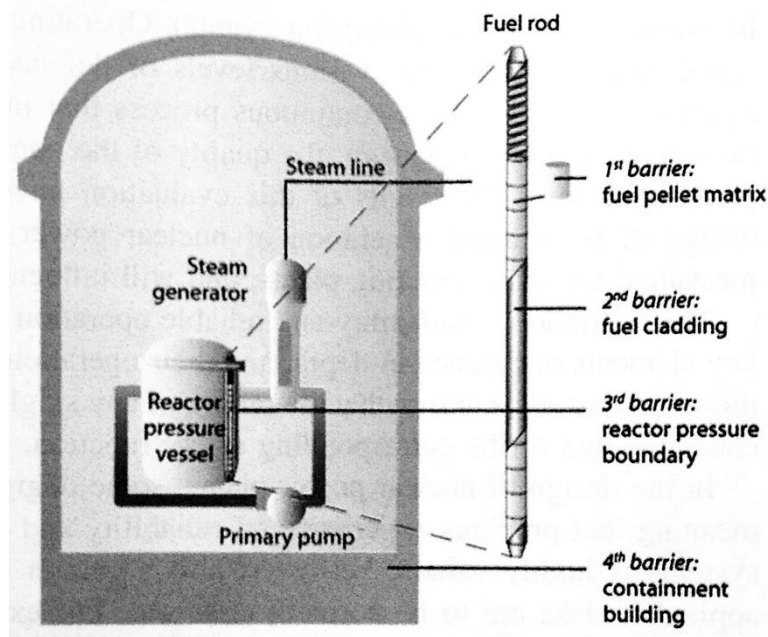
Figure 6 The representative barriers for each level in the Defence-in-Depth safety systems [9].

The typical barriers related to each of the level are presented in Figure 6. Among many, the fuel pellet matrix (1st barrier), fuel cladding (2nd barrier), reactor pressure boundary (3rd barrier) and containment building (4th barrier) can be distinguished. The radiation from the fission of radioactive materials is mostly prevented by the first and the second barriers. It can be seen that the nuclear reactor pressure vessel is a crucial component in operational and safety system, as a container for the core of the nuclear reactor and primary circuit of coolant (typically water) [9].

The design of each nuclear vessel is different as there are many factors that have to be adjusted to the chosen technology and conditions of the certain power plant. It forces manufacturers to conduct research for constantly increasing the quality of the materials to ensure durability, longer lifespan and meeting the safety standards by the elements of new plants with a greater capacity. Often the life span of a power plant is perceived as a life span of a Reactor Pressure Vessel, as the one of the most crucial element. The steel used during manufacturing RPV, the cover of the most common Pressurized Water Reactors, is SA508 grade 3.

2.1.2. SA508 grade 3 steels

The SA508 steels are a low-alloy ferritic material, which presents relatively better resistance during operation at higher temperatures and under higher pressure environment together with the resistance to the radiation embrittlement. *Table 5* presents the chemical composition for each of the grade according to the ASTM. As the mechanical properties are strongly related to the chemical composition the further division for grades and classes is presented in *Table 6*, together with related values of the tensile strength, the yield stress and absorbed energy. Further in this work *Figure 62* presents the continuous cooling transformation curve of SA508 grade 3 class 1 and class 2, where the difference in the transformation start temperatures for the related phases can be observed due to the differences in chemical composition (mostly C, Mn, Ni and Cr). Due to the various conditions of the running of phase transformation, each of the grades demands a characteristic heat treatment scheme [3]. For manufacturing nuclear Reactor Pressure Vessel the SA508 grade 3 class 1 and grade 2 class 1 are commonly used, because of their weldability, toughness and strength with low cost at the same time [20], [21]. The SA508 grade 4N is a material, which is under investigations as the new candidate for the modern designs of the nuclear power plants. Some interesting properties, like higher tensile strength, toughness and irradiation embrittlement resistance, were reported, but this material is still under rigorous inspection before it will be allowed for wider use in industry [3].

Table 5 Compositions of SA508 steel in weight percent according to the ASTM [3], [4]:

	Grade 1	Grade 2	Grade 3	Grade 4N
Carbon	0.35	0.27	0.25	0.23
Manganese	0.40–1.05	0.50–1.00	1.20–1.50	0.20–0.40
Nickel	0.40	0.50–1.00	0.40–1.00	2.80–3.90
Chromium	0.25	0.25–0.45	0.25	1.50–2.00
Molybdenum	0.10	0.55–0.70	0.45–0.60	0.40–0.60
Silicon	0.15–0.35	0.15–0.35	0.15–0.35	0.15
Sulphur	0.25	0.25	0.25	0.25
Phosphorus	0.25	0.25	0.25	0.25
Vanadium	0.005	0.005	0.005	0.005

From both of the tables (*Table 5* and *Table 6*) it can be seen that the chemical content range of the elements are wide enough to provide different mechanical compositions. Grade 3 class 1 and grade 2 class 1 of the SA508 are usual materials for the pressure vessels forgings, with tensile strength of 550 MPa. Higher classes of these steels have higher strength, on the level 620 MPa, like SA508 grade 3 class 2 steels, which are used for the Steam Generator forgings. There are different values of the mechanical parameters for the SA508 grade 3 class 1 and class 2, despite the same chemical composition specifications given. Such effect can be achieved due to the changes of the alloying elements content within the range and with the related changes of the tempering parameter. The strength and toughness can be increased, but one has to pay attention on the properties like toughness or weldability. Such counterweight relationships must be always under consideration during manufacturing of the SA508 steels. For example, the chemical composition related factor called carbon equivalent (Ceq) increases together with the tensile strength and 0.2% yield strength, which decrease with the increase of the temper (Larson-Miller) parameter. On the other hand the best values from the Charpy test are achieved using the temper parameter within the particular range. Also, the strength of the material increases together with the decrease of the toughness, what can inflect the

hardenability. Such degradation one can fight by increasing the amount of the alloy elements, but this can in turn affect weldability [21].

New technologies of the IV Generation nuclear plants require better materials, which higher strength allows for building greater size of the elements and/or reducing their weight, which leads to advantages like reduction of manufacturing costs, improving the resistance to the natural disasters like earthquakes (Fukushima accident for example) and enhancing the durability of the elements [21]. The SA508 steels are commonly used worldwide in nuclear systems designs for manufacturing many of the elements due to their good strength to toughness balance, weldability and resistance to the radiation embrittlement [22]. Recently the steel SA508 grade 4N is being developed as a material for power plants of Generation IV reactors. In *Table 7* one can see that the presented in *Table 5* higher content of nickel and chromium, with decrease of manganese content, allowed for achieving better than in SA508 grade 3 steel strength and toughness, but at the expense of elongation [20].

Table 6 Mechanical properties and chemical composition of SA508 steels according to ASME [21]:

T.S. level (MPa)	Material	Requirement for chemical composition (wt. %)									0.2% Y.S. (MPa)	T.S. (MPa)	Absorbed energy (J)		
		C	Si	Mn	P	S	Ni	Cr	Mo	V			Temperature (°C)	Average	Each
550	SA508 Gr.2 Cl.1	≦0.27	0.15/0.40	0.50/1.00	≦0.025	≦0.025	0.50/1.00	0.25/0.45	0.55/0.70	≦0.05	≧345	550/725	4.4	≧41	≧34
	SA508 Gr.3 Cl.1	≦0.25	0.15/0.40	1.20/1.50	≦0.025	≦0.025	0.40/1.00	≦0.25	0.45/0.60	≦0.05	≧345	550/725	4.4	≧41	≧34
620	SA508 Gr.2 Cl.2	≦0.27	0.15/0.40	0.50/1.00	≦0.025	≦0.025	0.50/1.00	0.25/0.45	0.55/0.70	≦0.05	≧450	620/795	21	≧48	≧41
	SA508 Gr.3 Cl.2	≦.025	0.15/0.40	1.20/1.50	≦0.025	≦0.025	0.40/1.00	≦0.25	0.45/0.60	≦0.05	≧450	620/795	21	≧48	≧41
725	SA508 Gr.4N Cl.3	≦0.23	0.15/0.40	0.20/0.40	≦0.020	≦0.020	2.8/3.9	1.5/2.00	0.40/0.60	≦0.03	≧485	620/795	-29	≧48	≧41
	SA508 Gr.4N Cl.1	≦0.23	0.15/0.40	0.20/0.40	≦0.020	≦0.020	2.8/3.9	1.5/2.00	0.40/0.60	≦0.03	≧585	725/895	-29	≧48	≧41
	SA543 Type B Cl.1	≦0.20	0.15/0.40	≦0.40	≦0.020	≦0.020	2.25/4.00	1.00/1.90	0.20/0.65	≦0.03	≧585	725/860	-	-	-
795	SA508 Gr.4N Cl.2	≦0.23	0.15/0.40	0.20/0.40	≦0.020	≦0.020	2.8/3.9	1.5/2.00	0.40/0.60	≦0.03	≧690	795/965	-29	≧48	≧41

It is of great importance to quickly introducer newer, safer and better materials, although the SA508 grade 4N steel is still being developed. Compared to the SA508 grade 3 steel researches have shown better mechanical properties, but there is a lack of data from the actual in-service operation [3], [4], [20]. The SA508 grade 3 steel was commonly used for manufacturing of pressure vessels, compressors and steam generators for over 40 years [23]. The amount of empirical data taken during work of the plants makes this material a reliable option, although there is still lack of professional and well conducted research upon it. Due to the high safety standards and vast consequences of failure the nuclear market is very reserved in terms of using new materials. The admittance and gradual introduction take a great amount of time. Even if the new and relatively better materials like SA508 grade 4N are being designed, in many cases it is still economically favourable to conduct research on the older grades, like SA508 grade 3, to improve its outcome and prolong its lifetime [3], [4].

Table 7 Mechanical properties of various chemical composition of SA508 steel [3], [4]:

	Tensile strength [MPa]	Yield strength [MPa]	Elongation [%]
SA508 Grade 1	515	345	16
SA508 Grade 2	611	448	18
SA508 Grade 3	611	468	29
SA508 Grade 4N	725	585	18

The properties of the SA508 steels allow for joining together of different elements of the Reactor Pressure Vessel by arc welding [20]. It is an important feature as in the case of Nuclear Reactor Pressure Vessels the dimensions are very large and one unit has to be combined from smaller welded components (Figure 7) [4].

The steel intended for the manufacturing of the crucial components of the nuclear power plants must have appropriately high strength to work at high temperatures and under increased pressure. Also, to minimalize the potential risk of failure during unforeseen events, the high fracture toughness is needed to withstand instantaneous shocks. Reactor Pressure Vessels, which perform as the major safety boundary for the radiation from the nuclear reactor core are

especially exposed for this kind of risk. The irradiation embrittlement caused by the free neutrons violate the integrity of the construction by increasing the temperature of the ductile to brittle fracture transition. This phenomenon can significantly reduce the life span of the element as fast fracture has higher probability to occur [4], [24].

2.1.3. Reactor Pressure Vessel manufacturing

Various factors have to be considered during the manufacturing processes of each of the Reactor Pressure Vessel, what makes the design of each element unique. However, some of the rules that must be followed in every project are common. The process is described in general terms below.

The scrap steel is melted down in an electric arc furnace. The chemical composition of the melt is carefully controlled to avoid the addition of such elements as phosphorous, sulphur or copper. These elements increase the susceptibility for embrittlement, which in this case is especially dangerous, and are generally unwanted in steels due to the bad impact that they have on the mechanical properties [4], [25], [26].
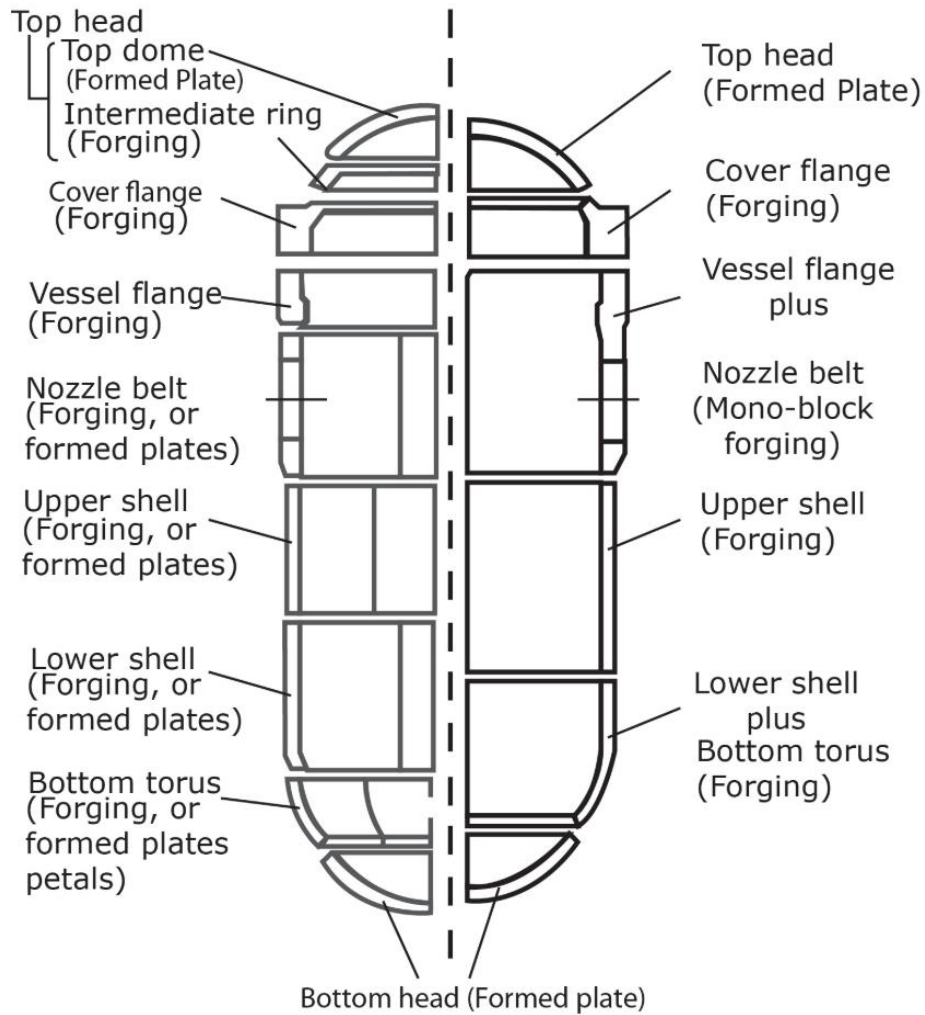
Figure 7 Reactor pressure vessel design. Modern approach on the right [4].

Pous-Romero [4] presented how the development of the metallurgical knowledge over the years helped decrease the level of the deleterious elements in steel. From the 1970s to 1980s the percent weight content of sulphur in steel decreased from around 0.016 – 0.008 to 0.007 – 0.003, when in the 2010s it dropped below <0.0001. The percent weight content of phosphorus was in a wide range between 0.015 – 0.01 in 1970s. In the middle of the 1980s this content was lowered to around 0.008 to below the <0.0001 [4].

Achieving the lowest as possible level of hydrogen, oxygen and nitrogen is very important, so the melted steel is degassed through the vacuum stream method. This process is performed during pouring the melt to the moulds.

The vacuum carbon deoxidation can cause the extended grain growth during production of the large size steel elements. To prevent this aluminium can be added to the melt or such refining method is replaced by a different available one [4], [27]. Although it has been reported that changing the refining method has an insignificant impact on the yield strength and ultimate tensile strength, the methods that are used to decrease of the level of sulphur have a beneficial effect to fracture toughness [4], [28], [29]. Vacuum Carbon Deoxidation affects segregation patterns in large size forgings destined for reactor coolant pump manufacturing, which improves cold cracking resistance caused by segregation and decreases the possibility of strain-induced embrittlement in heat affected zones (Figure 8) [27].
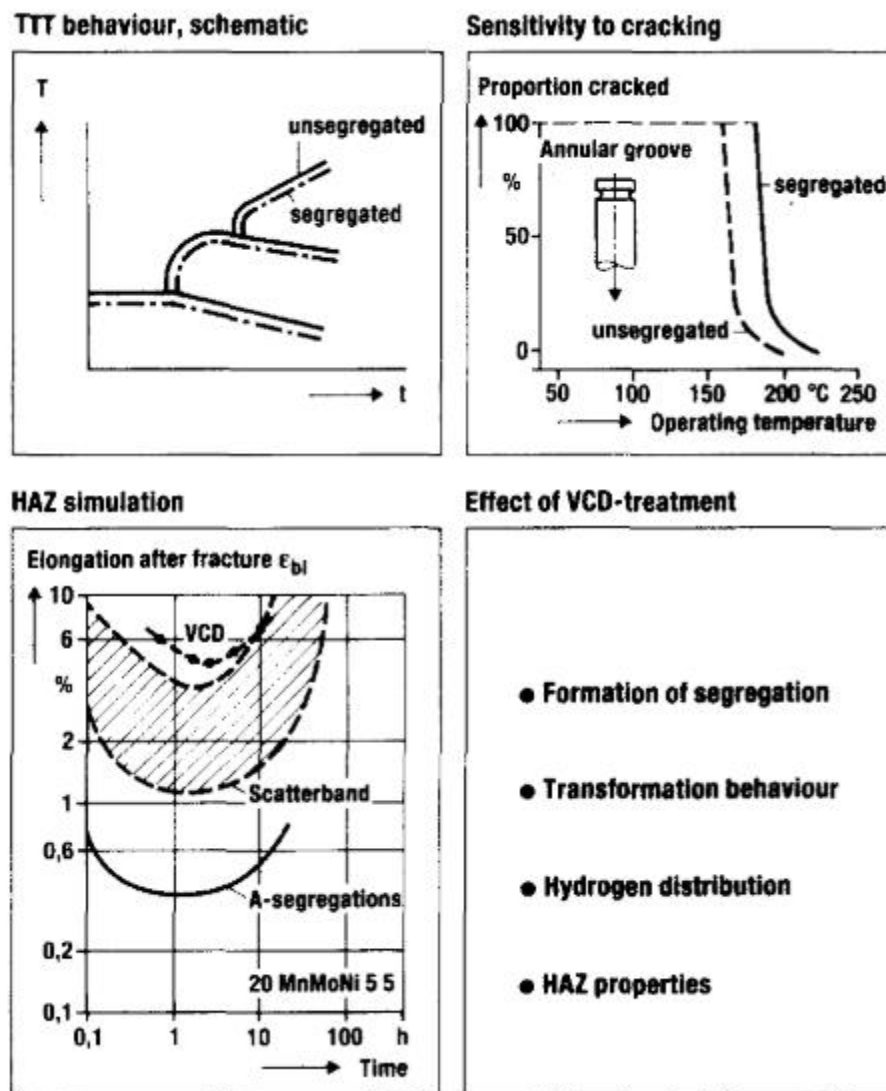

Figure 8 Vacuum Carbon Deoxidation benefits to the structural characteristics [27].

After cooling down, the ingots are forged to obtain the specific shape of the element. Due to the economic and structural reasons the forging process is carried on in the austenitic phase of the material, above the Ac_3 temperature, between 880 and 1250°C, where the force needed to deform the workpiece is lower. Manufacturers have to design each of the processes carefully to implement as few as possible instances of reheating of the ingot to keep the temperature up, because such operation increases the time of production and is associated with higher costs [4].

In modern plastic deformation processes obtaining the required shape of the element is only part of the goal. An issue of a great importance is to change the initial as-cast microstructure, which can suffer from clusters of inclusions, high porosity and segregation. It is a significant condition to ensure a sufficient level of a degree of deformation to induce the dynamic recrystallization and change the microstructure (*Figure 9*) [3], [4], [30].

The degree of the deformation is a key parameter in plastic deformation processes. It determines how much the original microstructure of the material has changed through the given processes. This is strongly associated with the properties of the finished product and also allows for comparing various technological processes in relation to the level of the microstructure change for the same material. There are many ways to calculate the degree of forging, depending on the operations used and the geometry of the input shape. The simplest ways are associated with the most basic operations. For elongation, similarly to the elongation factor, it is the ratio of the area of the initial section S_0 to the resulted area S [30], [31]:

$$\lambda = \frac{S_0}{S}, \text{ or } \lambda = \frac{l_0}{l}, \tag{2}$$

For upsetting, it is the ratio of the height of the input material h_0 to the height of the upset forging h.
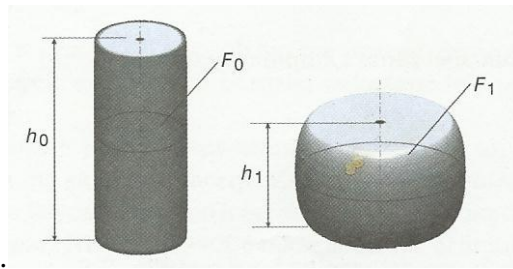
$$\lambda = \frac{h_0}{h}. \tag{3}$$

Figure 9 Material dimensions when calculating the degree of forging in the upsetting process [30].

Determining the degree of deformation is very important because even a small forging reduction changes the mechanical properties and structure of the metal. The largest changes can be observed at the beginning when the element has an ingot structure. Ingots crystallize in a very heterogeneous manner. Their structure is presented in Figure 10. The segregation increases with the content of alloy elements in material; the more microelements, the larger effect of the segregation occurs. When designing forging technology, it is therefore very important to take into account the order and number of processes to eliminate this structure.
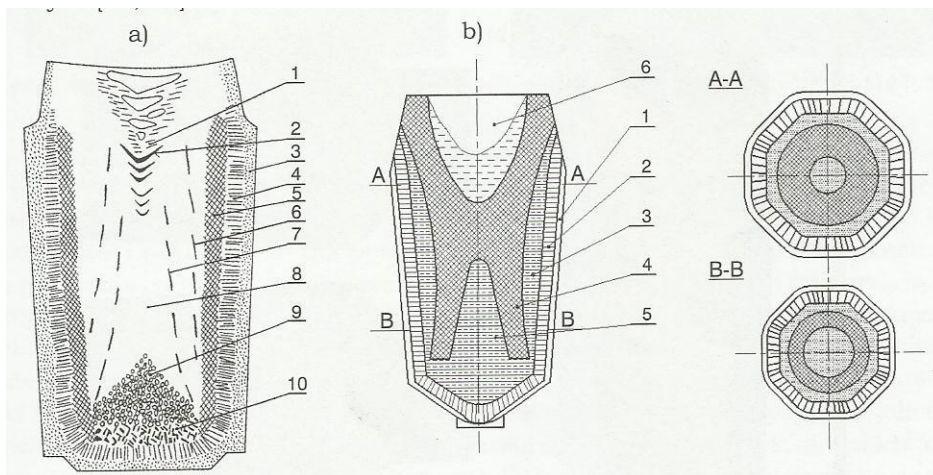
Figure 10 Structure of the forging ingot: a) an overview diagram, where 1 - positive segregation, 2 - V segregation, 3 - small, frozen crystals, 4 - bar crystals, 5 - transition zone, 6 - external segregation lines "reverse V", 7 - internal segregation lines "reverse V ", 8 - the zone of various axis crystals, 9 - the sedimentation cone - negative segregation, 10 - sediment oxides; b) range of segregation zones in the ingot, where: 1 - a layer of frozen crystals, 2 - a

26

layer of bar crystals, 3 - transition zone of multidirectional crystals, 4 - segregation zone (possible streakiness), 5 - equiaxed crystals zone, usually quite thick - segregation negative, 6 - solidification zone in the last phase (without pronounced segregation), omnidirectional crystals quite fine [30].

Analytical studies have shown that when the degree of forging is:

- 1 – 3; in the free crystal zone of the ingot the visible fibers appear, and in the middle zone, in which the pillar crystals are located, the dendrite axes are slightly deflected from their original position;
- 4 – 6; the deviation of the dendrites from their location is very pronounced, and in a further increase in the degree of processing in the entire forging volume a fibrous structure appears [30], [31].

To produce a structure that will ensure the right properties, the process conditions must be selected specific to the particular manufactured element. Among the many important parameters are for example the direction of fiber arrangement, which cannot coincide with the direction of the metal flow or deviations which can be caused by uneven deformation. To improve the properties, generally small degrees of deformation are used in all directions. As it increases, the metal's properties improve the most in the direction where the largest deformation was imposed, which also results in a deterioration of properties in other directions. Such phenomenon has a special influence on impact strength, necking and elongation [30], [31].

However, it is impossible to produce the ingot without segregation, especially when the weight can be up to 300 tonnes. The usual method is to simply remove these parts of the ingot, which contain most of the detrimental defects, like shrinkage voids or clusters of inclusions, but this can only be done where the final shape of the element allows material removal. Most of the segregation effects are in the core of the ingot, and also at the bottom and at the top. However, removing of all of these parts is not possible during manufacturing open-ended cylindrical vessels. During manufacturing of the blind-ended vessels some of the inclusions stays within the element as the method of boring cannot remove the negative segregation effects in the core. Another method for open-ended cylindrical component is hollow ingot technique, which reduces the cooling time of the ingot, which has a tremendous effect on segregation [3], [4], [25], [32].

The degree of deformation in forging used in practice:

- 3 – 4.5; during free forging. Due to this value of the forging degree, the material has quite good longitudinal and transverse properties in terms of strength and construction,

- 3 – 6; if the material will be used as a die forging input;

- 10≤; used for making elements with high homogeneity of construction, very good mechanical properties in one direction and high fatigue resistance;

- 1.1 – 1.5; if the element has already been forged or rolled in previous operations [30], [31].

The method of deformation and the degree of processing also affect the internal structure by shaping the size of its grains. The most favourable situation for material properties is when the grains have the smallest possible dimensions. Such situation favours deforming of the material at high speed and with large reductions. The presence of a fine structure in the material before starting the process is also beneficial.

However, when the material is deformed from the so-called critical reduction, after recrystallization, a coarse-grained structure will be formed, which is the reason for the very unfavourable properties of the material. The critical reduction is in the range of $2 - 10\%$, depending on the type of material. When the material is subjected to deformations of a value lower than the critical reduction, despite the fact that the heat requirement is maintained for recrystallization to occur, only the healing process will take place in the material and it will result in the formation of a coarse-grained structure [30], [31].

As it was mentioned that the manufacturing of the element for Reactor Pressure Vessels from large-size ingots varies depending on the particular design. However, most of the elements are cylindrical or shell shaped, so before the final stages some of the processes can be distinguished, which are common for most of the designs. Corresponding with pictures in Figure *11* these are:

a, b – cogging; to break the internal ingot structure, very high reduction ratios are needed, at least 75%. At the initial stage of the forging the ingot undergoes such processing along its longitudinal axis. The aim of this procedure is to achieve the change of the microstructure before obtaining the final shape.

c – upsetting; in this stage the increase of the cross section of the ingot occurs at the expense of its height. The reduction ratio must be enough sufficient to start dynamic recrystallization, which changes the ingot primary structure.

d – trepanning; in this stage, the core of the ingot is removed. Due to the segregation, it is a very nonhomogeneous area. e, f – becking and drawing; these stages are very similar. The hole, which was bored inside the forging in the previous stage is broadened by a kind of special tool. Simultaneously the thickness of the wall is decreased. After achieving the required length of the forging, only the wall thickness is further reduced [3], [4], [33].
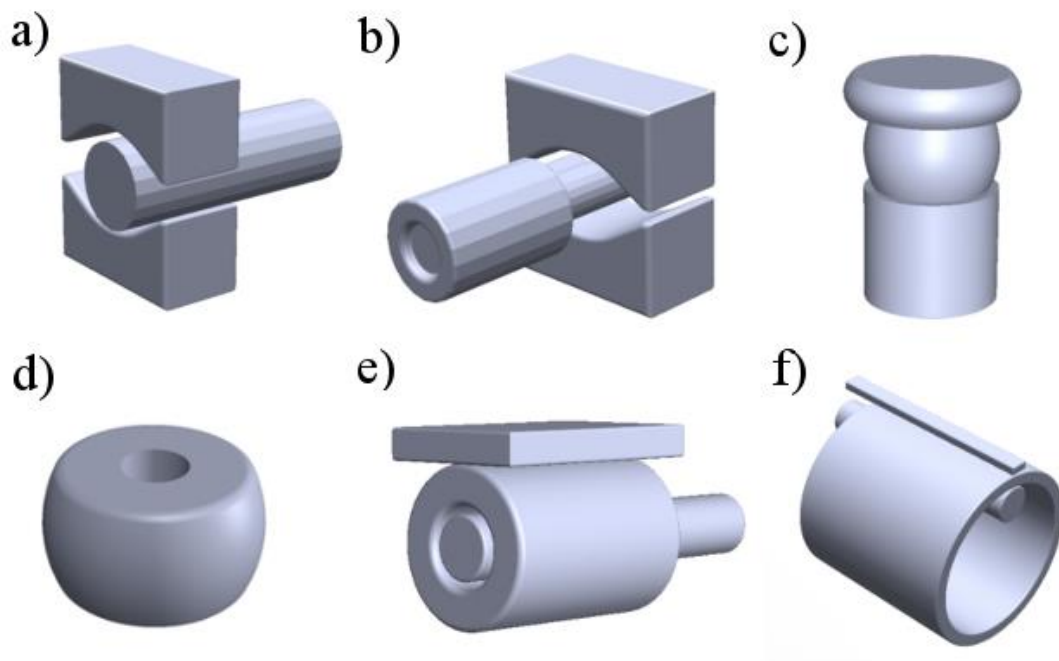
Figure 11 The general scheme of manufacturing reactor pressure vessel cylindrical element: a) first stage b) cogging c) upsetting d) trepanning e) becking f) drawing [3], [33], [34].

In *Table 8* a list of the manufacturing processes applied to the element for the Reactor Pressure Vessel production is presented. For each of the sections the key process parameters are highlighted. Such processes can take up to 12 months, depending on the complexity of the design [32].

Table 8 Stages of the Reactor Pressure Vessel element manufacturing process with major process parameters [32].

Stage	Major process parameters
1. Steelmaking	Teeming temperature
2. Ingot transfer	Ingot temperature
	Transfer time
	Ingot size (weight)
3. Ingot soaking	Soak temperature
	Soak time
4. Initial forging and discards	Discard size
5. Finish forging	Forging reduction (consolidation)
	Grain flow
	Minimum forging temperature
6. Primary heat treatment	Austenitising temperature
	Treatment time
7. Preliminary machining and UT	Defect size
8. Quality heat treatment	Austenitising temperature
	Tempering temperature
	Treatment time
9. Quenching	Quenchant flow
	Agitation

	Quenchant temperature
	Transfer time
	Immersion time
10. Machining to rectilinear profile, UT inspect and mechanical test	Defect size
11. Final machining	Dimensional control
	Corrosion protection
12. Final NDE, inspection, pack and dispatch	Lift point locations
	Packaging

The constantly developing nuclear industry market, driven by the world's growing energy needs, increases the demands for the forgings of very large dimensions and weight [19], [26], [35]. The large dimensions of the Reactor Pressure Vessels come ahead to the demands of the market, which go towards longer lifespan of the power plants and increasing their capacity. Such a trend forced manufacturers to increase the size of Reactor Pressure Vessels. It is commonly known that the large single elements instead of numerously smaller ones welded together perform better due to the smaller amount of potential failure areas. It is also economically preferable, as such system needs less of a periodic weld control [19], [27], [36], [37]. In Figure 7 the Nuclear Reactor Pressure Vessel designed in the conventional way is shown on the left and in modern, with a few less elements, is presented on the right. Such approach ensures the faster manufacturing, no complicated supervising control, simplicity in preservation and increase the integrity between the elements of the plant [4], [24], [27], [38].

Increasing the dimensions of the Reactor Pressure Vessels means increasing the width of their walls, which can reach between 200 and 700 mm [39]. Many researches from the past assumed the microstructure on the cross section of the wall as bainitic throughout, but modern research showed that there are some significant variations there, mostly due to the difference in the cooling rate on the through-wall distance during the austenitisation [23]. It means that within the forging there is a serious risk of the occurrence of areas, which do not meet the required standards for properties. Although in literature there is no reported evidence of failure caused

directly by the material damage in the Reactor Pressure Vessel, such discovery forces the manufacturers to design the heat treatment based on the slowest cooling rate existing in the element [3], [4].

2.1.4. Heat treatment

The material's properties result directly from its microstructure. It is very important to know the microstructure of the material that one is going to use. The knowledge of the processes, which led to creation of the microstructure allows for the control over it, which results in achieving the required properties. Under the term of 'microstructure' one understands structure of the grain crystal lattice, distribution of precipitates and the phases inside the material. The scale of these objects can be various, from nanometres to even decimetres, although observation of the microstructure in steel is typically conducted between 100 nanometres to 100 micrometres. The developing of the new microstructure can be described in terms of thermodynamics and kinetics, where the growth and expansion of the new phase is connected with its kinetics, and thermodynamics refer to energy levels and driving transformation forces [20].
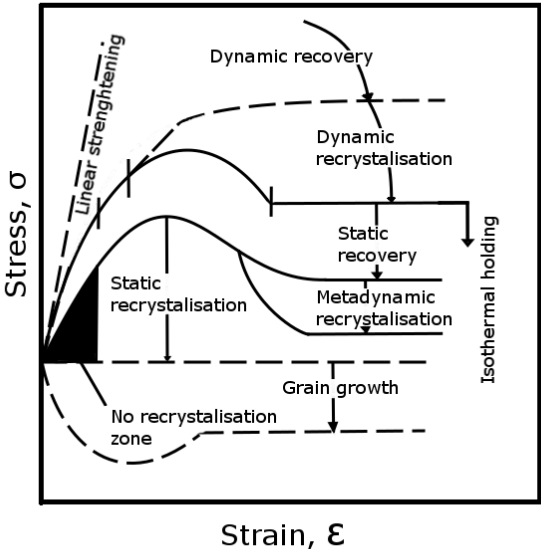

Figure 12 The influence of the strain and stress on the thermal activated mechanisms in the material [40].

One of the basic methods of changing the microstructure is to subject the material to the controlled heat treatment (*Figure 13*). The heat treatment processes can be divided into the primary and quality stages.
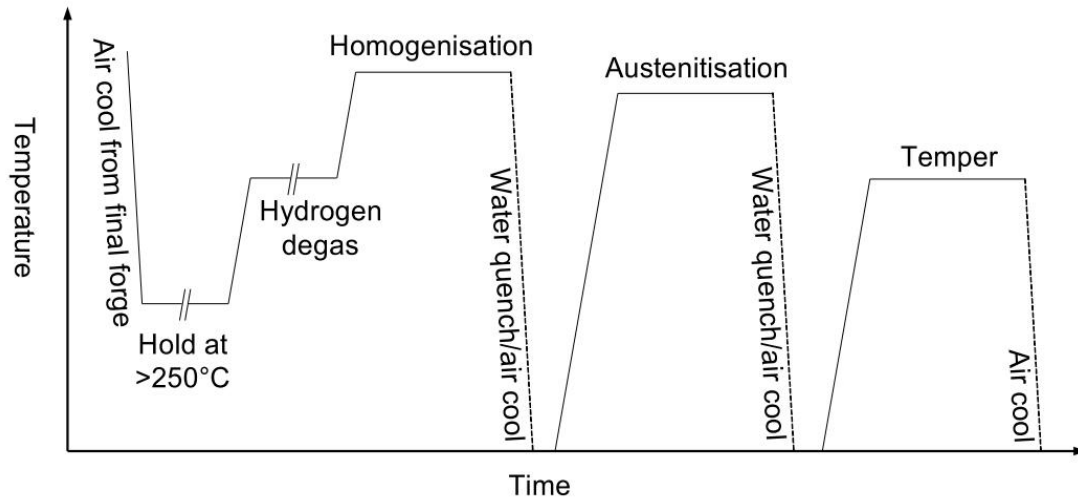

Figure 13 The primary heat treatment scheme of the large elements [33].

The first one is performed after the forging and its purpose is to ensure the clarity of the ultra-sonic investigations. It consists of the following steps [33]:

a) Transformation from forging; during the forging process the strain induced at the higher temperature introduces so much energy into the material that the process called dynamic recrystallization begins (Figure 12). Dynamic recrystallization occurs during the process of hot metal deformation (Figure 14). The driving force for that process is the deformation stored in the material, with the change enabled by the increased temperature. The low stacking-fault energy favours its start, which is also connected with the speed of deformation, the chemical composition of the material and the history of deformation of the material. Dynamic recrystallization leads to the creation of a metastable structure, because the new grains that are created are immediately subjected to stress causing deformation [40]. As noted before, forging is performed when the material is fully austenitic. After the forging the temperature drops and the

transformation to ferrite starts. In this stage the element is left as long as it is needed for the whole structure to transform to ferrite, i.e., below 500°C. The most important factor is to keep the temperature above 250°C because of the phenomenon called hydrogen cracking, which can lead to the catastrophic failure of the element and necessity of re-melting [33]. Hydrogen embrittlement is caused by the monatomic hydrogen, which diffuses below the surface and inside of the material, where it tends to create groups of atoms. It is very harmful process, of which the driving mechanisms through many years of proposing models is still heavily discussed [41].
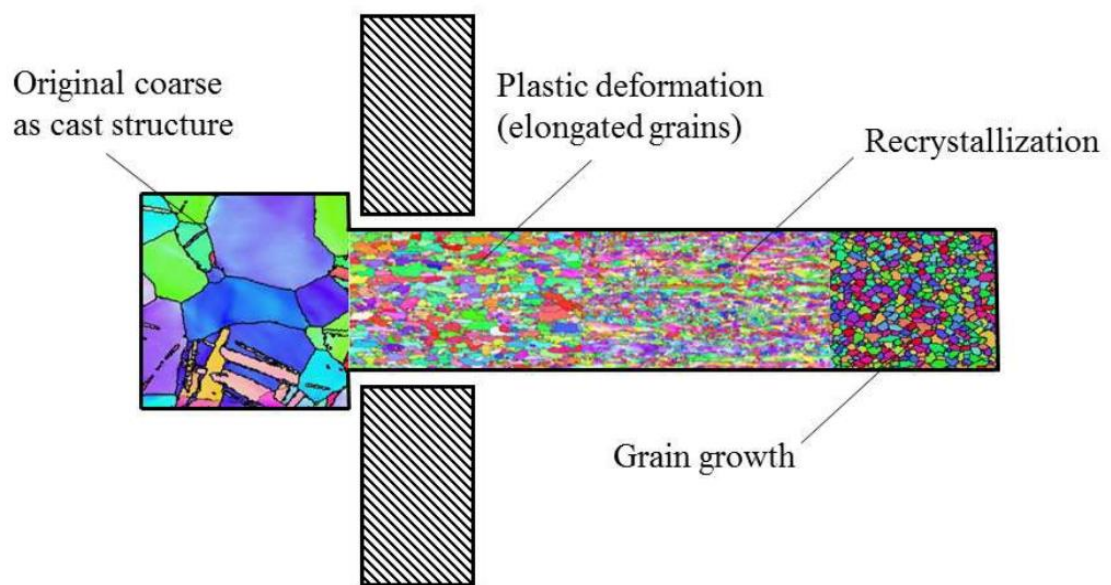

Figure 14 The dynamic recrystallization during forging [42].

b) Degas; hydrogen can be dissolved in both steel states, liquid and solid and is characterized by of the ability of quick diffusion within, but its presence is detrimental to the properties of steel [43]. Using hydrogen's high ability to diffuse it is removed from the material by heating up the element to the temperature of ~600 – 650°C, at which the forging is processed. During this action the hydrogen leaves by evaporating through the element surface. The time of this stage is related to the amount of the hydrogen within the forging at the beginning of the process. It lasts until this element reaches the desired level and can take up to several weeks for the very large cross-sections (>500mm).

c) Homogenisation; in this stage the forging is heat treated at 900 – 950°C, where second phase particles are dissolved. The time of holding at this temperature is related to the dimensions of the element. After heat treatment, cooling is applied. It is important to ensure that the whole structure transformed into ferrite. Two methods are performed, air-cooling and water quenching, where the second one is more popular due to the relatively better results in grain refinement processes.

d) Additional austenisation; as sufficient material transparency for ultrasonic inspection is one of the aims of the primary heat treatment additional austenitising is often undertaken. This heat treatment is at 860 – 890°C and followed by water-quenching, which can increase the clarity of the results during ultrasonic.

e) Tempering; the heat treatment of the forging causes the scale on its surface due to the oxidation of the material. To achieve clear images during ultrasonic investigation such surfaces have to be removed from the forging by the machining process, which is preceded by the tempering heat treatment. After the process, conducted at 600 – 650°C, the heated material is easier to remove during the machining, which is economically beneficial.

After the primary heat treatment (*Figure 13*), the ultrasonic investigation is performed to ensure that the material is free from defects. This stage is especially important for achieving the desired mechanical properties [33].
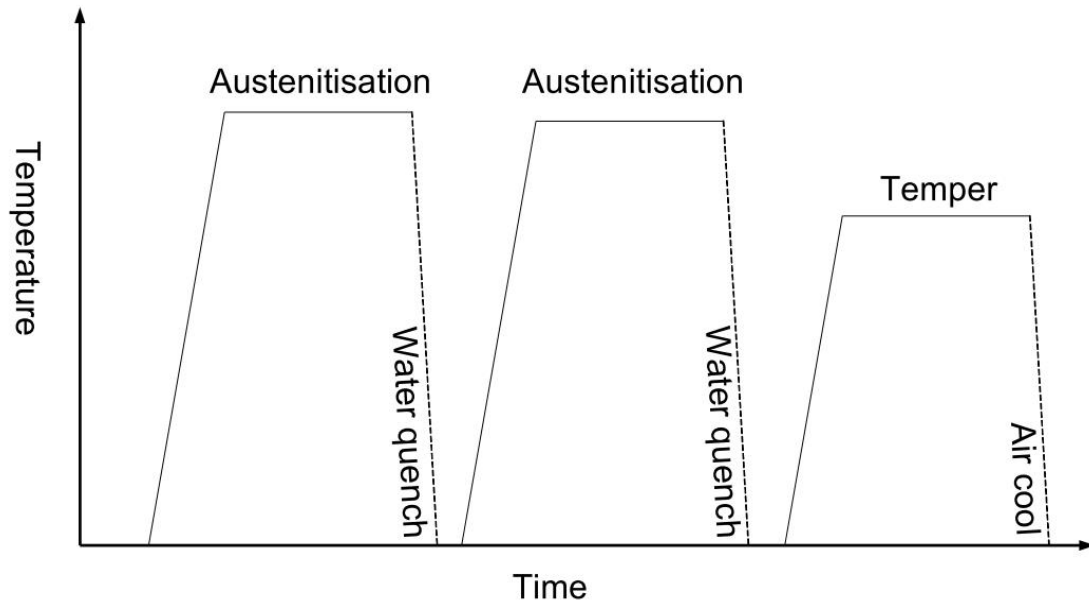
Figure 15 The quality heat treatment scheme of the large element [33].

A schematic of the quality heat treatment stages is presented in Figure 15. Before starting, the forging is machined to as close to net shape geometry as possible, taking into account the additional material which will oxidize during heating. The precise calculation of these dimensions is a very important because of the economic point of view, as the more material will be removed from the forging it will be less energy needed for the thermal operations on it. Also, the thinner wall thickness of the forging may be subjected to a better control over temperature profile during quenching, which has a tremendous impact on the microstructure development. The cooling rate, which is one of the most important driving factors in such a process, varies through the depth of the material, which can be responsible for the difference in the properties between the surface and the core of the thick-wall components.

During the quality heat treatment of the particular element the cycles of austenitisation with water quenching can be repeated until the desired microstructure is achieved before tempering. Due to the thermal inertia of the large scale mass during heat treatment it is a challenge to maintain the same temperature every time, so to avoid the risk of excessive grain growth, the temperature of each of the cycle is decreased progressively. As an example Cogswell in [33] described it as follows: if in the first cycle the austenitisation temperature is around 870 – 890°C, then in the following step this range is set up to 860 – 880°C.

At the end of the quality heat treatment, after the austenitisation and water quenching cycles, tempering is conducted. The key factors of the process, like time or temperature, are specific for the chemical composition and the forging [44]. The purpose of this stage is similar to these from primary heat treatment, which is softening of the material and making it more ductile at the expense of the strength. After tempering, the forging is machined to the final dimensions and then passed to the welding process. As noted before, the weld regions are the weakest point of the structure, so the final efficiency of the integrated vessel is related to the quality of the welds [33].

2.1.5. The pinning effect during grain growth

Developing sufficient strength and toughness of a steel element is one of the main objectives in metallurgical processing nowadays. Among many important factors, the grain size makes a great contribution to controlling of this feature. It is well known that heating of the material leads to grain growth, which is followed by a decrease in the yield strength of the material according to the Hall-Petch equation (4), and by the decrease of the material toughness. The equation presents the relation between the yield point σ_y and the refinement of the microstructure and indicates that the yield strength of the material is related to diameter of the grains d:

$$\sigma_y = \sigma_0 + kd^{-\frac{1}{2}} \tag{4}$$

where σ_0 is a internal friction stress and k is the material constant [45].

The control of the grain size also has a great impact on the hardenability, which is especially significant in the case of SA508 gr. 3 steels, which after the austenitising are often subjected to more than one tempering processes [4], [34], [46], [47]. In the low-alloy steels there are two main approaches to grain size growth control – austenitisation and particle pinning [4], [48].

As grain growth is related to increasing temperature or holding the temperature during heating, grain size control during austenitisation is clearly related to the temperature control. Figure 16 presents ways of developing microstructure using cooling rate, phase transformation and recrystallisation during cooling from the austenite phase in the microalloyed steels, which

contain Nb, Ti, V and Mn. The use of thermodynamic processes allows a wide spectrum of grain sizes to be achieved in the manufactured element, thus controlling the mechanical properties of the material [49].

INGOT STRUCTURE

Preheating of charge
(T_c, t_R, T_R)

Recrystallization:
– dynamic
– meta-dynamic
– dynamic + meta-dynamic

Austenite (A1, γ)

Static recrystallization

T_{ZR} { – precipitation process
– lack of static recrystallization

Recrystallized austenite

Hardened austenite

$(+)$

$– T_s = f(\varepsilon_\alpha, CR, D_\gamma, [M]) \approx A_{r3}$

Recrystallization of ferrite

$\gamma + \alpha$

$– T_f \approx A_{rt}$

ferrite (A2, α)

$d_\alpha = 6 \div 10 \mu m$

$d_\alpha = 1 \div 3 \mu m$

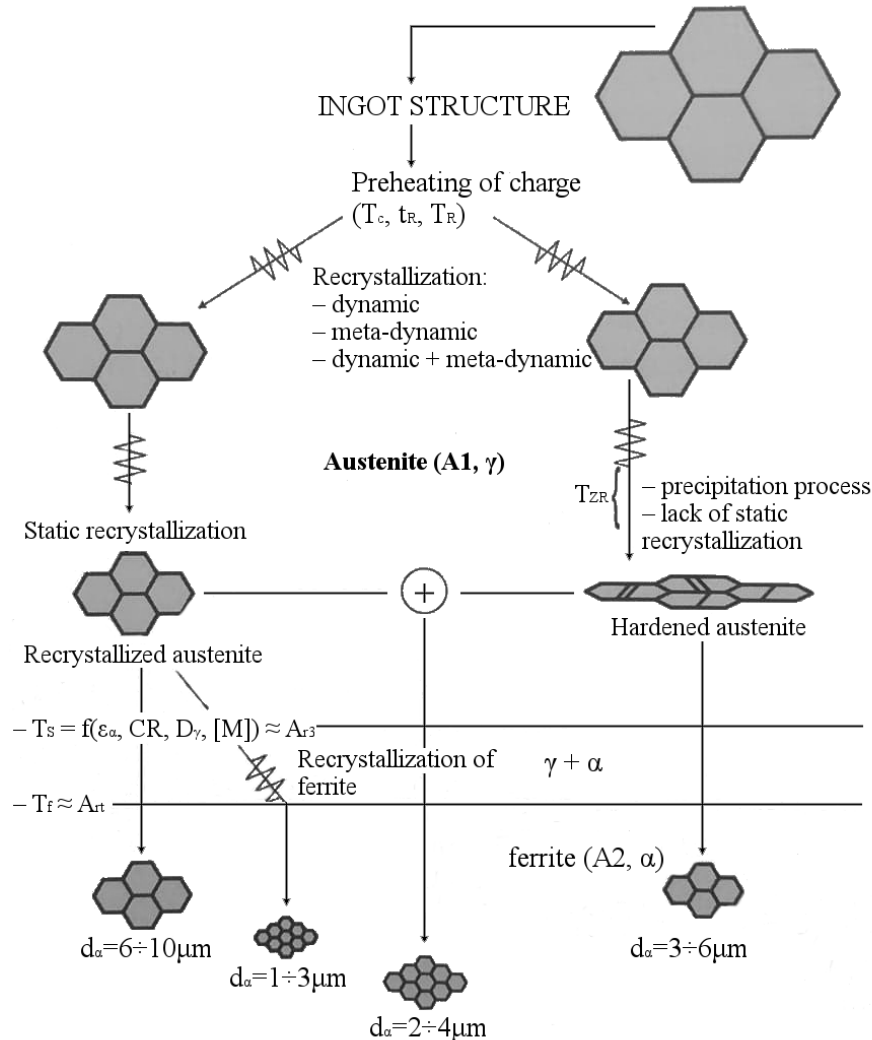$d_\alpha = 2 \div 4 \mu m$

$d_\alpha = 3 \div 6 \mu m$

Figure 16 The ways of thermomechanical processing use in order to obtain highly refined structure in microalloyed steels (Nb, Ti, V, Mn) [49].

Grain growth occurs through the motion of the grain boundaries. Particle pinning is a mechanism which holds back these movements. It involves the presence of an obstacle, like a particle of a different phase or a carbide in the matrix, which pins the moving grain boundary, interfering with it and delaying its motion. In the kinetic and thermodynamic equations which describes the grain growth, the initial austenite grain size of the material is a factor, which plays an important role. Such grain size is calculated from the time at which the material

microstructure is fully austenitic. During determination of the initial austenite grain size Pous-Romero in [4] reported that during the austenitisation of the SA508 gr. 3 steel there are two regimes of isothermal grain coarsening. As presented in Figure 17, it was estimated that during heating up to given temperature and holding for ~12h the increase in the grain size for temperatures up to 910°C is relatively small, not exceeding 10 μm. Above the 910°C grain growth increases rapidly and grain sizes can grow up to ~130 μm from the initial size of ~30 μm at the temperature of 990°C.

Such behaviour is typical for the presence of the particles, which pin the moving grain boundaries, holding back the grain growth, until the temperature of the material increases to the point where they are going to dissolve in the matrix. Above the 910°C the pinning particles in the SA508 gr. 3 disappeared, which allowed for the unrestricted expansion of the grains. Although there was no reported earlier evidence of such particles, Pous-Romero, using thermodynamics, high-energy X-rays, transmission electron microscopy and microanalysis, identified these as aluminium nitrides [3], [4], [34]. Increasing the aluminium content for the grain refinement was also reported in [50] to use the 20 MnMoNi 5 5 steel for thick steam generator tube sheet forging and also in SA508 gr. 3 steel in [51].
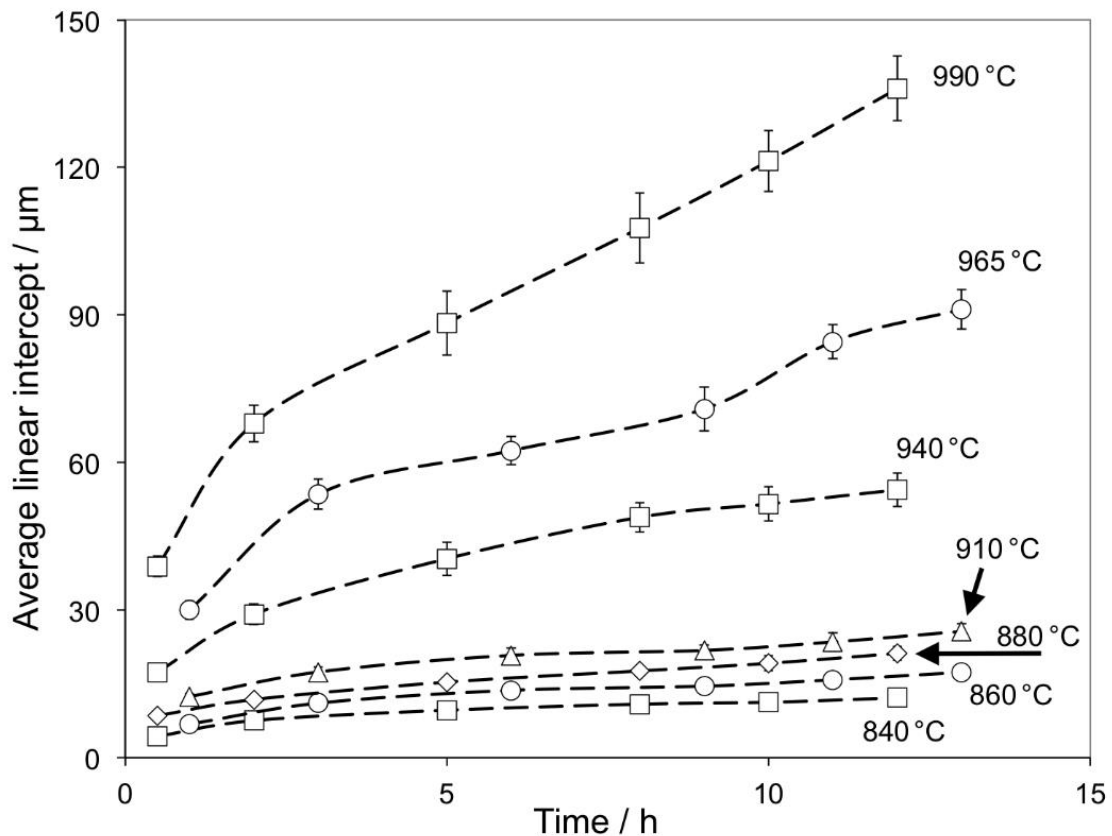

Figure 17 Grain size growth during isothermal austenitisation in SA508 gr. 3 steel [4].

2.1.6. Phase transformation

The phase is a homogeneous part of an alloy, with different properties and separated from it by an interface, which, together with a number and types of phases, depends on the chemical composition of the alloy [40]. A given phase presents an arrangement of atoms that is characteristic for it and is related to the amount of free energy accumulated within the material. Atoms always try to minimise the amount of energy. Where there is a change of the energy, for example through the applied stress or by increasing/decreasing temperature, atoms can rearrange their positions, which results in a change of the phase and properties of an alloy.
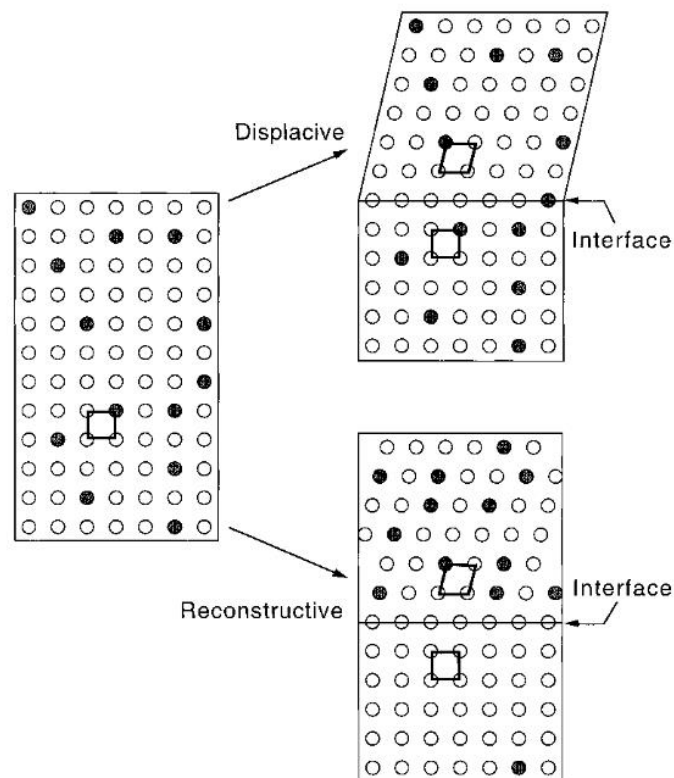

Figure 18 Reconstructive and displacive mechanisms of transformation in an alloy. On the right only the upper halves of the samples are transformed [52].

Transformations can be subdivided into two categories, reconstructive or displacive (Figure 18). Displacive transformations involve the cooperative movement of atoms, which, because the transformation is constrained, occurs in the form of thin plates. Because of the cooperative nature of the transformation, there is no diffusion in the transformation and

therefore the transformation can occur at temperatures where diffusion is very slow. But such mechanisms leave the material in a metastable state, in other words the atoms are not in their most favourable energetic positions. This situation can be compared to the solute trapping mechanism, where solute is leading inside the mixture under the conditions (pressure or temperature) far more preferable for such phenomenon to occur than the conditions in which the element will be working.

RECONSTRUCTIVE
Diffusion of all atoms during nucleation and growth.
Sluggish below about 570°C.

- ALLOTRIOMORPHIC FERRITE
- IDIOMORPHIC FERRITE
- MASSIVE FERRITE
  No change in bulk composition.
- PEARLITE
  Cooperative growth of ferrite & cementite

DISPLACIVE
Invariant plane strain shape deformation with large shear component.
No iron or substutitutional solute diffusion.
Thin plate shape.

- WIDMANSTATTEN FERRITE
  Carbon diffusion during paraequilibrium nucleation & growth
- BAINITE & ACICULAR FERRITE
  Carbon diffusion during paraequilibrium nucleation.
  No diffusion during growth.
- MARTENSITE
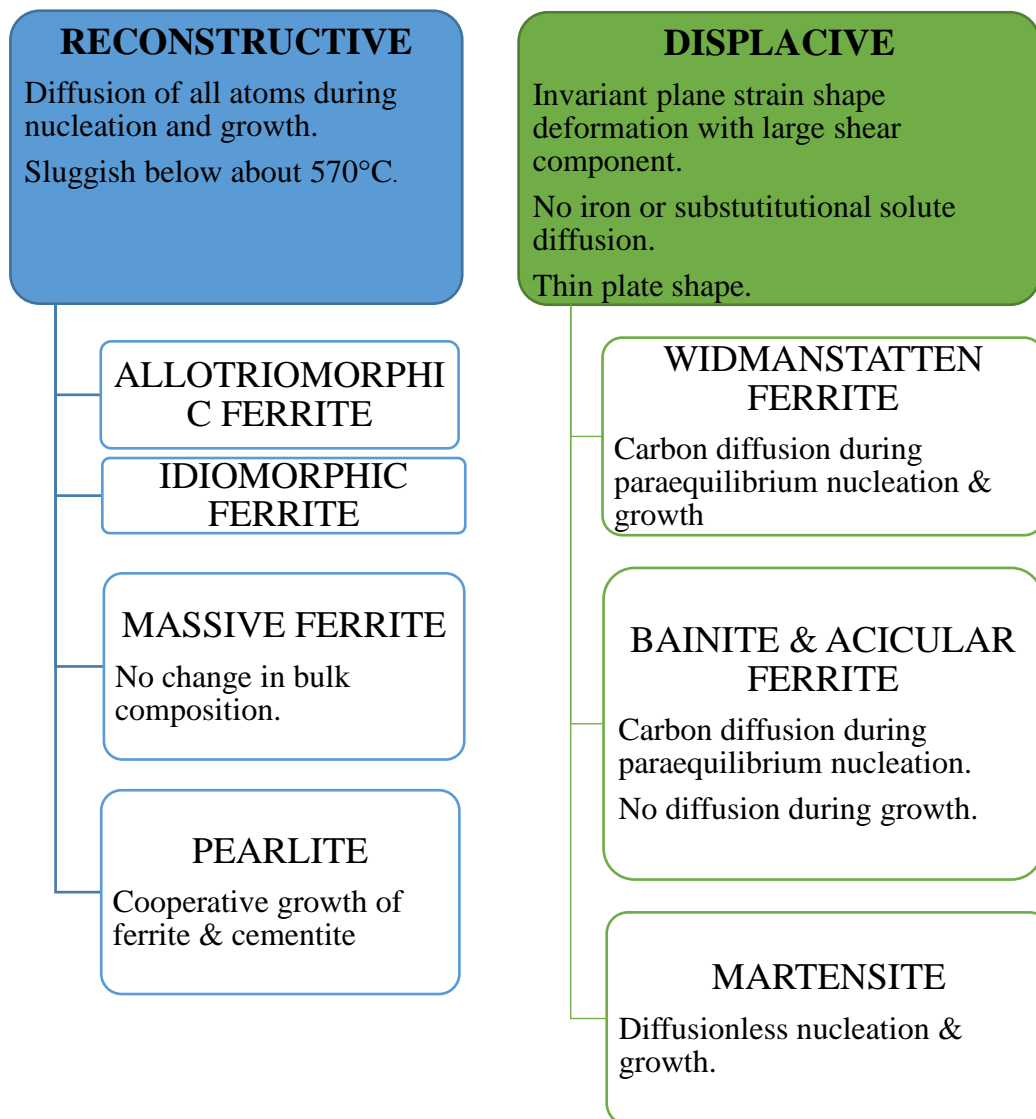 Diffusionless nucleation & growth.

Figure 19 Essential features of the transformations of solid state in steels [52].

Reconstructive transformations are diffusion controlled and therefore time dependent, which is driven by a reduction in free energy as the system moves towards thermodynamic equilibrium. In this kind of transformation the shape deformation occurs in a way that only volume change effects are accommodated in the material when the shear component effects are neglected. Different kinds of transformation in steels are presented in Figure *19.*

Dislocations introduced into a material through the plastic deformation affect the nucleation of the transformations in various ways. The formation of the products of the displacive transformations, like Widmanstätten ferrite, bainite, martensite and mechanical twinning is delayed after application of the plastic deformation to the parent phase, austenite. This is associated with glissile interfaces in microstructure. The motion of such interfaces play a significant role during the displacive transformation, but can be disturbed by obstacles in the form of defects [52]. This causes the retardation of the transformation, which is called mechanical stabilisation [53] which is unique to displacive transformations as during the reconstructive transformations the plastic deformation of austenite accelerates the formation of the products, like in case of the formation of allotriomorphic ferrite, pearlite and in recrystallization reactions [52].

As noted before, the main steel used in this project is SA508 used for construction of the reactor pressure vessels, which are crucial parts of the reactor in nuclear power plants. For many years the microstructure of the vessels was assumed to be fully and homogeneously bainitic. The research of Pous-Romero [4] showed that for the such large components the difference of the cooling rate value at the cross section of the thick wall affects the microstructure and causes occurrence of many product phases.

Duffy in [20] studied SA508 grade 3 and SA508 grade 4N steels during the investigations of the electron beam welding conducted on thick-section steels for critical components of nuclear reactors. He concluded that in SA508 gr. 3 steel primary phases are mostly the body-centred cubic ferrite and face centred cubic austenite, which are thermodynamically stable. Other phases like cementite or carbides are likely to occur, but their presence is not thermodynamically preferable. Figure 20 shows the phases that are possible to nucleate for the chemical composition presented in table 9 and reached at least 1% volume in the solution.

Table 9 The SA508 grade 3 composition adapted from [54]:

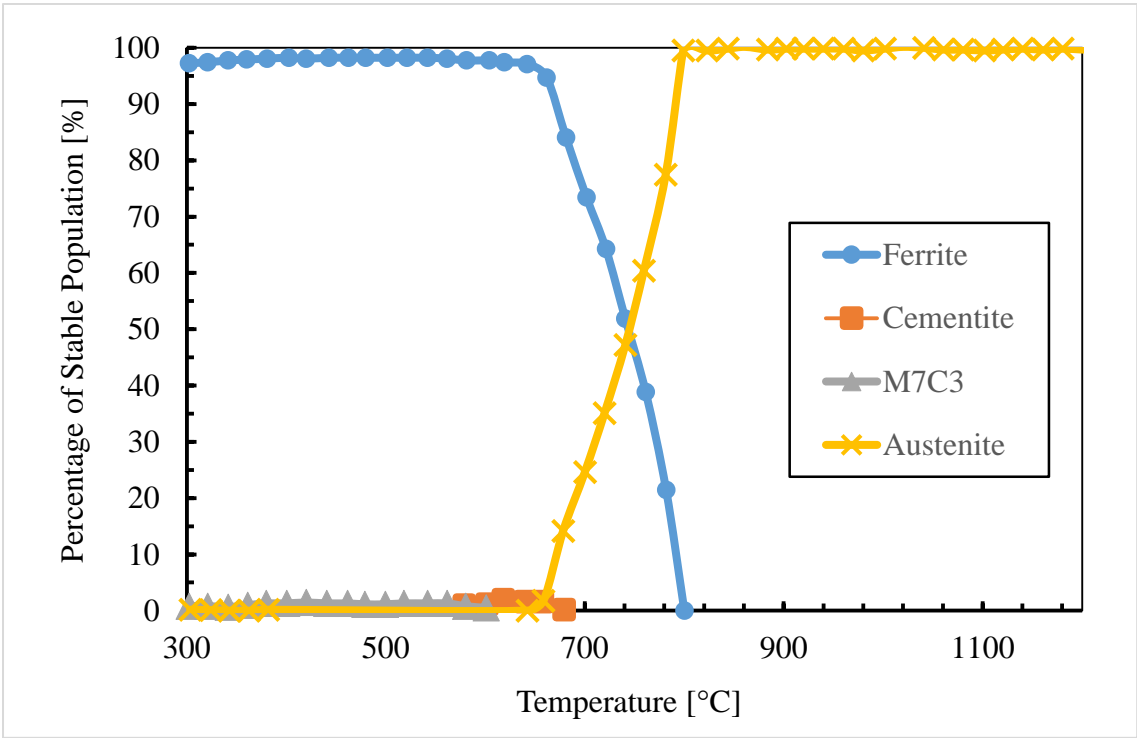| Element	Content [%]
Carbon	0.170
Silicon	0.248
Manganese	1.382
Nickel	0.774
Molybdenum	0.520
Chromium	0.236
Vanadium	0.002

Figure 20 Phases of SA508 grade 3 steel under stable thermodynamically conditions [54].

In Figure 20 the presented transformation start temperatures can be clearly distinguished: Ae3, which is around 800°C, and Ae1, around 660°C. These temperatures are commonly known as a boundaries of stability for ferrite and austenite; above the temperature Ae1 the ferrite starts

becoming less thermodynamically favourable phase, what leads to its complete vanishing as the temperature Ae3 is reached. Austenite in the opposite way starts to be stable above the temperature Ae1, to reach the full stability above the Ae3. The temperatures depend on the chemical composition of the steel and were calculated using software called MTDATA in [20].
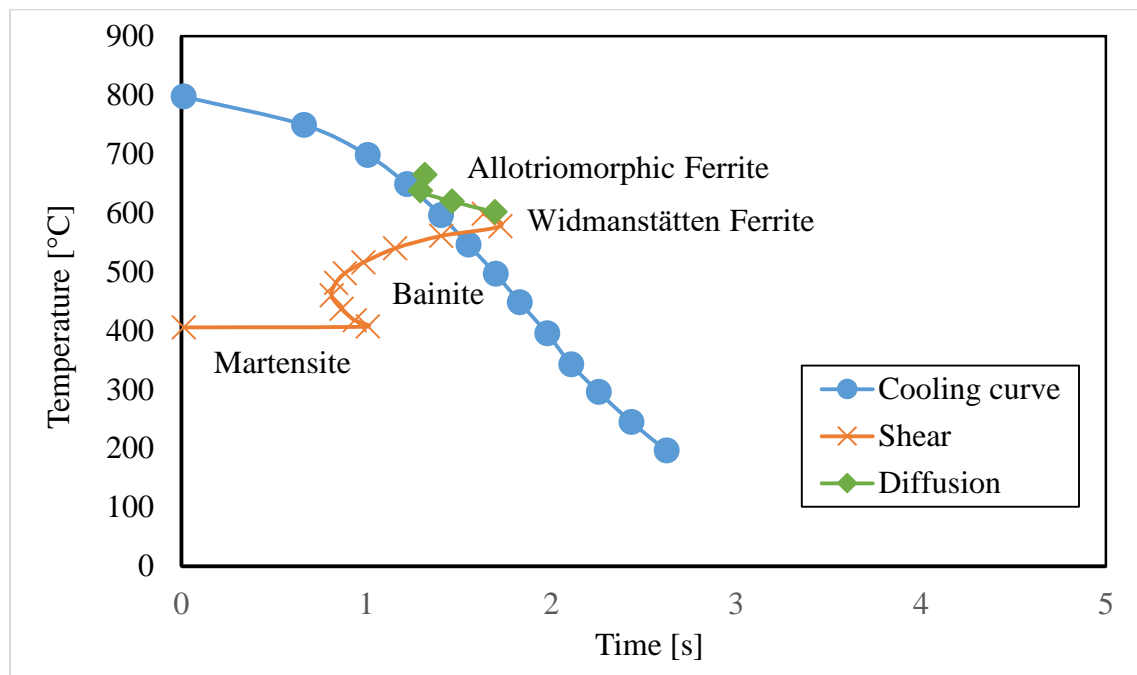
Figure 21 Time-Temperature-Transformation diagram for SA508 grade 3 steel with calculated cooling rate curve [20].

In Figure 21 the Time-Temperature-Transformation (TTT) diagram is presented for steel SA508 grade 3, obtained through calculations based on theory of thermodynamics, nucleation and kinetics. It allows the prediction of which phases are possible to nucleate during the heat treatment of particular steel. Such diagrams consist of the so-called c-curves, which mark the start of the phase transformation, the time in which particles of a new phase start incubating. The curves inherited their names after the characteristic shape, which is related to the incubation times for diffusive transformations and indicates that the smallest amount of time needed for the transformation to start is at the nose of the c-curve. The example of such temperature point is Ae1, where the austenite is no longer the thermodynamically stable phase and transformation to ferrite occurs. When material is cooled down below the Ae1 the driving force is proportional to the difference between the temperature of the material and the Ae1 temperature point. The

times needed for the incubation (nucleation) of the ferrite are shorter then, as the driving force value grows. The cooling continues to the moment where the thermal energy needed for diffusion is not sufficient enough, which increases times needed for incubation, creating the c-shape [20], [55].

Figure 21 presents an example of a cooling curve, calculated using the mucg65 software, developed by Professor H.K.D.H. Bhadeshia of the University of Cambridge at the Department of Materials Science and Metallurgy. The details of the welding process, in which it has been used are described in [20]. It is a good example of microstructure prediction using the TTT diagram and changes of temperature of an element in time. As it can be seen in Figure 21 the phases, which can nucleate in the SA508 grade 3 steel are allotriomorphic ferrite, Widmanstätten ferrite, bainite and martensite, with the great majority of the bainite and martensite with trace amounts of the other phases [20].

Allotriomorphic Ferrite - allotriomorphic ferrite is a phase which grows from the grain boundaries of austenite. The main mechanism of growth is diffusion, which is more favourable at these regions. The rate of growth of the nucleated grains is parabolic as it is related to the concentration of carbon in newly formed ferrite and austenite. The interstitial solubility of carbon in ferrite is lower than in austenite that results in rejecting carbon atoms from ferrite to austenite. The difference of concentration of carbon atoms in austenite and ferrite at the beginning of the process is greater than at the end, which translates to the speed rate of diffusion. The similar pattern is connected with the atoms of substitutional solutes, but these particles are treated as fixed during diffusion of carbon atoms, due to their size [20], [55], [56].

Widmanstätten Ferrite and Acicular Ferrite – primary Widmanstätten ferrite grows from the austenite grain boundaries. When an allotriomorphic ferrite has already formed in these regions, Widmanstätten ferrite grows directly from it, taking the name 'secondary'. The formation occurs at high temperatures, close to the temperature Ae3, where the driving force for the transformation is small. It creates the metastable environment, which forces carbon atoms to diffuse in the austenite at the top of the ferrite plate. The appearance of the ferrite is similar to a wedge, but the researches have shown its more plate- or lath-like character [57], [58]. The direction of growth of the longitudinal plates makes them reach inside the austenite grain, where the concentration of the carbon is not impacted by the transformation phenomenon at the grains, what favours the diffusion. Although the diffusion of carbon atoms in the austenite controls the growth of the Widmanstätten ferrite's plates, the formation of the ferrite is

displacive, as it is connected with the lattice change. The atoms of iron, as well as particles of the substitutional solutes are fixed and do not diffuse.

The formation process can be held by growth of acicular ferrite, a bainite-like structure, which nucleates at the non-metallic inclusions and oxide lattice impurities within the grain. Its resemblance to bainite structures is very high, which suggests that this is a bainite, which nucleates under unusual circumstances. The shapes that are taken by the acicular ferrite are lenticular plates [20], [55], [56], [59], [60].

Bainite - bainite forms at lower temperatures compared to the ferrite and pearlite high temperature transformations but at higher temperatures than martensite. It consists of fine ferrite platelets, which are called sub-units. The space between the sub-units is filled with untransformed austenite or cementite. Bainite nucleation needs much more energy from undercooling than Widmanstätten ferrite and starts at the austenite grain boundaries, where they are connected with each other, gathered in so-called sheaves. Two forms of bainite can be distinguished: upper and lower. The names are related to the temperature in which they are formed, and the main difference is connected with the diffusion of the carbon atoms. In upper bainite diffusion of carbon from the ferrite platelets to the surrounding matrix is sufficient to allow carbides to form in between the ferrite plates. The only difference with lower bainite is that the carbides only form within the ferrite plates as the diffusion distance is smaller because of the lower temperature. The diffusion of the carbon atoms is related to the lower solubility of carbon in the ferrite than in the austenite, but the transformation of austenite to the bainite phase is considered as displacive and it is connected with invariant plane strain shape change of transformed area [20], [60], [61].
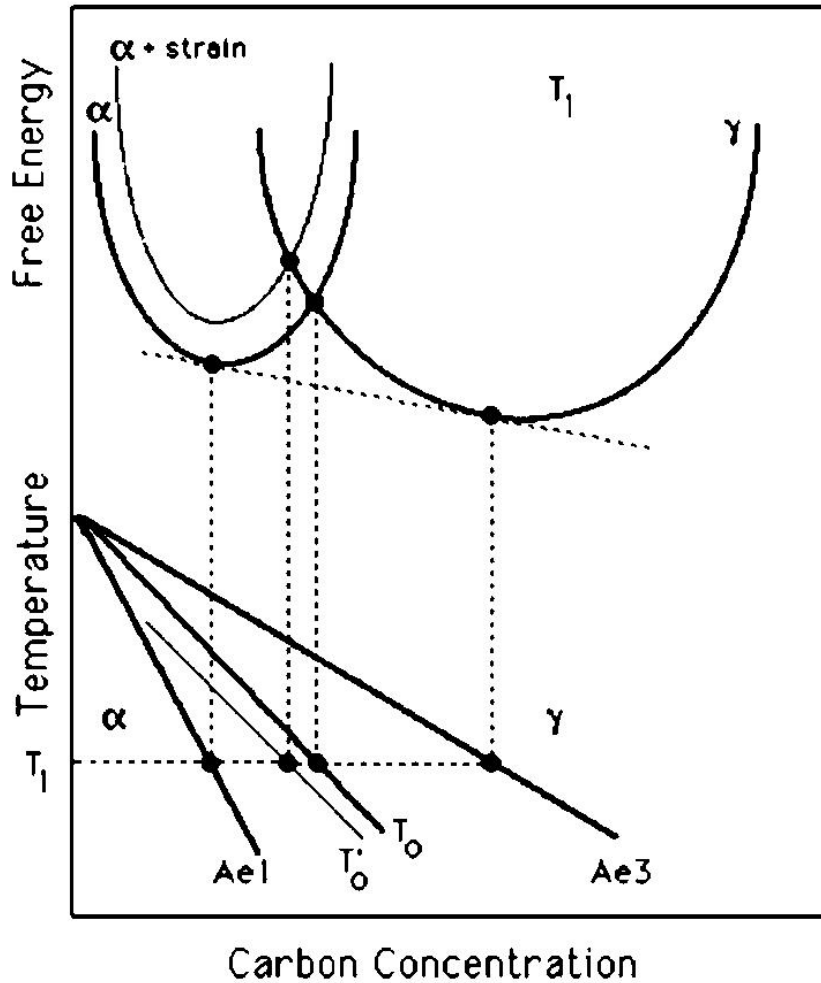
Figure 22 The representative example of T0 and T'0 curves in a para-equilibrium diagram [20], [62].

A representation of T_0 and T'_0 curves construction on a para-equilibrium diagram is shown is presented in *Figure 22*. The diagram is used as a representation of the growth of bainite as a transformation from austenite to ferrite. The T_0 curve represents the carbon concentration as a function of temperature and is related to the amount of free energy of ferrite and austenite. The black points on the curves T_0 and T'_0 on a diagram relate to the amount of the free energy common for the austenite and ferrite; the related curves intersect. The curve T'_0 relates to the free energy of ferrite, which is corrected for the strain, necessary in the bainitic transformations. The bainite forms when the free energy of the austenite of the same composition is higher. Three cases during the bainite platelet growth can be distinguished: there is no diffusion of the carbon, the carbon atoms are trapped inside the bainite, leaving it supersaturated; the excess

atoms of carbon can diffuse to the austenite; and the case in between, where bainite is partially supersaturated as only some of the atoms are diffused to the austenite.

It has been experimentally demonstrated that it is impossible for bainite to grow at temperatures above T_0, which leaves the remaining austenite in the non-equilibrium state. It is because the growth of the bainite platelets generally involves the diffusion of the excess carbon atoms out to the surrounding austenite. It means that the concentration of the carbon atoms in austenite, where the new platelet is going to grow is constantly growing to the point of T_0 for the given temperature, giving the barrier for the nucleation of new platelets and leaving concentration of carbon atoms in austenite far from the equilibrium (given by Ae3). Such a situation creates an impression of incomplete reaction from austenite to ferrite. Due to the correlation of the T_0 temperature with the carbon atom concentration, the amount of the bainite which can be transformed from austenite grows with the undercooling beneath the B_s, which is the temperature above which no bainite transformation occurs [20], [62].

Martensite - martensite is a phase which emerges in steel only by the displacive mechanisms, without the diffusion of atoms, which is indicated by several facts. The temperature of the nucleation and growth can be very low, at the temperatures where diffusion is too slow for a diffusional transformation. The speed of the growth of martensite can be extremely high, even compared to the speed of the sound inside the steel. Again, the process of diffusion cannot happen at such high rates of transformation. In reconstructive transformation mechanisms, there is a change in the chemical composition of the parent phase by diffusion. In martensite there is no difference in chemical composition between the parent phase and the product phase. These factors with high probability suggest the diffusionless character of the phase transformation of austenite to martensite.

The martensite phase offers excellent combination of strength, which can reach over 3500 MPa, and toughness, which can be over 200 MPa×m$^{1/2}$ in steels. The characteristic aspect of the martensite is the presence of the habit plane, which on the macroscopic scale is the plane between the parent and the product phase. It can take a shape of a straight line when the martensite phase can grow in an unconstrained manner. However, in normal cases, the martensite that forms is surrounded by the parent metal, which constrains its growth, resulting in the classic lenticular shape due to the energy minimization (constrained transformation) (Figure 23) [20], [63]**.**
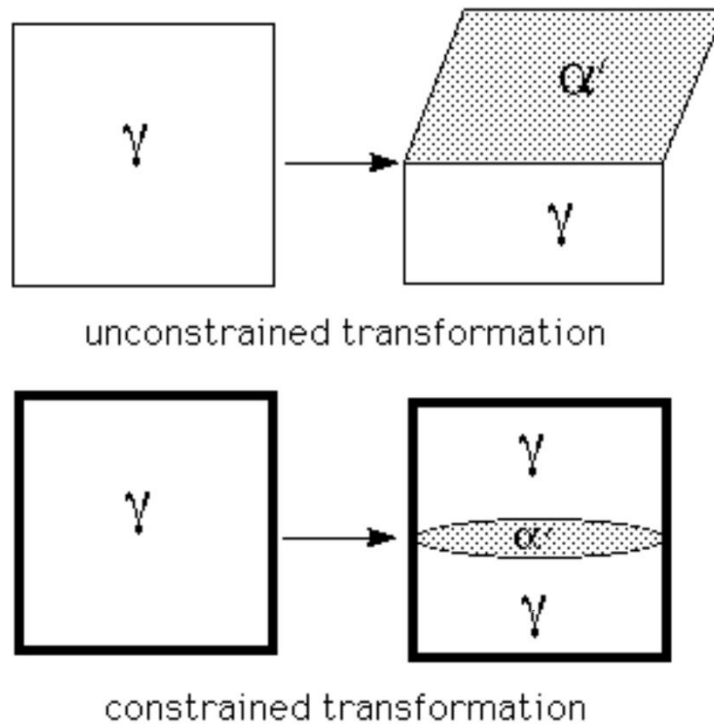
Figure 23 Schematic representation of the unconstrained and constrained transformation from austenite into martensite phase [63].

In the martensite the relationship between the parent metal and the product phase can be observed, which occurs due to the synchronised and simultaneous change of all of the atoms in the transformation at same the time. These correlations are presented below, although they are irrational; there are difficulties in their description by the rational numbers.

Kurdjumov-Sachs: $\{1\ 1\ 1\}_\gamma \parallel \{0\ 1\ 1\}_\alpha$

$<1\ 1\ \bar{1}>_\gamma \parallel <0\ 1\ \bar{1}>_\alpha$

Nishiyama-Wasserman: $\{1\ 1\ 1\}_\gamma \parallel \{0\ 1\ 1\}_\alpha$

$<1\ 0\ \bar{1}>_\gamma \sim 5.3°$ from $<0\ 1\ \bar{1}>_\alpha$ to $<\bar{1}\ 1\ \bar{1}>_\alpha$

Greninger-Troiano: $\{1\ 1\ 1\}_\gamma \sim 0.2°$ from $\{0\ 1\ 1\}_\alpha$

$<1\ 0\ \bar{1}>_\gamma \sim 2.7°$ from $<1\ 1\ \bar{1}>_\alpha$ to $<\bar{1}\ 1\ \bar{1}>_\alpha$

The phase transformation of martensite is athermal. It means that even if the change of a volume of material occurs in some period of time, the nucleation and growth of particular plate

is not dependent temperature, due to its very high velocity. The transformation start (Ms) temperature can be calculated, above which no transformation occurs. The amount of the martensite formed is related to the level of undercooling below the Ms temperature. Relatively fast cooling rates mean that the transformation process does not proceed in equilibrium conditions. The lattice is changed, but the chemical composition of the parent metal is preserved. The diffusion, which could minimize the free energy by the atom's redeployment, is absent. The shape deformation that accompanies the martensite transformation, introduces substantial strain into the material. This results in considerable residual stress in the martensite that has to be removed by tempering. The phase diagram with the bainite transformation marked and with taking into account the mentioned strain is presented in Figure 24 [20], [63].
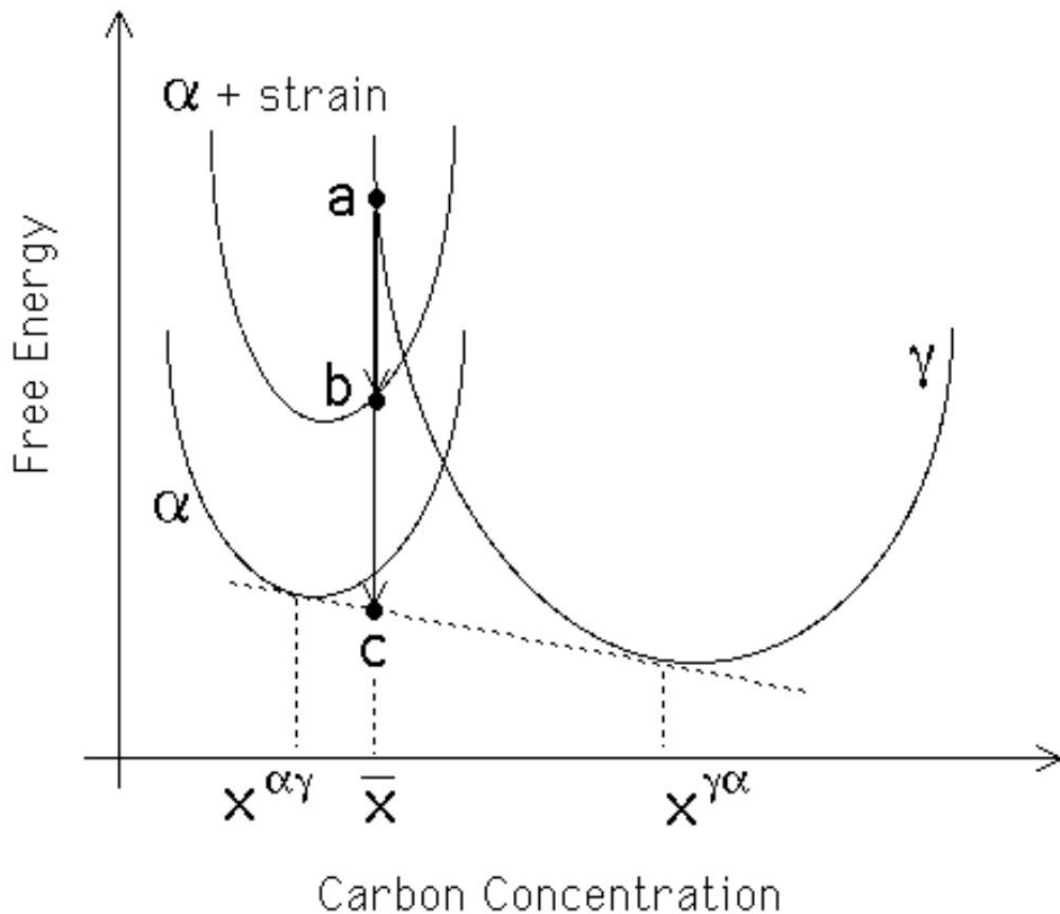
Figure 24 The relationship between carbon concentration and free energy during transformation austenite to ferrite with taking into account the strain accompanying the bainite transformation presented on phase diagram [63].

The equilibrium cooling of the austenite with the carbon composition of $\bar{x}$ leads to decomposition of the austenite to the ferrite with carbon concentration of $x^{\alpha\gamma}$ and the austenite with carbon composition of $x^{\gamma\alpha}$. In the case of martensitic transformation, the change in chemical composition does not occur, so there is no carbon partitioning. The austenite changes its lattice by displacive mechanism, but the arising strain energy has to be accounted, for locating the carbon concentration in point b, instead of c [20], [63].

2.1.7. Origins of residual stresses

The residual stresses are the stresses which exist inside the non-loaded material, which is in equilibrium with the surrounding system and which are not necessary to maintain this equilibrium [64]. The most common division of the residual stresses group them into three main categories: mechanical, thermal and structural. Mechanical stresses arise within the material during heterogeneous plastic deformation, causing macro– and micro-stresses. Thermal stresses are caused by irregularities in heat distribution during heat treatment, i.e., uneven cooling/heating, and is especially visible in large-size products. The stresses appear due to the changes in temperature-dependent thermal expansion coefficient in adjacent areas with various specific volumes. The structural stresses occur between various structural components, developed as products during the phase transformation [65], [66]. The dimension change caused because of changes in the specific volume of particular structural components are more significant than those that occur due to the thermal expansion. Nevertheless, thermal shrinkage and phase transformation are the main reasons of the stress generation [67], [68].

In addition to mechanical, thermal and structural stresses, the occurrence of self-stress in large-size forged products may occur by chemical interactions (heterogeneity of chemical composition, formation of chemical compounds). Natural stress also arises during welding or surfacing operations quite often accompanying the process of manufacturing a large-size product. Welding or surfacing processes cause three types of internal stress. Self-stressing joints can also cause hydrogen embrittlement. The surface layer may have a different chemical and phase composition than the core material of the bulky product. The differences may also concern the microstructure, texture and density of defects. The stress state may be affected by

differences in the thermal conductivity of individual material fragments, plastic flow and creep occurring in the surface layer.

It can be generally said that the residual stresses of any kind are generated by the misfits that occur between the adjacent areas within the element. In a practical approach it is necessary to connect the origins of the residual stresses with the area upon which they occur and self-equilibrate. It is of significant importance to investigate the stress field in order to apply the appropriate experimental measuring technique. Taking this into consideration the three types of stresses are mentioned in the literature:

- The macro-stresses (type I),
- The intergranular stresses (type II),
- The atomic scale stresses (type III).

It is important to mention that the residual stresses are not perceived as detrimental in general. By using forging and thermal techniques it is possible to improve the properties of the element by introducing the stresses, which remain after the treatment or working is done and which counterwork the loads applied during element exploitation prolonging their life span. [43], [64], [69], [70].

Table 10 Brief presentation of stress measuring techniques. Detailed description is presented in [64]:

| Method	Penetration	Spatial resolution	Accuracy	Comments
Hole drilling (distortion caused by stress relaxation)	~1.2 × hole diameter	50 μm depth	± 50 MPa, limited by reduced sensitivity with increasing depth	Measures in-plane type I stresses semi-destructive
Curvature (distortion as stresses arise or relax)	0.1 – 0.5 of thickness	0.05 of thickness; no lateral resolution	Limited by minimum measurable curvature	Unless used incrementally, stress field not uniquely determined; measures in-plane type I stresses
X-ray diffraction (atomic strain gauge)	<50 μm (Al); <5 μm (Ti); <1 mm (with layer removal)	1 mm laterally; 20 μm depth	± 20 MPa, limited by non-linearities in $\sin^2 \psi$ or surface condition	Non-destructive only as a surface technique; sensitive to surface preparation; peak shifts: types I, <II>; peak widths: type II, III
Hard X-rays (atomic strain gauge)	150 – 50 mm (Al)	20 μm lateral to incident beam; 1 mm parallel to beam	± 10 × 10⁻⁶ strain, limited by grain sampling statistic	Small gauge volume leads to spotty powder patterns; peak shifts: type I, <II>, II; peak widths: types II, III
Neutrons (atomic strain gauge)	200 mm (Al); 25 mm (Fe); 4 mm (Ti)	500 μm	± 50 × 10⁻⁶ strain, limited by counting statistic and reliability of stress free references	Access difficulties; low data acquisition rate; costly; peak shifts: type I, <II>, II; (widths rather broad)
Ultrasonic (Stress related changes in elastic wave velocity)	>10 cm	5 mm	10%	Microstructure sensitive; types I, II, III
Magnetic (variations in magnetic domains with stress)	10 mm	1 mm	10%	Microstructure sensitive; for magnetic materials only; types I, II, III
Raman	<1 μm	<1 μm approx..	$\Delta\lambda \approx 0.1$ cm⁻¹≡50 MPa	Types I, II

53
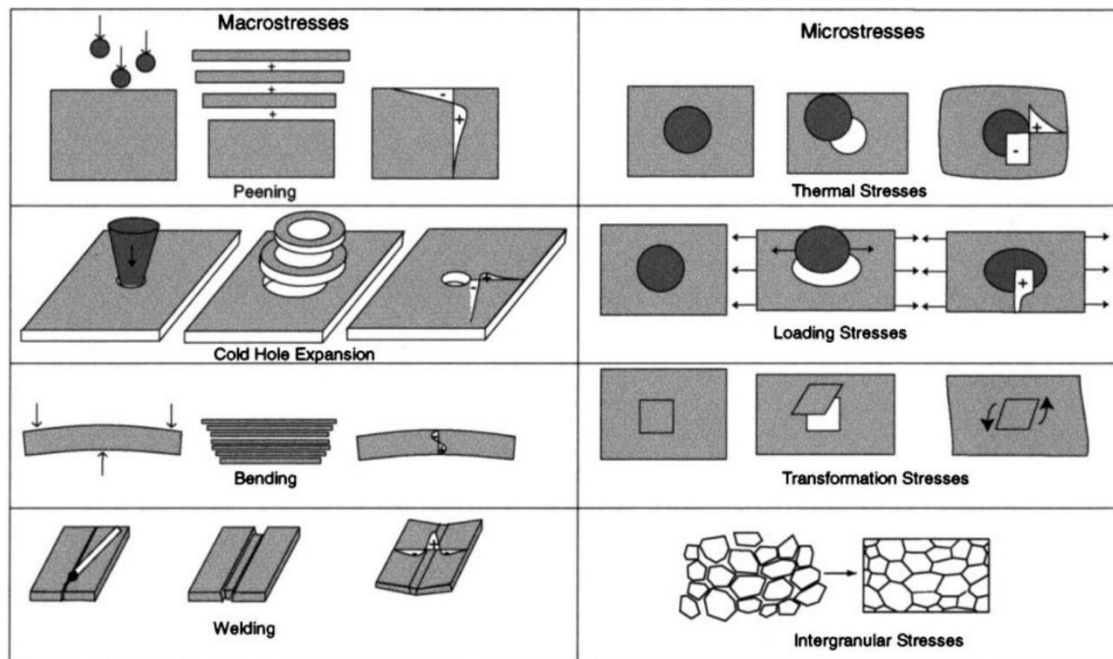
Figure 25 The examples of the residual stress of different origins and which self-equilibrate on various scales within the element [64].

The first type I are the stresses, which impact on the largest area. They can arise from non-even distribution of mechanical or thermal field over a large impact area, like non-uniform plastic deformation on a beam or a high temperature gradient between the edges of the beam.

The second type II are stresses which react between the grains within the material. These strains arise because of misfits from the different elastic and thermal properties of grains, as each one of them is characterised by different parameters and orientation relatively to each other. Due to the fact that such irregularities always occur in the polycrystalline materials the stresses of type II are also always present, on relatively higher or lower level. These kind of stresses play an important role in the material, which consists of many phases or during the heat treatment process, when phase transformation occurs.

The third type III are stresses that occur over the shortest distances. These are stresses caused by the phenomena in crystallographic structures, like defects, interstitial atoms, vacancies, dislocations, coherency etc. Figure 25 summarises the origins of the residual stresses [43], [64], [69], [70].

2.1.8. Thermal expansion

Thermal expansion, also called dilatation, is the ability of solids to reversibly increase their volume during an increase of the temperature. The heating of the material causes the increase of the energy of the vibrating atoms within, which leads to the higher values of lattice parameters and density of the equilibrium vacancies. Thermal expansion of metals is related to the intermolecular forces and to the specific order of atoms in the crystallographic lattice. It is described by a thermal expansion coefficient, which is a value characteristic for a given material describing how material will increase its length or volume, when its temperature will arise by 1K, or decrease, in a case of cooling:

$$\alpha = \left(\frac{1}{V_0}\right)\left(\frac{dV}{dT}\right) p = const, \tag{5}$$

where V_0 is an initial volume, T is a temperature, p is a pressure.

In a case of metals, their anisotropy must be considered. It is taken into consideration by linear thermal expansion coefficient:

$$\alpha = \left(\frac{l}{l_0}\right)\left(\frac{dl}{dT}\right) p = const, \tag{6}$$

where l_0 is an initial length in a given direction, assuming the final length as:

$$l = l_0(1 + \alpha\Delta T), \tag{7}$$

The volumetric thermal expansion coefficient is sometimes used, but in the case of isotropic materials the expansion is approximately the same in every direction, so the expression presents as follows:

$$\alpha_V \approx 3\alpha_l \tag{8}$$

The ability of the metals to expand under the thermal influence is relatively higher at increased temperatures, similar to the heat capacity. The thermal expansion coefficient is determined experimentally by using dilatometry. The thermal expansion of solids is related to the anharmonic vibrations of the atoms in the lattice structure [71].

All of the objects in the crystal lattice are connected together by a system of molecular forces. The atoms are vibrating around their lattice positions, what is related with mutual

55

interactions in the lattice and the thermal energy within the material. Two forces of the opposite directions act on a single atom, accordingly to its distance from the other atoms, the force of attraction F_a and repulsion F_r. The resultant force F_w indicates the behaviour of the atom. The example of such interactions are presented in Figure 26. There is an equilibrium position at $r=r_0$, where the forces are balanced $F_a=F_r$, and resultant force equals zero $F_w=0$. Considering two adjacent atoms on the short distances, below r_0, the repulsion forces are dominant, on the distances larger than r_0 the attraction forces are prevailing. The distance r_0 is the distance between two atoms at the equilibrium conditions, neglecting the influence of the temperature.
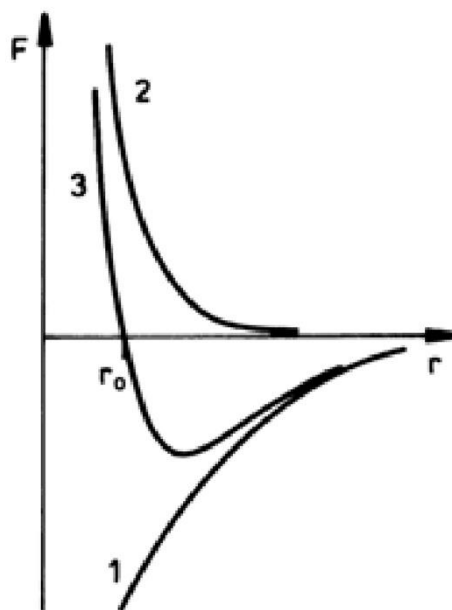
Figure 26 The intermolecular forces F related to the distance between the atoms r. 1 – attraction forces F_a, 2 – repulsion forces F_r, 3 – resultant force F_w, r_0 – the equilibrium position, where $F_a=F_r$.

The state in which a crystal possesses the minimum free energy is when all of the atoms are as close as possible to their equilibrium positions, called nodal points. Increasing the temperature of the material results in an increase of the vibrations, i.e. in the deflections of the atoms from their nodal points. The ideal vibration around the point can be described by the harmonic oscillator model. Such oscillator obeys Hooke's Law, where on the object moved from the equilibrium acts a restoring force of a magnitude proportional to the deviation. But the

deviation of the particle during vibration in the crystal lattice is not harmonic, because it is not symmetric to the equilibrium position of r_0.
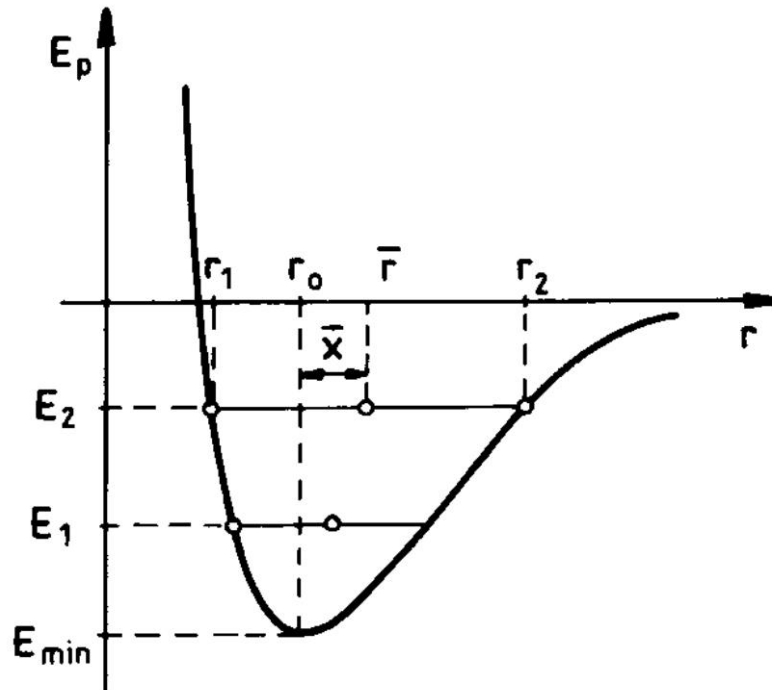
Figure 27 The potential energy of intermolecular forces related to the distance between the atoms based on the anharmonic oscillator model.

The resultant restoring force, which brings the atoms to their original position in the crystal lattice is not linear in the surrounds of the r_0, what results in asymmetric behaviour of the curve, which describes the potential energy and distance between the atoms relationship (Figure 27). The atom of a potential energy E_{min} vibrates around his nodal point r_0 and cannot vibrate with a greater energy than it possesses. When the potential energy of the atom increases, its average location $\bar{r}$ changes position, moving away from the equilibrium position r_0 to higher values. It has to be noted that such approach is only an approximation, assuming only two atoms and neglecting the chemical bond between them. Connections of atoms in crystal lattice are more complicated, although the presented above model describes the phenomena of thermal expansion in metals very well.

The force which acts on the vibrating atom can be described in an approximation by the equation of the force in the model of anharmonic oscillator:

$$F = -cr + br^2 \tag{9}$$

where $F = -cr$ is the part, which describes the force proportional to the displacement with c as a coefficient of elasticity and br^2 is a nonlinear part, which describes the deviation from the harmonic movement. When temperature is rising it can be seen that average distance between the atoms is different from the r_0 about the $\bar{r}$, which is proportional to the material temperature:

$$\bar{r} = \frac{bkT}{c^2} \tag{10}$$

where k is a Boltzmann constant and T is an absolute temperature. It can be seen from (10) that, as already noted, heating of the material causes linear and volumetric expansion. The mentioned linear thermal expansion coefficient can be presented as:

$$\alpha = \frac{1}{r_0} \frac{d\bar{r}}{dT} \tag{11}$$

By inserting the (10) into the (11) one get linear thermal expansion coefficient, which takes into account the above considerations [72]–[74]:

$$\alpha = \frac{bk}{r_0 c^2} \tag{12}$$

2.1.9. Summary

The numerical representation of the RPVs manufacturing process needs to cover a lot of reciprocal theoretical factors from different fields on every stage of development. Though modelling explicitly all of them is impossible, takes too much effort, especially in industrial conditions, and the better results as the output from such approach are unlikely to achieve. In principle the models presented in the literature have to focus on chosen important aspects of the process, like methods, numerical modelling techniques, manufacturing processes or microstructure evolution, enhancing particular problem.

2.2. Overview of the literature modelling approaches

2.2.1. Basic reciprocal factors for residual stresses modelling

A lot of effort has been put into solving the residual stresses problem, which arises during the manufacturing of steel, as it is one of the essential issues of the plastic deformation and heat treatment processes in general, like in [64], [75]–[81] among the vast number of examples. Many factors have various impacts on the final residual stresses in a finished element and one of them is a relation with the size of the part [54], [65], [82]. Over the time it has been discovered that the joint areas of the systems, where many small elements are involved, are in greater risk of failure due to disturbances that occur in between them. Nowadays such systems are modernized in a way of replacing fewer elements with a bigger single unit whenever it is possible [26], [51]. The aim is to avoid various contact problems, such as different thermal expansion coefficients, different heat capacity, different heat exchange coefficients, friction, dissimilarities in chemical compositions or a need to use a complicated geometry of weld path. However, it should be noted that the major development of new methods of welding processes are promising. The constantly growing standards that are demanded from the very key plant elements, like, for example, shafts in nuclear reactors, rotors of the turbines of the wind power plants engines, nuclear powered submarines or reactor pressure vessels in the nuclear power plants, which work in very hard environments for a very long period of time, create a field for the investigations of the way of manufacturing one large elements instead of joining many smaller ones. Also, the increase of the unit power generation capacity forces developing the greater size units, which guides researches in directions of reducing the thickness and increasing the mechanical properties of the elements [21].

The 'large-size' forging is not quite specific description. It covers elements from ~100t to even up to 600t [21], [83], [84]. They can be used in such industries as nuclear, offshore oil & gas, power generation, steel production, elements for mills and presses, defence and steel rolls [85] . It is clear that the attempts to solve residual stress problems in a traditional way in such large elements lead to large errors. Investigation of a new approach in residual stress

management based on the present knowledge and industry day-to-day experience is clearly required.

The manufacturing process of large ingots is a long and complex operation. When dimensions of the element are relatively big the production of one piece could take even one year [32], [83]. The work experience of the design engineers is very important, because every element has to be designed separately and is quite unique. In calculating the chemical elements content, the best forging and heat treatment parameters for manufacturing it is necessary to use numerical modelling programs, which are usually based on the Finite Element Methods (FEM). This approach implemented into the technological methods is essential in an economic terms; with such large dimensions of elements it is a cheaper for a company to invest more in a strong research and development department than in laboratory tests, which consume a lot of expensive material in a destructive test. Beside, most of these tests are restricted to the surface areas of the product in terms of obtaining the relevant information about stresses [86].

As mentioned before, there are many factors that have an impact on the value of the residual stresses during heat treatment. The main three coupling factors which influence the microstructure of the material, presented in Figure 28, are inseparably related to the residual stresses that occur during the heat treatment and plastic deformation [80], [87]–[90]. These factors are the base for the numerical simulations of heat treatment process.

One of the most important parameters of the stress investigations during heating, holding, quenching and tempering stages of the heat treatment is the temperature, due to its relations with the stress induced from the differences of the part size within the individual element and control of the phase transformation in the various regions of the part. The differences in the temperature field are responsible for the different local size of the material in the same element. The significant differences are visible especially at the beginning of the cooling process from the austenite phase on the surface of the element, where locally the temperature is much lower than the core. This results in a situation where the inner material exerts sufficient stress to potentially burst the surface of the element. The difference in larger and smaller specific volume between the surface and inner areas is the main cause of the stresses. In elements with very large dimensions and complicated geometry the difference can be so great that it results in destruction of the element [91]. The additional heat that significantly affects the material is generated from plastic deformation as well as from the latent heat of the phase transformation. Phase transformation occurs at some temperature intervals, where the

changes of the temperatures within the element leads to microstructural transformations. This occurs during both heating, holding and cooling stages. As the local temperature exceeds the phase transformation temperature during heating, austenite formation from the pre-existing structures is observed, while martensite, pearlite, bainite, ferrite and iron carbide are formed as a result of austenite decomposition during the cooling stage when the local temperature within the volume reaches the corresponding phase transformation temperature.
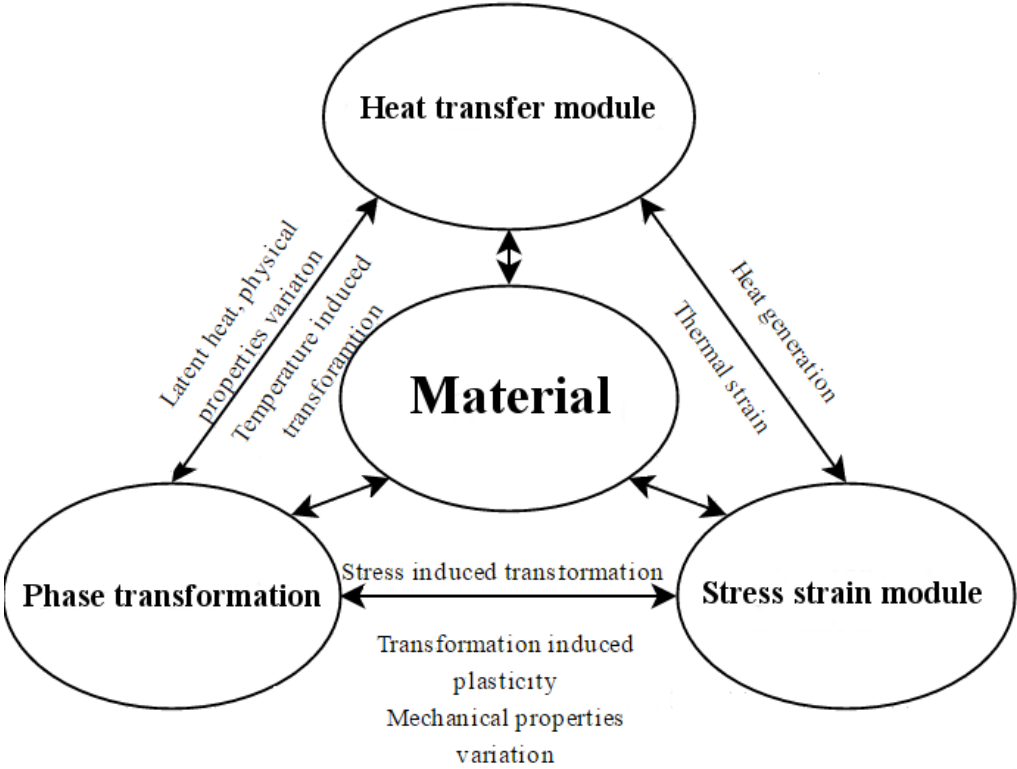
Figure 28 Schematic representation of reciprocal coupling between heat transfer, deformation and phase transformations during heating/cooling of large forgings [87].

There are many factors that impact on the phase transformation start temperature, like the temperature, cooling rate, strain, strain rate, etc. Some of the most important parameters that influence its value are the cooling rate and the strain within the material. The deformation force applied to the element introduces the outer stress into the material, causing the strain that also changes its microstructure. The stress raised from the deformation causes the changes in the geometry and in turn in the temperature field that causes the local difference in the values of the temperature-dependent parameters. The heat from plastic deformation also influences the temperature distribution within the part by affecting the phase transformation process. The new

phases, such as martensite, bainite, pearlite that appear in the material have different microstructures and parameters. Also, there are differences of the local chemical composition of the material within the region of the same phase. It is related with the distribution of the carbon content during the formation of the structures of the new phases during decomposition of the austenite structure. Phase transformation can be induced by strain, which boundary value is determined by a temperature–dependent yield stress. The certain values of such parameters like the transformation rate and the transient stress state, can lead to plastic deformation that occurs below the yield stress. When the stress exceeds the yield strength, the material will be permanently deformed due to the combined effect of the differences in local temperature and the microstructure, which can even lead to destruction. As can be seen, the phase transformation of the microstructure has a crucial effect on a final part condition. Its proceeding can be very complex, what is related with many reciprocal factors, influencing the kinetics of the new phases appearing. The modelling of these processes, although strictly related to the factors presented schematically in Figure 28 can, due to reciprocal coupling between the heat transfer, the deformation and the phase transformations, be down to the details on very deep level [80], [87]–[90].

2.2.2. State of the art – residual stress modelling

Although all factors mentioned above constitute a model of an extensive, complicated system with many reciprocal connections between the different modules, creating such detailed multi-scale model is impractical in the industrial environment, as all of the mentioned elements implemented at the same time can easily overload it. It seems to be an ineffective approach since it can lead to instabilities and unnecessary increase of the computational time [92]. The art of the stress state modelling is based on the most influential main co-operative factors, strictly related with the process and expected results. In the case of this work, the subject is related with the large-scale forgings, numerical representation of quenching process and methods of phase transformations simulation.

Kim et al. [93] used the finite element method to simulate the ultra – large ingot forging process to develop the optimum stress distribution to achieve the inner void closing effect [93], [94]. Dye et al. [95] developed the model that is capable of measuring the residual stresses in

the two-dimensional elements after the quenching process, which was tested on a relatively small 40 kg forging. Bokota and Kulawik [65], [79] developed a numerical model of phase transformation during low carbon steel elements quenching, which takes into account the heat conduction and equilibrium equations. The macro-scale model is based on IT diagrams and the mechanical phenomena, where particular emphasize was put on the influence of the hardening process with the mobile heat source, but again, the sizes of the treated elements were relatively small. Zhou et al. in [96] used ABAQUS software to create a numerical model for residual stress prediction after the cooling of the thin hot-rolled steel strip on the run-out table. To simulate the phase transformation the approach was taken, in which the expansion coefficient was implement as the function of cooling rate, phase composition, temperature and data from CCT diagram. The model was tested on the carbon steel. Similarly, Wang et al. [89] used FEM package Abaqus created an elasto-plastic constitutive model to simulate the cooling of the hot rolled steel strip, where he investigated the deformations in product final shape in relation with the phase transformation and uneven cooling. The Esaka phase transformation model was implemented via Hetval subroutine. The model was validated in industrial production. To fully represent the stress state after the cooling the model covered the aspects of conventional elastic and plastic strains, thermal strain, transformation phase volume change strain and transformation induced plastic strain (Greenwood-Johnson model with Leblond terms).

As the RPVs are created by welding of the smaller elements together a lot of concern is put in modelling the residual stress distribution and microstructure around the weld path [97]–[100], both for usual SA508 gr 3 and in newer materials like SA508 gr. 4N [101]. Although many interesting research has been conducted and the simplified welding-related numerical calculations are performed at the end of this project, the welding process itself is not of concern of this work. Nevertheless, this research can be a source of detailed phase transformation knowledge. For example, Obasi et al. in [102] used ABASUQ software to predict residual stresses that arise in the SA508 gr. 3 steel around the weld path. The material was subjected to rapid welding-like thermal cycles. The solid-solid phase transformation was implemented to the model through the FORTRAN subroutine. Among the find outs there can be highlighted the influence of the cooling rate on the amount of retained austenite or impact of grain size of the austenite on formation of allotriomorphic ferrite, Widmanstätten ferrite and bainite. Also, Dai et al. in [98] used final element code Sysweld to model stress distribution in the SA508 gr. 3 steel after placing the single weld bead on the surface, where he investigated the influence of the phase transformation on that distribution, together with related volume changes and

Greenwood-Johnson transformation plasticity relations. The phase transformation was modelled as Kirkaldy's reaction rate equations and was implemented via subroutine. The important result was that the phase transformation can't be omitted during modelling of the stress distribution. Also, similar as in [66], it was enhanced, that in case of process, where the impact of the outside strain on the phase transformation is investigated, there is a need for implementing into the model the variant selection aspect, as it is a crucial component during modelling transformation of bainite and martensite. During these kinds of transformation the shear component makes greater impact than dilatational component, which can make the variant selection more influential to the stress distribution than volume changes. These findings were confirmed by Francis et al. in [103] where the effects of loading the material on the phase transformation were investigated. But, as noted, the RPVs work in extreme environment due to the high temperature, pressure and radioactivity. The welds and its surrounds are the high-risk places exposed to irradiation embrittlement, so a lot of focus is put on the stress distribution and microstructure around the weld path [104], [105].

Pous-Romero in his thesis enhanced the paucity of the microstructure investigations of the SA508 gr. 3 steel large forgings after heat treatment, as in many works the homogeneous structure in final elements has been reported, which he proved to not be true [4]. Byun et al. in [106] reported, that using automated ball indentation (ABI) the differences in mechanical properties on through-the-thickness distribution were found even up to 20%. As the causes he suggested the segregation during solidification, inhomogeneous deformation and various cooling rates during water quenching in the quality heat treatment process, in which the last one he indicated as the most influential.

As noted before, the mechanical properties are determined by the microstructure. During heat treatment of the ferritic steel the final microstructure is formed by the phase transformations, which is controlled by the change of the temperature in time. So, the prediction of the behaviour of the microstructure during the heat treatment is crucial in achieving the demanded mechanical properties of the product. Garcia de Andres et al. [107] presented the importance of the dilatometry test in solid-solid phase transformation modelling, its ability to calculate the phase quantities in relation to the cooling rate and its continuous character. It helps predicting the new phase amount and thus can be used to the residual stress prediction due to the local expansion of the material. Talamantes-Silva [32] notes the essential significance of cooling rate control, as too fast cooling can lead to quench cracking, but too slow could not

create the desired microstructure in the mid-wall of the large-size forging, where the resulted microstructure can vary from that on the surface.

As dilatometry is a well-known method, linking it with the other more modern methods broadens the scope of the results. Pickering et al. [108] used dilatometric test together with the in situ synchrotron X-ray diffraction (SXRD) to investigate the continuous cooling transformation behaviour for various cooling rate's values for the SA508 gr. 3 and SA508 gr. 4N steels. He reported differences in the ferrite volume fraction measured from the dilatometry and SXRD and of the extent of the allotriomorphic ferrite formed at slow cooling rates during cooling of SA508 gr. 3 steel. These differences were accounted for by the retained austenite, which cannot be measured during the dilatometric test. The transformation start temperatures obtained by both methods were similar. Boyadjiev et al. [109] noted that in addition to the CCT method, there are two further approaches to calculating transformation. Thermodynamics, kinetics and diffusion laws and also the use of Avrami equation together with the Scheil's additivity rule can be used. In Boyadjiev et al.'s approach the thermal stresses are predicted by the calculation of the thermal expansion coefficient, which is presented as a function of the cooling rate, phase composition and temperature. Here, cooling rate controls the transformation start temperature, which is used to calculate the amount of the transformed phase. The expansion coefficient consists of two components related to the temperature and the transformed phase. A similar approach was taken by Milenin [110] who investigated the elastic-plastic bending of the crankshaft during the heat treatment after forging. The uneven thermal expansion due to the transient temperature field and dilatometric effect due to the phase transformation was modelled using finite element method (FEM). In this work the influence of the latent heat, heat conduction equation describing the exchange with the cooling medium and thermal-related properties were implemented. To model the phase transformation the Johnson-Mehl-Avrami-Kolmogorov (JMAK) approach was used, in which the vital parameters were estimated by the inverse analysis. The use of the dilatometric results were also reported as a good method for verification of the phase transformations' parameters. The developed code was directly used in larger industrial software and allowed for optimization of the process. As the result it was presented that through the phase transformation during cooling the sign of the stress changes its value three times in general. Such formulated rule can be used in further developments of the numerical models. These results were used later in this thesis as an approach in which the expansion of the elements during transformation was modelled through changes of the thermal expansion coefficient sign three times.

Although the residual stress in large size forgings for construction of reactor pressure vessels is the subject of this thesis, which still needs detailed investigation, outside the field of manufacturing the elements for nuclear purpose the topic are described quite well. A good example is the aeronautical industry, which uses the relatively large aluminium elements for production of extra-large panel components, such as upper and lower wing skin for aircrafts, stringers and stabilisers [111]–[113]. Aluminium alloys are widely used in automotive and aerospace industries as they provide high strength to weight ratio, high stiffness to density ratio and good dent resistance, when compared to steels. Their advantages are especially valuable in these industries, where there is pressure on reducing weight of the components because of economic and ecological reasons. To achieve the desired shape the elements from aluminium alloys can be formed in many types of processes under various conditions such as cold, warm or hot. Their good mechanical properties are achieved later, in a complicated, multi-stage heat treatment [112], [114]–[116]. The highest strength among all of the aluminium alloys provide the 7000 series, used for large scale panels [112], which is unfortunately connected with the problem of poor ductility at the room temperature. Processing at higher temperatures improves the ductility, but has an impact on the microstructure as the recrystallisation, healing phenomena and grain growth occurs [117]. Among the many hot processes, there can be distinguished superplastic forming SPF, quick plastic forming QPF and hot form and quench HFQ® [118]. Although the constantly conducted investigations improves the quality of these processes the residual stress is still a problem within the aluminium alloy manufacturing. The well-known issue during the forming of the high-strength aluminium alloys is spring-back, which occurs due to the residual stress, left in the element after the forming load is removed.

The conventional way of manufacturing large-size panels from high strength aluminium alloys for aircraft production begins with hot forming. Then the elements are heated in solution heat treatment process (SHT) and quenched. After quenching the elements are cold compressed and aged. At the end the part is machined to the final shape [119]. The many variants of this way are proposed to achieve the best quality microstructure with as less as possible residual stress presence in final products. Zheng et al. [119] suggested the 3-stage process, consisting of water quenching, cold rolling and constrained ageing, which resulted in reducing the residual stress level from ~300MPa to ~100MPa within T-section panels. Such an approach comes from the aluminium alloys processing. It assumes solution heat treatment and quenching to achieve oversaturated solution, which in turn is aged for a desirable microstructure. These methods result in residual stress induced during quenching, where the tensile stresses appear in the core

of the material and compressive stresses are just under the surface due to the cooling rate gradients. As mentioned earlier, optimizing the quenching process to achieve the most possible even distribution of cooling rate values is crucial for obtaining homogeneous microstructure and mechanical properties [120]. Lam et al. [121] investigated the springback behaviour in aluminium alloy plates from 7000 series with the use of FEM modelling, influenced by the machining-induced residual stress. The initial values of the residual stress were introduced into the material during creep-age forming (CAF) method, which simultaneously relax the element by creep and heat treat it by ageing. The controlling parameters of the method are focused more on microstructure development, than stress-relaxation, which results in residual stress presence and springback. After forming the element goes through the machining to final shape process, which in turn adds another level of residual stress, affecting the overall stress state and complicating the springback prediction. Assuming the higher initial stress level, the prediction of the springback by FEM model was better [113]. The stress-relaxation behaviour during aging was investigated by Rong [122], where the plates of aluminium alloy from 6000 series were aged at 160°C for 12h, with various initial levels of strain introduced into the samples. Introducing the strain to the plastic levels accelerated coarsening of the precipitates (β'') due to the higher amount of the dislocations in the sample. Although it did not cause any changes to the yield strength, because of the balance of softening, a result of precipitation coarsening, and hardening, due to the dislocations. There was an impact on the level of the relaxed stress, both in elastic and plastic zones, where the rate of relaxation was the highest in elastic region and was decreasing towards the plastic regions. The mechanism responsible for stress-relaxation was identified as dislocation glide. The amount of relaxed stress was higher if the initial introduced strain was also higher [111].

Heat treatment like quenching introduces residual stress into the material, similarly to any other process, which changes local volume within the part or which violates the balance in its stress-state. As the presence of the residual stress can be detrimental to the final product and a lot of effort is put into eliminating them, most of the time it is not possible, therefore the stress-relieving process must be applied. In the case of manufacturing aluminium alloys many kinds of methods were proposed, like cold working, thermally induced stress-relaxation, retrogressive and re-aging, uphill quenching, increasing quenchant temperature or post quenching delay [119], [123].

Croucher in several publications grouped in [82] presented the residual stress relaxing method for aluminium alloys called uphill quenching, which is based on the improved cooling

rate control by replacing the quenchant from traditional cold/hot water to polyalkylene glycol solution of concentration dependent on the particular process. Then the element is subjected to cryogenic cooling and rapidly heated by high velocity steam [76], [82], [91]. Unfortunately this method, like many other reported, although presenting high effectiveness in eliminating residual stresses, are often not practical to apply to large size elements due to the logistic or economic issues [119], [124].

Pan et al. [124] proposed cold rolling as a method which can be applied to large components, where it is possible to eliminate the stress present in the core of the element. In this work, the quench-induced stress detected at the surface was ~ 260 MPa, while peak stress within the element was ~200 MPa. It was possible to reduce this value to -120 MPa – 40 MPa, which is very good result, compared to value in the article of 30% effectiveness of relaxation-aging. Although this method is able to eliminate tensile stress in the core of the element, it can create high stress at the surface, nevertheless this can be counteracted by different actions. These findings were confirmed in [123], where was reported that the cold rolling performed under the certain conditions turned the core stresses into compressive stresses of values under -100 MPa, when the surface stresses were reduced to above 150 MPa. Cold rolling also redistributed the residual stress more evenly in the specimen.

The chosen examples of the modelling, managing and relaxing the residual stresses in the large panels from high-strength aluminium alloys for aeronautic industry illustrate that the problem of RS is interdisciplinary. As it is impossible to exhaust the subject here, only an attempt to present various modelling approach is taken. Zheng et al. [125] and Rong et al. [126] both proposed constitutive modelling of stress-relaxation age forming approach, simulating the coupled system of precipitate hardening and creep, to predict the springback of the large element from aluminium alloys. Such an approach is based on the development of parameters to constitutive equations, which are used to describe the material behaviour during the process. But although the constitutive law modelling approach can give very detailed description of the material behaviour and it can be very useful for manufacturing very long aircraft components, it is of great concern to cut the computational time of the modelling, which in case of the ultra-large forging is very important factor, especially in industrial conditions.

Although there are many approaches in modelling phase transformation processes [127], the Johnson-Mehl-Avrami-Kolmogorov model is widely and effectively used [52], [110], [128]–[132]. The main advantages of this model are simplicity and small computational cost,

which together with the satisfying accuracy of obtained results are very preferable in industrial environments. The JMAK model was originally developed for the isothermal conditions, which remains its main disadvantage. The problem of the inaccuracies that could arise is usually solved by using JMAK model together with the Scheil's additivity rule.

Carlone and Palazzo [86], [87] presented an advanced thermo-mechanically coupled finite element model capable of taking into account the solid-solid phase transformation during steel cooling process. The approach, assuming the Johnson-Mehl-Avrami-Kolmogorov (JMAK) model with the Scheil's additivity rule, demonstrates satisfying abilities in terms of stress distribution prediction within the steel samples during heating and holding stages. And although the approach does not consider the effects of transformation plasticity, phase change strain and stress induced phase transformation effects, the JMAK approach modelling together with the Scheil's additivity rule is very common in investigations of large size forgings as providing satisfying results. In the article, the quantitative approach is used in calculations of diffusive phase transformations modelling, where austenite decomposition and forming of the new phases are strictly connected with the nucleation and growth processes. The JMAK approach is usually based on the various form of the same equation, in this case presented as:

$$F_i(T) = 1 - \exp[-\alpha(T)t(T)^{n(T)}] \hfill [13]$$

where F_i is a fraction of the transformed new phase; t is a time calculated from the transformation start point; α, n are the material parameters, dependent on the isothermal temperature T and newly formed phase; t(T) is the time needed for the conversion of a specific amount of the new phase F_i at the isothermal temperature T:

$$t(T) = \left[\frac{-\ln(1-F_i)}{\alpha(T)}\right]^{\frac{1}{n(T)}} \hfill [14]$$

where α is a diffusional coefficient and n is a transformation exponent. These parameters are material dependent, possible to determine with use of the IT diagram, taking into account the time τ_s (start) and τ_f (finish) needed for the conversion, in isothermal conditions, of detectable start and finish volume fractions of the forming phase, indicated respectively as F_s and F_f, [86], [87].

The used JMAK model is schematically presented in *Figure 29*.
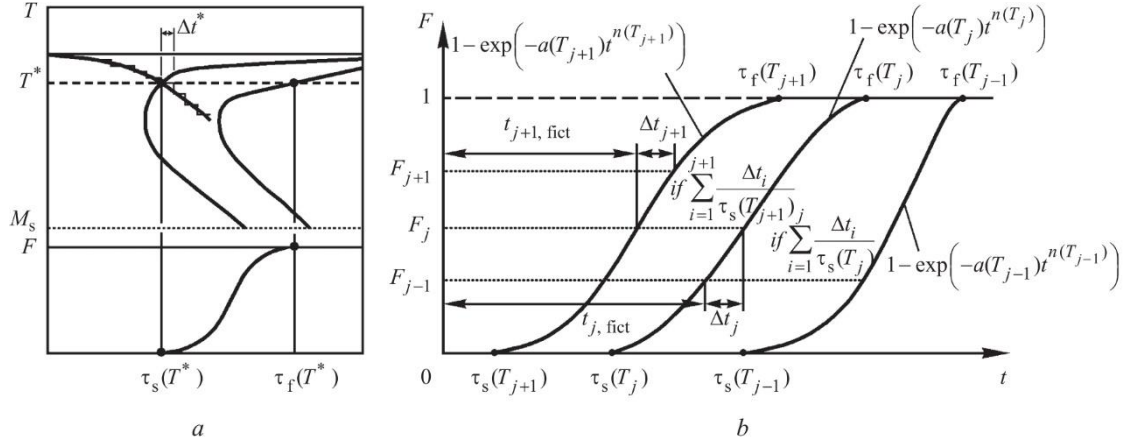
Figure 29 The scheme of the Johnson-Mehl-Avrami-Kolmogorov model with Scheil's additivity rule [86].

As equation [13] is derived from isothermal conditions, the taken approach was based on dividing the transformation temperature range on the isothermal intervals. At every interval the isothermal conditions were assumed, which allowed for the use of isothermal kinetics and the additivity rule. To apply the Scheil's additivity rule the certain conditions have to be met, mostly connected with the nucleation, incubation and growth of the new phase particles. The detailed discussion is presented in [86]. Through the process, at the beginning of the each isothermal step $\Delta t_j(T_j)$ the fictitious time $t_{j,fict}$ is calculated, using the equation [15]:

$$t_{j,fict}(T_j) = \left[\frac{-\ln(1-F_{i,j-1})}{\alpha(T_j)}\right]^{\frac{1}{n(T_j)}} \tag{15}$$

where the time $t_{j,fict}$ is the time needed to transform the amount of the new phase $F_{i,j-1}$ in the actual step $\Delta t_j(T_j)$, which was transformed and cumulatively added in all previous steps together. The equation [16] represents the total time t_j, which consists of the sum of the fictitious time $t_{j,fict}$ and the time step Δt_j:

$$t_j = \Delta t_j + t_{j,fict} = \Delta t_j + \left[\frac{-\ln(1-F_{i,j-1})}{\alpha(T_j)}\right]^{\frac{1}{n(T_j)}} \tag{16}$$

The equation [17] presents the transformed phase at the end of the step time Δt_j:

$$F_{i,j} = 1 - \exp\left[-\alpha(T_j)t_j^{n(T_j)}\right] \tag{17}$$

The equation [18] presents the condition, which has to be met to allow the transformation to begin, due to the Scheil's additivity rule:

$$\sum_{j=1}^{n} \frac{\Delta t_j}{\tau_S(T_j)} \geq 1 \qquad\qquad\qquad [18]$$

where τ_s is the incubation time at the relevant time step. It means that the time of the relevant time step, divided by the incubation time at this time step $\tau_s(T_j)$ is the fraction of the total nucleation time required for the transformation to begin [86].

The advanced physical phase transformation models distinguish the austenite-ferrite stages such as nucleation, growth and site saturation [133]. These models are connected with other models describing pearlitic, bainitic and martensitic transformations. Such models, when implemented into the FE code, allow for simulation of microstructural phenomena under varying thermal conditions showing good predictive capabilities [134]. An Avrami-type equation describing the kinetics of phase transformation is very often used in the case of the simplified approaches [135]. As has been shown earlier by other authors [136], the dilatometric transformation curves obtained under constant cooling rate can be described by an Avrami equation as a function of time [137]. The transformation curves present two differentiated zones that correspond to the austenite to proeutectoid ferrite and remaining austenite into pearlite transformation, taking into consideration that the amount of pearlite is significantly smaller than the amount of ferrite for relatively low cooling rates.

As already established, the development of the new numerical approach of the residual stresses investigations in large size forgings is a main aim of this project. To achieve that the commercial FE packages, such as MSC Marc 2013.1.0 and Abaqus/Standard 6.14, were used to create the set of numerical models rooted in a certain base of assumptions, which were developed by Krzyzanowski et al. [138], where a thermo-mechanical finite element model capable of taking into account changes in the specific volume during austenite to ferrite transformation during cooling was obtained. The significant ability of this model was a possibility of coupling with any of the existing phase transformation models that allows for simulation of the sample contraction due to both thermal contraction and the dilatometric effect. The geometry of the model was the upper half of the cross section of the tubular dilatometric sample (Figure 30).
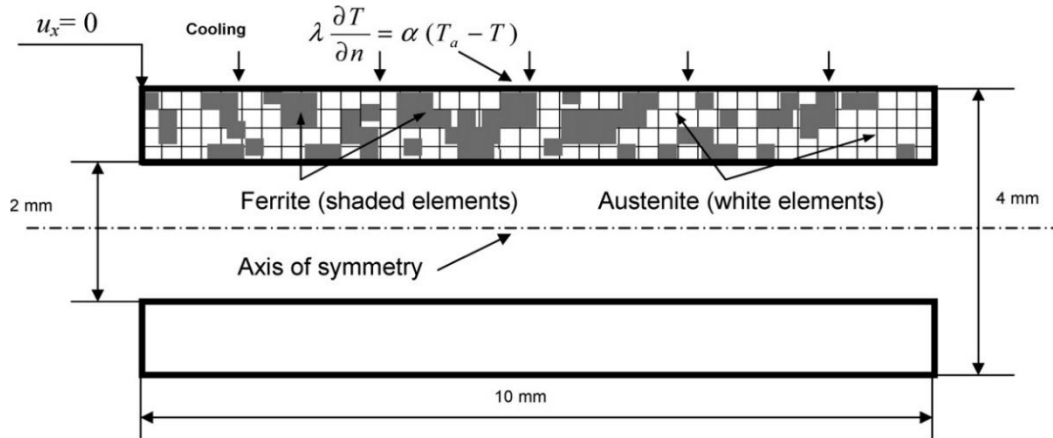
Figure 30 2D axisymmetric model of phase transformation in a dilatometric sample presented in [138].

As it can be seen in *Figure 30* axisymmetric conditions were used. On the left edge of the cross section the displacements constraint $u_x=0$ was applied, while contraction displacements of the sample right edge were allowed. A sample was cooled down with a constant rate by connecting its outer surfaces with the ambient of the lower temperature. Simulation of such a cooling process is described through an equation of the energy balance for the outer boundary surface, presented as:

$$\lambda \frac{\partial T}{\partial n} = \alpha(T_a - T)$$ (19)

where: λ is the thermal conductivity, n is a coordinate normal to the surface, α is the thermal transfer coefficient, T_a and T are the ambient and the boundary surface temperature, respectively. The thermal transfer coefficient was a variable, with changes allowed for the cooling rate control in the range of interest, which was $0.5 – 163°C/s$. The phase transformation was implemented into the model in such a way that the new phase has its origins randomly distributed within the geometry of the model (Figure 30). The corresponding newly grown ferritic phase elements at a given time were scattered within the area of the cross section of the sample, if the required temperature for the transformation start was achieved. At every time step the ratio between the number of austenite and ferrite elements within the local area was determined by eq. (21) and the transformation from austenite into ferrite of every element could happen once during the process. It is noteworthy that during simulation of the cooling with higher rates the differences in the temperature field within the cross section rose up to $4 – 5°C$. Under such conditions the numerical calculations of the new phase relied on the dividing the

whole temperature range of the phase transformation into temperature intervals (Figure 31). This assumption considers that the origin of the new phase appears within the areas of the same temperature, which are characterized by the single value.
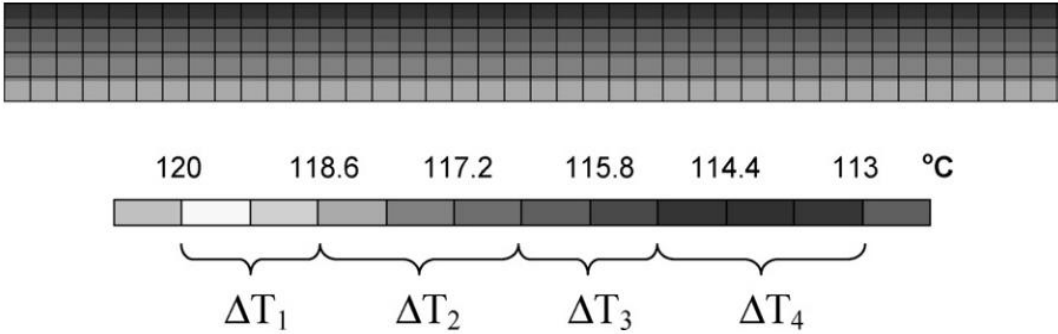
Figure 31 The predicted temperature field of dilatometric sample cooled down with 163°C/s cooling rate. Below, the schematic representation of the temperature intervals, used to calculate the fraction of the new phase is presented [138].

Although it was not the concern of this project, Krzyzanowski emphasized that assuming random distribution of ferritic phase in a specimen, which was undergoing phase transformation, was a new approach of dilatometric test interpretation. In previous models reported in the literature the measured changes of the specimen length during γ–α transformation corresponded to a gradual transformation of the whole specimen volume [138].

2.2.3. Summary

In the past, most of the literature related to the ultra-large size forgings from the SA508 grade 3 steel has been devoted to improving metallurgical quality of the steel, overall forging manufacturing process, the void closure problem during the forging and the numerical modelling of the welding process connected with joining the elements of RPV. Today, as the modern approach is focused on the development of the best quality microstructure and ensure the highest element integrity, companies around the world deal with problem of stresses that arise both from the heat treatment and from the phase transformations, based on their long empirical experiences from the past [27], [32]. Stress management and mapping the residual stress within the whole volume in ultra-large size forgings for RPV elements during heat

treatment process should be constantly improved through wide scientific investigations, because of the strong growing demand resulting from the energy industry development direction. There are a vast number of papers devoted to the numerical analyses of the phase transformations of material, presenting investigations under a wide range of conditions, process and materials. However, in the author's opinion, the problem of residual stress arising during the quenching of the large size forgings is the matter which, from the scientific point of view, was not explored enough as there is still lack of practical methods of control of residual stresses, which can be used in industrial conditions. Assuming the above the certain approach of modelling of the phase transformation directed to the large-size forgings for RPV's production purpose was developed and implemented in the thermomechanical models that has been created for this project. This work broadens the very important subject of residual stress management by taking the new perspective of the modern nuclear materials production for the recent systems of energy production.

3. Numerical procedures

To investigate the stress development during the heat treatment of the elements for RPVs construction, the parameters of steel SA508 gr. 3 were used – a material for large ingot production. Such material has to be characterised by relatively high fracture toughness, sufficient strength and resistance to irradiation embrittlement to prevent early failure caused by aging degradation, as it operates under high temperature and pressure conditions and also is exposed to the radiation source [54], [139].

Taking into account the scale of the elements, which are subjected to investigations, it is necessary to take advantage of numerical packages. It is important to emphasize that the developed models and the calculated results, supported by experimental examination like hardness and dilatometric tests, are the main outcome of this work. The numerical packages used were Simulia Abaqus and MSC Software Marc Mentat. These programs are able to create 2D and 3D finite-element (FE) based models, which helped to simulate heat treatment processes performed on the SA508 gr. 3 steel samples, taking into account the phase transformation. As the main causes of the stress development inside the material during the heat treatment were dynamic nucleation, growth of the new phases and uneven expansion/contraction within the element caused by non-homogenous heating/cooling, these phenomena were modelled by testing various approaches, described in detail further in the text.

The numerical procedures were supported by the experimental tests, which are presented later in the Validation section. However, it has to be mentioned now, that the particular attention was paid to the dilatometric tests, which helped to establish the set of the experimental thermal expansion coefficients of the material for the different temperature regimes, which were then implemented into the numerical model. Experimental procedures of this work have supplementary character for the methods used in the Numerical Modelling part.

3.1. Methods

The numerical methods selected on the way to develop the final numerical model, which was used for stress analysis in large size forgings, were strictly related to the expected outcome. As the final model consists of many modules, each one had to be carefully investigated, hence the influence of the possible variations on the outcome were checked. The various modifications of the particular modules of the model were tested in accordance with the level of the model advancement. The emphasis was put on modelling of the two main factors responsible for the stress generation during the quenching: the heat exchange between the coolant and the element and the phase transformation parameters. The details of the modules used in particular models are given in their description, together with the outcome. The main modules, which were investigated, are presented below:

- Geometry: the simplified at the beginning geometry (Figure 32, Figure 33) of the model allowed for adjusting the boundary conditions for the heat exchange module and the phase transformation controlled through the change of the strain sign. The models were presented in the small scale geometry (in millimeters units) like for the representation of the dilatometric test, or large scale (in meters units), like during the investigations of the stress distribution due to the quenching process of the large tubular forging with flange. The geometry investigations also included the proper way of fixing the element in the numerical space, as the handling of the element in the quenching pool has an impact on the heat exchange and local cooling rates. The computational time optimization was investigated through the symmetry condition use, where the element is calculated only partially, and also by using various dimensions (2D, 3D and axisymmetric).
- Material: the material type is implemented through the values of its parameters, like density, Young modulus, Poisson's ratio, yield stress, conductivity, specific heat and thermal expansion coefficient. Various parameters were calibrated and its relevance with the temperature was added through the development of the model. The thermal expansion coefficient is presented in three ways:
    - As a constant value;
    - As a temperature dependent value;

- As a resultant value of the mix of different phases, calculated by the function of cooling rate or through the Avrami equation, implemented through the UEXPAN subroutine.

- Heat exchange: a couple of approaches were tested:
  - The calculation of the temperature as the solution of the energy balance equation (eq. 12), where the speed rate of the heat exchange between the quenchant and the element was controlled by the alpha coefficient. The change in the quenching coefficient value during the process can be implemented, which allows for taking into account the quenching stages (like the cover of steam formation, which is the product of the boiling water from contact with hot element surface).
  - The linear change of the temperature of the whole sample, which reflected the cooling of the small dilatometric sample, where the differences between the surface and the core were negligible in the reference range.
  - The temperature change set as the implemented at the beginning, where the specific temperature values were assigned to the surface at the certain times in process. Such approach allowed for assignment the temperature values obtained directly from the dilatometric test or from the thermocouples attached at the elements in real industrial case.

  The proper description of the thermal exchange together with the right implementation of material parameters, like conductivity and specific heat, allowed for construction of the realistic transient temperature field within the element, where the map of predicted cooling rate values was possible to create, both at the surface and at the depth.

- Phase transformation: the different phase transformation models on the various development stages were implemented. The phase transformation was presented as:
  - The simple three times change of the sign of the thermal expansion coefficient (TEC) assigned to the finite elements at the certain temperatures.
  - The implementation of the Avrami equation, which was used for calculations of the new phase amount at the certain stage of the cooling process for assignment the proper value of the TEC, which is resultant from the mix of phases.
  - The system in which the two first approaches were combined – the three times change of the sign of the TEC in the elements calculated by the Avrami equation.

   o The assignment of the temperature-related TEC value, obtained from the dilatometric test performed with the certain cooling rate.

   o The assignment of the TEC value, which is the function of the cooling rate and the temperature, obtained from the set of dilatometric tests.

   The transformation start temperature is calculated from empirical equation, which was adjusted to the actual conditions by the selection of certain parameters, obtained through the dilatometric test. The parameters of the phase transformation were found with the use of the Inverse Analysis methods.

- Modeling: for investigation of the mechanical respond of the heated/cooled element, the coupled thermomechanical calculations were chosen. The mesh in the model was related to the geometry, the different numbers of finite elements, from 64 to 26606, and the different kinds of finite elements, like 2D quadrilateral, triangular, 3D hexagonal, tetragonal were applied.

Below, the first two models are presented explicitly, constituting the basis of the taken approach. The presented geometry, the way of implementing the material properties, the heat exchange process and the phase transformation model present the principal methods used in this project. Then, the Inverse Analysis is described, which was used for investigations of the phase transformation model parameters. After these sections, the development of the final model, based on the cooling rates obtained from the dilatometric test is presented, where the mentioned above modules were investigated under various conditions and were described in detail. The Fortran codes with the written instructions for the phase transformation are presented at the end of the work in Appendix A.

3.2. Heat transfer modelling

The first model that was created was based on the approach described in the literature review section (Figure 28), taking into consideration phenomena which arise from the two reciprocal factors: heat transfer module and phase transformation, where the third, the plastic strain effects, was neglected. The model was able to calculate numerical problems of the transient temperature fields and the thermally induced phase transformations using finite

element analysis. It was able to simulate the stages of the heat treatment such as heating, holding and cooling together with the changes in the specific volume of the material, regards to the differences of the thermal expansion coefficient. The model in a similar way took into account the transformation of the material from one phase to another, representing austenite to ferrite transformation. The geometry was simplified and presented as a 5×5×5mm cube that has been divided into 125 3D hexagonal elements with eight integration nodes. The cube had constrained movements in three axes on nodes located on three planes, in XZ, YZ and XY directions (Figure 32).

a) Plane XZ   b) Plane YZ   c) Plane XY
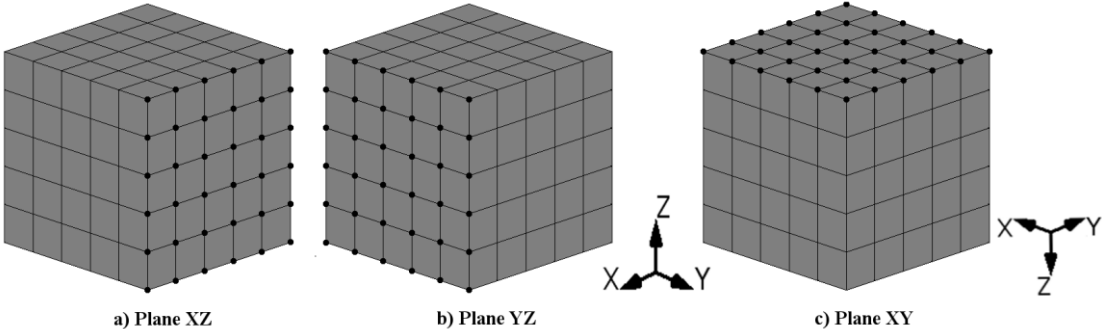
Figure 32 Schematic representation of the nodal constraints at the planes of symmetry [67].

The rest of the nodes were not restricted to movement, that allowed the cube to expand/contract and gave the impression of symmetry, as shown in Figure 33. For instance, the displacements in X direction or rotations around the axes Y and Z was not allowed for the nodes situated on the plane YZ. Similar constraining conditions were applied to ZX and YX planes of the section correspondingly:

$$
\begin{aligned}
u_1 = u_{r2} = u_{r3} = 0 \quad &\textit{for YZ plane} \\
u_2 = u_{r1} = u_{r3} = 0 \quad &\textit{for XZ plane} \\
u_3 = u_{r1} = u_{r2} = 0 \quad &\textit{for YX plane}
\end{aligned}
\tag{19}
$$
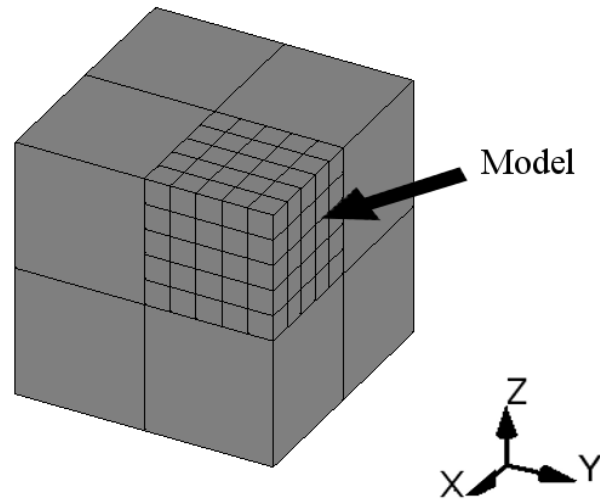
Figure 33 Schematic representation of the position of the modelled part in the whole element after application of the symmetry planes [67].

Similarly to Krzyzanowski's model [138] the change of temperature was performed by applying to the outer surface contact with water at room temperature. The energy balance was prescribed by implementing the same equation (19). The phase transformation was implemented by a subroutine written in the programming language Fortran. It allowed for transition of the elements in various sections of the model and it was prescribed for allowing random distribution of the new phase within the time, when the relevant conditions are fulfilled. It means that when the temperature reached the required value (transformation start temperature), the subroutine changed the way of calculating the thermal expansion in those elements, which represented the appearance of the new ferrite phase. The ratio between the number of transformed and untransformed elements within the area is determined for every time step by the fraction of ferrite with respect to the whole volume of the material determined in the phase transformation module for every time step. It is assumed in the model that when an element is transformed from austenite into ferrite its volume is changed according to changes of atomic volumes of the corresponding phases. The model is thermo-mechanically coupled, which means that some of the important mechanical and thermal properties are described as functions of temperature. The relevant model parameters, such as thermal conductivity, specific heat and density of the steel, necessary for heat transfer calculation, were introduced on the basis of available experimental data. The mechanical properties of the steel were assumed to be similar to the those used in the majority of FE models [20], [34], [66], [67], [140]–[143] and are presented in the Table 11.

Table 11 The thermal and mechanical parameters used in the model [67]:

Density [t/mm^3]	Young's modulus [MPa]	Poisson's ratio	Yield stress [MPa]	Conductivity* [mW/mm*K]	Specific heat* [kJ/kg*K]	Thermal expansion coefficient*
7.833e^{-09}	181135	0.3	345	23-41	400e^{+06} – 1700 e^{+06}	10.8e^{-06} – 22.3e^{-06}

*data temperature dependent

Considering the theory of stored energy in the unrecrystallised austenite, the transformation start temperature depends on the cooling rate, austenite grain size and retained strain. In this model the following simplified equation was implemented:

$$T_s = (825 - 27{,}6 \times \theta) + x_1 , \qquad (20)$$

where T_S is the transformation start temperature and Θ is the cooling rate [°C/s]. To optimize the model the simple type of the Avrami equation was implemented to control the kinetics of phase transformation:

$$X_f = 1 - \exp\left[-\ln 2 \left(\frac{t}{x_1} \right)^{x_2} \right] \qquad (21)$$

where X_f is the fraction of ferrite with respect to the whole volume of the material, x_1 and x_2 are the material parameters and t is defined as $t = [T_F\text{-}t(1)]/\Theta$, where $t(1)$ is the temperature of the node at the moment. The parameter x_1 corresponds to both the nucleation and growth rates of the new phase and can also be a function of the cooling rate, austenite grain size, steel chemical composition and temperature [144]. The presented kinetics of the phase transformation are sufficient at the beginning of the investigations, makes calculations faster and gives the relatively good solution of the problem.
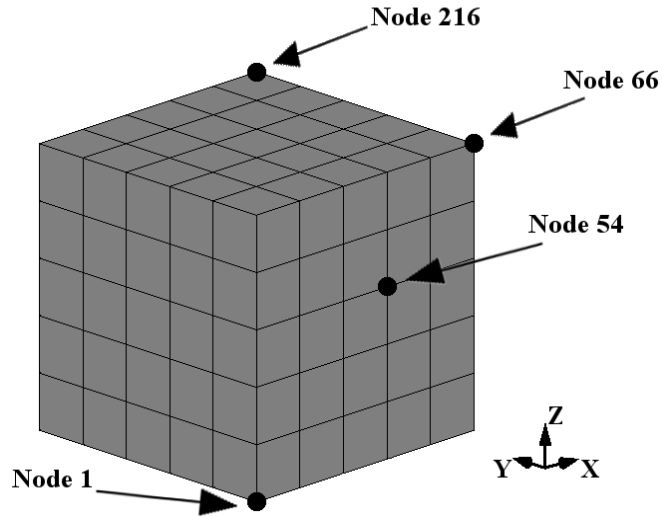
Figure 34 Representative nodes of the cube section chosen for the transient analysis [67].

In Figure 34 the four representative nodes numbered as 1, 54, 66 and 216 have been chosen for obtaining results of temperature transient field analysis. Node 1 is located in the middle of the cube, node 66 is chosen in the middle of the cube external edge. Node 216 represents the most remote from the middle of the cube point, while node 54 is located in the half-way from the middle to the surface.
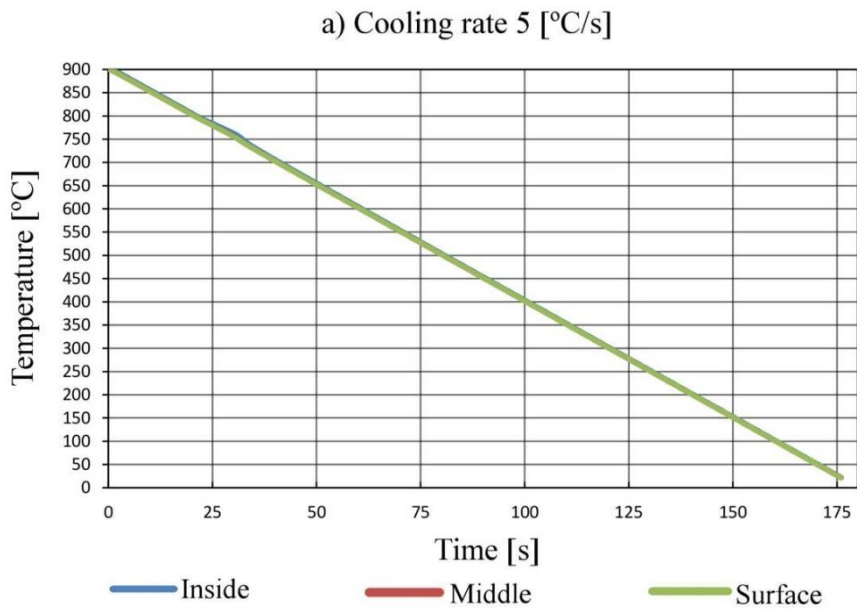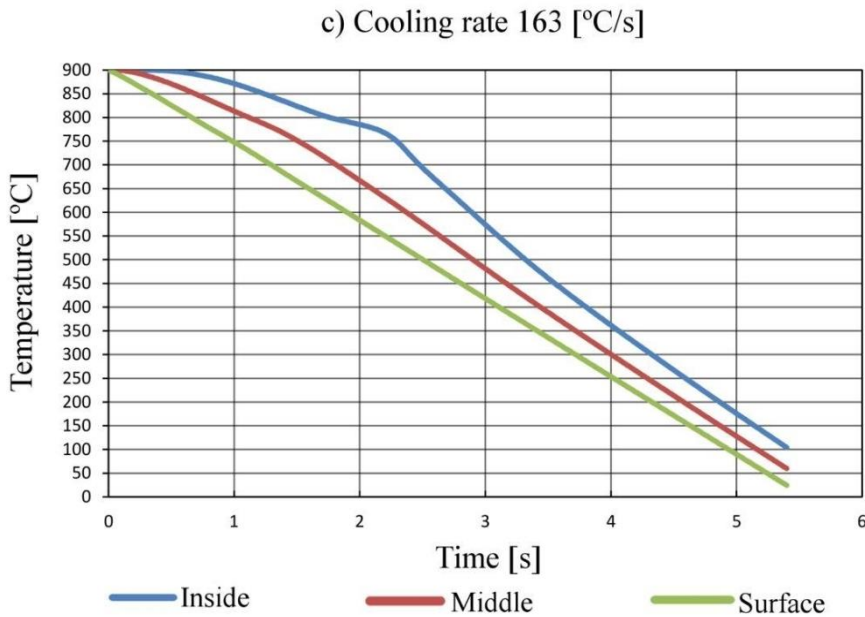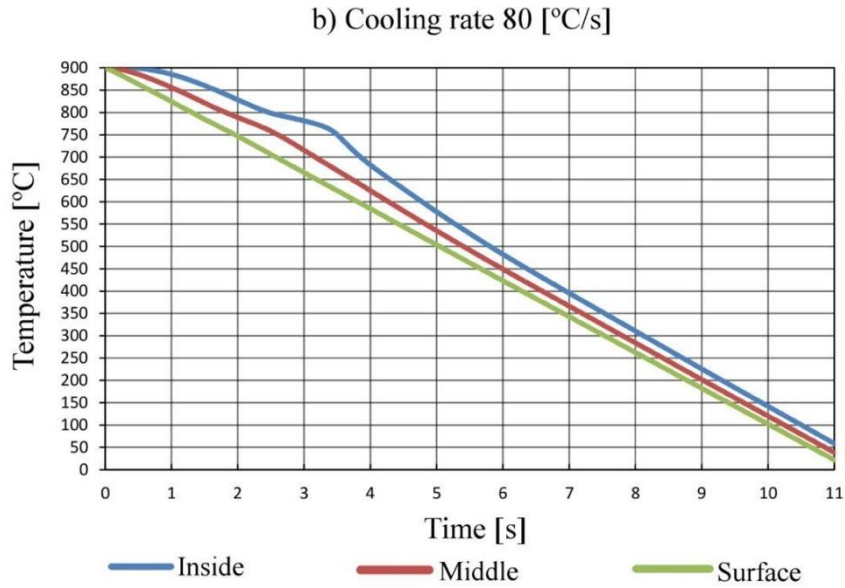
Figure 35 The change in temperature at the different nodes within the section predicted for the different cooling rates at the boundary surface: a) 5 [°C/s], b) 80 [°C/s], c) 163 [°C/s], for nodes 1 (inside), 54 (middle) and 66 (surface). [67].

As noted before, the transient temperature field during the process is one of the primary influential factors during stress analysis. The way in which it changes is mainly controlled by the change rate (heating or cooling rate). To investigate the ability of the developed model to simulate the change of temperature within the element, the boundary condition described by the energy balance (eq. 19) has been replaced by the boundary condition of the first kind, i.e.,

to the set of temperature values with corresponding times, which were prescribed to the outer surface of the model. Such an approach allowed precise control over the temperature change rate turning it into nearly linear. In Figure 35 three cooling stages with different cooling rates are presented. The time-temperature graphs illustrate the temperature values from the points located on the various place on the cube that has been shown in Figure 34 (points 1, 54, 66) within the time of cooling from 900°C to 20°C. The chosen points correspond to the inside of the cube, middle and the surface. The cooling takes significantly less time for the highest cooling rate, such as 163°C, relative to others. As can be seen in Figure 35a, the differences in temperature predicted at the node located in the middle of the cube and the node in the middle of the cube external edge are very small when the cooling rate is low, about 5°C/s. The actual cooling rate depends on, and can be controlled by, the heat transfer coefficient between the material and the ambient fluid. However, for higher heat transfer coefficients, which influence cooling of the boundaries with cooling rates similar to the cases illustrated in Figure 35b and c, the temperature distribution within the section is not homogeneous and the surface layers of the material cool down significantly faster than those situated deeper within volume of the section. The temperature inhomogeneity causes relative inhomogeneity in the distribution of the corresponding element volumes within the section due to the differences in their thermal contraction that would inevitably result in development of internal stresses within the volume of the section.
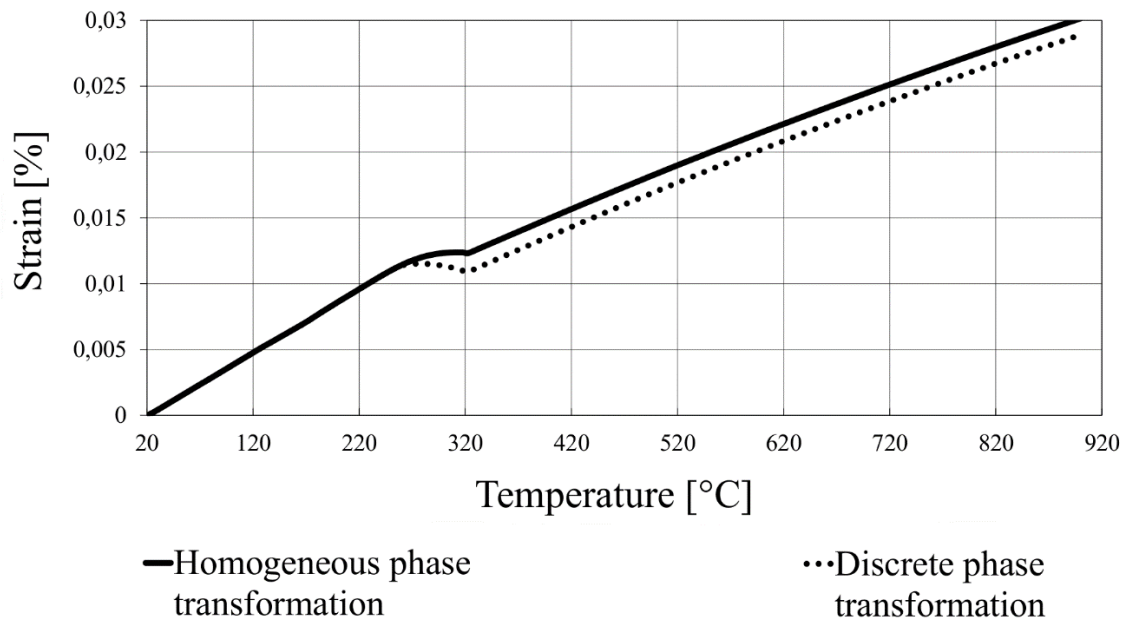
Figure 36 Dilatometric contraction curves predicted at node 216 for the cooling rate 5 [°C/s] assuming homogeneous and inhomogeneous appearance of the ferritic phase [67].

Figure 36 gives two dilatometric curves predicted assuming a random distribution of the ferritic phase appearing within the volume of the section (discrete phase transformation) and assuming the conventional approach (homogeneous phase transformation). In the case of discrete transformation, the Krzyzanowski approach [138] has been tested, which assumed phase transformation randomly distributed within the section and that the ratio between the number of ferrite and austenite elements during the phase transformation corresponds to the ferrite/austenite volume fractions at any time moment, according to eq. (21). The developed model fulfils those assumptions through reflecting the appearing ferrite phase within the volume as randomly distributed elements with expanded volumes relative to the remaining austenite elements, which refers to the changes in atomic volumes of the corresponding phases. The data were obtained from node 216, which is the most remote from the middle of the cube point located in its corner and represents the change in dimension in all three directions. The solid curve presents the strain response of the section registered at the same node 216 assuming the conventional approach representing homogeneous phase transformation modelled for the comparison.
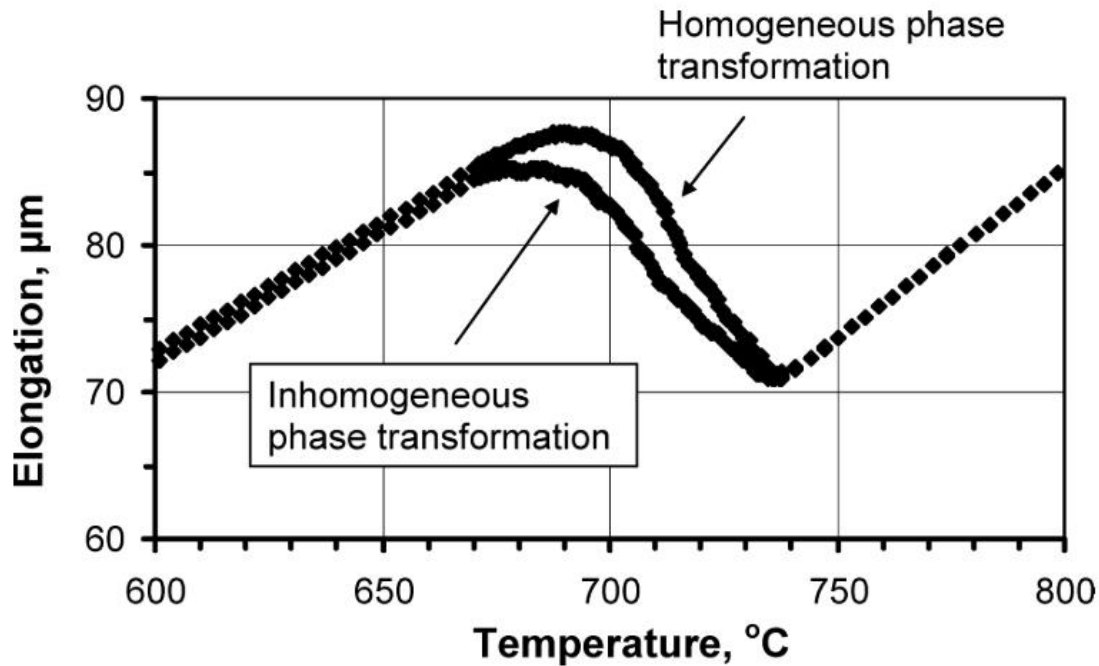
Figure 37 Dilatometric curves predicted for the cooling rate 3°C/s, calculated with two approaches, from [138].

The results presented in Figure 36 correspond with the results obtained in [138], presented in Figure 38. In both cases it can be seen that the random growth of the new phase's elements results in more gentle strain response of the section due to the constraints on strain induced by untransformed elements of austenite. But the visible difference between the deformation levels in Figure 36 occurs due to the position of the elements of the new phase. In the homogenous approach all new ferrite elements appears on the edges of the model that divides the model into two near equal parts. The highest stress values occur between these two sections. In discrete phase transformation the randomly distributed lonely elements in the model causes higher stress level, stretching the surrounding elements almost always in three directions, because it is rare for the elements nearby to expand in the same direction together with the new phase elements. It is observed that through the transformation order changes and it is possible to make an influence on shapes of the strain curves in various ways. Also, the model of the homogenous phase transformation places new elements of the ferrite in some privileged places. Because of that some of the places are more deformed than the others, especially in the area near the origin of the coordinate system. This again causes the region dependent results, which is an interesting subject for investigations in future.
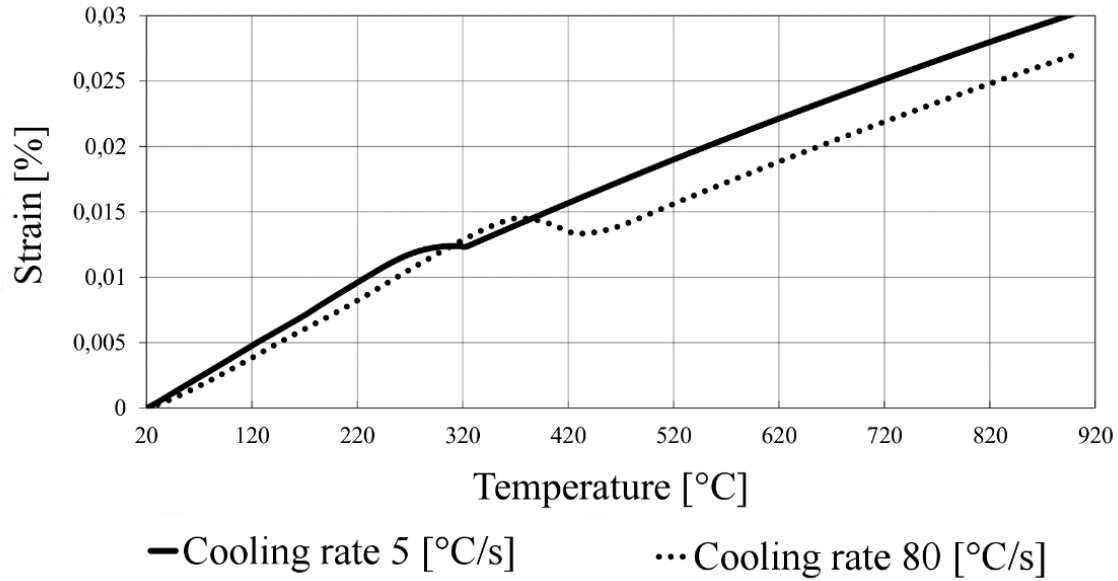
Figure 38 Dilatometric contraction curves predicted at node 216 for the different cooling rates [67].

The influence of the cooling rate on the phase transformation, registered as the changes on the predicted dilatometric curve, is illustrated in Figure 38. A clear delay of the transformation start temperature can be seen as the effect of the higher value of the cooling rate. During the simulation of the cooling with higher temperature change rates, the method described earlier (Figure 31) [138] of dividing the whole phase transformation temperature range into temperature intervals, where temperature within each interval can be characterised by some constant (characteristic) value is used. In terms of the austenite/ferrite transformation the assumption was taken that the phase transformation occurred in randomly distributed elements only within the corresponding regions of the equal characteristic temperature for the given time. The ratio between the number of transformed (ferrite) and untransformed (austenite) elements during the phase transformation time period within such areas corresponded to the austenite/ferrite volume fractions for the characteristic temperature and was controlled by eq. (21). In other words, not all of the elements that are allowed to change at the given temperature actually had a time to transform. The characteristic temperature value nearly always changed before all of the elements from the area allowed to transform did that. The change between the areas allowed to transform at the given time depended on the cooling rate. At the higher rates the differences in the local volumes of elements due to phase transformation and the differences due to higher temperature gradients resulted in larger value of the deformation, presented on the dotted curve (Figure 38).

87
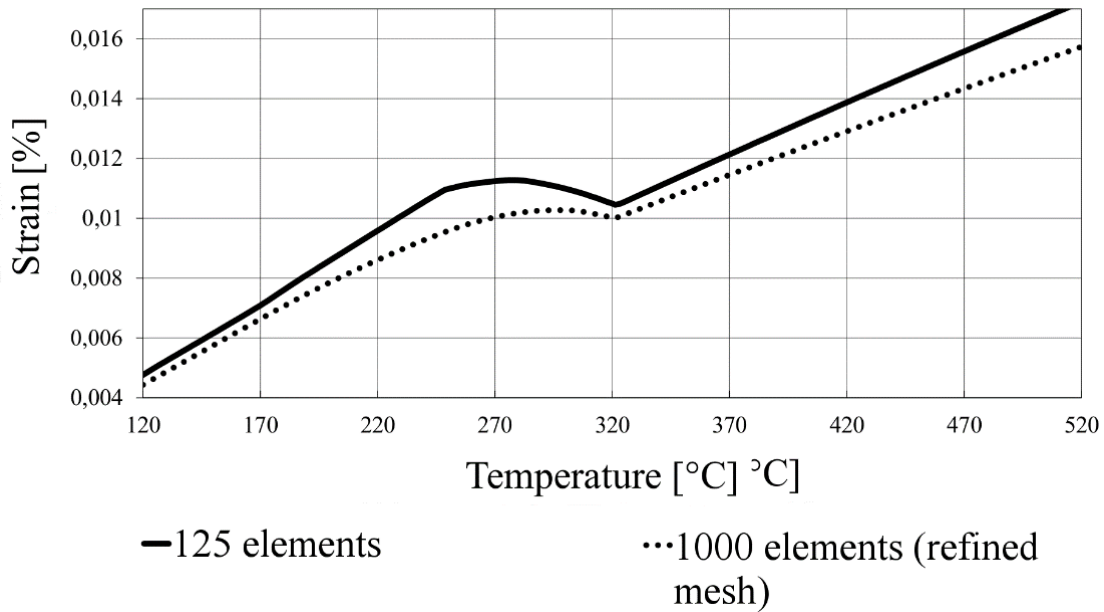
Figure 39 Dilatometric contraction curves predicted at node 216 for the cooling rate of 5 [°C/s] assuming different mesh refinement of the section and discrete phase transformation [67].

Two dilatometric curves are presented in Figure 39, predicted for the same process conditions, but as it can be seen, the dotted curve was calculated with the use of much more finite elements. The discrete approach assumes that the ferrite phase appears within the section volume as randomly distributed elements having slightly expanded volumes relative to the remaining austenite elements, as follows from the changes in atomic volumes of the corresponding phases. Such an approach causes differences in the predicted dilatometric curves during refinement of the finite element mesh even for the low cooling rates, such as 5°C/s. Thanks to this observation the effect has been taken into consideration during further analysis, when the optimum mesh size was chosen for the direct model. The effect of the mesh refinement is more pronounced for cooling of the section at high cooling rates.
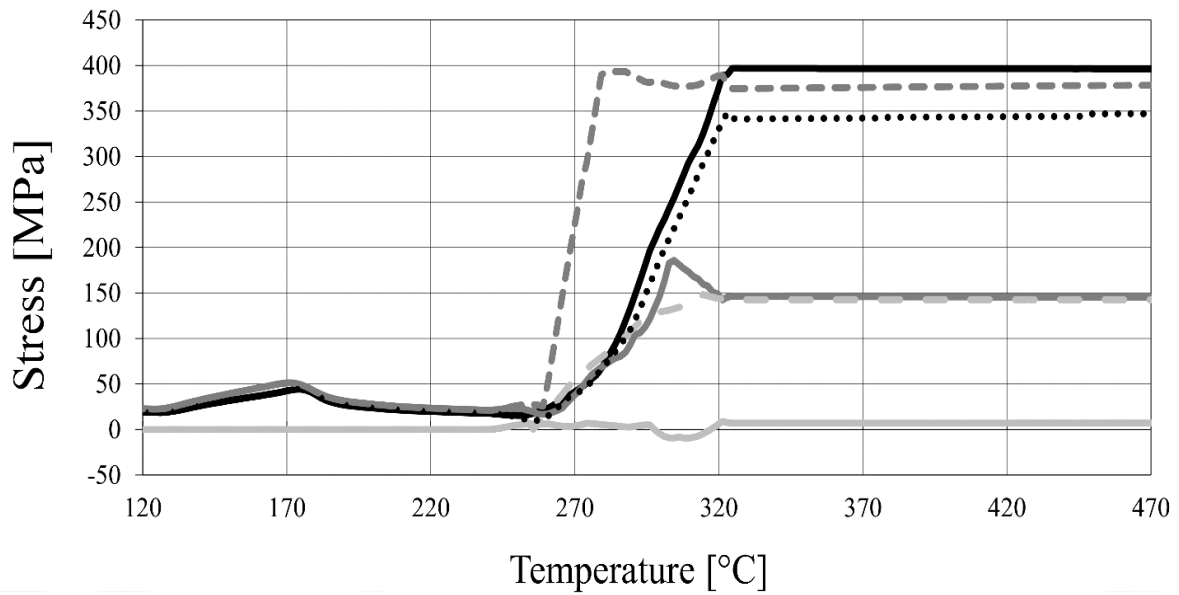
Figure 40 Changes in the equivalent stress predicted at nodes 1, 54 and 66 located within the section (Figure 34) for the different stages of austenite-ferrite phase transformation during cooling with 5 °C/s cooling rate assuming homogenous and discrete phase transformation [67].

Figure 40 presents the equivalent stress predicted at various locations within the cross section of the applied model geometry during cooling with the temperature change rate of CR=5°C/s. The location of the nodes is presented in Figure 34. The dashed curves correspond to the values obtained from the model with the discrete transformation method implemented. Looking at the solid curves it can be seen that before the applying the randomization method the stress values inside the material during austenite to ferrite phase transformation were very low and the almost stable. It was the lowest among the other stress values predicted at other locations. The stress predicted on the surface was the highest due to the dilatometric effect and the local differences in volumes of the finite elements, influenced by their inhomogeneous thermal contraction under higher temperature gradients. The elements located just below the surface of the geometry were located between the areas of high and low cooling rates that resulted in a relatively moderate level of stress values. It can be noticed that randomising the

89

phase transformation induced much more stresses within all of the cross section of the model. It can be observed that the stresses on the surface were somewhat lower, but started growing much faster around the temperature of 260°C. The stresses inside the material grew to the level of near-the-surface location before randomisation and the stress level recorded near-the-surface grew really close to the highest level, but not surpassing the stress recorded on the surface. This means that the randomisation of the appearance of the new phase during the phase transformation causes the stress distribution inside the material to be much more extensive and relatively higher in the near-to-surface and surface locations.

With the development of the new thermo-mechanical finite element model, which simulates contraction of the modelling section during cooling through the austenite–ferrite temperature range the first steps in the new approach were made. There results were presented, which proved that the developed model was able to predict the transient temperature field during the heat treatment of the material of the interest, had a certain sensitivity for the influential factors like cooling rate, was able to simulate corresponding with the cooling rate the phase transformation dilatometric effect and due to that was able to predict changes in stress distribution within the geometry. In the further work the next improvement of the implemented phase transformation model is presented.

3.3. Numerical modelling: various approaches of phase change modelling

As already mentioned, the coupled thermo-mechanical finite element model able to perform stress analysis in the dilatometric sample was developed. The stresses, which occur during the heat treatment are related to the homogeneous expansion/contraction of the part's subregions. The difference in the volume change can occur from the uneven temperature distribution within the material, due to its geometry, and due to the different thermal parameters of the new phases appearing during phase transformation. The nucleation of the new phase occurs randomly within the element due to the local process conditions, such as chemical composition and cooling rate [86], [87].

The developed model simulated the above described phenomena to calculate the transient temperature field and predict the change of the sample dimensions. The change was controlled through the temperature dependent thermal expansion/contraction coefficient. Like the temperature, the other of the two main implemented factors responsible for the dimensions change during heat treatment was modelled – the phase transformation.
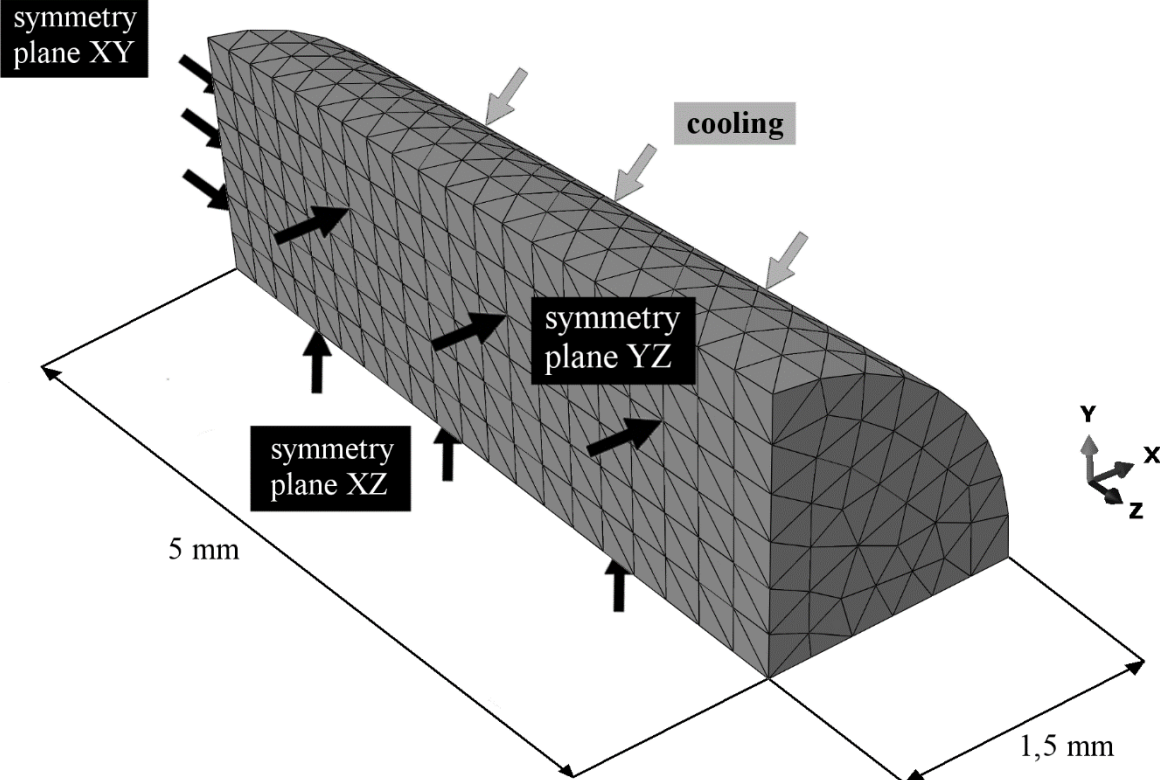
Figure 41 The finite element model geometry; 1/8 of the dilatometric test sample with symmetry condition on planes XY, YZ and XZ applied.

In the presented model the dilatometric test was simulated by applying the geometry of the dilatometric sample to the already developed model, presented in Figure 41. Similarly, the prescribing energy balance for the outer boundary surface (equation 19) was implemented, but the cooling process could be simulated alternatively by the changing temperature value at the surface of the part with time. Such boundary conditions were applied in this work, as the dimensions of the dilatometric sample for the tests was small enough to allow for linear change.

The used FE package, Simulia Abaqus allows for many methods of implementing the thermal expansion/contraction coefficient. The Fortran subroutine used for the purpose of this work allowed for detailed description of the conditions in which the certain set of the coefficient values were assigned to the elements through the process time. At this stage of the investigations there were assumed three states for each element, each one with different value of the thermal expansion coefficient: before the phase transformation, during the phase transformation and after the phase transformation. Such formulated approach, although simplified and with the necessity of the data from the dilatometric test support, can be applied to any geometry and to the different material types. Together with the dilatometric test results performed with the various cooling rates, described in detail in the Experimental chapter, and the use of SA508 gr. 3 steel samples the ability of the model to perform the residual stress analysis was proved.
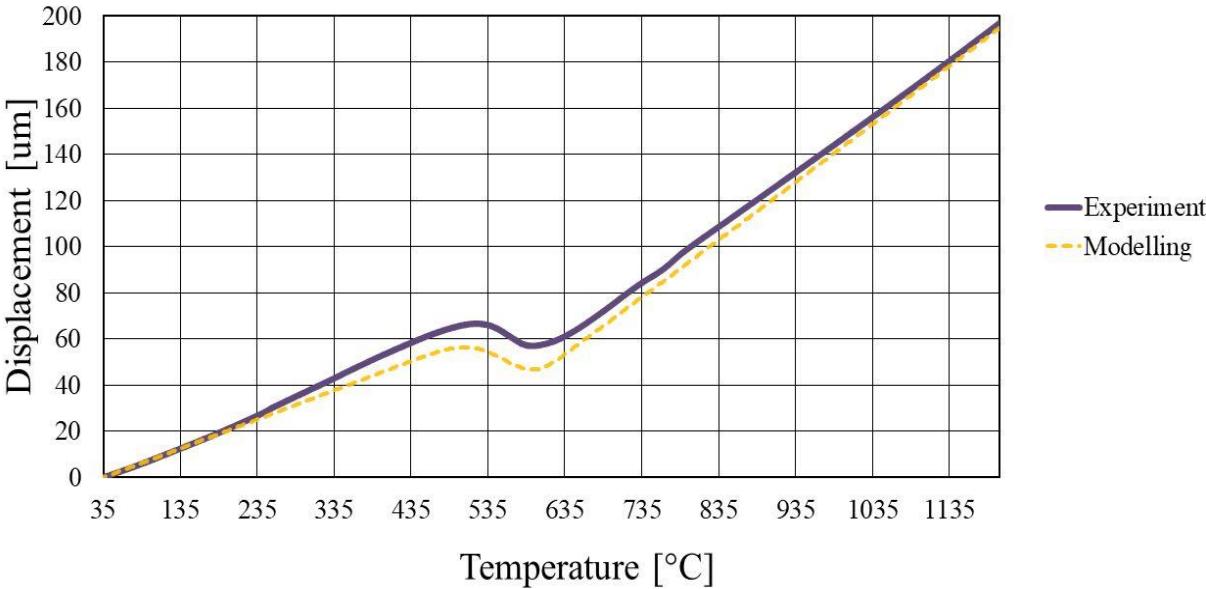
Figure 42 The cooling dilatometric curves with cooling rate of CR=0.5°C/s, predicted from numerical model (dotted orange line) and obtained from dilatometric test (solid violet line).

Two curves are presented, obtained respectively from the numerical simulation and the experiment, in Figure 42. The dilatometric curve, chosen for the test of the prediction ability of the model was the one obtained from the sample called 'Points', heated with very slow cooling rate to achieve equilibrium-like conditions and cooled down with the temperature change rate of 0.5°C/s. The details of the sample preparation are in the Experimental chapter. The presented results show relatively good approximation of the predicted curve in comparison to the experimental one. As it can be seen under the certain conditions like the significantly low

92

cooling rates, the phase transformation is providing relatively small level of the distortion inside the material. Due to that the residual stresses are on the very low level, not exceeding the yield stress. Although such slow cooling rates are not sufficient for providing the microstructure characterized by high material strength, the obtained results initially validate the model, which can be useful in future researches of residual stresses within the large-size forgings.

The impact of the different cooling rates on the predicted in the model dilatometric curves due to the changes in the phase transformation are presented in Figure 43.
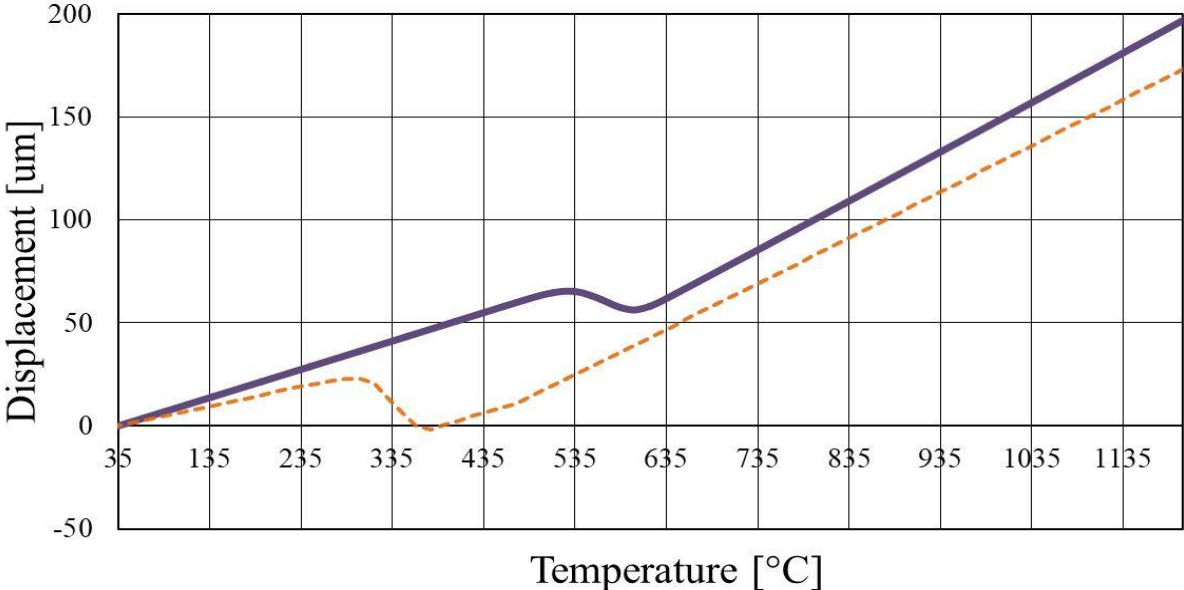
Figure 43 The impact of the various cooling rate on the phase transformation, registered in dilatometric test, where: purple solid line: CR=0.5°C/s, orange dotted line - 5°C/s differences are prediction of the developed model.

One of the dilatometric curve (violet solid line) was obtained from the numerical simulation calculated with the cooling rate CR=0.5°C/s. The second (dotted orange line) was also numerically calculated, same conditions applied, but with the cooling rate CR=5°C/s. This semi-empirical approach is based on the dilatometric curves obtained from dilatometric test. The cooling with the higher temperature change rate was performed using the approach of dividing the whole temperature range of the phase transformation into intervals, where temperature of each interval is described not as a range, but as a constant value instead described earlier (Figure 31).

It can be noticed that higher cooling rate delays the phase transformation start temperature, which for the dilatometric curve with CR=0.5°C/s was around 435°C, and for the other curve around 635°C. At the higher cooling rate, the differences in the local volumes (elements) due to phase transformation and the differences due to higher temperature gradients results in the larger value of the deformation. The performed calculations are a relatively good aproximation to the dilatometric experimental curves. The probable phases resulted from the cooling process with such cooling rates were analysed further in the work.
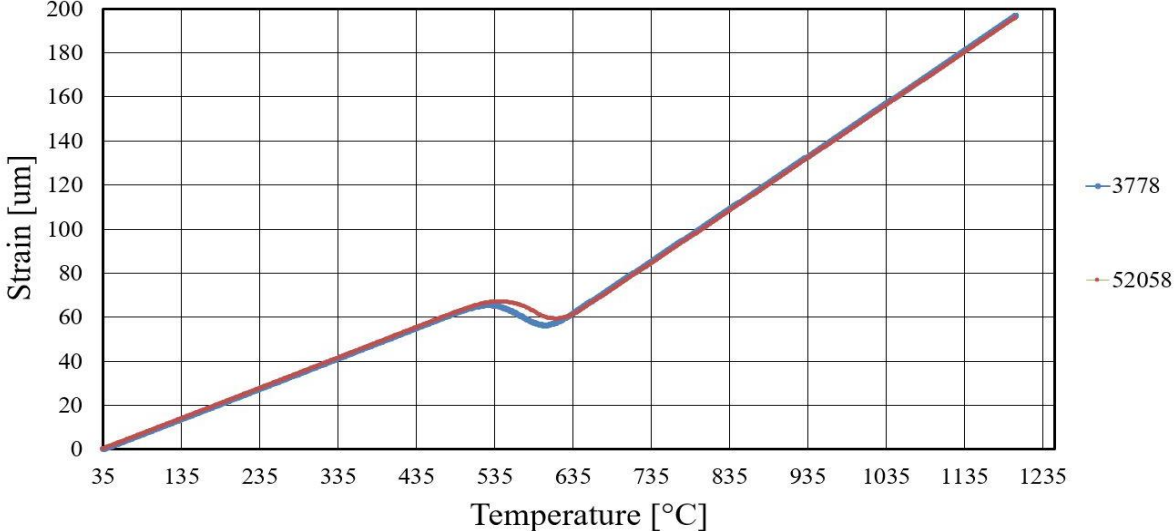
Figure 44 The differences in prediction of the dilatometric curves due to the different element number used in the model.
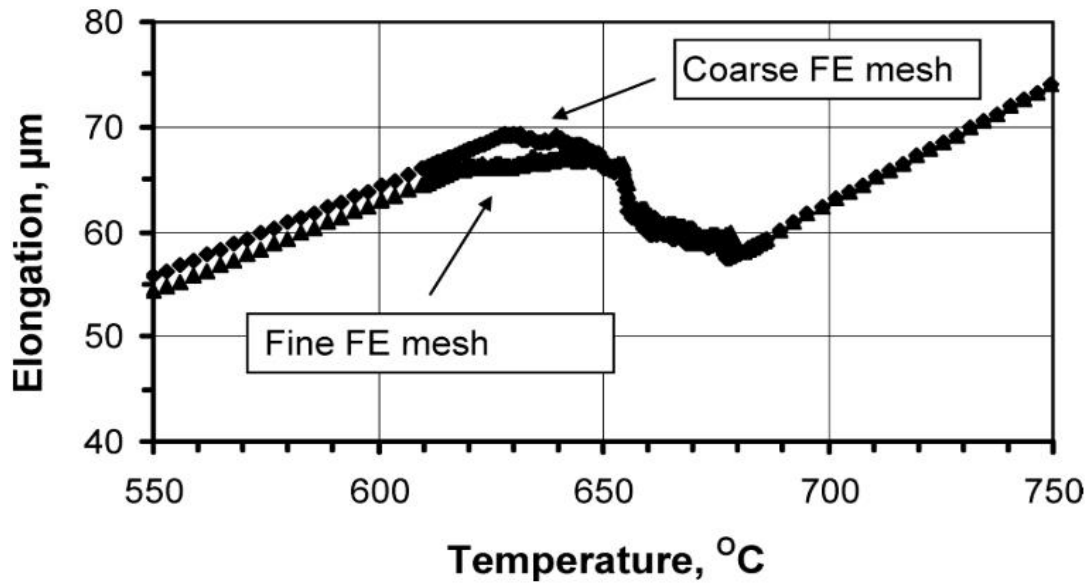
Figure 45 The influence of the finite element number in the mesh, which was put upon the model geometry on the dilatometric curves predicted for the cooling rate 163°C/s obtained from [138].

As can be seen in Figure 44 and Figure 45 the refinement of the finite element mesh, which was applied to the geometry model had an impact on the obtained results. The first figure presents the dilatometric curve predicted from the developed model for cooling rate of CR=0.5°C/s. The mesh was significantly refined from 3778 elements to 52058 elements, which caused the gentler strain response of the dilatometric curve. The difference is relatively small, on the level similar to the result presented on the second figure, obtained from the cooling with 163°C/s cooling rate from [138]. Although it was hard to establish the manner in which the curve changes due to the refinement of the mesh, it was clear that the mesh sensitivity analysis had to be done before the final model will be used for simulations of the heat treatment processes for the large size forgings.

The differences in the temperature distribution within the material during cooling with the various cooling rates are illustrated in Figure 47. For each of the seven dilatometric test simulations with various cooling rates the values of the temperature from the certain reference points were taken. The localizations of the points on the modelled geometry of the dilatometric sample are shown in Figure 46.
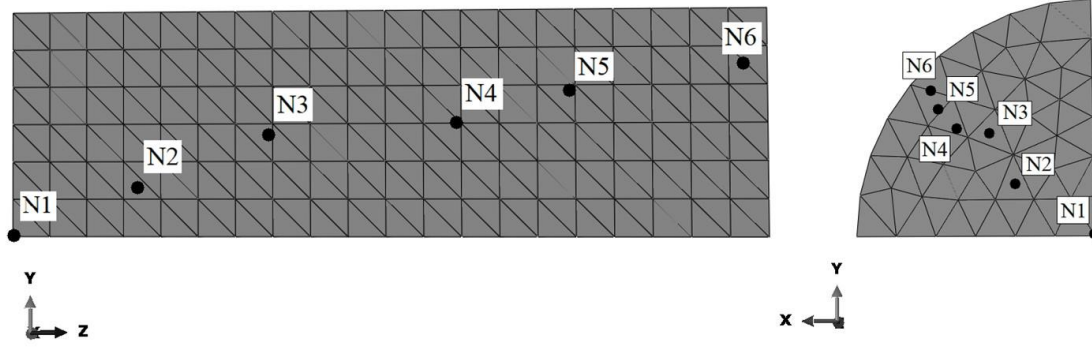
Figure 46 The locations of the reference points from which the results were obtained.

The values were taken from the beginning of each cooling process from the same point of the time. Because of the applied symmetry conditions presented sample in Figure 41 and Figure 46 has 6 mm of length and a diameter of 1.5 mm. The point N6 is placed just beneath the cooled surface of the dilatometric sample, and the point N1 is in the centre of a sample.
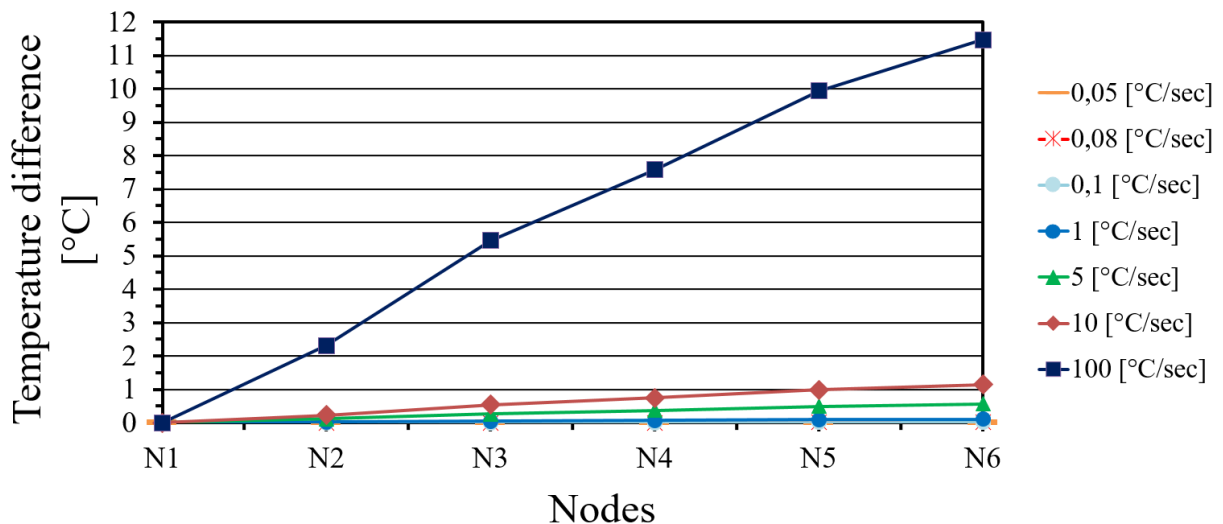
Figure 47 The difference in the temperature at the different depths within the sample cross section, in reference to the temperature on the outer surface predicted for the different cooling rates.

Figure 47 presents the temperature profile within the sample at the given time. The subsequent N# numbers present the temperature difference at the nodes between the N1 (inside the part) and N# (further in the surface direction) node. The differences were obtained for the various cooling rates. It can be seen in that the lowest temperature difference value is inside the material and the highest is just below the surface, although the main difference is caused due to the cooling rate. The difference grows as the nodes are closer to the surface of the sample. The

highest differences between the temperature in the depth of the part and on its surface can be seen at the highest cooling rate CR=100°C/s and their values are significantly greater (11.5°C) than temperature values measured in the same locations for other cooling rates (~0 – 1°C). Such small difference values for the lower cooling rates can be explained by the relatively small dimensions of the sample. Although it was used to show the noticeable difference in obtained values in small dimensions, such high cooling rate as 100°C/s is not used in industry practice as it introduces too high stress level between the parts within the element, what increase the risk of its failure. It also provides too high differences in the cooling rates between the depth and the surface of the component, what is not preferred, because it causes higher heterogeneity of the microstructure.
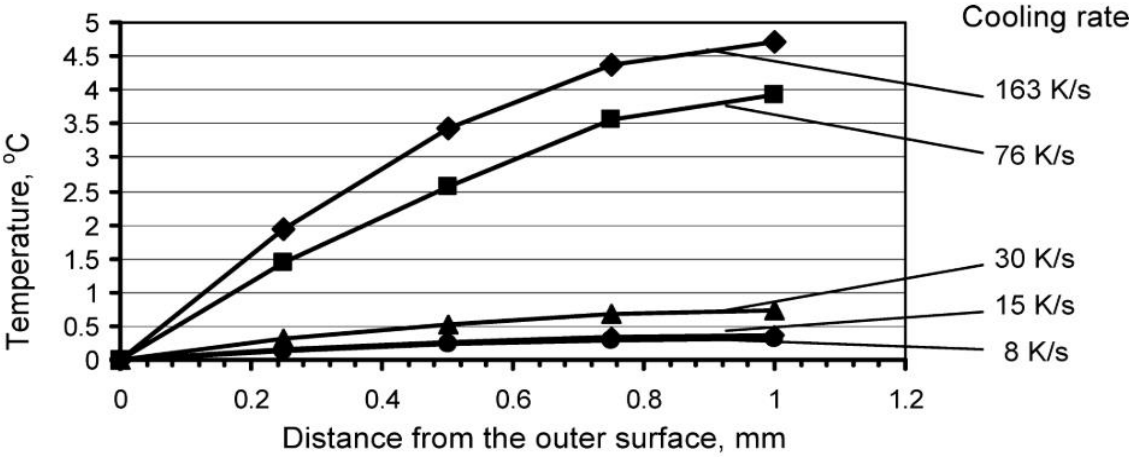
Figure 48 Temperature difference at the different depths within the sample cross section, relative to the temperature on the outer surface predicted for the different cooling rates obtained from [138].

The obtained results correspond relatively well with those from [138], presented in Figure 48. These results are presented in a little different manner, as the difference of the temperature is measured from the surface into the depth of the material. But also the highest temperature differences between the surface and the depth of the material were achieved with the relatively higher cooling rates, like 163°C/s or 76°C/s, as the heat transfer did not have much time to occur and distribute within the cross section of the sample. The results are not identical, because of the different materials used for investigations.

As mentioned before, the model was being designed as a multi-task tool that would be able to predict the possibility of appearing of the various microstructures within the cross

section of the element due to different conditions of the heat treatment process. Based on the local cooling rate and temperature value the model will estimate the percentage composition of phases in certain areas and calculate their local expansion or contraction. The approach taken assumes that the level of the residual stresses, which are the most significant during the designing part of the manufacturing, is as high as the differences in volume between the areas within the material. Indication of areas with approximately the same cooling rate and temperature would allow for relatively better residual stresses predictions.
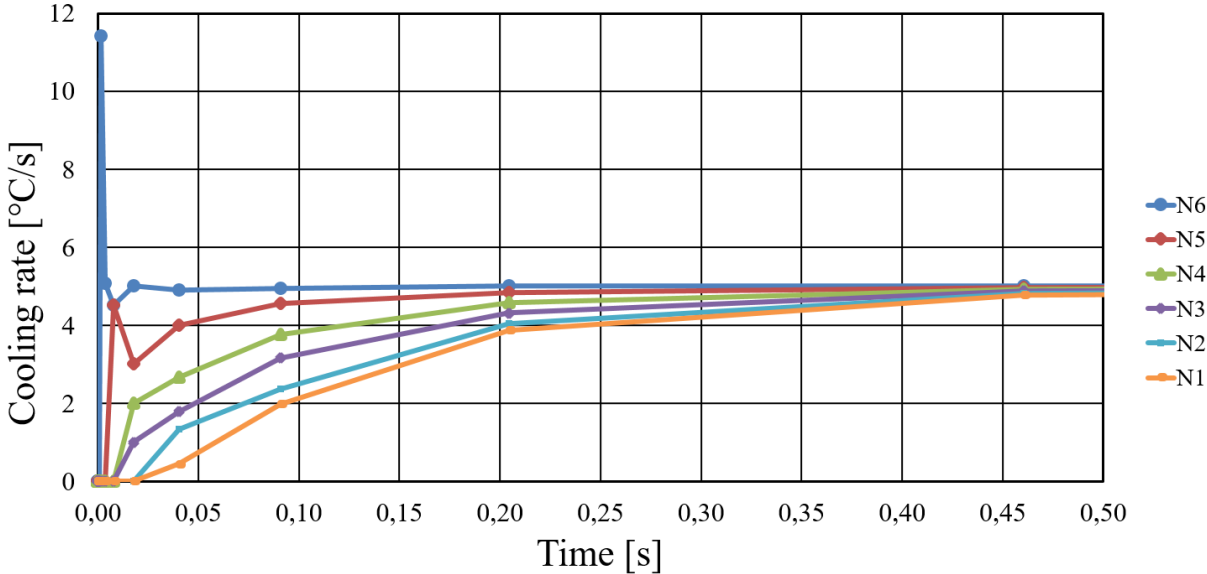
Figure 49 The local cooling rate values in the areas within the cross section of the sample cooled down with CR=5°C/s at the beginning of the process, the locations of the reference nodes are presented in Figure 46.

The local cooling rates at the reference points within the sample are presented in Figure 49. The location of the points is shown in Figure 46. Due to the relatively low cooling rate for the outer surfaces of the sample (CR=5°C/s) in comparison to its small dimensions the differences that can be observed occur at the very beginning of the cooling process, in a range of 1 second. At this time, near the surface (N6 node), the highest value of the cooling rate was registered. Similarly, the lowest value was registered at the same moment, but in the middle of the sample (N1 node). Together with the process development the local cooling rates located at the various levels of depth of the sample were aligning, aiming to finally achieve the cooling rate of the surface (CR=5°C/s). The differences in cooling rates values within the subregions of the same part can cause significant growth of the residual stresses and in the case of the irresponsible heat treatment of the large scale elements can lead to damage of the part or even its destruction.

To perform a complex analysis of the residual stresses that arise during the heat treatment of heavy and large forgings, within the range of 300t – 600t and a couple of meters length, the investigations of a simplified 3D thermo-mechanically coupled numerical model based on the FE method has been developed. It is capable of taking into account changes in the specific volume during both austenite-ferrite transformation and the local thermal contraction during cooling from austenite temperature region. The model is able to predict the local values of the cooling rate at the depth of the material during cooling. It is shown that the differences between temperature values measured at the same point in a material are greater for higher values of the cooling rates, which can cause the higher values of residual stress. It is also shown that the highest values of the local cooling rates appears at the beginning of the cooling process at the surface. The differences are noticeable for a very short time (up to 200ms), that is related to the small dimensions of the simulated dilatometric sample. The change in the cooling rate value causes delay in the transformation start temperature, which is related to the different transformation ratio between austenite and ferrite elements in time periods of the phase transformation. This means that for the different cooling rate there is a different amount of the transformed phase that corresponds with the volume fractions for the characteristic temperatures. The dilatometric curve presents relatively good approximation comparing with the experimental results, which validates the predictive abilities of the developed model.

3.4. Inverse method

It has to be emphasised again that the term 'phase transformation' covers an enormous number of the phenomena, where the kinetic and thermodynamic factors are quite individual for the process and the material. The mathematical equations describe many aspects like whether or not a process or reaction can occur, is there a change in free energy, what is the speed of the process or how and how many of the new phase atoms arrange in a crystal lattice. The necessary assumptions, which had to be taken, cover a lot of these questions, but at some point of the model development, the complexity of the phase transformation modelling required a certain calibration method of the parameters. Inverse analysis was chosen, which principles allows for the application of the reverse calculation technique to identification of phase transformation model parameters. The use of this method has been widely reported [128], [138], [145]–[149]. The method can be divided into two separate parts. The first one is a direct

problem, which is based on the use of a mathematical model of the dilatometric testing procedure in order to calculate some parameters that can be measured experimentally in the test. The second part is an inverse problem, where optimisation techniques are used for minimisation of the cost function formulated as a distance between vectors of the experimentally measured *e* and calculated *d* parameters (Figure 50).
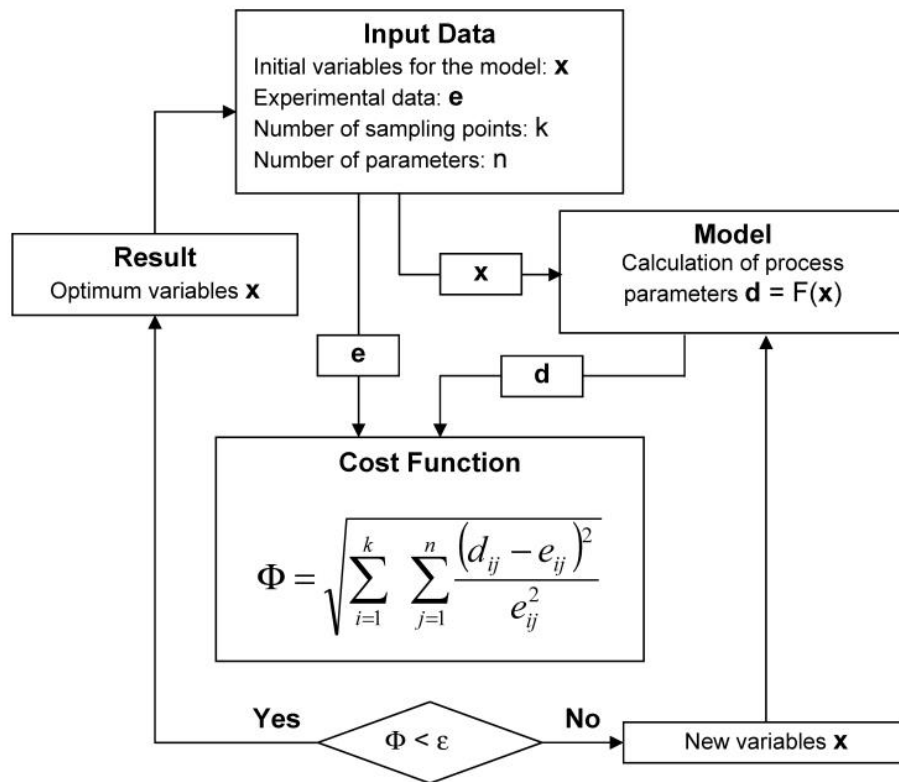
Figure 50 Inverse analysis procedure, used for identification of the phase transformation model parameters (for symbols see text) [138].

The inverse analysis can be described as a semi-empirical method that is used to certain calibration of parameters of the model to the conditions of the actual process and to the material factors. From the description of the algorithm presented elsewhere [147] (Figure 50) one can obtain that the inverse analysis method usually consists of the following three parts:

● Experimental tests, such as dilatometric test in the case of this project, from which the empirical parameters of the real process are obtained. Such data like dilatometric curves are used as the input for the optimisation process.

● Numerical modelling. The calculated theoretical parameters are used to obtain the numerical result from the finite-element model and the output is compared with the results measured in the experimental investigations in the first step of the inverse analysis.

● Optimisation. In this part, the cost function, formulated as a distance between vectors of the parameters measured in the experiment and the parameters obtained from the numerical modelling, is minimised through the one or a few optimization methods and the corresponding change in the control parameters is applied. Then the second step is repeated using the corrected parameters.

To solve the problem it is necessary to group all the above described parameters in vectors.

$$d = F(x,e) \hspace{4cm} (22)$$

The e vector consists of the parameters of the direct problem model, the d vector consists of the parameters that are calculated from the numerical model. Then, to calculate the material parameters, that are described as a vector x, the cost function is formulated, which is further minimized to the value less than ε through the one or few optimisation techniques. The main advantage of the inverse analysis is its flexibility and possibility to apply it to the any process and any material. In this example the cost function Φ is presented as a difference between the increase of the length that occur during the cooling of the sample, measured in a dilatometric test and calculated in the numerical model.

In the work [128] inverse analysis was used to achieve some volume fractions of various phases, when the cost function was formulated as the matrix of experimental and calculated results including the start and stop temperatures of the phase transformation for constant cooling rates. As the material several eutectoid steels were used, but the experimental data used as input for the cost function were not measured directly in the test. In this project, the cost function Φ is formulated as a distance between sample elongations measured directly during cooling in the dilatometric test and predicted using the finite element model:

$$\Phi = \sqrt{\sum_{i=1}^{k} \sum_{j=1}^{n} \frac{\left(d_{ij}-e_{ij}\right)^2}{e_{ij}^2}} \hspace{3cm} (23)$$

where: d_{ij} and e_{ij} are predicted and measured sample elongations of the dilatometric test specimen during cooling through the austenite–ferrite transformation temperature range; k is the number of sampling points and n number of parameters [138]. The elongation of the sample is predicted on the basis of the phase transformation model described above, implemented into the thermo-mechanically finite element model by the Fortran subroutine code. The results are presented in the next sections.

3.5. Numerical model development

Several numerical models of element cooling were developed through the project, rooted in a similar approach, but using various configurations of boundary conditions and testing different stages of advancement of the transformation model. The main aim of this part of the work is to present the main configurations of the boundary conditions, causing various impacts on the results and to present these results. The models differ in such parts like geometry, time and step of the process, type of the boundary conditions regulating the temperature at the surface of the element, the mesh, the way of fixation geometry in numerical space or the Fortran subroutine code, which controls the phase transformation. The details are presented below.

The author divided the part of the numerical investigations due to the level of development of the models. The initial models (models 1 – 4) are relatively simple, as they are dedicated for testing particular fragments of the problem, for example adjusting the boundary conditions, choosing the solving method of thermal equations or reducing the impact of the fixation of the geometry in numerical space. The dilatometric models (models 5 – 7) are focused on using the dilatometric test results as a reference. The dilatometric tests were described before in the text. In turn, the obtained models here were used as a component in the last group of models, called the comprehensive models (models 9 and 10). The Inverse models (models number 8) are dilatometric models, in which the inverse method was applied for identification of the main factors controlling the phase transformation.

All presented models show the main approaches of numerical modelling of the cooling process with account for volume change due to the solid-solid transformation and thermal shrinkage and allow for better understanding the stages of development towards the final model, which was used for calculations in the real industrial process, presented in the Validation part

of the work. It is important to mention that the units for each of the models are presented in a form connected with the dimensions used in the particular model. The model constructed in millimetres [mm], present the mass in tonnes [tonne] and the model constructed in metres [m], present the mass in kilograms [kg], as such approach is derived from FE packages like ABAQUS.

3.5.1. Initial models: Model 1, table fixation

The model presented here is based on the theory described in detail in chapter 3.2 of this work. In this case the fixation of the model geometry, which was a cube $10\times10\times10$ mm, was performed by fastening it to the bigger and inert, table-like element, not included in the calculations.
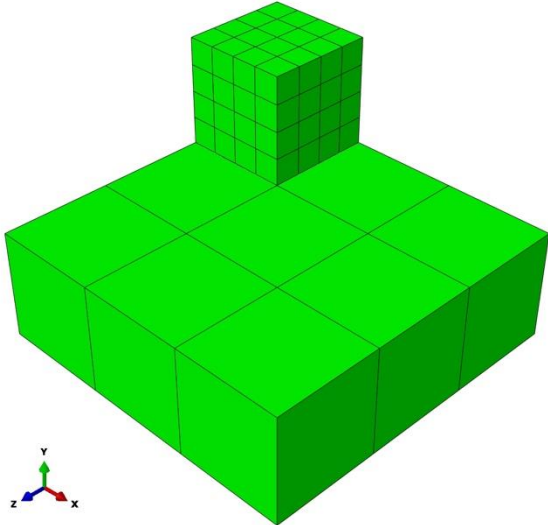
Figure 51 The geometry of the model fixed to
the indifferent ground.

Figure 51 presents the geometry of the model. The material properties used are presented in Table 12. The impact of the solid-solid transformation was not included, and the thermal expansion coefficient was set as an embedded value of 14.4×10^{-6} K^{-1} (Table 12a). It can be seen that, like the thermal expansion coefficient, all of the parameters do not change

either due to temperature or the time. The initial temperature of the geometry was set to 900°C uniformly distributed (Table 13). The ambient temperature was set to 20°C through the type of interaction option called surface film condition, of which details are given in Table 14. The model simulates the water cooling as the film coefficient was set to 0.5 W/m^{2}K. To achieve 20°C at the core of the part at the end of the process, the time was set to 200s (Table 15), but as it can be seen in Figure 52 around 75% of that time the temperature was dropping slowly from around 60°C to the final temperature due to the lower thermal force, proportional to the difference between the temperature of the part and the ambient.

Table 12 The material properties used for the simplified models.

Material properties							
Conductivity [W/mK]	Density [t/mm^3] (Uniform Distribution)	Elastic		Expansion [K^{-1}] (isotropic)	Plastic		Specific heat [mJ/tK] (Constant volume)
		Young's modulus [MPa] (Isotropic)	Poisson's ratio		Yield stress [GPa]	Plastic strain	
58	7.9×10^{-9}	105459	0.3	1.44e×10^{-6} [a) Subr. Uexpan[b)	85.1	0	4.9×10^{-8}
					435.1	0.274	

Table 13 The parameters of the initial temperature assigned to the element at the beginning of the calculations:

Predefined field					
Type	Step	Region	Distribution	Section variation	Magnitude [°C]
Temperature	Initial	All surfaces	Direct specification	Constant through region	900

Table 14 The parameters of cooling interaction applied to the model during numerical calculations:

Interaction	
Type	Surface film condition
Step	Cooling (coupled temperature – displacement)
Region	Outer surfaces
Definition	Embedded coefficient
Film coefficient [W/m^{2}K]	0.5
Film coefficient amplitude	Instantaneous
Sink definition	Uniform
Sink temperature [°C]	20
Sink amplitude	Instantaneous

Table 15 The parameters used to control time step during the numerical calculations of the first model:

Step	Time period [s]	Response	Max allowable temperature change [°C]	Increment size		
				Initial	Min	Max
Cooling	200	Transient	10	1×10^{-3}	3×10^{-5}	1

Table 16 presents the details of the mesh of the finite elements, which was created within the geometry of the model. The model was really basic with 64 elements and 125 nodes. Such rough mesh gives respectively generalised results, but definitely cuts the calculation time, which was a desirable factor at this stage of model development.

Table 16 The details of the mesh applied upon the part in the models:

Element type						
Element library	Geometric order	Family	Analysis type	Element type	Total number of nodes	Total number of elements
Standard	Linear	Coupled Temperature-Displacement	3D stress	C3D8T	125	64
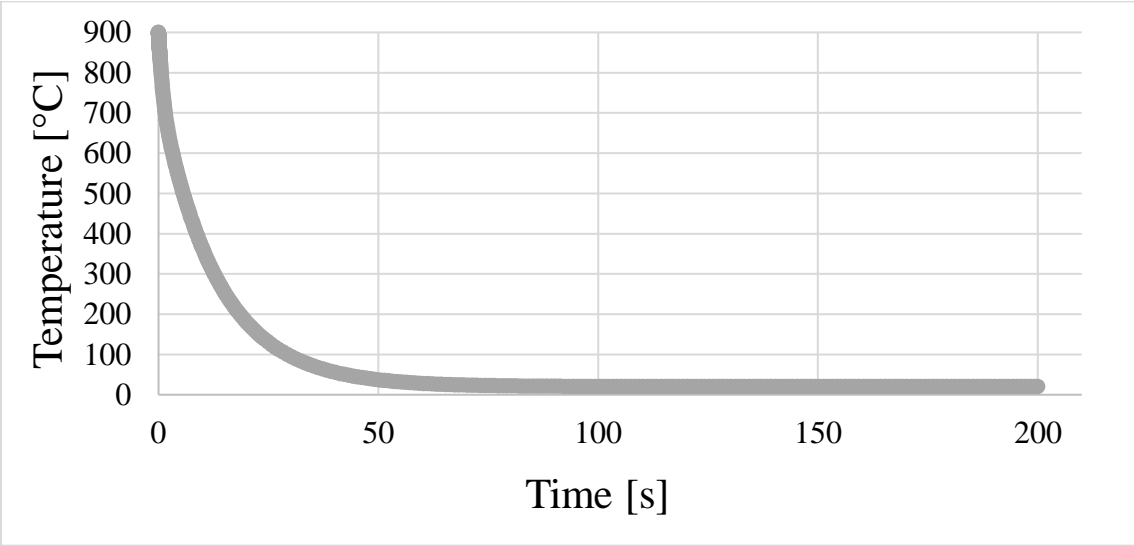
Figure 52 The calculated temperature in time of the process, recorded in the representative node placed on the furthest corner of the cube in (1,1,1) direction in the first model.
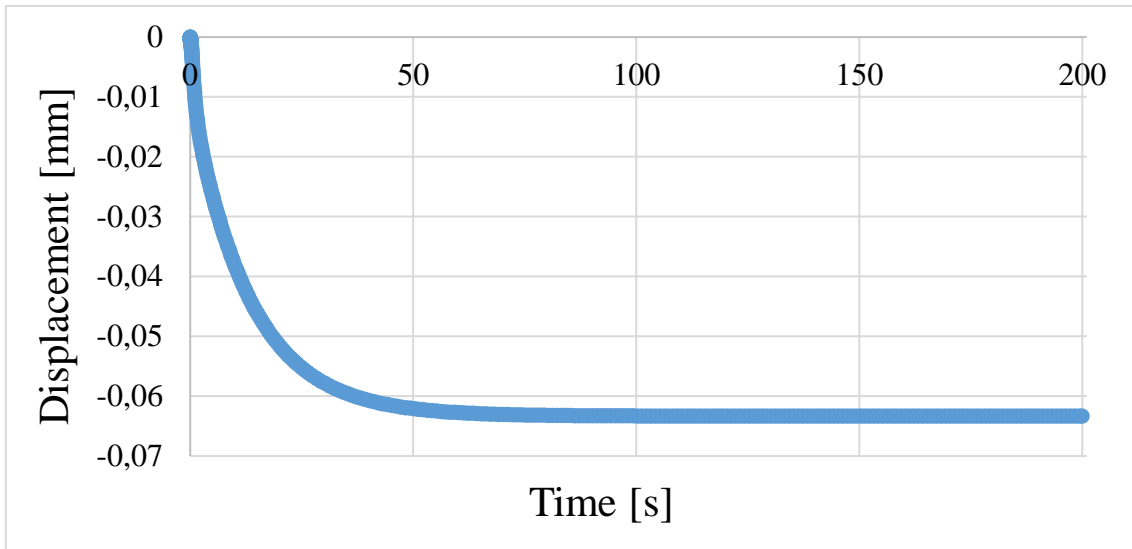
Figure 53 The calculated displacement in time of the process, recorded in the representative node placed on the furthest corner of the cube in (1,1,1) direction in the first model.
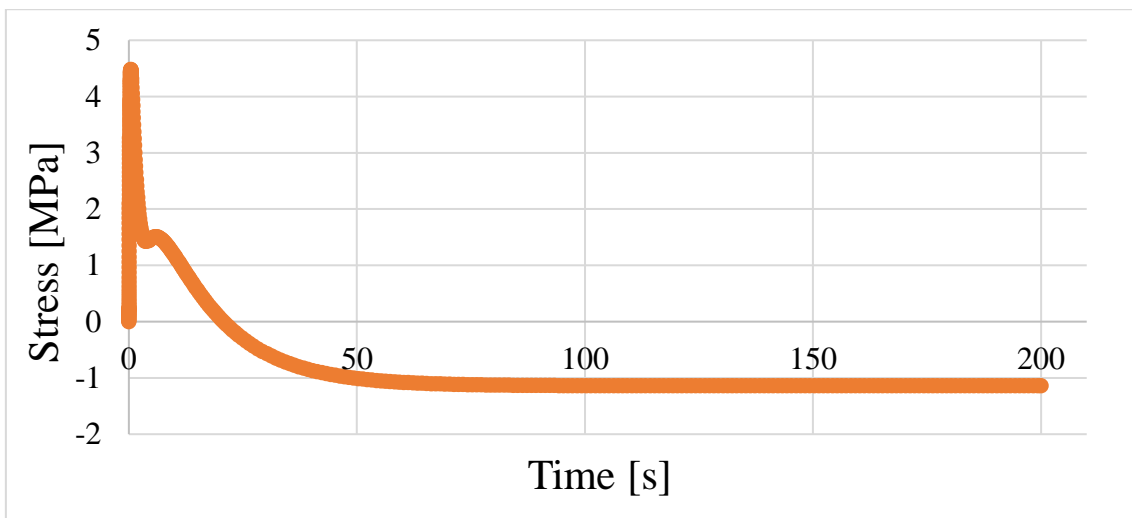
Figure 54 The calculated stress in time of the process, recorded in the representative node placed on the furthest corner of the cube in (1,1,1) direction in the first model.

Figure 52, Figure 54 and Figure 53 present the temperature, the displacement and the stress at the representative node through the time of the cooling process. The location of the reference node is the same for all of the models in this work with cube-like geometry and is described in Figure 34 as the corner node of the cube at the end of the diagonal, which begins at the point 0,0,0. As noted before, due to applying the surface film condition interaction, the ending took the most time of the cooling process. It can be seen as the flattening of the curves

in all of the three figures, recorded from 50s to the end. The displacement goes in the negative direction (below zero) in Figure 53, because it is modelled as a shrinkage. The shape of the curves is similar to each other, the beginning is very rapid cooling (Figure 52), the displacement is proportional to the temperature, but due to absence of the solid-solid transformations included, there is lack of characteristic dilatometric peaks. The strongest irregularities of the recorded stress can be seen at the very beginning of the process, where the temperature gradients were the highest. Although the values of the calculated stress were surprisingly low, probably due to not implementing any of the mechanism of structure transformation and due to the lack of temperature dependence of the material parameters. Also, while the model presented reasonable results of the transient temperature field, the recorded stress, especially at the bottom of the model in the region of contact with the table seemed to be too high, relatively to the rest of the model.

3.5.2. Initial models: Model 2, symmetry condition

The main characteristic change in the next model is boundary condition of symmetry (Table 17). There is not any surface like table in the previous model, the cube 5x5x5mm is fixed by symmetry. This approach was described in detail earlier and presented in Figure *32* and Figure *33*. The model was used before for calculation of transient temperature field using MSC Software Marc Mentat (Figure *35*). It was transferred to Simulia Abaqus with the changes presented below, necessary for the further development.

Table 17 The boundary conditions of symmetry in the second models:

Boundary conditions			
Type	Symmetry	Symmetry	Symmetry
Step	Initial	Initial	Initial
Region	YZ plane	XZ plane	XY plane
Description	X symmetry (U1=UR2=UR3=0)	Y symmetry (U2=UR1=UR2=0)	Z symmetry (U3=UR1=UR2=0)

The material properties presented in Table *18* are updated in relevance to the previous model; the conductivity and specific heat are temperature dependent. The Young modulus is set to 205 GPa (Table *18*a), the density of the material is corrected to 7.83e-9 t/mm^3, the plastic properties were incorporated as the tensile stress strain curve between the yield point and the UTS, rather than assuming linear hardening between the two. The predefined temperature field and interaction parameters remained the same (Table 13 and Table 14).

As it was seen in the previous model most of the calculation time was spared for the cooling at the end of the process, which was not influential for the final results of the residual stress. In this approach the model was calculated again with a shorter time (Table 19a and b) and with finer mesh. The element type also remained the same, although there is a different number of nodes and elements in the model, (27 nodes in 8 elements in the first model and 216 nodes and 125 elements in the second model).

The expansion was calculated using simple Fortran subroutine code UEXPAN, which calculates at the given element the possibility of transformation of the austenite element into ferrite element by changing its thermal expansion coefficient. All of the codes used during the research are given in Appendix A at the end of this work. The subroutines used in the second model have the randomization part, described earlier. The temperature-related expansion coefficients given in the subroutine in the model, which was cooled down till the end (20°C) was estimated and multiplied to emphasise the dilatometric effect, as the main purpose here was not to achieve the actual shrinkage values, but to establish the manner how the elements should behave during the proposed transformation model.

Table 18 The material properties used for the simplified models with temperature dependence:

Material properties												
Conductivity [W/mK]	41	40	37	32	30	25	23	34	95			
Temperature [°C]	0	200	400	600	690	730	820	1450	1500			
Density [t/mm^3] (Uniform Distribution)	7.83×10^{-9}											
Elastic												
Young's modulus [GPa] (Isotropic)	205 [a] 181.135 [b]											
Poisson's ratio	0,3											
Plastic												
Yield stress [MPa]	205	344.47	415	486	557	627						
Plastic strain	0	0.0018	0.00654	0.0183	0.0509	0.131						
Expansion [mW/mm^2] (isotropic)	Subroutine UEXPAN [a] 13.269×10^{-6} [b]											
Specific heat [mJ/tK] (Constant volume)	450×10^{-6}	600×10^{-6}	600×10^{-6}	700×10^{-6}	760×10^{-6}	800×10^{-6}	920×10^{-6}	1700×10^{-6}	1000×10^{-6}	620×10^{-6}	650×10^{-6}	800×10^{-6}
Temperature [°C]	200	400	500	600	650	720	750	760	790	800	810	1500

Table 19 The parameters used to control time step during the numerical calculations of the second models:

Step	Time period [s]	Response	Max allowable temperature change [°C]	Increment size		
				Initial	Min	Max
Cooling	176[a] 40[b]	Transient	10	1×10^{-7}	1×10^{-11}	1
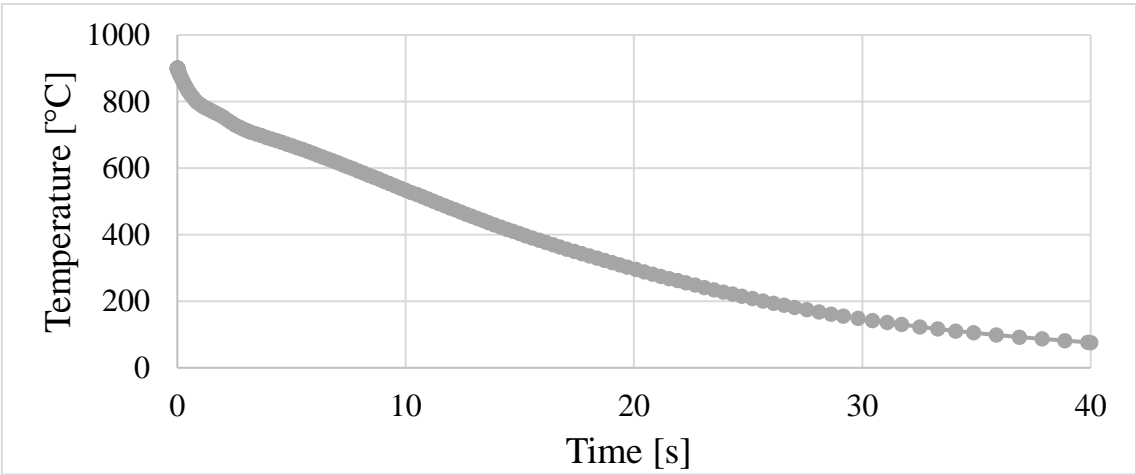
Figure 55 The calculated temperature in time of the process, recorded in the second model.
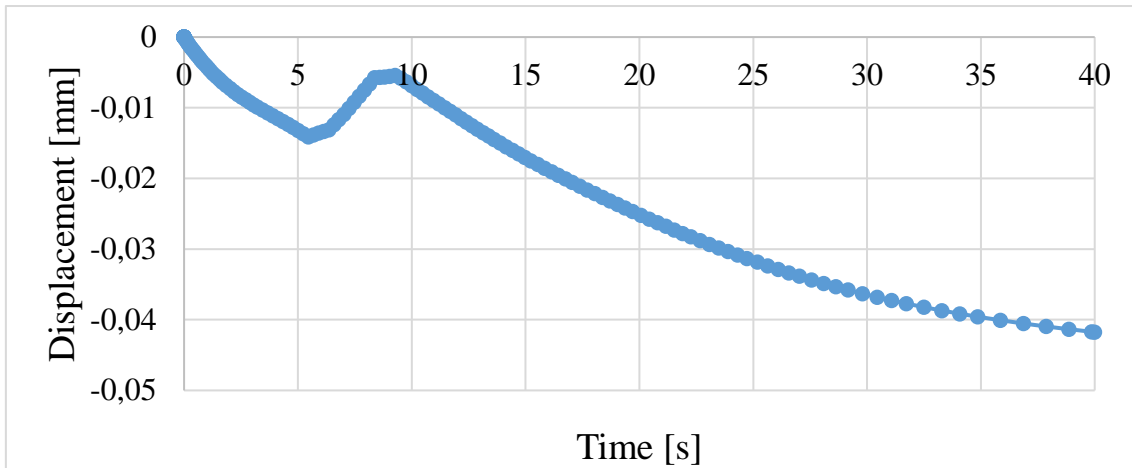
Figure 56 The calculated displacement in time of the process, recorded in the second model.
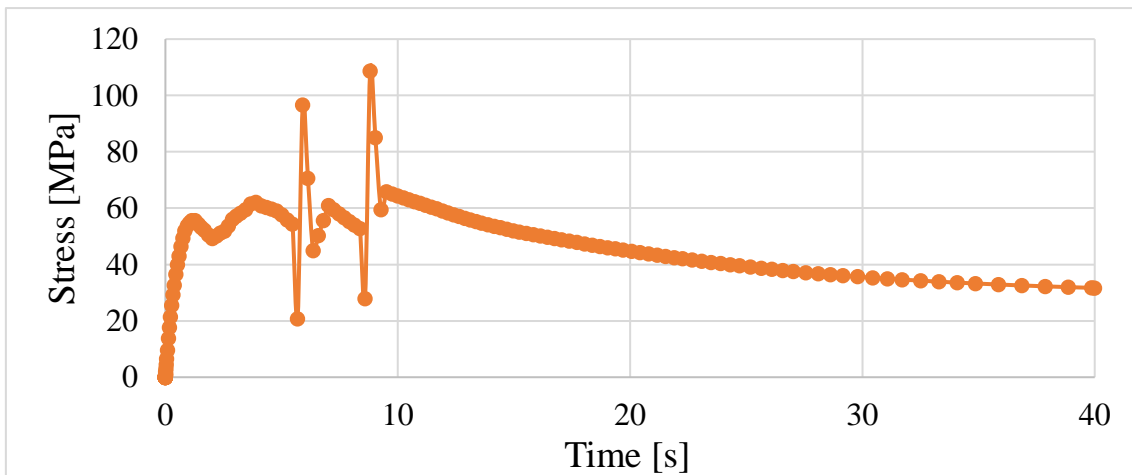
Figure 57 The calculated stress in time of the process, recorded in the second model.

Figure 55, Figure 56 and Figure 57 present the calculations from the model, respectively temperature, displacement and stress at the same location as before. These results are obtained from the model, where the calculation time was reduced from 176s to 40s. It can be seen that the temperature descends with an even rate but starts to slow down around 30s cooling due to the thermal energy balance described earlier. The transformation start temperature was calculated from equation 14 around 700°C and it can be seen the characteristic dilatometric effect on the displacement curve presented in Figure 56, what covers with the stress value in Figure 57. Stress value significantly increases at the beginning of the process due to the highest temperature gradients between the surface of the geometry and its core. The various thermal

expansion coefficient at the elements inside the model due to the transient temperature field and transformation causes the fluctuations of the stress until the end of the transformation.
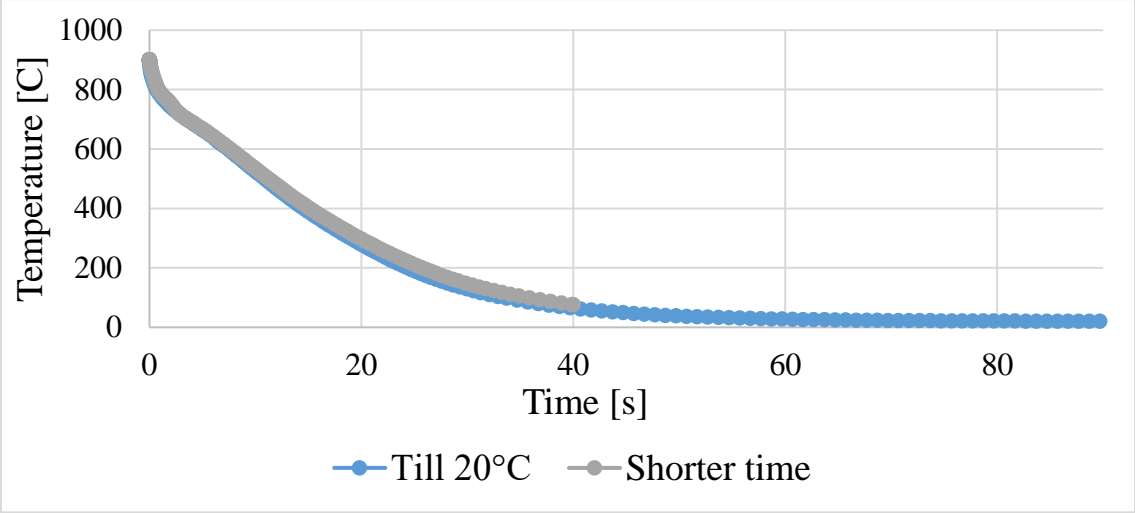
Figure 58 The temperature calculated in the second model till the 20°C and terminated after 40s.
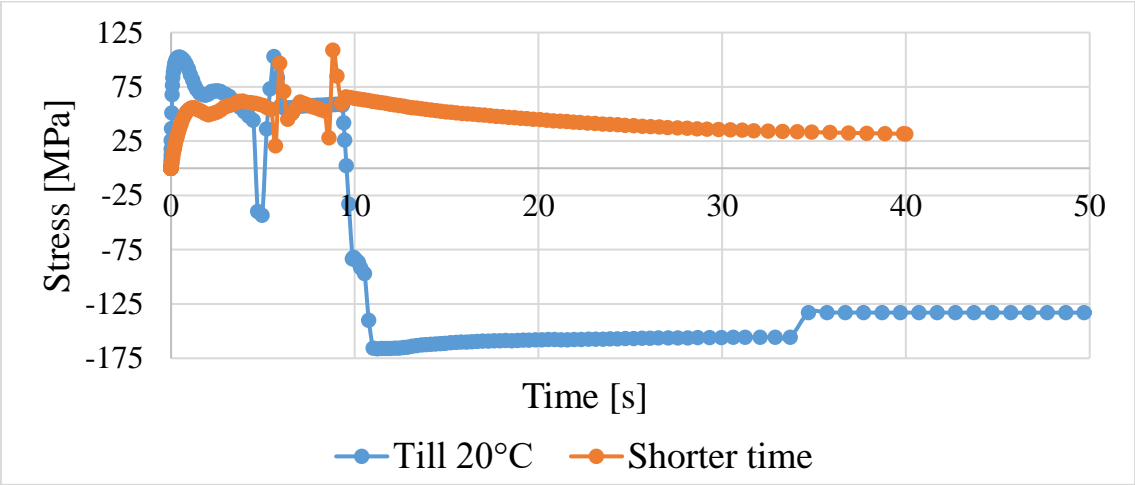
Figure 59 The stress calculated in the second model till the 20°C and terminated after 40s.

The effects of faster termination of the calculations and the influence of the finer mesh are presented in Figure 58 and Figure 59, respectively in temperature and stress values at the representative node. It can be seen here that the finer mesh had minor impact on the cooling process and the temperature is nearly the same in both cases. Although the fluctuations on the curves of the stress look different from each other, the actual trace is similar, because of the fact that the thermal expansion coefficients in the full time cooling model were multiplied and the obtained peaks are exaggerated. The main conclusions from this model are that there is a

113

possibility of shaping the transformation in the model by the change of the thermal expansion coefficient of the particular parts of the geometry.

3.5.3. Initial models: Model 3, symmetry and pinning conditions

The third model, similar to the first one, was used for testing different ways of fixing the geometry in numerical space and its impact on the temperature and stress distribution. The material properties were simplified (Table 12), but the transformation was implemented through a simple subroutine, based on the change of the thermal expansion coefficient of the element due to the temperature. The predefined temperature field and the interaction module remained the same (Table 13 and Table 14). The finite element mesh was finer with total number of nodes 1331 and total number of elements 1000, but with unchanged details (Table 16). The time of the cooling process was set to 120s (Table *20*). There were three different approaches of fixing the geometry applied, giving the different results.

Table 20 The parameters used to control time step during the numerical calculations of the third models:

Step	Time period [s]	Response	Max allowable temperature change [°C]	Increment size		
				Initial	Min	Max
Cooling	120	Transient	10	1×10^{-2}	3×10^{-3}	1

a) Fixing points 1 – without symmetry, the interaction condition was applied on all of the geometry surfaces, which were fixed in the numerical space through the set of the nodes with restricted motion. The details are given in Table 21.

Table 21 The first way of fixing boundary conditions set up in the third model:

Boundary conditions			
Type	Displacement/Rotation	Displacement/Rotation	Displacement/Rotation
Step	Initial	Initial	Initial
Region	Point (1,0,1)	Point (0,0,1)	Point (0,1,0)
Description	U1=0	U2=0	U3=0

b) Symmetry – the interaction condition was applied on the three outer surfaces of the geometry, simulating the contact with cooling water, the details are given in Table 17.

c) Fixing points 2 –the same as in a), but the different set of nodes was chosen. The details are given in Table 22.

Table 22 The second way of fixing boundary conditions set up in the third model:

Boundary conditions		
Type	Symmetry/Antisymmetry/Encastre	Displacement/Rotation
Step	Initial	Initial
Region	Point (0,0,0)	Point (1,1,1)
Description	Pinned (U1=U2=U3=0)	U1=0; U2=0; U3=0; UR1=0; UR2=0; UR3=0
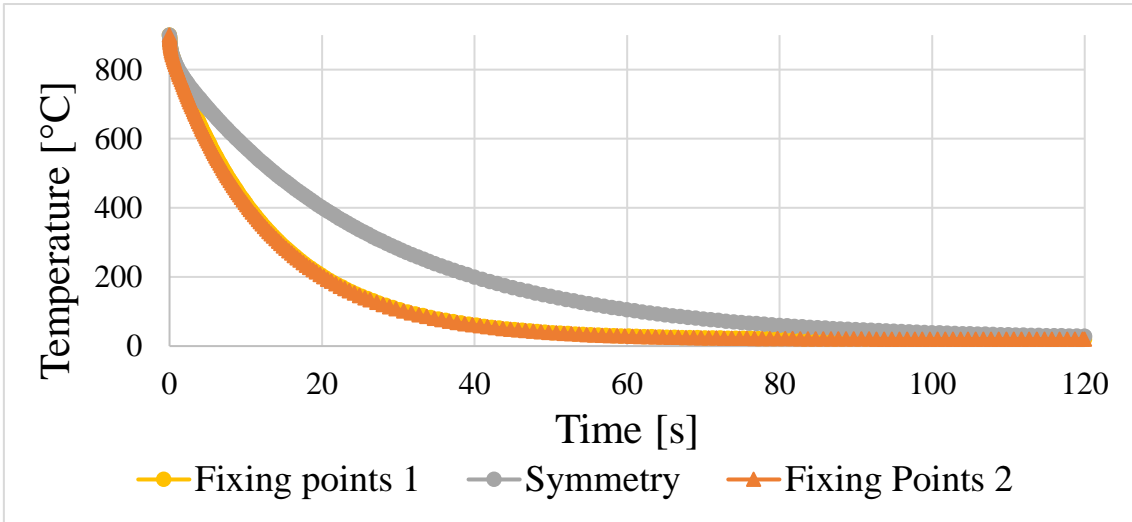
Figure 60 The temperature calculated in the third model using various ways of fixing the geometry in the numerical space.
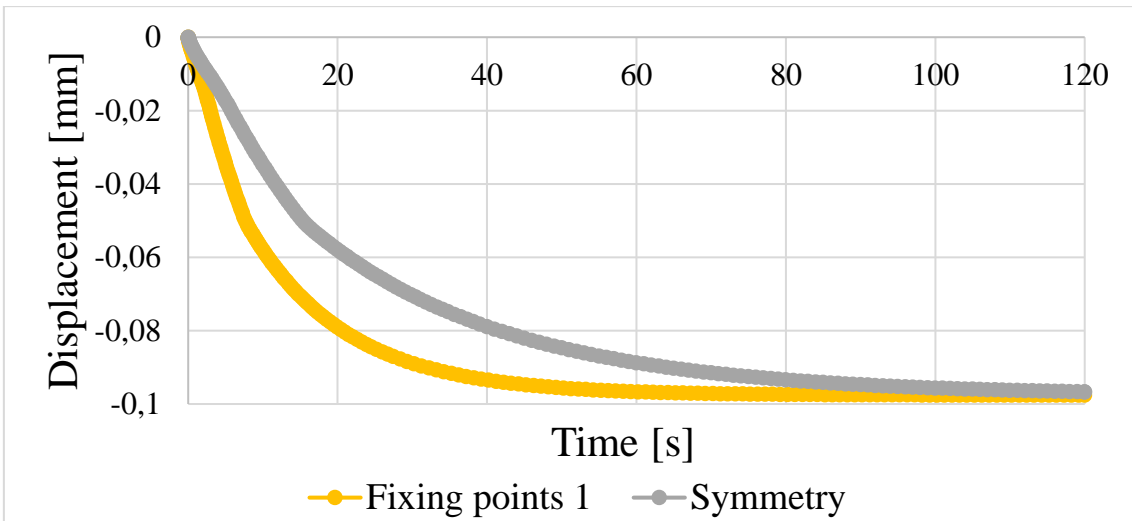
Figure 61 The displacement calculated in the third using various ways of fixing the geometry in the numerical space.
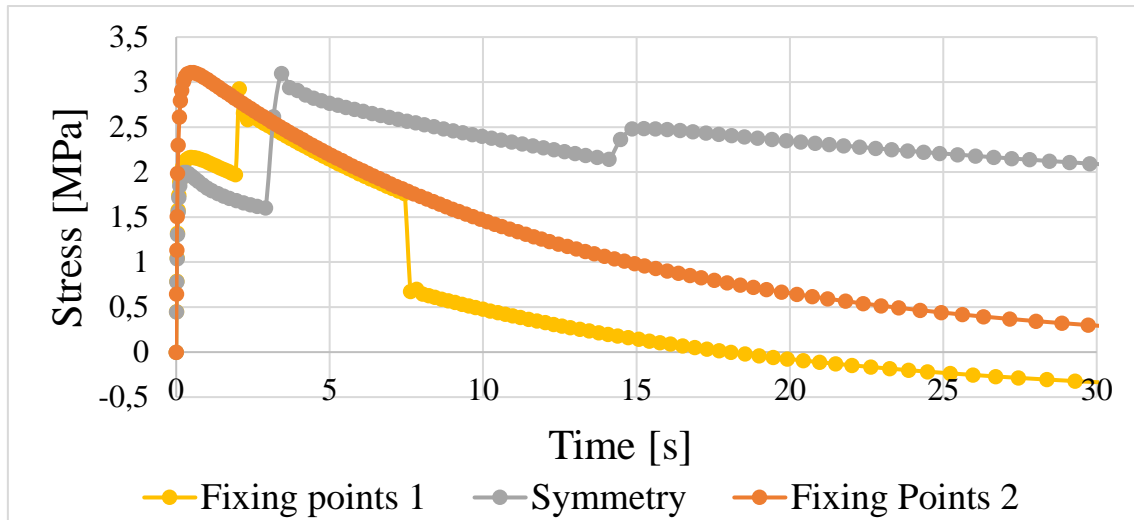
Figure 62 The stress calculated in the third model using various ways of fixing the geometry in the numerical space.

Figure 60, Figure 61 and Figure 62 present respectively temperature, displacement and stress results obtained at the representative node in third model. It can be seen that the cooling is the same for models, which were fixed in the numerical space through the set of nodes with restricted motion. The difference probably comes from the fact that symmetry boundary conditions turn the geometry into a part of the bigger, hidden object and change the volume, which is cooled, what should take a larger portion of time. As the thermal expansion coefficient is proportional to the temperature, the displacement is also related to the temperature in the case of Fixing points 1. However, the displacement results of Fixing points 2 are not included in Figure 61, because this set did not prevent the geometry from moving in the space, what caused disruption. The implemented simplified subroutine, which controlled the transformation of the microstructure from austenite to ferrite did not have much impact on the displacement in such cases, although it can be seen that there are some peaks of the stress values around the start temperature transformation (~750°C) at the very beginning of the process. Due to the obtained results, the symmetry boundary conditions were chosen for the further development of the model.

117

3.5.4. Initial models: Model 4, axisymmetry and pinning

Symmetry condition can provide satisfying results without introducing unnecessary stress due to pinning the geometry in the numerical space. The large dimensions of the forgings, which is of course the focus of this work, requires a further reduction of the calculation time. This model tests the axisymmetry approach, where the geometry is reduced to only two dimensions, representing the cross section of the cylindrical pipe (Figure 63). The pinning of the model is applied as node located in the left upper corner of the geometry with details given in Table 23.
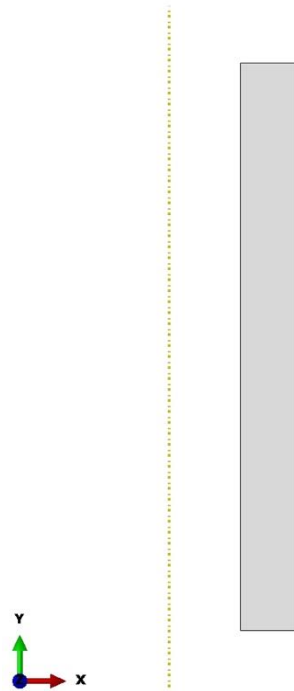
Figure 63 The two dimensional geometry of the cylindrical pipe in the fourth model.

Material properties used in this model are simplified (Table 12), the initial temperature field was set to 900°C (Table 13) and the cooling interaction was applied to all of the outer surfaces (Table 14). The time of the cooling process was set to 100s (Table 24). The model uses the very simplified subroutine to change the thermal expansion coefficient around 600°C to give an impression of the full transformation of the microstructure from austenite to ferrite.

Table 23 The encastre boundary condition details, applied in the fourth, axisymmetric model:

Boundary condition	
Type	Symmetry/Antisymmetry/Encastre
Step	Initial
Region	Point; left up corner
Description	Encastre U1=U2=U3=UR1=UR2=UR3=0

Table 24 The parameters used to control time step during the numerical calculations of the fourth model:

Step	Time period [s]	Response	Max allowable temperature change [°C]	Increment size		
				Initial	Min	Max
Cooling	100	Transient	30	1×10^{-3}	1×10^{-5}	0.1

The Table 25 presents the details of the mesh of the finite elements, which was created within the geometry of the fourth model. The geometry was divided into 160 elements with 205 nodes. The linear quadrilateral elements of type CAX4T were used.

Table 25 The details of the mesh applied upon the geometry in the fourth axisymmetric model:

Element type						
Element library	Geometric order	Family	Analysis type	Element type	Total number of nodes	Total number of elements
Standard	Linear	Coupled Temperature-Displacement	3D stress	CAX4T	205	160
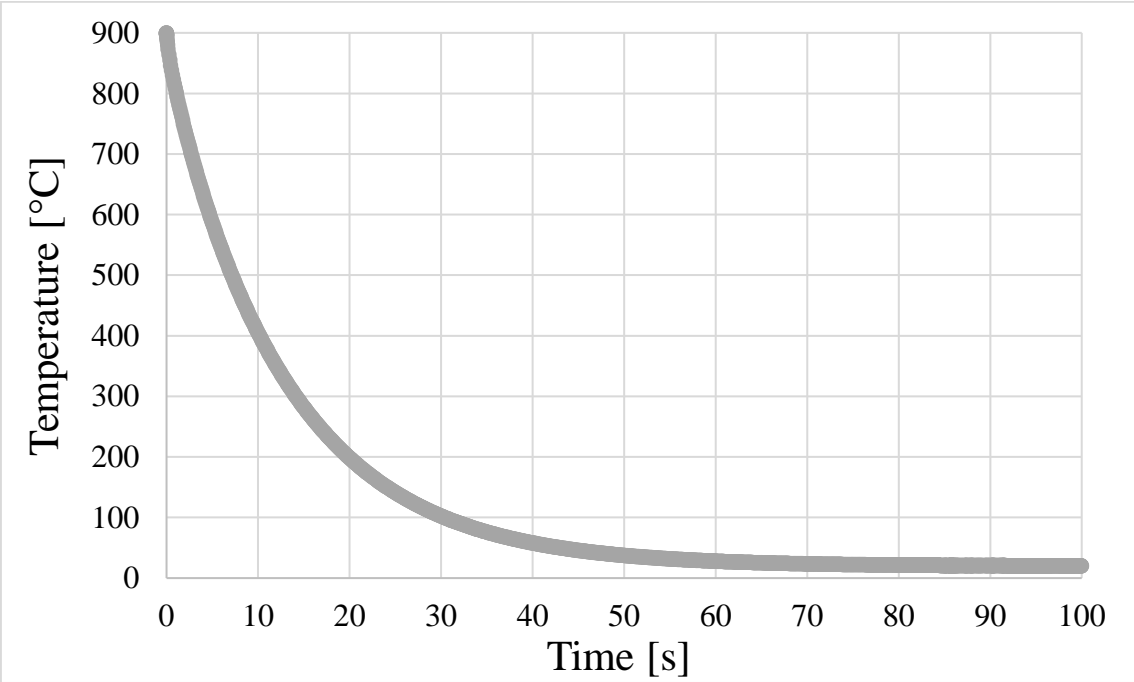
Figure 64 The calculated temperature in time of the process, obtained from the fourth, axisymmetric model.
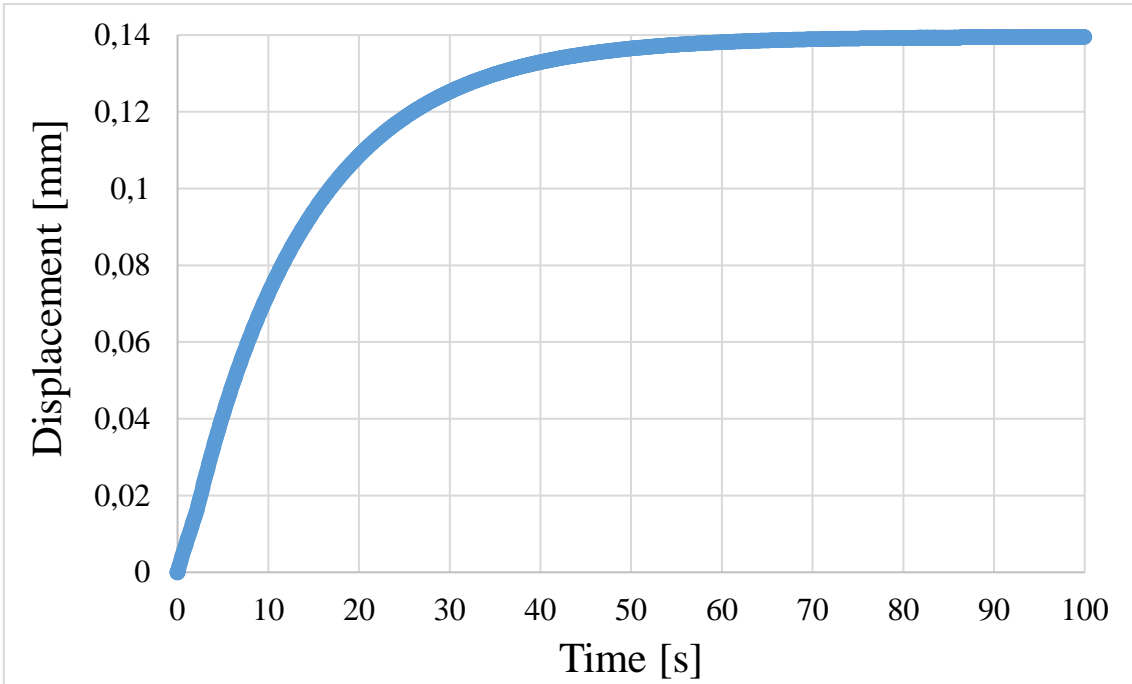
Figure 65 The calculated displacement in time of the process, obtained from the fourth, axisymmetric model.
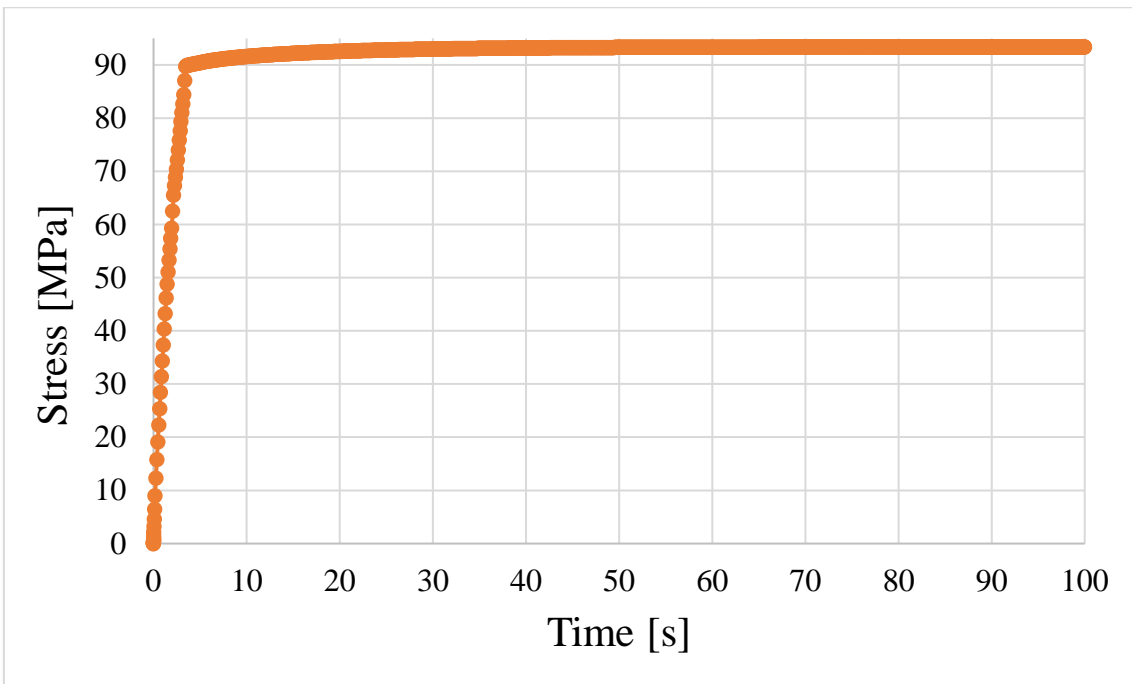
Figure 66 The calculated stress in time of the process obtained from the fourth, axisymmetric model.

Figure 64, Figure 65 and Figure 66 present respectively temperature, displacement and stress results obtained at the representative node in the fourth, axisymmetric model. The calculated temperature and the displacement are proportional, the displacement changes in the same manner as the temperature drops down. The very high stress values are connected with the thermal expansion coefficient given in the subroutine and multiplied to emphasize the effect of the change in microstructure. The break in the stress curve visible around 5s of the process is probably due to the change of the thermal expansion coefficient implemented through the subroutine around 600°C. The main result of this model was the relatively shorter time of calculation, which was around 5minutes, compared to the previous models, where calculation times were around 30min. The axisymmetric approach was used again in the next models of larger dimensions.

3.5.5. Dilatometric models: Model 5, dilatometric sample

The first dilatometric model is rooted in the third model with the geometry, which reflects the small cylindrical sample of diameter of 3mm and length of 10mm, typical for the dilatometric test. The material properties were temperature-dependent (Table *18*b) and the transformation was implemented through an UEXPAN subroutine (Appendix A), based on the change of the thermal expansion coefficient of the element due to the temperature. The predefined temperature field details remained the same (Table 13), except the value of the temperature, which was set to 1200°C. There was a lack of interaction module, which controlled the heat exchange between the ambient and the sample surface before. Instead, the cooling was implemented through the temperature boundary condition as the time-dependent temperature applied at the surface (Table 26) and the cooling rate was set to 0.08°C/s. Such an approach could be performed due to the fact that the temperature control during the dilatometric test on the small samples is sufficient to assume the linear temperature drop. The fixing of the model was performed by applying the symmetry conditions on the three surfaces in the manner described in Figure 41. The finite element mesh was constructed with total number of nodes 897 and total number of elements 3778, with type element of C3D4T and rest details described in Table 16. The time of the cooling process was set to 14562.5s (Table 27).

Table 26 The temperature boundary condition details, applied in the fifth, dilatometric model:

Boundary conditions	
Type	Temperature
Step	Cooling (coupled temperature-displacement)
Region	Outer surfaces
Description	Uniform
Magnitude	1
Amplitude	Applied

Table 27 The parameters used to control time step during the numerical calculations of the fifth model:

Step	Time period [s]	Response	Max allowable temperature change [°C]	Increment size		
				Initial	Min	Max
Cooling	14562.5	Transient	10	1×10^{-7}	1×10^{-11}	10
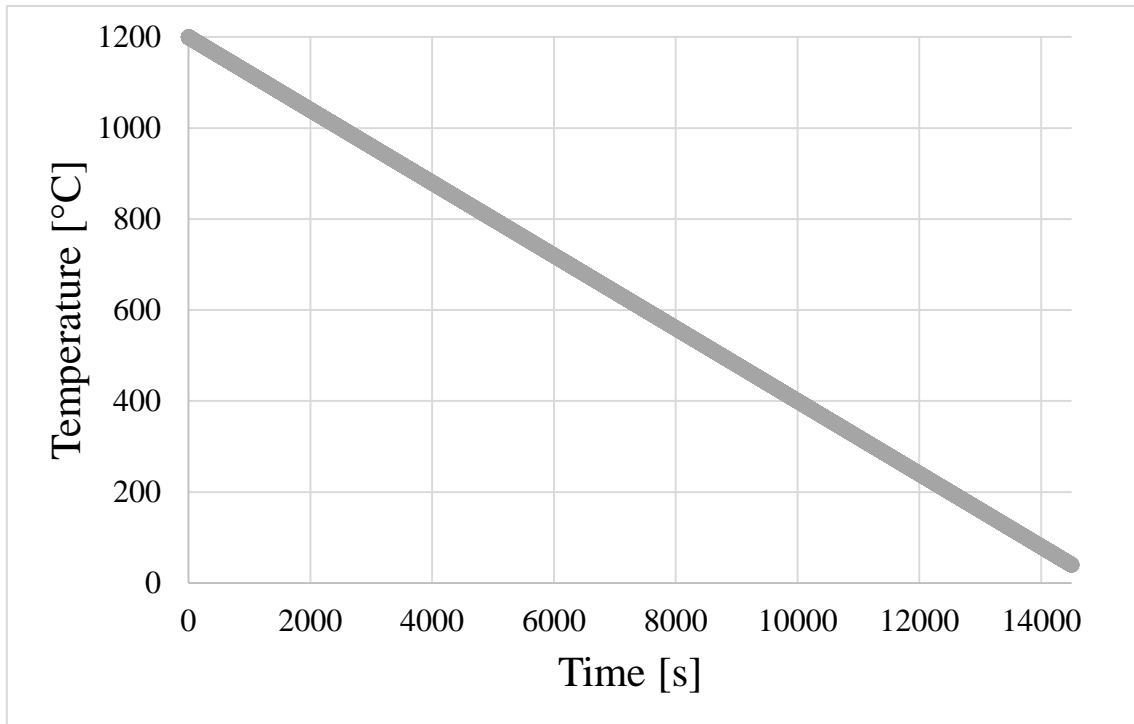
Figure 67 The calculated temperature in time of the process, obtained from the fifth, dilatometric model.
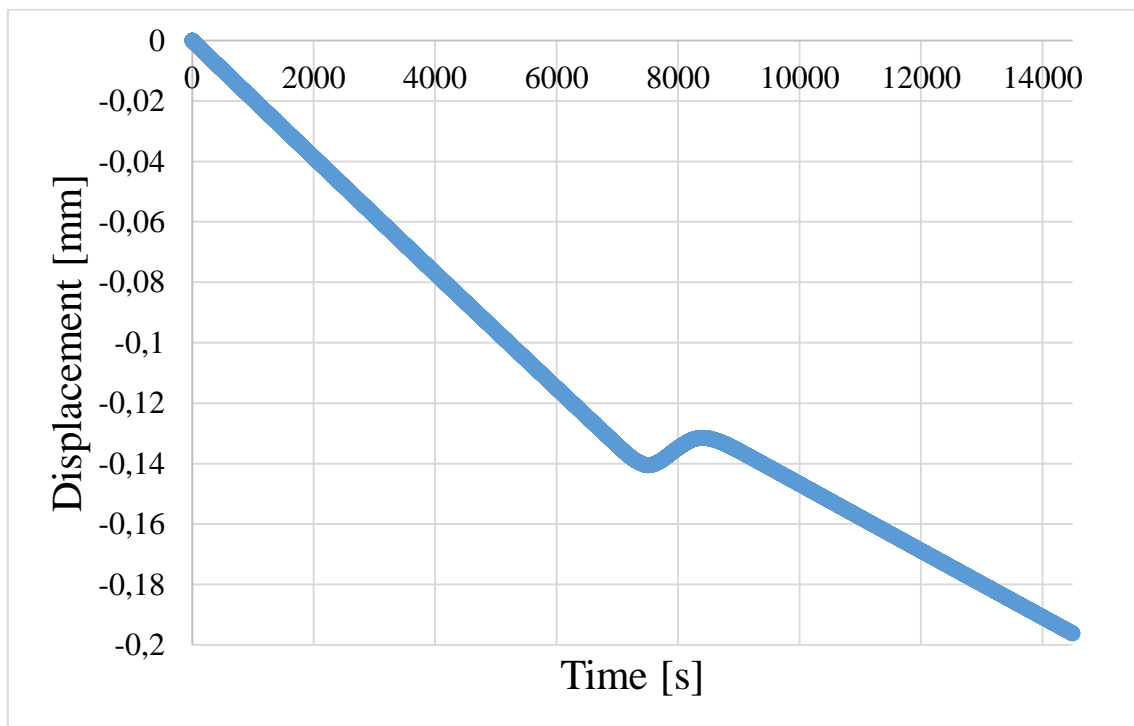
Figure 68 The calculated displacement in time of the process, obtained from the fifth dilatometric model.
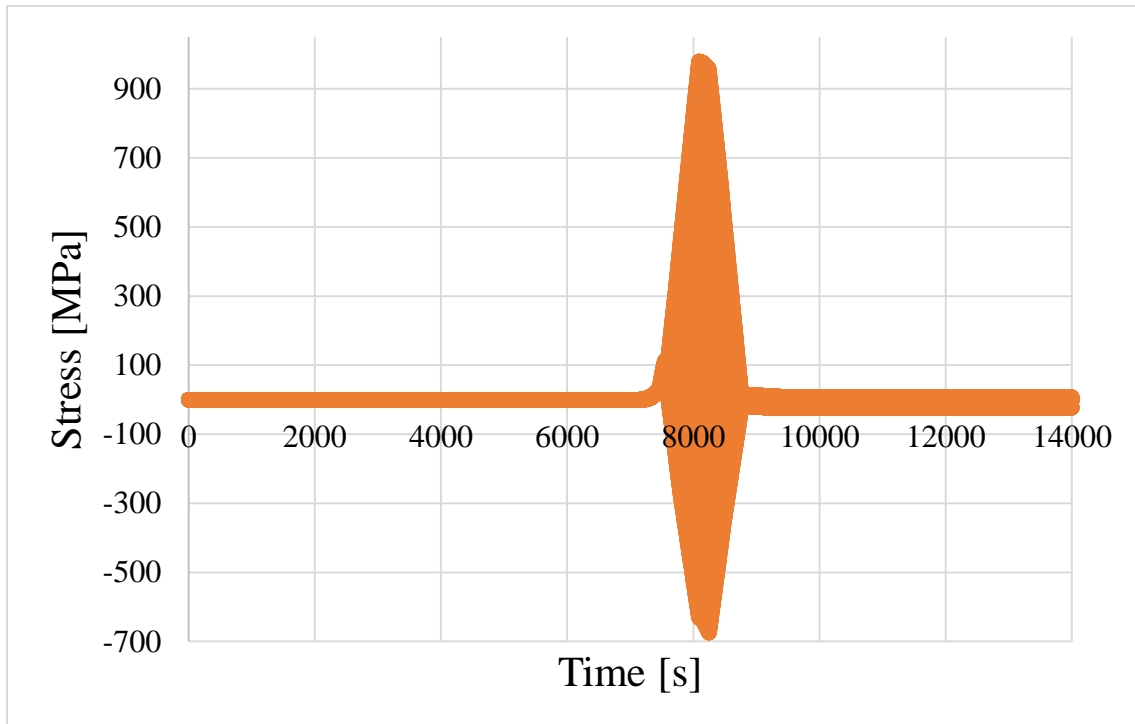
Figure 69 The calculated stress in time of the process, obtained from the fifth dilatometric model.

Figure 67, Figure 68 and Figure 69 present respectively temperature, displacement and stress results obtained at the representative node in the fifth, dilatometric model. The temperature drop can be seen as linear due to the small dimension of the sample and the relatively good control of the temperature during the dilatometric test. The displacement is related to the temperature, but a characteristic dilatometric peak can be seen due to the presence of the microstructure transformation. The transformation parameters were calibrated in such a way that the curve reflects actual displacement of the dilatometric cooled down with the cooling rate of 0.08°C/s. The implemented transformation is simulated as before, as a change in the thermal expansion coefficient during the gradual change of the microstructure from austenite to ferrite, which impacts on the displacement of the different parts of the geometry during the cooling and reflects as a peak on the stress curve in Figure 69. The obtained stress peak has an informative character, the developed approach was used in the models described further.

3.5.6. Dilatometric models: Model 6, seven heating/cooling rates

The second dilatometric model is a numerical projection of the dilatometric experiment, described earlier in this work. This model is crucial for the rest of the work. The aim was to create the base sets of parameters, which could control the model in such way it would reflect the material displacement during heating and cooling with a given temperature change rate in the same manner as in the performed dilatometric test. In the results the six heating and cooling processes were calculated giving the different outcome like temperature field, displacement of nodes and stress between the different parts of the material in the relation to time and microstructure transformation.

The geometry remained the same from the previous dilatometric model (diameter of 3mm and length of 10mm). The material properties were temperature-dependent (Table *18*b). The first calculations transformation process was implemented through an UEXPAN subroutine (Appendix A), based on the change of the thermal expansion coefficient of the element due to the temperature, which was a development of the previous subroutines and is presented in two forms, with or without the presence of Depvar objects, specifying solution-dependent state variables. The results from the second approach based on the dilatometric test are described in detail below in the text. The predefined temperature field details remained the same (Table 13), but the temperature value was set to 890°C (1200°C in case of the first model called 'Points'). Similar to the previous model the cooling was performed through the temperature boundary condition instead of interaction module (Table 26). The Amplitude module allowed for strict dependence of the temperature and time, which resulted in the precise control of the cooling rate at the surface of the sample during the process. There were fourteen simulations performed, heating and cooling separately for each one of the seven samples, respectively: a) HR=0.08°C/s; CR=0.5°C/s b) HR=4.98°C/s; CR=0.05°C/s c) HR=4.74°C/s; CR=0.1°C/s d) HR=4.99°C/s; CR=1°C/s e) HR=5.00°C/s ;CR=5°C/s f) HR=5.01°C/s; CR=10°C/s g) HR=5.01°C/s; CR=100°C/s, where HR - heating rate, CR - cooling rate. The fixing of the model was performed by applying the symmetry conditions as before (Figure 41). The finite element mesh was mostly constructed with a total number of nodes of 6758 and a total number of elements of 4270, with the element type of C3D10MT, with the rest of the details described in Table 16 (expect for models with cooling rates 0.05°C/s and 100°C/s, where were 990 nodes and element

type of C3D4T). The time periods of the cooling process were each time different to achieve the various cooling rates and are presented in Table *28*.

Table 28 The parameters used to control time step during the numerical calculations of the sixth model:

Step	Time period [s]	Response	Max allowable temperature change [°C]	Increment size		
				Initial	Min	Max
Cooling	2383.23[1) 14463.8[2) 8699.53[3) 862.43[4) 177.66[5) 94.25[6) 16.889[7) 16.97[8)	Transient	10	1×10^{-7}	1×10^{-11}	10

The great impact on the displacement of the nodes had thermal expansion and contraction, which were implemented into the model through the change of the thermal expansion coefficients. The sets of the coefficients related to the given temperature and heating/cooling rate were calculated from the curves obtained from the dilatometric experiments. From every experimental dilatometric curve of each heating/cooling rate, for every ten degrees Celsius temperature change the thermal expansion coefficient was calculated and extracted to the vector, what gave fourteen vectors (seven different heating and cooling rates). When the model was set to constant heating/cooling rate, the corresponding vector of thermal expansion coefficients was implemented through the subroutine UEXPAN into the model, where every time step the temperature at the node was calculated and due to its value

127

the correct thermal expansion coefficient was assigned to the particular node from the vector (subroutine in appendix A).
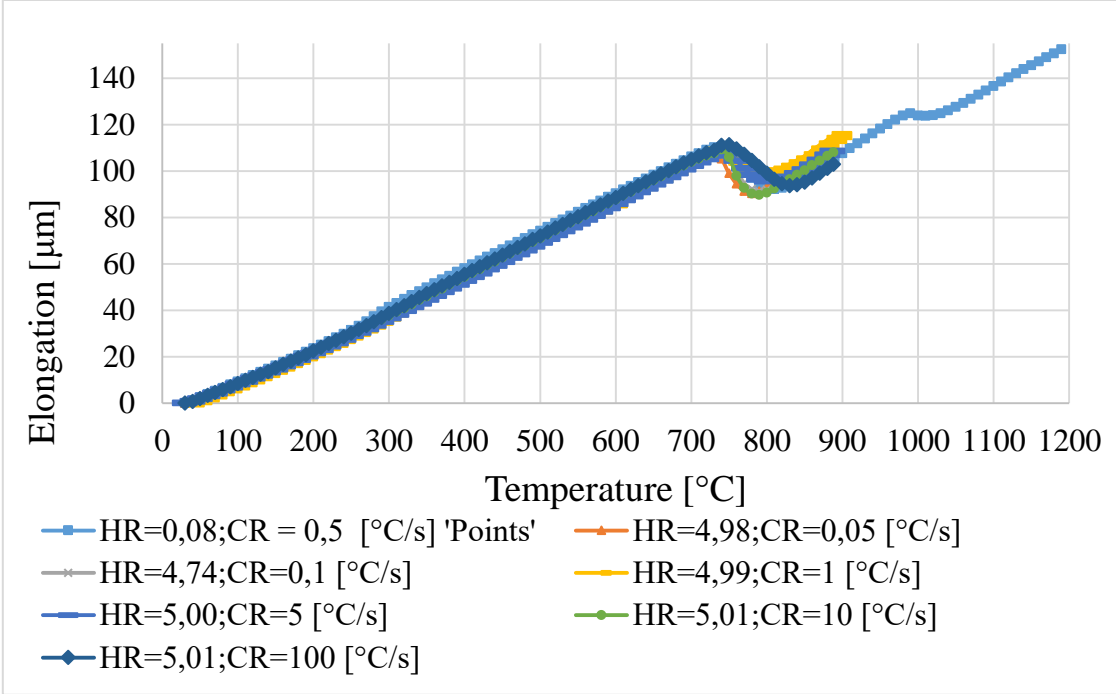
Figure 70 The heating curves for all samples taken together at the collective chart, where HR – heating rate, CR – cooling rate.
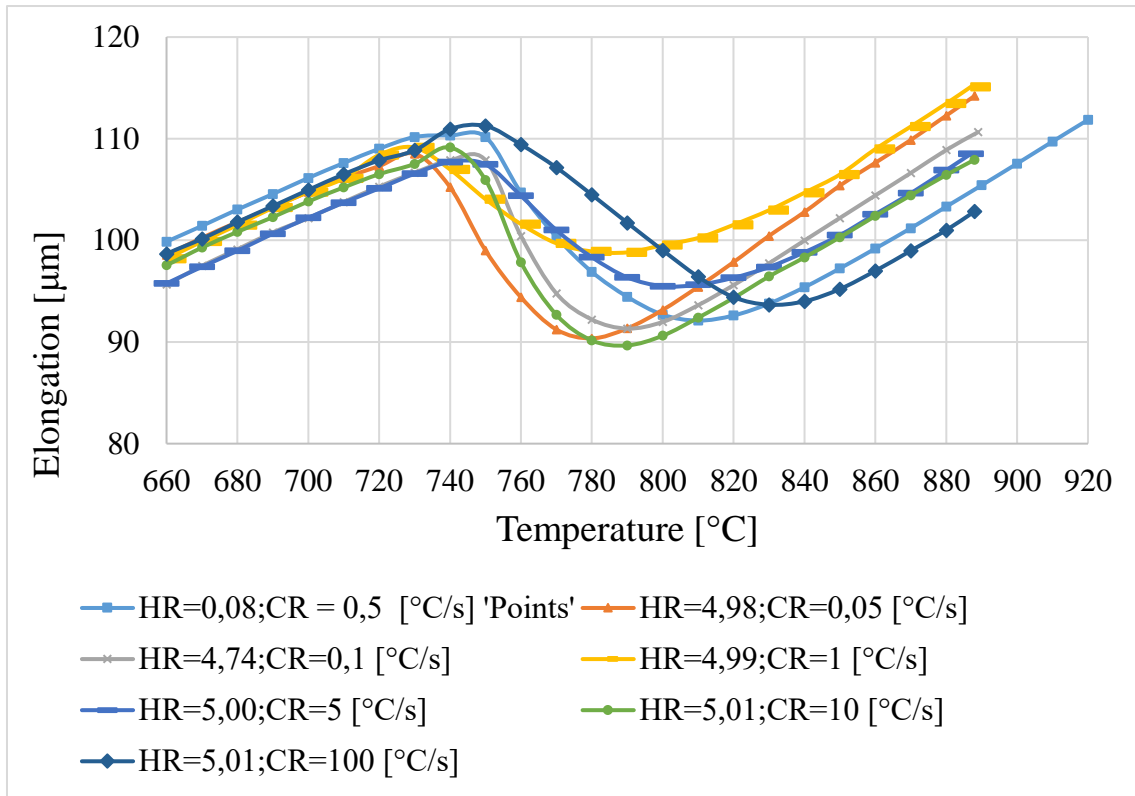
Figure 71 The microstructure transformation on the heating curves for all samples taken together at the collective chart, where HR – heating rate, CR – cooling rate.

Figure 70 and Figure 71 present the dilatometric heating curves for all six samples in view for the whole curves (Figure 70) and for transformation only (Figure 71). All of the samples, except the sample called 'Points', were heated with nearly the same heating rate of 5°C/s. These samples elongated to nearly the same length in range of 100 – 110μm. The microstructure transformation from ferrite to austenite started at the same temperature around 720°C. The samples were later cooled with the different cooling rates, which was described further in the text. The sample 'Points' were heated to the temperature 1200°C with the slowest rate to achieve the near-to-equilibrium conditions of the process, but there were no significant differences between it and the rest of the samples, except for the peak around 990°C. It probably could be caused by the dissolving of the nitrides, reported by Pous-Romero [4], [150], however it would be around 100°C higher than in his results.
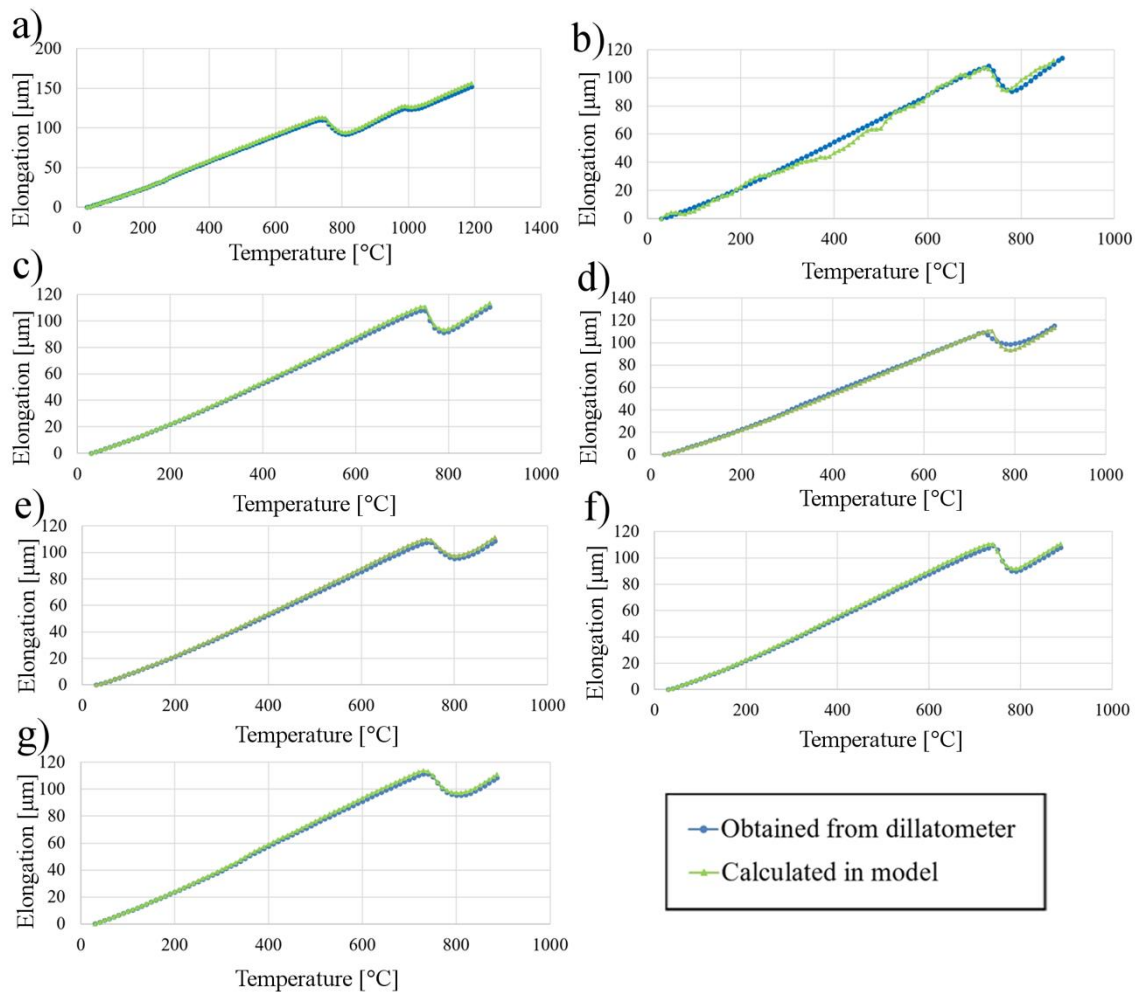
Figure 72 The heating dilatometric curves obtained from the experiment for seven cases: a) HR=0.08; CR=0.5 b) HR=4.98; CR=0.05 c) HR=4.74; CR=0.1 d) HR=4.99; CR=1 e) HR=5.00; CR=5 f) HR=5.01; CR=10 g) HR=5.01; CR=100, where HR - heating rate, CR - cooling rate [°C/s].

Figure 72 presents the elongation of the samples due to the temperature, obtained from the dilatometric test during the heating of the samples. The heating rate was set to 5°C/s for all of the samples except the first one called 'Points', where was set to 0.08°C/s. It can be seen that the main differences between all of the registered curves can be visible during the transformation, but still, these differences are not significant. After the heating, the samples were held at the temperature of 890°C (1200°C for the sample 'Points') for the period sufficient to achieve the fully austenitic microstructure. It can be seen from figures presented above that the assumed approach of the modelling the thermal expansion/contraction allows for relatively high precision of mapping of the displacement of the nodes during the process.
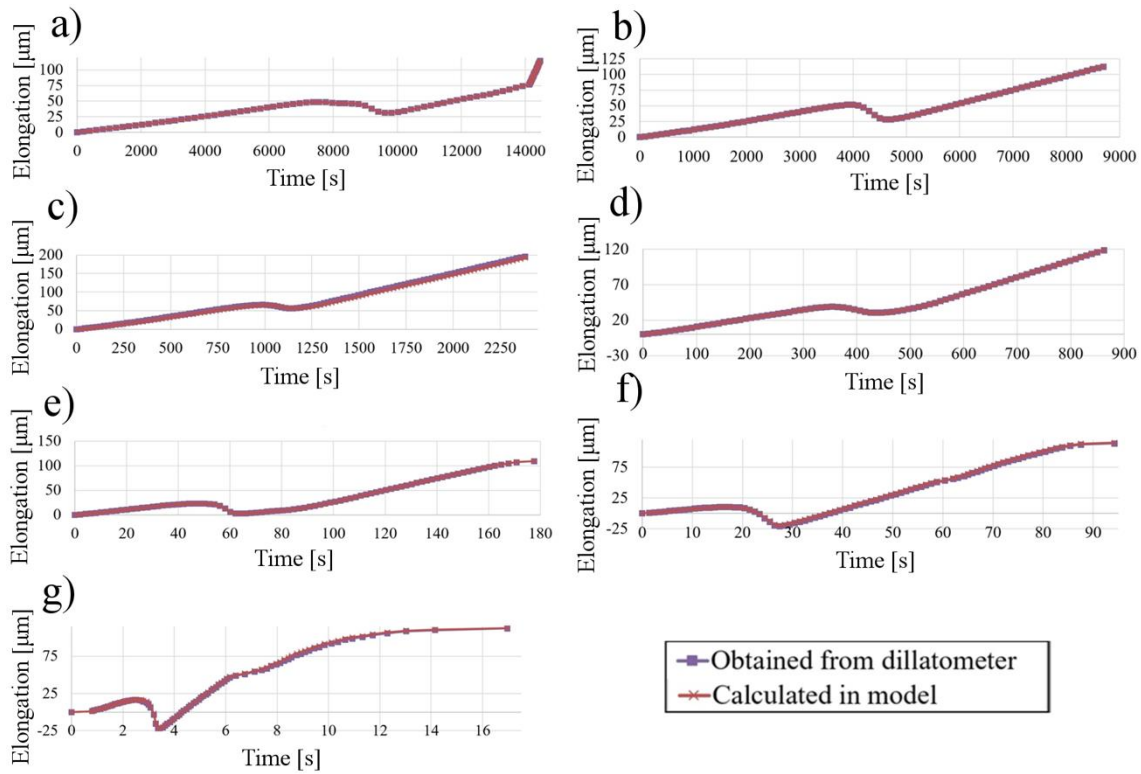
Figure 73 The cooling dilatometric curves obtained from the experiment for seven cases: a) HR=0.08; CR=0.5 b) HR=4.98;CR=0.05 c) HR=4.74; CR=0.1 d) HR=4.99; CR=1 e) HR=5.00; CR=5 f) HR=5.01; CR=10 g) HR=5.01; CR=100, where HR - heating rate, CR - cooling rate [°C/s].

Figure 73 presents the elongation of the samples due to the temperature, obtained from the dilatometric test during the cooling of the samples with different cooling rates, with values that were presented before. Similar to the chart in the previous figure, these results also confirm the relatively high ability of mapping the displacement of the nodes during the thermal elongation of the sample. The most significant fact from the figures is the relationship between the cooling rate and the microstructure transformation start temperature. It can be seen that the higher value of the cooling rate in the process indicates the greater delay in the start temperature of the microstructure transformation. The achieved results are in agreement with the TTT diagrams, presented earlier in the work. The developed approach allowed for the construction of the set of the models, which were assembled together in one model, presented with different geometry for large dimensions forging at the end of this chapter and which was validated at the end of this work using the real industry process.

3.5.7. Inverse models: Model 7

The inverse analysis is a method of identification of the parameters which control the given process, using numerical calculations and the experimental results. Such a method is widely used for the identification of the parameters which describes the flow of the material in constitutive laws. To directly apply the known parameters in the model to simulate its behaviour during the deformation or the heat treatment is called the direct method, but to investigate the unknown controlling parameters the Inverse method can be introduced [147], [149], [151]–[153]. In this model the Inverse method was used for identification of the parameters used in the Fortran subroutine code for microstructure transformation control. The subroutine used for such calculations is the same as for the first dilatometric model (fifth model, Appendix A). This approach uses the Avrami equation to estimate the percentage of the transformed microstructure within the part to assign the correct heat expansion coefficient to the corresponding elements and is described in detail in chapter 3.2.

The model used the geometry of the small dilatometric sample, described earlier. The material properties were temperature-dependent (Table *18*b), and the predefined temperature was set to 1200°C (Table 13), the cooling was set as a temperature boundary condition (Table 26) with the time of 116.5s, what simulated the cooling rate of 10°C/s. The symmetry conditions on the three surfaces in the manner described in Figure 41 were applied. The finite element mesh upon the element contained 897 nodes and 3778 of C3D4T type elements (Table 16).

The dilatometric test performed for the cooling with 10°C/s rate the displacement in time curve was extracted and part of the curve, which reflected the dilatometric peak, was selected to serve as the target values for the inverse method. In the next step the analysis was run repeatedly, each time calculating the new phase transformation controlling parameters in relation to the results from the previous step. For the detailed mechanism of the Inverse method see chapter 3.4. Calculations stopped when the differences between the target and the calculated parameters were lower than the predetermined value.
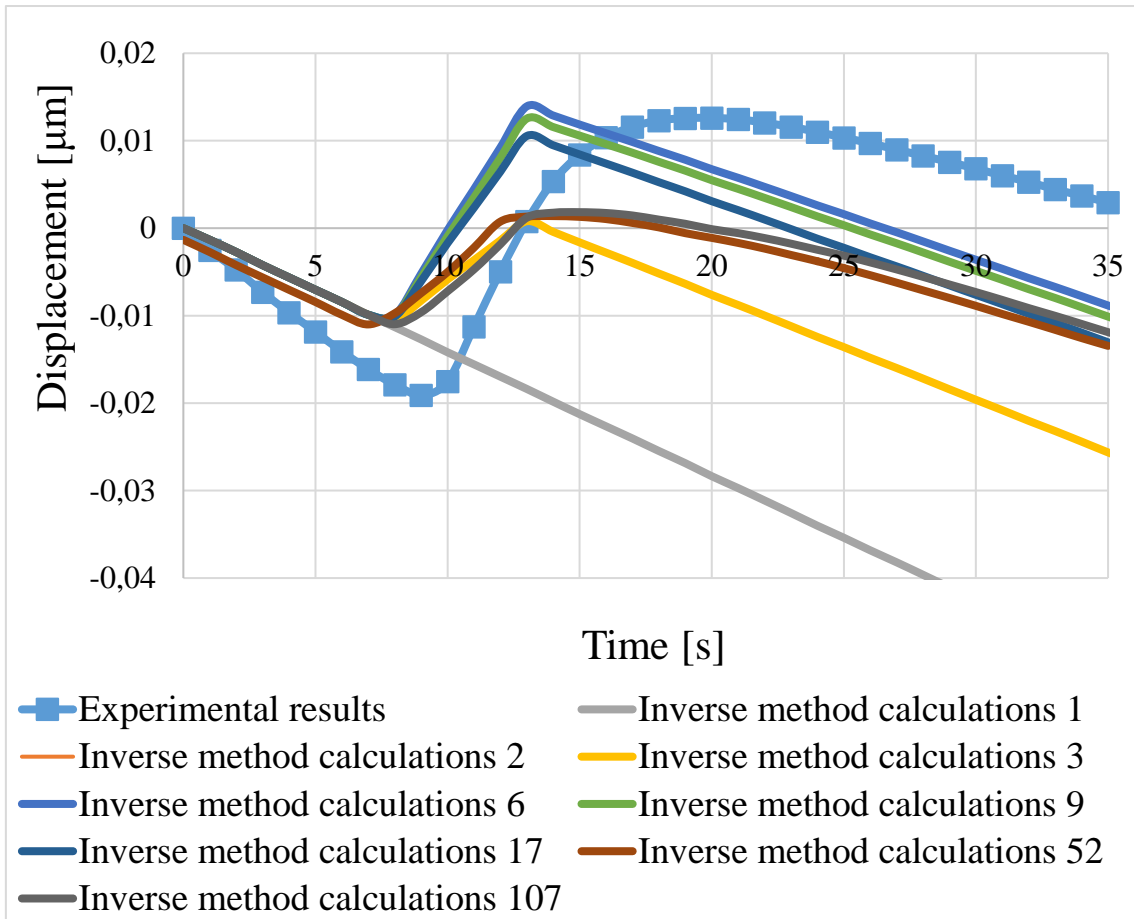
Figure 74 The chosen results of the inverse analysis investigations for different phase transformation controlling parameters.
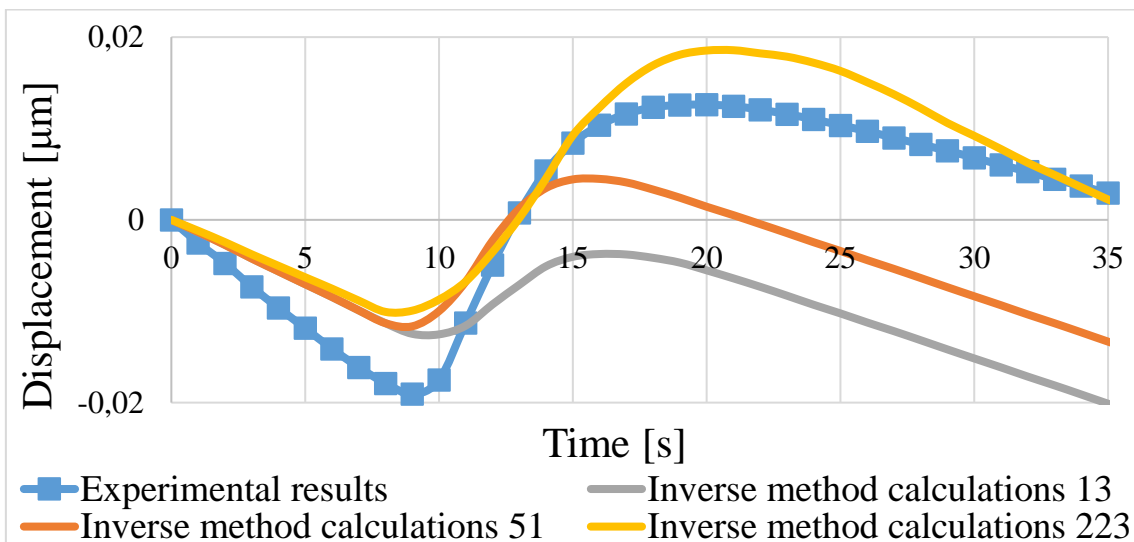
Figure 75 The chosen results of the inverse analysis investigations for different phase transformation controlling parameters – part 2.

Figure 75 and Figure 74 present some of the results from the calculations of the Inverse analysis. The blue square-dotted curves on both of the figures are representing the results obtained from the dilatometer. The progression of the results is clearly visible in the figures, as in Figure 74 the first calculations gave nearly straight line, when on the second curve there is already a characteristic peak, which deepens with the number of calculations. The differences between the subsequent results are not significant, so only the chosen ones are shown on the chart. At the end of the Inverse analysis performed this particular time it can be seen that between the calculations numbers 52 and 107 the difference is relatively very small and there was no point in running it again. The method had to be interrupted and the initial parameters had to be changed. The result from the second launch of the Inverse analysis are presented in Figure 74. The output parameters from the previous launch were set this time as an input (starting) parameters. The vector of the smallest sufficient differences between the targeted and the calculated values, the same as the incremental value, were lowered. In Figure 75 there can be seen that after the performed analysis, in final 223rd calculations, the results are much closer to the original curve obtained from the dilatometric test, than in the first launch, presented in figure before.

The results proved that there is a possibility of using the Inverse method to obtain the parameters for proposed microstructure transformation mechanism described by the Fortran subroutine code, as the method is sufficient to provide the results on relatively satisfying level. The developed approach will be investigated more in the future projects, as the other method of calculating the displacement of the nodes during the microstructure transformation, based on the obtained during dilatometric test sets of the thermal expansion coefficients, was developed further in this work.

3.5.8. Comprehensive models: Model 8, large dimension forging with flange.

The geometry of the first of comprehensive models is a large cylindrical forging with two flanges at both ends. The radius is 2m and the length is 3m. Figure 76 presents the cross section of the model geometry in axisymmetric view about the O axis. The model was 3 dimensional,

the 45° rotation about the axis O was performed and the symmetry condition was applied at the bottom edge and both surfaces at planes XY and YZ (after rotation).
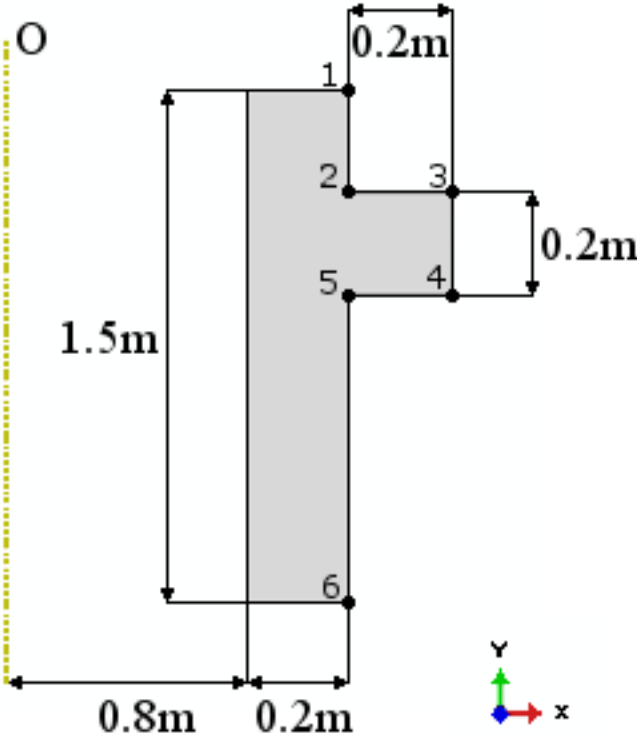
Figure 76 The cross section of the geometry of the 3D comprehensive model and the geometry of the axisymmetric comprehensive model., nodes marked 1 – 6 are locations of obtained results.

The material properties were temperature-dependent (Table 18a, the units adjusted for the meter unit). There was no implemented transformation this time, as this model was used to calculate the transient temperature field in relations to the axisymmetric geometry, which is the base of the transformation model. The transformation was added in the further development of the model. The predefined temperature field details remained the same (Table 13), except the value of the temperature, which was set to 890°C. The cooling process was performed through the interaction module with details presented in Table 14. The time of the cooling was set to 862.43s to achieve the cooling rate of 10°C/s at the surface of the geometry (*Table 34*). The finite element mesh was constructed with total number of nodes 5824 and total number of elements 4526, with type element of C3D8T and the rest of details is in Table 16.

The subroutine implemented in this model used Depvar function, based on the solution-dependent state variables, which calculated the cooling rate, registered at the representative nodes in two manner. SDV2 (solution-dependent variable) is the average cooling rate calculated at the node since the beginning of the process and SDV3 is the momentary cooling rate, which was calculated between the time steps.

Table 29 The parameters used to control time step during the numerical calculations of the eighth comprehensive model

| Step	Time period [s]	Response	Max allowable temperature change [°C]	Increment size		
				Initial	Min	Max
Cooling	862.43	Transient	20	1×10^{-7}	1×10^{-11}	10
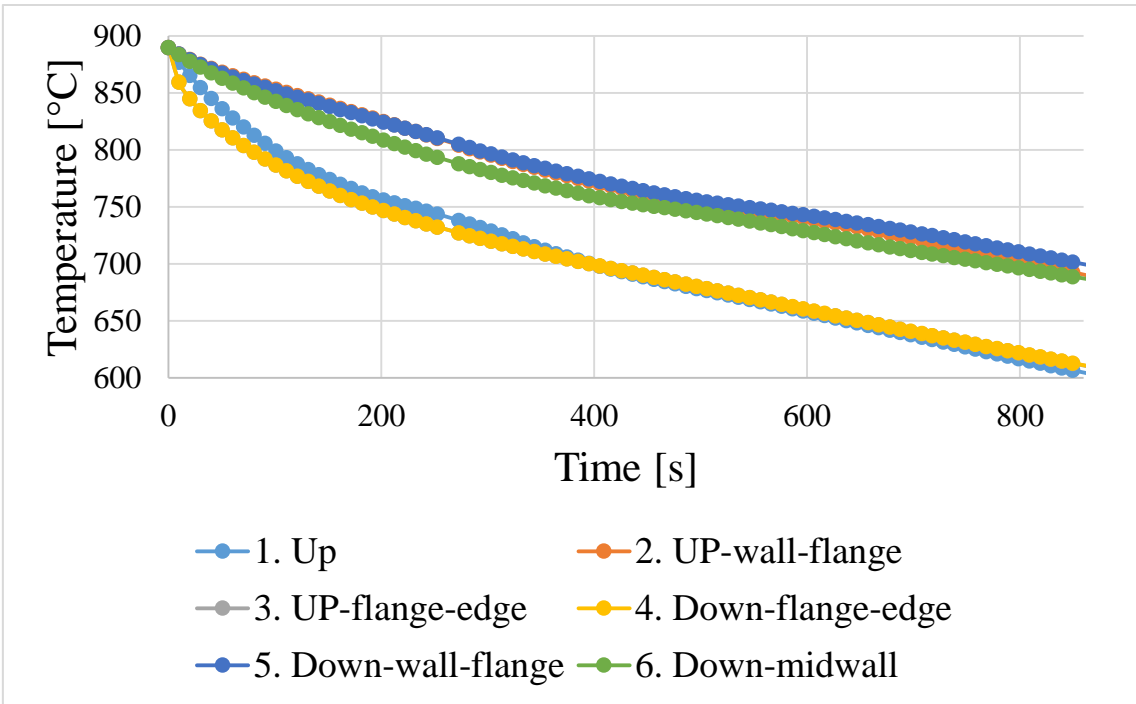
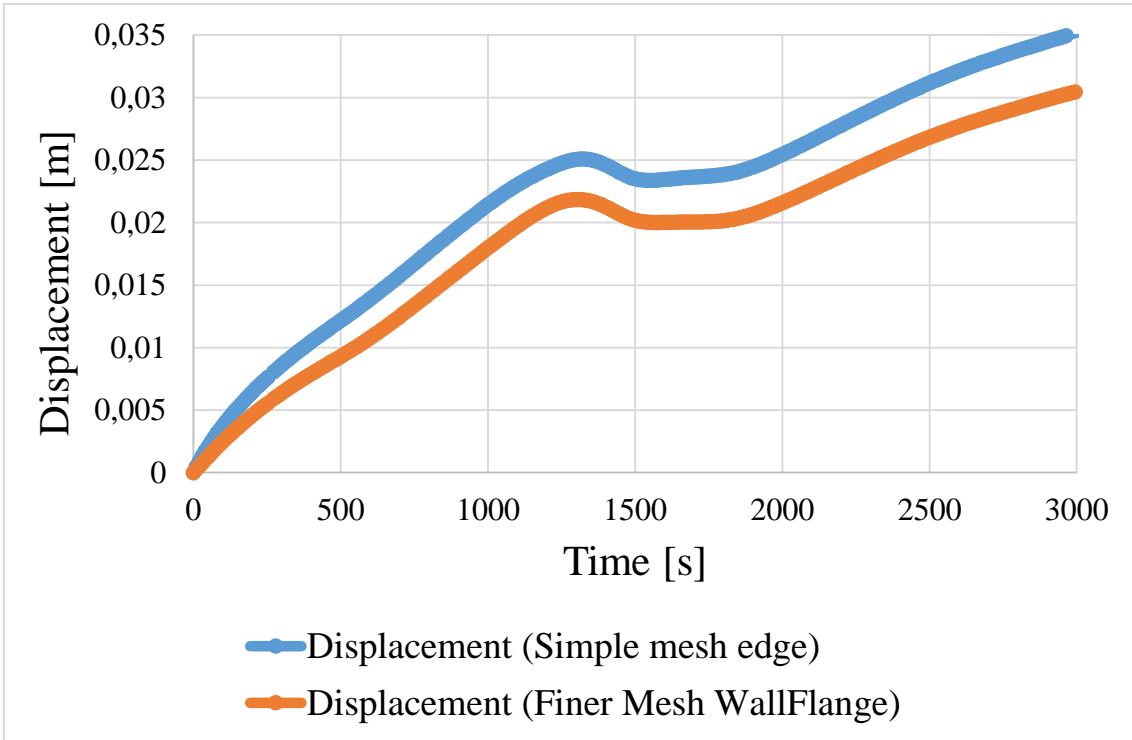Figure 77 The calculated temperature in time of the process, obtained from the eighth comprehensive model.
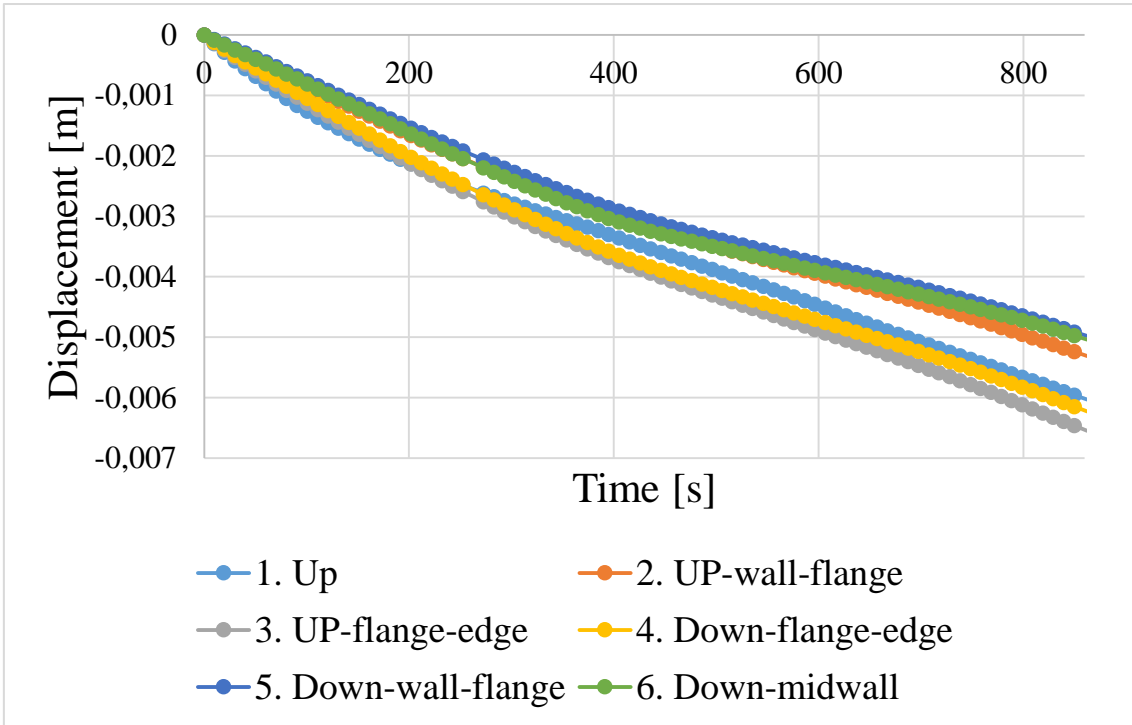
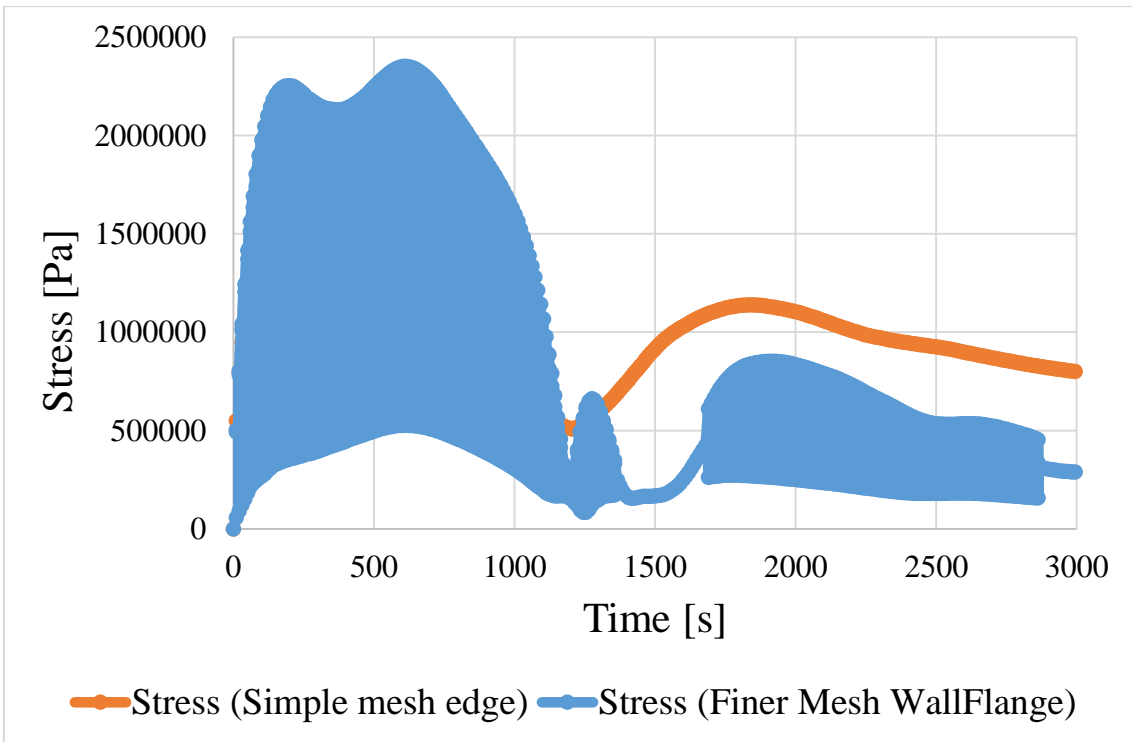Figure 78 The calculated displacement in time of the process, obtained from the eighth comprehensive model.
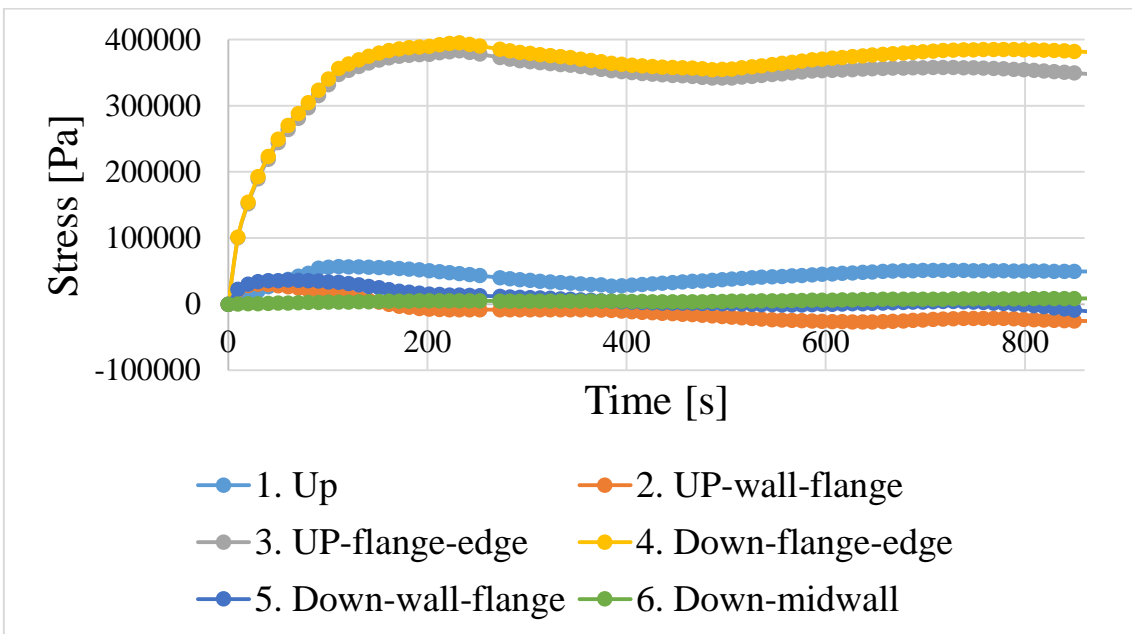
Figure 79 The calculated stress in time of the process, obtained from the eighth, comprehensive model.

Figure *77*, Figure *78* and Figure *79* present respectively temperature, displacement and stress results obtained at the representative nodes in the eighth comprehensive model. The locations of the nodes are numbered from 1 to 6 and are presented in Figure 76. It can be seen

that the main difference in cooling between the nodes is created in the first 100s. After such time, the regions are cooled down with the same cooling rates. Nodes 1, 3 and 4, located respectively at the upper left edge, upper flange edge and down flange edge are more exposed to the cooling factor than the rest of the locations. It causes the higher values of the cooling rates in these regions at the beginning of the process before the temperature gradient within the geometry is evenly distributed. The displacement of the representative nodes is proportional to the temperature, what implies the highest values of displacement in regions, where there was highest change of the temperature in time of the process. The stress distribution within the geometry of the model reached relatively high values for the model without any phase transformation implemented. The regions in which such results were registered cover the regions of the highest temperature gradients and highest displacement, but it has to be mentioned that the obtained stress results can be disturbed by applying the sharp edges instead of the fillets.
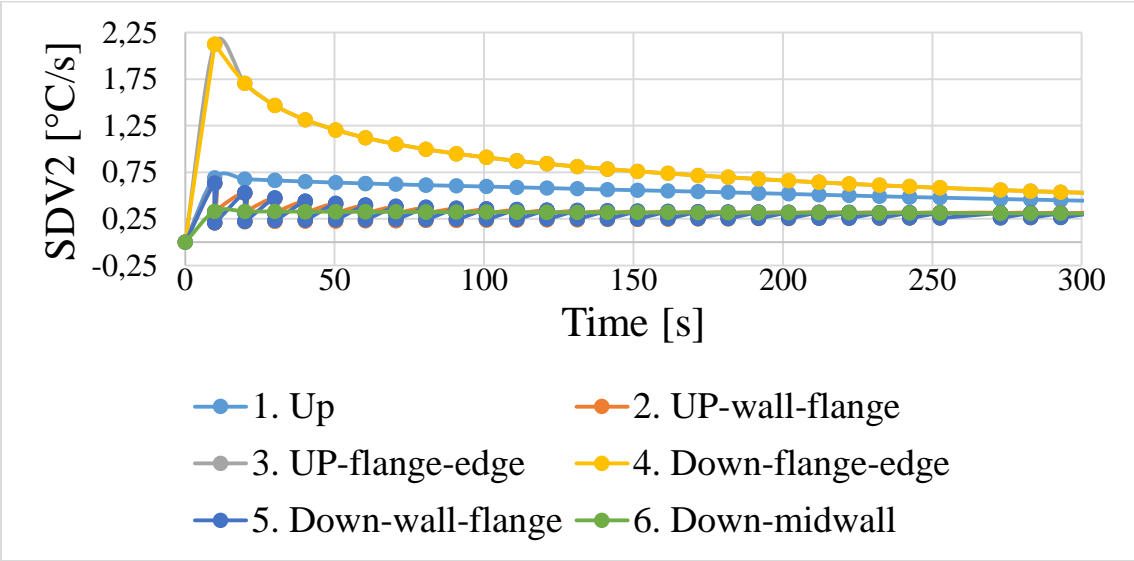
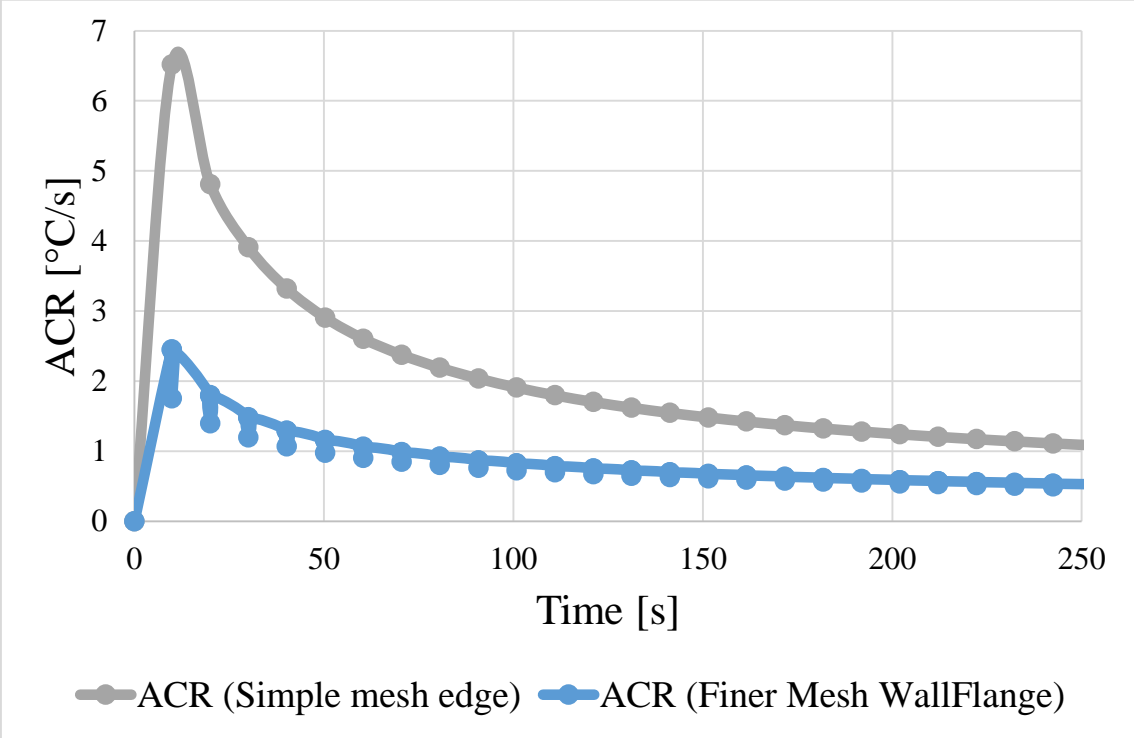Figure 80 The calculated average cooling rate in time of the process, obtained from the eighth comprehensive model at the beginning of the process.
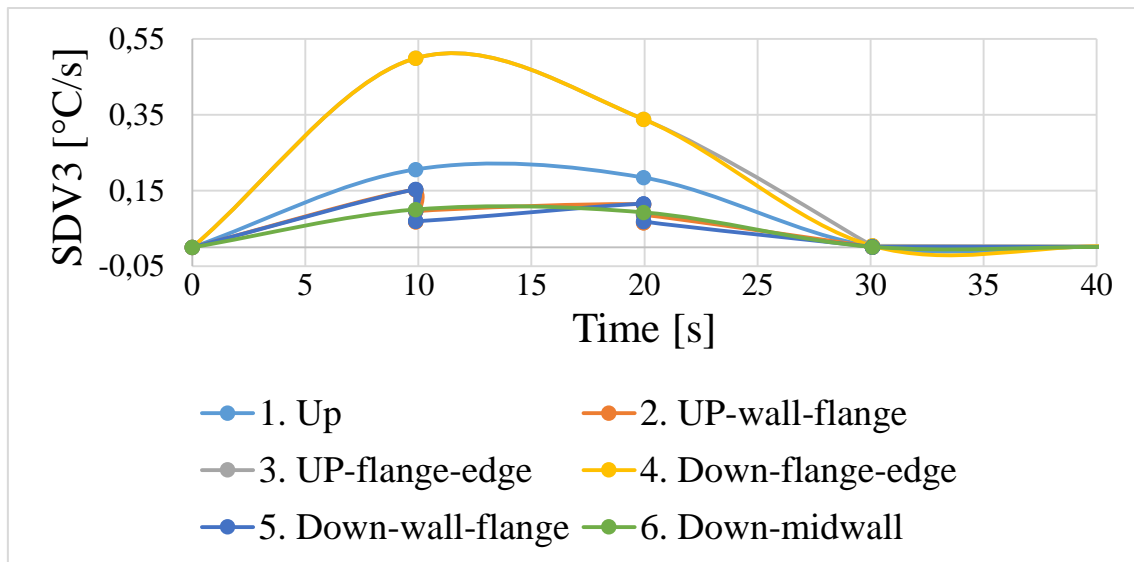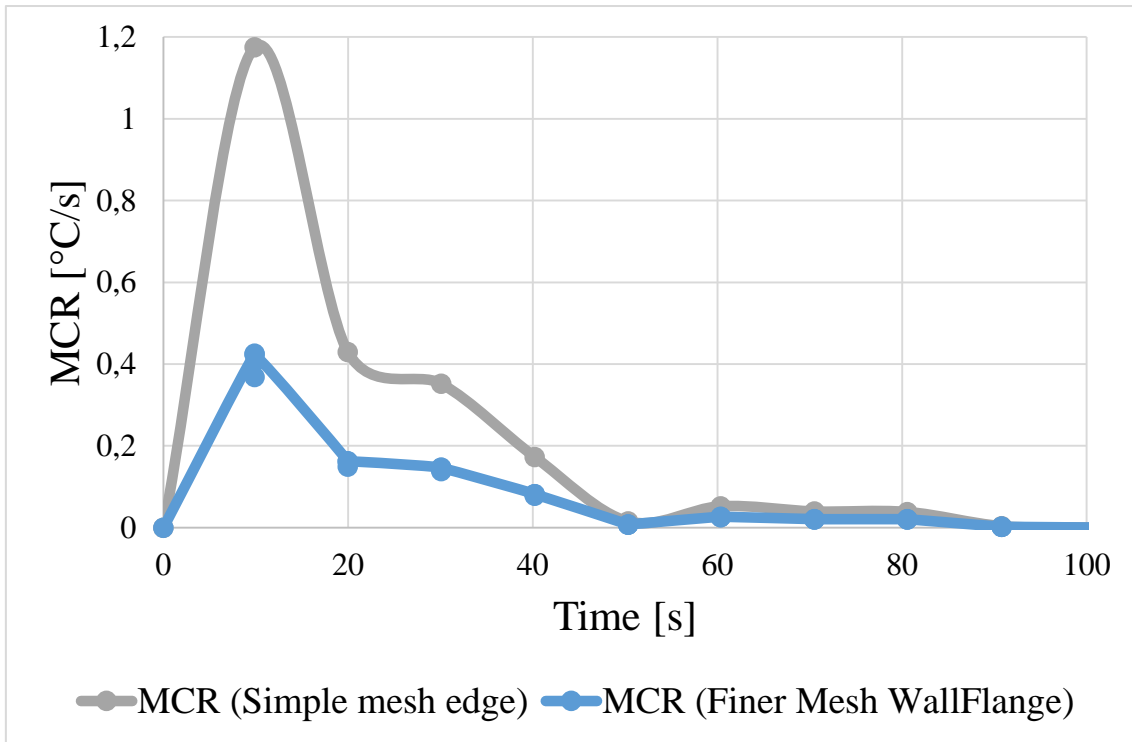
Figure 81 The calculated momentary cooling rate in time of the process, obtained from the eighth comprehensive model at the very beginning of the process.

Figure *80* and Figure *81* present the calculated cooling rates at the representative nodes shown in Figure 76, respectively as a change of temperature from the beginning of the process and as a change of temperature from the previous time step. It can be seen that in both of the cases the greatest differences in cooling rate at the different regions of the model are at the beginning of the process, in the first 100s. It is consistent with the earlier stress results, where the highest values were registered at the upper and lower edges of the flange, the higher values were registered at the upper edge of the geometry and the lowest values were at the mid-wall region of the forging. This is probably caused due to the amount of the material that surround the last node blocking the coolant and giving the possibility of heat concentration.

The developed cooling rate calculations were subsequently used in the next model for assigning the corresponding thermal expansion coefficient, extracted from the dilatometric test values.

3.5.9. Comprehensive models: Model 9, axisymmetric model.

The geometry of the second comprehensive model is an axisymmetric cross section of the three dimensional model described in detail section earlier and presented in Figure 76. The symmetry condition was applied at the bottom edge (Table 30). Most of the parameters were as in the model 8. The material properties were temperature-dependent (Table *18*a, adjusted for meters unit). The predefined temperature field details remained the same (Table 13), with the initial temperature of 890°C. The cooling process was performed through the interaction module with details presented in Table 31.

Table 30 The symmetry boundary condition details, applied in the ninth comprehensive model

Boundary conditions	
Type	Symmetry/Antisymmetry/Encastre
Step	Cooling (coupled temperature-displacement)
Region	Edge at x axis
Description	YSYMM (U2=UR1=UR3=0)

There were two calculations performed with the two finite element mesh placed on the part, with total number of nodes respectively 5611 and finer of 22021 and total number of elements 5400 and for finer mesh 21600 with type element of CAX4T. The rest of the details were described in Table 16.

Table 31 The parameters used to control time step during the numerical calculations of the ninth, comprehensive model

Step	Time period [s]	Response	Max allowable temperature change [°C]	Increment size		
				Initial	Min	Max
Cooling	3025.27	Transient	20	1×10^{-7}	1×10^{-11}	10

The subroutine implemented in this model also used Depvar function and cooling rates were calculated in two manners like before. This time the transformation was implemented through an UEXPAN subroutine (Appendix A), based on the change of the thermal expansion coefficient of the element due to the temperature. In the subroutine the set of the thermal expansion coefficients obtained from the dilatometric test, using the previously developed models and described earlier in this chapter, was used.
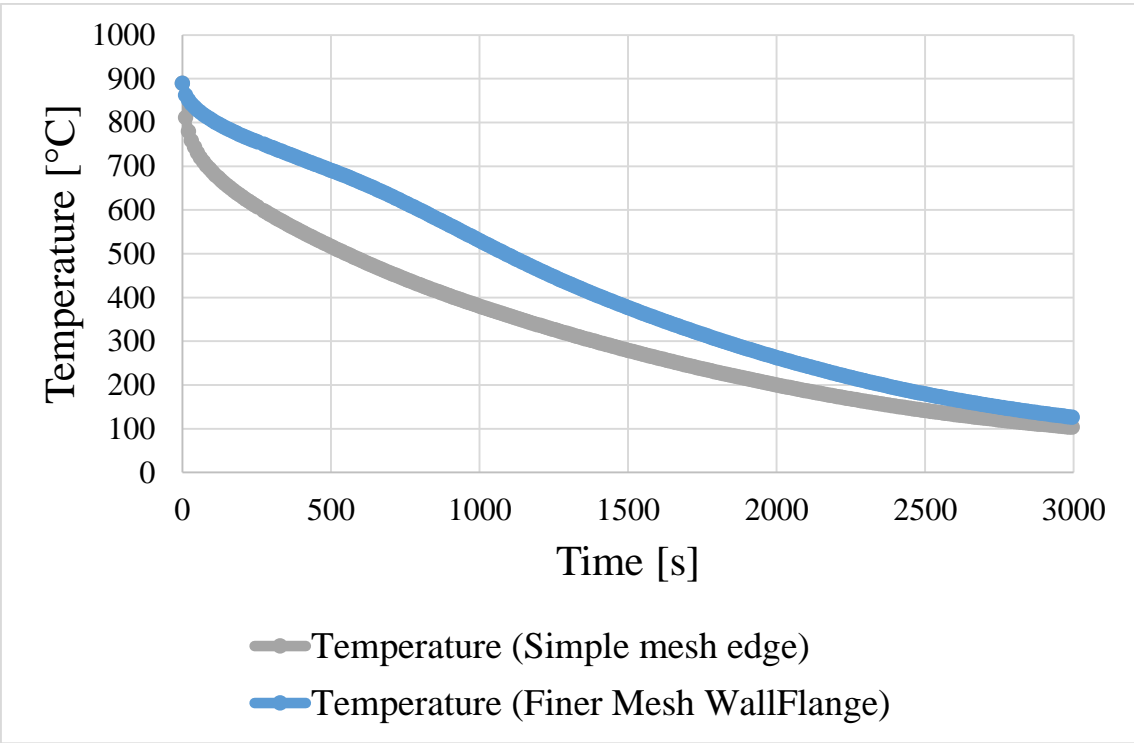
Figure 82 The calculated temperature in time of the process, obtained from the ninth, comprehensive axisymmetric model.

Figure 83 The calculated displacement in time of the process, obtained from the ninth, comprehensive axisymmetric model.

Figure 84 The calculated stress in time of the process, obtained from the ninth comprehensive axisymmetric model.

Figure 82, Figure 83 and Figure 84 present respectively temperature, displacement and stress results obtained at the representative nodes numbered 1 and 2 (Figure 76) in the ninth comprehensive model. The results from the model with finer mesh were compared with the results from the model with simple mesh, but no significant differences were registered. The results of both models are shown, but for different locations. It can be seen that at the edge of the model the cooling rates were higher than at the node located between the wall and the flange. As before this is probably caused by the greater exposure of this location to the coolant. Nodes at the edges had greater contact surface with the ambient (coolant), which had lower final temperature, which made the heat transfer relatively easier and faster. The greatest difference in cooling rate occurred at the first 1000s (~30%) of the process. The faster cooling influenced the displacement of the material, causing the greater strains at the edge nodes. Unfortunately, the registered stress is disturbed, probably by the lack of fillets in this location. It can be also seen that the dilatometric peak, characteristic for the starting microstructure transformation occurred around 500 – 400°C.

Figure 85 The calculated average cooling rate in time of the process, obtained from the ninth, comprehensive axisymmetric model at the beginning of the process.

Figure 86 The calculated momentary cooling rate in time of the process, obtained from the ninth, comprehensive axisymmetric model at the very beginning of the process.

Figure 85 and Figure 86 present the calculated cooling rates at the representative nodes, respectively as a change of temperature from the beginning of the process and as a change of temperature from the previous time step. It can be seen that the greatest differences in cooling rates were at the very beginning of the process and as it was said before in the location of the outer edges of the model geometry. Such an effect was crucial for the transformation model as the choice of the thermal expansion coefficient set for the given node was dependent on the cooling rate at the beginning of the transformation.

The developed model was used in the next chapter to calculate the displacement and the stress of the forging during heat treatment process to validate the level of its utility in the industrial environment.

4. Experimental tests and model validation

4.1. Material

4.1.1. Samples preparation

For these investigations the SA508 gr. 3 steel was used. It is a structural, low alloy, ferritic steel commonly applied for manufacturing of large forged elements, which are welded together to create reactor pressure vessels (RPV). The extreme high temperatures and radiation damage creates a hard working environment for the RPV with the resultant potential for radiation embrittlement, loss of toughness, time-dependent deformation (creep), fatigue, radiation swelling, thermal aging, corrosion, oxidation and many others [14].

To prepare the sample for the dilatometric investigation the part of the forged flange was cut in a way presented in Figure 87. The chemical composition of the steel sample, obtained by the spark atomic emission spectrometer (AES) test, is given in Table 32.

Table 32 The chemical composition of the SA508 gr. 3 steel forged flange:

Grade/elements	Fe	C	Si	Mn	P	S	Cr	Mo	Ni	Al	Co
SA508 gr.3 steel	96.6	0.17	0.266	1.33	0.01	<0.003	0.2	0.495	0.799	0.0248	0.004

This test did not register the presence of nitrogen, which is favourable. The level of nitrogen is important due to the possible effects of cracking. The values of levels obtained from Sheffield Forgemasters Engineering Ltd. from the various forgings adopted from Pous-Romero [4] are presented in Table 33 below.

Table 33 The level of nitrogen after degassing of the melted steel. Data obtained from Sheffield Forgemasters Engineering Ltd from [4]:

Nitrogen level [wt%] measured in various forgings										
0.015	0.025	0.018	0.014	0.015	0.022	0.024	0.022	0.020	0.024	0.015

The SA508 grade 3 steel samples used in this work were produced in this company. The AES investigation revealed the level of the sulphur, phosphorous, copper and nitrogen of the sample, and these are presented in Table 34. The values indicate that the level of harmful elements in ingots produced by this company is within the modern standards of high purity.

Table 34 The level of detrimental elements of the sample of SA508 grade 3 steel used in the work:

SA 508 grade 3			
S [wt%]	P [wt%]	Cu [wt%]	Ni [wt%]
0.003	0.0064	0.0461	0.799

The flange was formed from an ingot of ~2m diameter (Figure 87a). After rolling in the blooming mill, the bottom and the top of the ingot was cut (Figure 87b). The ingot was upset in 3:1 ratio (Figure 87c and d) and sawn in half in parallel axe direction (Figure 87e and f). After that, a hole was machined in the bottom half and the element was punched making the flange (Figure 87g and h). Then, the flange was subjected to the heat treatment in a way presented schematically in Figure 88. To make the specimens from the flange a cross section in the perpendicular axial direction (Figure 87i and j) was cut and the upper part of it was further used (Figure 87k). Then, nine samples were cut from the selected part. Six samples in the 'as-received' state were cut from the different areas of the non-punched side of the cross section, as shown in Figure 87l as 1, 2, 3, I, II and III, and were prepared for microscopic investigation followed by hardness and dilatometric tests. Additionally, three further samples were taken from the middle of the cross section of the obtained element (Figure 87i). The sample, which

was used for heating and cooling dilatometer investigations in near-equilibrium conditions was called "Points". Two other samples were quenched under different conditions (QS_I and QS_II) to obtain information about precipitation dissolution, as mentioned by Pous-Romero in [3], [4].
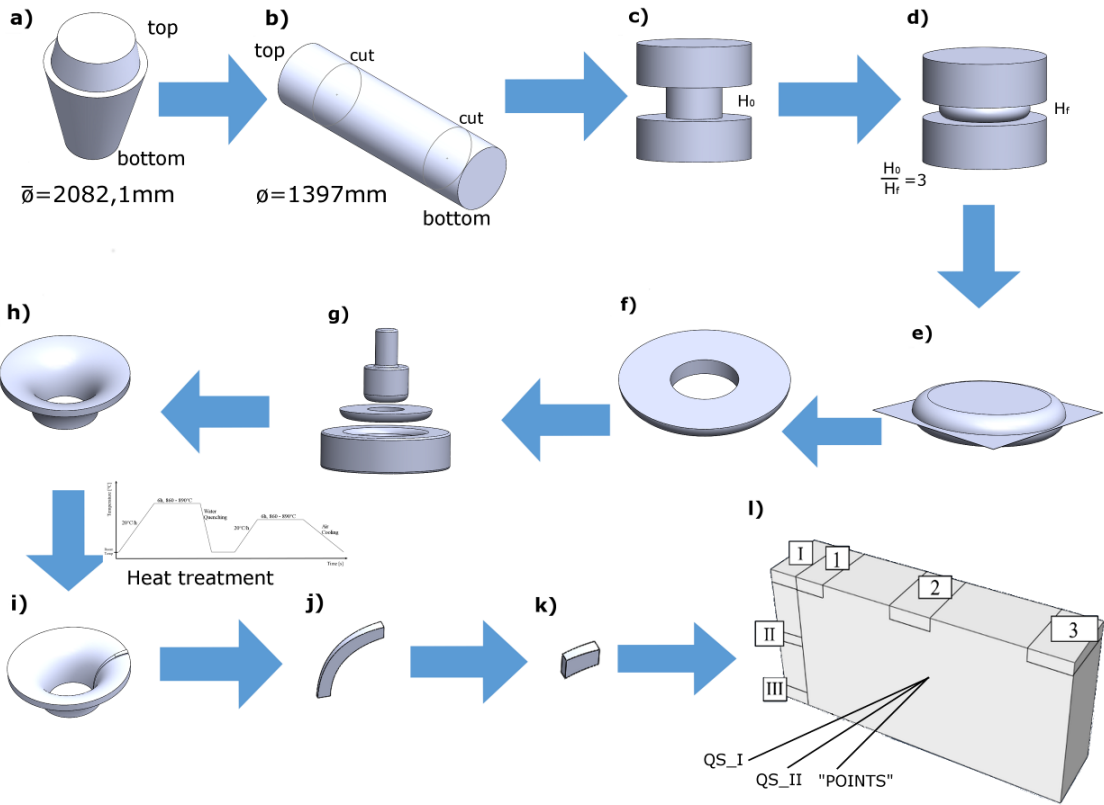
Figure 87 Schematic representation of the sample preparation route.
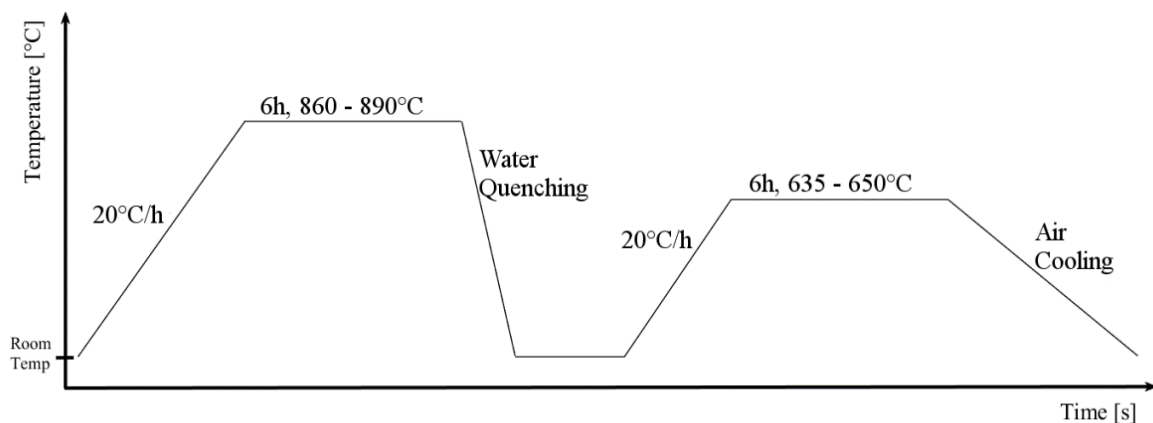
Figure 88 Heat treatment scheme of the flange, from which the sample was taken.

For the dilatometric investigations the dilatometer Linseis L78 RITA (Rapid Induction Thermal Analysis) was used. The dimensions of cylindrical sample 'Points' were as follows: 3 mm diameter and 10 mm length. After heating this sample to 1200°C with a heating rate HR=0.08°C/s and holding for 2h, the sample was cooled down to 20°C (room temperature) with the cooling rate of 0.5°C/s and then the hardness and the microscopy studies were conducted, after the dilatometric testing. The samples QS_I and QS_II were only prepared for hardness testing and optical microstructure observations. The sample QS_I was heated to 890°C and the sample QS_II was heated to the temperature of 1100°C. They were both held for 30 minutes at the corresponding temperatures and then were quenched in water. After the heat treatment, microscopy examination and hardness tests were performed. For the hardness test Vickers hardness test machine ZWICK 3212002 was used with 5kg test load. All of the experimental tests were performed at the University of Science and Technology AGH in Cracow, Poland.

4.1.2. The results of hardness test and microscopic observations of the as-received samples I, II, III, 1, 2, and 3.

The material for the experimental investigations, which was obtained from the forged flange in the scheme showed in Figure 87 was subjected to the hardness test, the results are presented in Table 35.

Table 35 The results of Vicker's hardness test for various locations in the sample (see Figure 87). The standard deviation of the data is presented as the error:

HV5	1st	2nd	3rd	Average
III	246	249	250	248±2
II	249	256	248	251±4
I	231	247	245	241±9
1	240	240	235	238±3
2	234	226	223	228±6
3	244	233	239	239±6
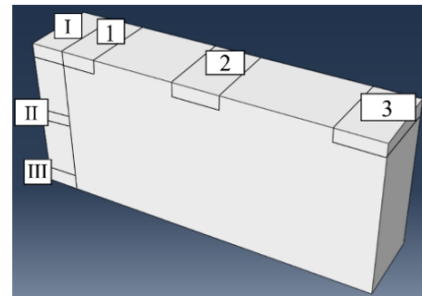
Numerous micrographs were obtained from the samples using the optical microscope with various magnifications. The preparation of the samples for these tests was as follows: the dilatometric samples were embedded in bakelite. Afterwards the samples were ground on SiC paper with increasing level of grain gradation in order 200, 400, 800, 1200 and 2000 and then polished with the suspension of the aluminium oxide and etched in 2% solution of the nitric acid (Nital). The chosen micrographs are presented below.
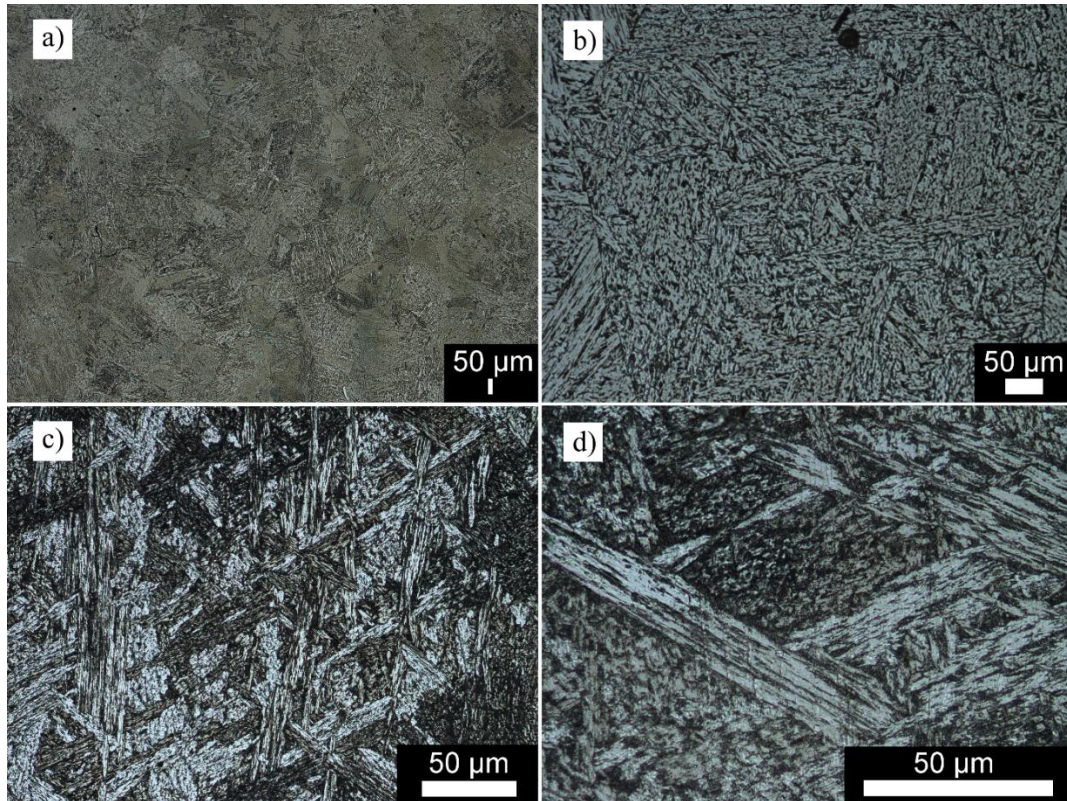
Figure 89 Micrographs from the optical microscope of as-received sample with different magnifications a) ✕2.5; b) ✕20; c) ✕50; and d) ✕100.

The dimension of the part cut from the forged flange was approximately 180✕110✕30 mm (Figure 87l). Optical microscopy does not allow precise phase identification, but the various phases in steel have characteristic morphology. The detailed description of the microstructure evolution is presented further in this chapter. The microstructure presented in Figure 89 is the mix of phases such as martensite, bainite, Widmanstätten ferrite and probably acicular ferrite (Figure 89c) [20], [66]. The characteristic structures are acicular with what appears to be carbides inside. The grain size is relatively large, differing in the range of 300 – 400µm, which confirms that the plastic deformation was performed in high temperature. The hardness values are relatively low, around 240±15HV5, which correspond with the large grains size (Table 35).

The hardness values of the two quenched in water samples, together with the hardness of the dilatometric sample used for microstructural investigations are presented in Table 36.

Table 36 The results of Vickers hardness test for quenched samples QS_I and QS_II and for sample heated with very slow heating rate HR=0.08°C/s 'Points'. The standard deviation of the data is presented as the error.

HV5	I	II	III	Average
Sample QS_I 890°C	412	434	449	432±19
Sample QS_II 1100°C	405	387	409	400±12
Sample "Points", slow heating, 1200°C	244	260	231	245±15

As can be seen, the higher cooling rate in the first two water quenched samples significantly increased the hardness in comparison with the sample 'Points", which was cooled down in air at 0.5°C/s. Such a big difference is probably the effect of the larger participation of the martensite phase in the water quenched samples and longer holding time (2h) of the sample 'Points', which favours the grain growth. The sample QS_I had higher hardness than the sample QS_II, which was cooled from the higher holding temperature. This difference can be caused by the dissolving of precipitation of aluminium nitrides mentioned by Pous-Romero [4]. The aluminium content of the sample, presented in Table 32, is relatively high (0.0248 wt%), which favours the precipitation of these particles.

The micrographs prepared from the sample 'Points', heated in close-to-equilibrium conditions with heating rate of HR=0.08°C/s and cooled with cooling rate CR=0.5°C/s, are presented below in Figure 90.
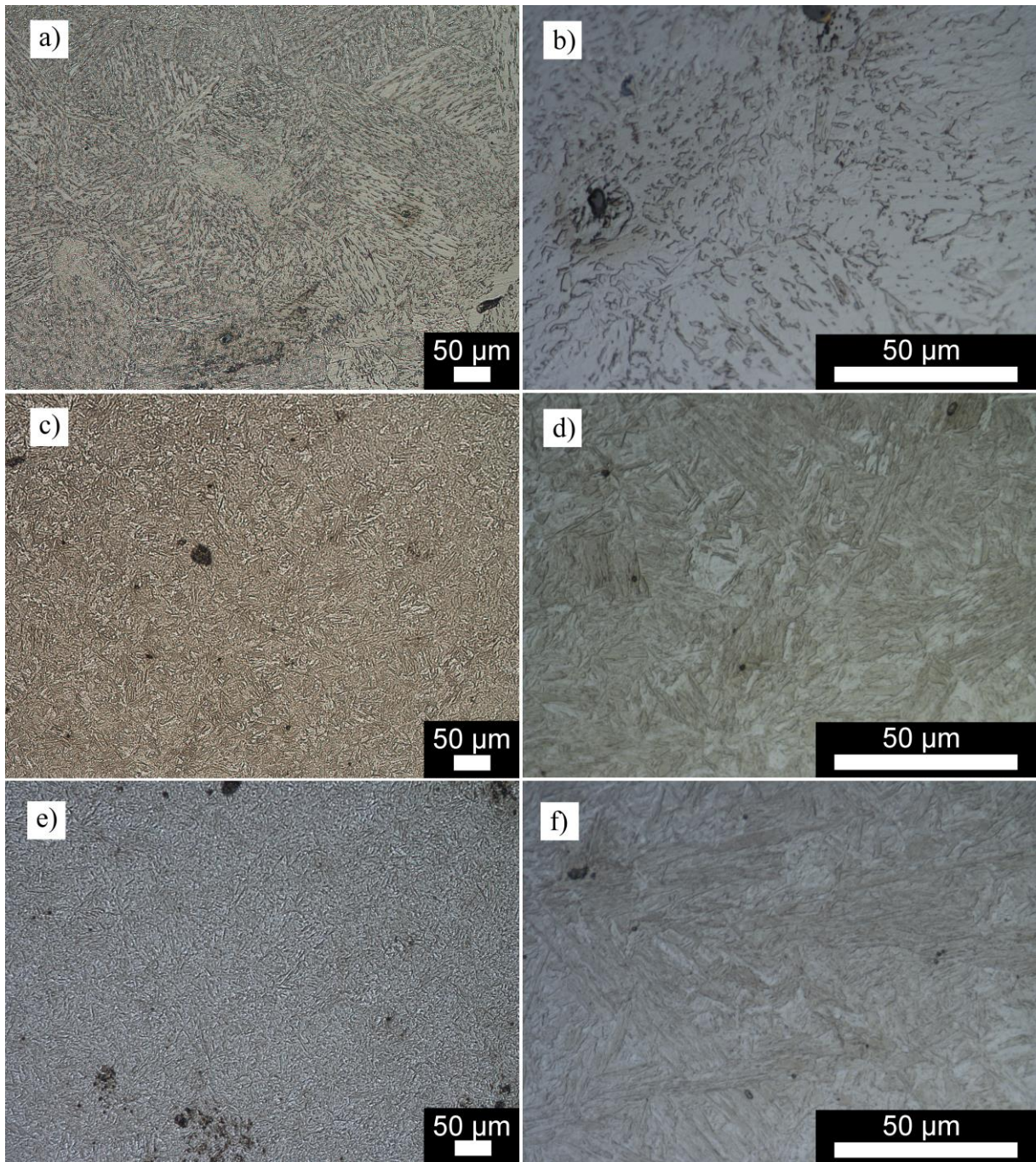
Figure 90 Micrographs of samples a), b) "Points"; c), d) QS_I 890°C; and e), f) QS_II 1100°C
with magnification ✕20 and ✕100.

It can be seen the relatively large size of the grain, around 300μm, in Figure 90a, although the detailed phase identification requires further investigation. As it was mentioned, the micrograph presented here are only of illustrative character, as electron microscopy is required to fully identify the resulting phases. Nevertheless, analysing the hardness values (Table 36) and dilatometric curve of the sample 'Points' (Figure 91) overall assumptions can be made, which were given further in the text.

152

The micrographs of quenched samples (QS_I and QS_II) are presented in Figure 90. The micrographs were obtained in order to investigate precipitation of the carbides and microstructure of the material at high temperatures. It can be seen that there is no visible presence of AlN carbides, what can suggest that they dissolved in both cases, at the temperature 890°C (Figure 90c and d) and 1100°C (Figure 90e and f), or, more likely, that they were too fine to resolve by optical microscopy. The microstructures of both of the quenched samples, QS_I and QS_II, are very similar, but it can be seen, that sample QS_II, which was quenched from the higher temperature has smaller grain size. Both of the quenched samples have a homogenous martensitic structure, but the hardness values presented in *Table 36* are quite low, compared to the hardness of the dilatometric samples quenched with controlled cooling rates 1, 5, 10 and 100°C/s, presented further in the text. Nevertheless, the difference in the hardness between the two quenched samples is relatively small and can be related to the grain size, probably due to the AlN dissolution.

4.2. Dilatometric tests with various cooling rates.

As mentioned before, one of the crucial problems during the manufacturing of heavy forgings of large dimensions is to ensure the cooling rate on the level sufficient to provide homogeneous microstructure both on the surface and inside the element. For this purpose, the dilatometric tests with different cooling rates were performed on Linseis L78 Rapid Induction Thermal Analysis dilatometer (RITA). A further six cylindrical samples were cut from the piece of the forged flange presented earlier (Figure 87). The dimensions of 3 mm diameter and 12 mm length were taken. After heating to 890°C, which is typical temperature for HT of the SA508 gr. 3 (Figure 88), and holding for twenty minutes, the samples were cooled down to room temperature, each with different cooling rate. The results from the cooling process of the sample 'Points' have been also added to the presented sets.

Similar to the previously obtained samples, hardness test and microscopy studies were conducted after the dilatometric test. Vickers hardness testing was undertaken on a ZWICK 3212002 with a 5kg load. These data were used in further numerical model development. In Figure 91 and Figure 92 the results from the dilatometric test of heating and cooling performed on seven samples are presented. The preparation of the first sample called 'Points' was presented earlier. All of the other samples were heated with the same heating rate of

HR=0.5°C/s, but the cooling rates were as follows: 0.05°C/s, 0.1°C/s, 1°C/s, 5°C/s, 10°C/s and 100°C/s. The first derivatives were calculated and plotted for each of the curves for identification of the transformation ongoing within the sample, as the peaks registered at the characteristic times points correspond with the dimensional change in respect to the temperature [154]. The obtained data were used directly in the calculations of the cooling rate dependent thermal expansion/contraction coefficient. From each of the curves the set of such values was made and was used in the model development presented further in the text.
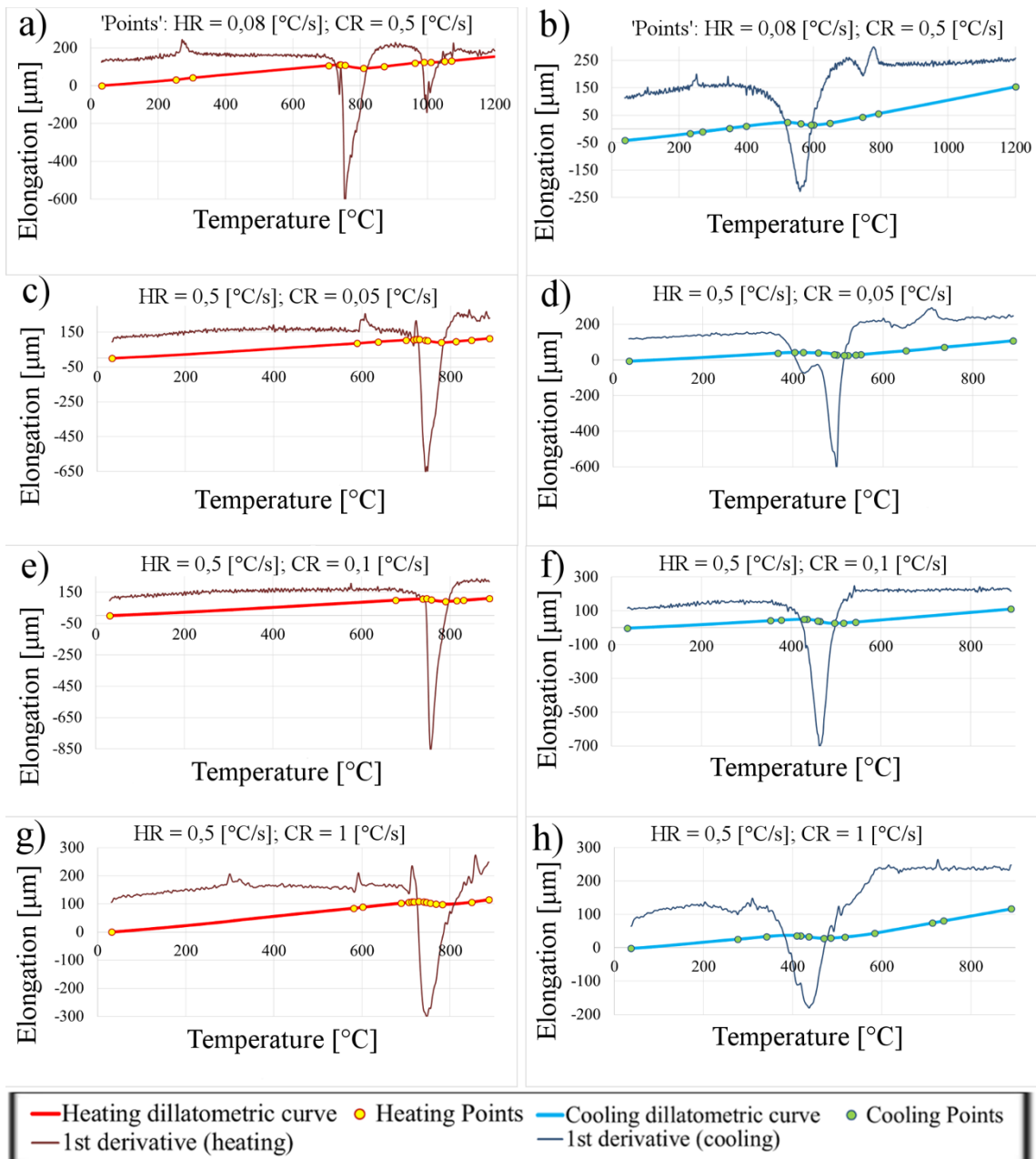
Figure 91 The heating (a, c, e, g) and cooling (b, d, f, h) curves obtained in dilatometric test with corresponding 1st derivative curve indicating the phase transformation peaks, where characteristic points where highlighted. HR – heating rate, CR – cooling rate. The presented cooling rates: a), b) 0.5°C/s, c), d) 0.05°C/s, e), f) 0.1°C/s, g), h), 1°C/s.

It can be seen that the heating curves, beside the described earlier sample 'Points', heated with the same heating rate of 0.5°C/s are similar to each other. There is the same level of deformation, around 100μm, and the phase transformation occurs at the same time related temperature. The interesting thing is the dilatometric peak at the samples presented in Figure

91a) and g) and Figure 92e). These peaks occur in the temperature range of 350°C - 400°C for cooling, which probably can be related with the Curie point transformation or martensitic transformation in case of higher cooling rates.
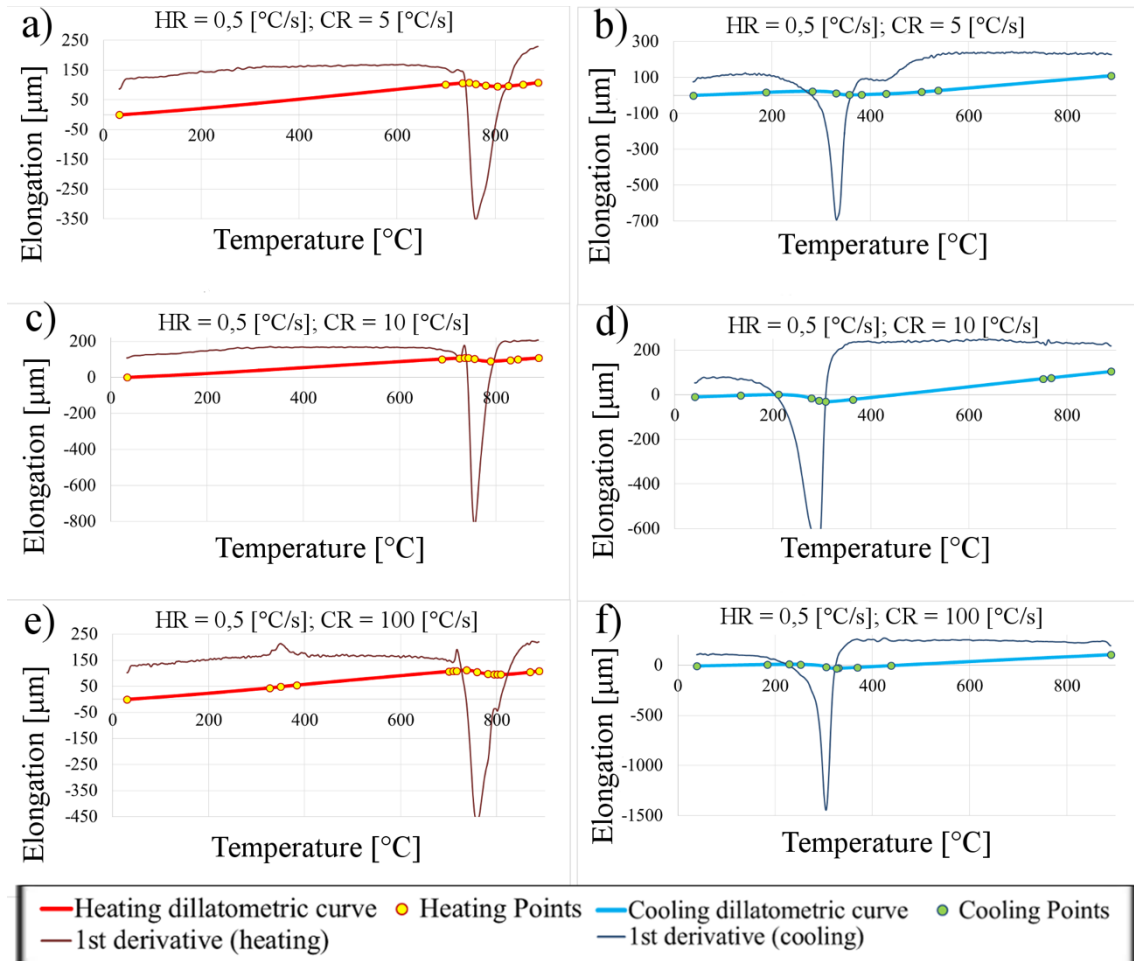
Figure 92 The heating (a, c, e, g) and cooling curves (b, d, f, h) obtained in dilatometric test with corresponding 1st derivative curve indicating the phase transformation peaks, where characteristic points where highlighted. Various cooling rates. HR – heating rate, CR – cooling rate. The presented cooling rates: a), b) 5°C/s, c), d) 10°C/s, e), f) 100°C/s.

It can be seen that each subsequent peak at the derivative curves is moved to lower temperature, except sample 'Points' (*Figure 91*). It is probably caused by the delay of the temperature start transformation together with the increase of the cooling rates, corresponding to Figure 94. The difference between sample 'Points' and the rest of the samples is probably caused by the difference in the grain size. All of the other samples were held just for a couple of minutes at 890°C, while the 'Points' sample were held for 2h at the temperature of 1200°C.

The high grain size relativity of the phenomena in the SA508 gr. 3 steel has been reported [3], [34].
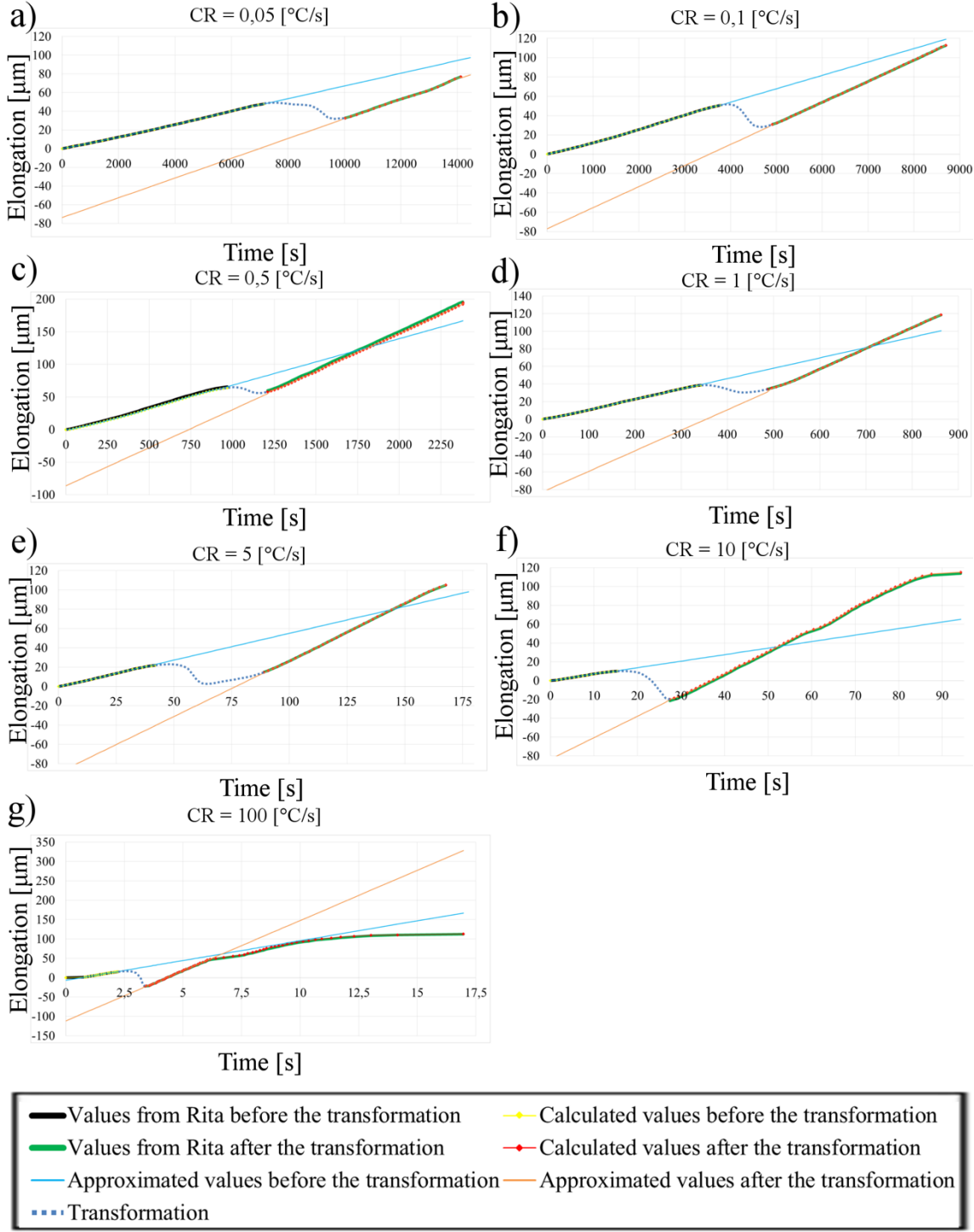
Figure 93 The elongation vs time curves obtained during the dilatometric test with various cooling rate, together with interpolated lines and numerical projection.

The dilatometric curves obtained during the cooling of the sample, together with the numerical projections of these curves, are presented in Figure 93. The projected curves were calculated using the final model of this work, described further in the text. The model used the sets of the thermal expansion/contraction coefficients related to the cooling rate determined in the chapter. Each of the curves was divided into three stages, the first related to the time before the transformation, the transformation itself, and the third related to the time after the transformation. From the elongation values of the first and the third stages, approximations were taken and set in such a way that the lines were created to suggest no change of the thermal expansion/contraction coefficient, as if there was no influence of the phase transformation. Two sets of thermal expansion coefficients were obtained from both of the curves, before and after transformation. These values were used in construction of the phase transformation model described later.
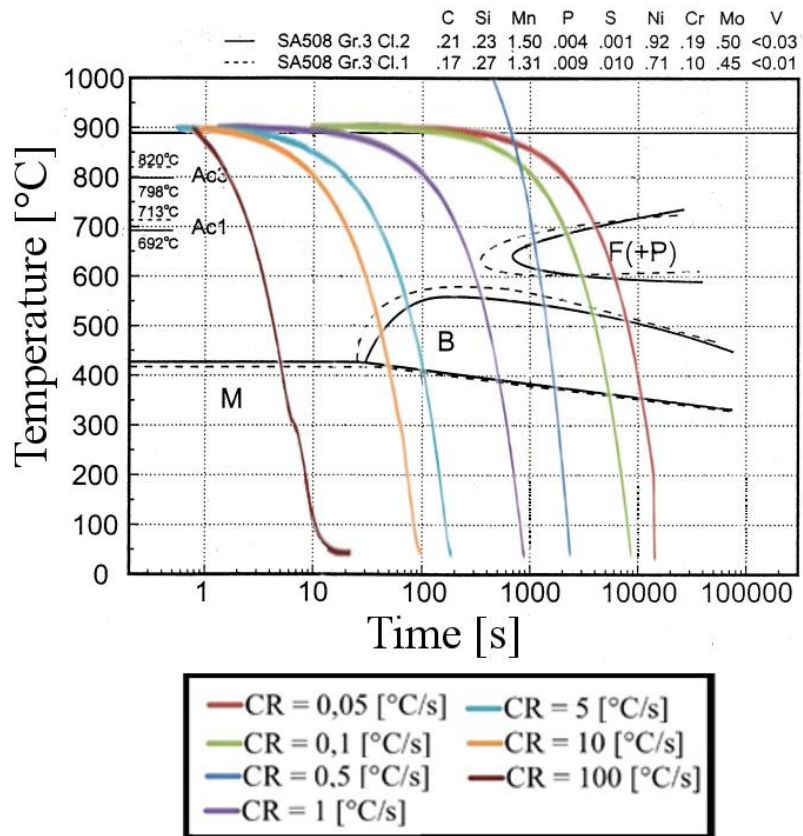
Figure 94 Curves of CCT of the SA508 reactor pressure vessel steel for class 1 (solid) and class 2 (broken) of grade 3 [66].

The cooling curves obtained from the dilatometric test were presented in Figure 94. On the x axis, where the time of the process are shown, a logarithmic scale was used. The curves

were imposed on the CCT diagram, obtained from [66]. The results correspond relatively well with the phase transformation start temperature. Therefore, the peaks on the 1st derivative curves presented earlier (Figure 91, Figure 92) related to the transformation start temperatures are reflecting the temperatures indicated in Figure 94 for the corresponding cooling rate. The microstructures within each of the samples are described in detail in the next paragraphs.

Hardness

Vickers hardness tests were performed on all of the dilatometric samples. The results are presented in Table 37.

Table 37 The results of Vickers hardness test for each of the dilatometric samples, where I – V is the number of measurement:

CR	I	II	III	IV	V	Average
0.05	314.2	286.8	301.3	306.6	291.7	300.1
0.1	331.9	347.5	323.5	326.4	323.8	330.6
0.5	243.7	260.1	231.4	-	-	245.1
1	393.7	503.6	494.6	454.2	474.2	464.1
5	497.8	446.0	451.4	469.9	488.4	470.7
10	659.5	660.4	666.1	678.6	620.0	656.9
100	561.9	594.8	547.4	566.1	548.4	563.7

It can be seen from the results that the hardness increases with an increase of the cooling rate. Except the sample 0.5°C/s, which was the sample 'Points', heated up to the higher temperature (1200°C), this pattern can be seen up to cooling rate CR=10°C/sec, where the hardness suddenly drops. Although this phenomenon is reflected in the degree of microstructure fragmentation, more investigations are needed to achieve a clear explanation.

Microstructures

Figure 95 gives optical micrographs from the dilatometric samples at different cooling rates.
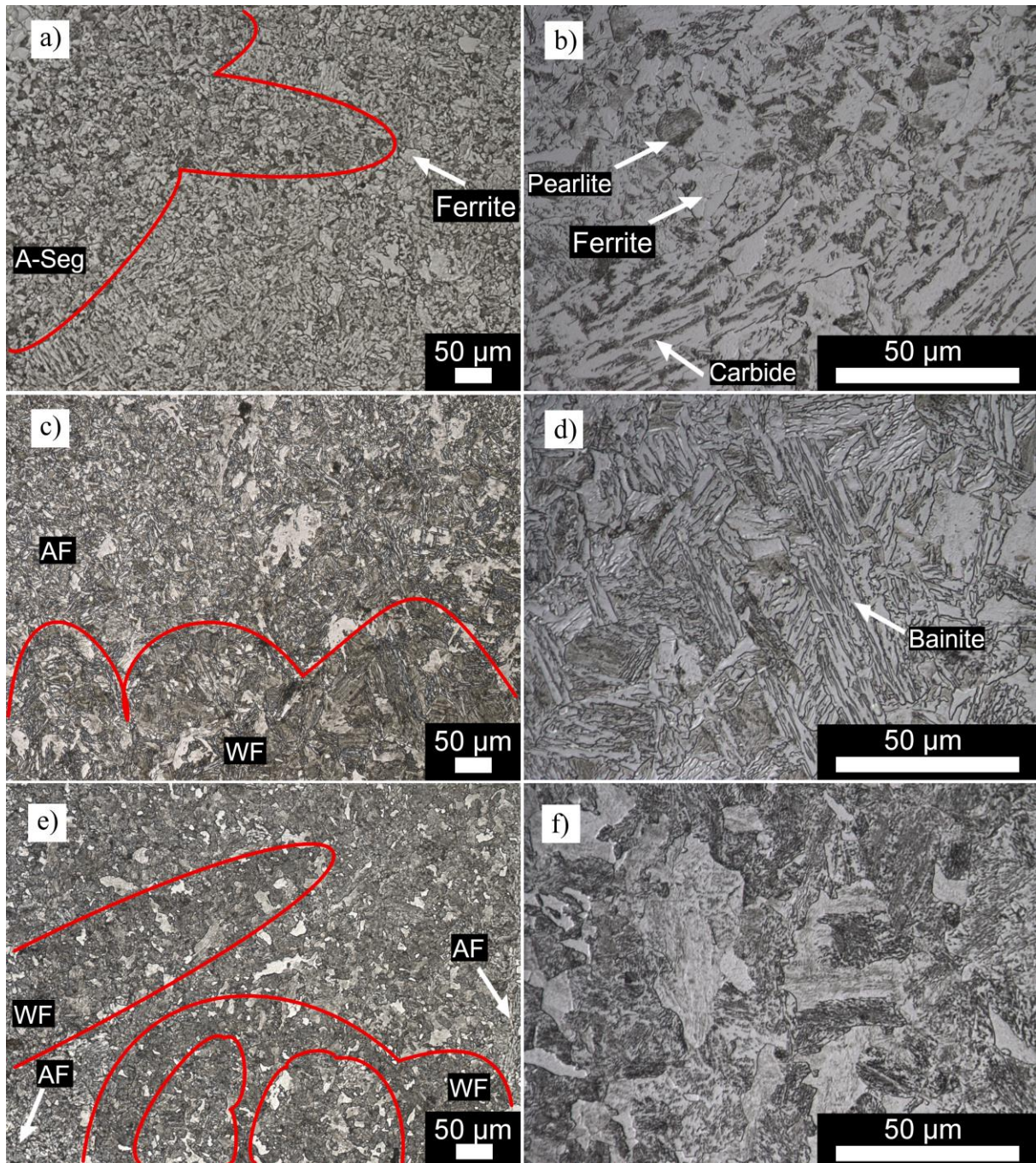
Figure 95 Optical micrographs of dilatometric samples cooled down with cooling rate CR a), b) 0.05°C/s; c), d) 0.1°C/s; e), f) 1°C/s with magnification ×20 and ×100; from different

localizations of the sample. A-seg – A-segregations, AF – Acicular Ferrite, WF – Widmanstätten Ferrite.

Micrographs shown in Figure 95 that with the higher cooling rate the microstructure has a finer grain size. The SA508 gr. 3 steel has a microstructure of mixed Widmanstätten ferrite (WF), allotriomorphic ferrite (AF), martensite and bainite. Although it is possible to distinguish the martensite from the mentioned phases in some of the figures, further microstructure investigations are performed and described later, based on the earlier presented hardness tests (Table 37), dilatometric curves (Figure 91, Figure 92, Figure 93) and the CCT diagram (Figure 94).
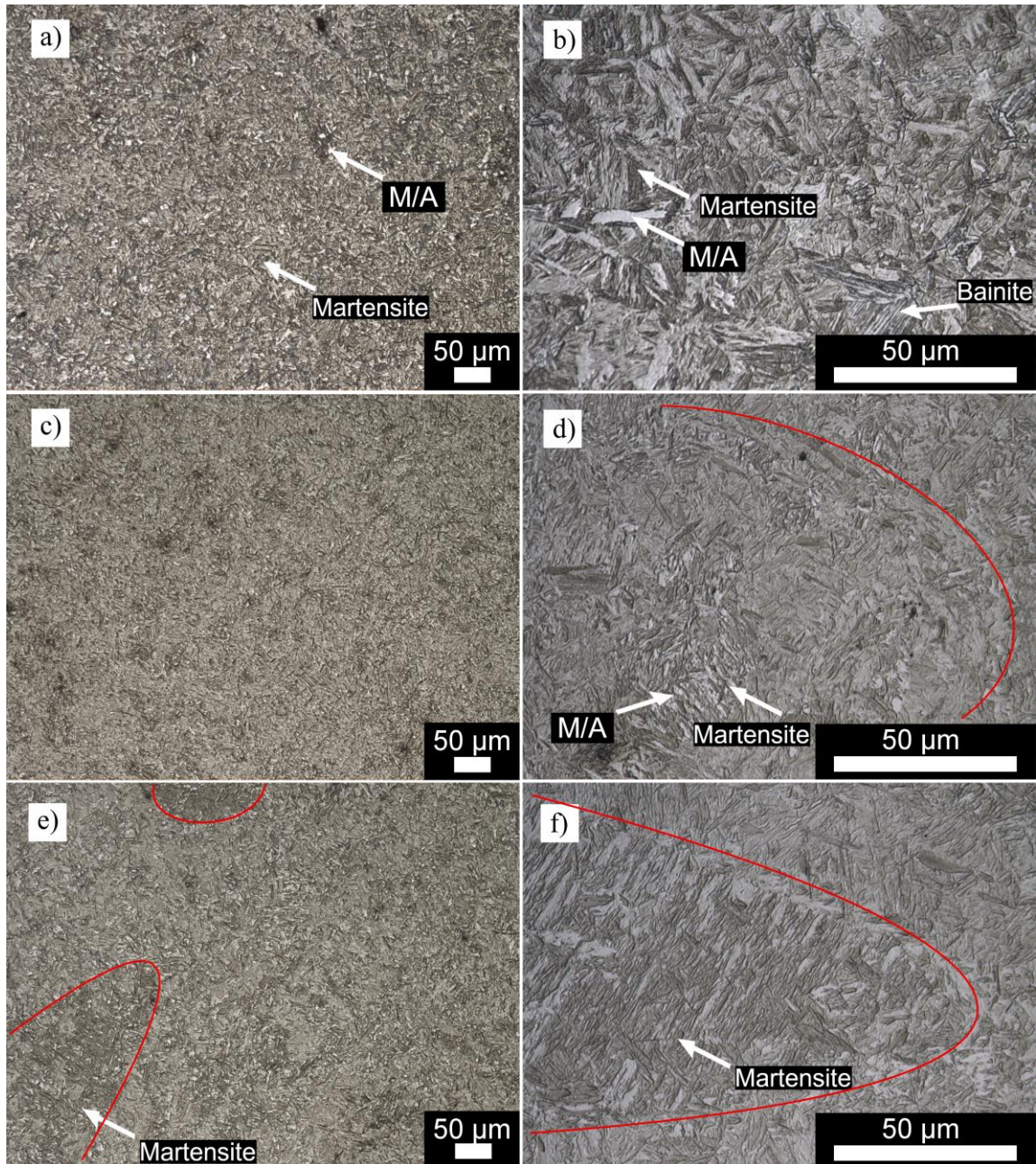
Figure 96 Optical micrographs of dilatometric samples cooled down with cooling rate CR a), b) 5°C/s; c), d) 10°C/s; e), f) 100°C/s with magnification ✕20 and ✕100; from different localizations of the sample. M/A – Martensite/austenite islands.

The optical micrographs were sufficient to characterize the material, presenting most of the typical SA508 gr. 3 steel features. The detailed description of the microstructure formation process, together with the discussion is presented on the basis of the available literature.

The microstructure investigation of the SA508 grade 3 steel is a problematic matter. As it was mentioned, the commonly recognized microstructure in the elements from SA508 grade

3 steel for years was upper bainite and the emphasis was put on the description of the connection between the precipitation mechanism and the mechanical properties [4], [21], [155]–[161]. For example, among many Im [158] and Lee et al. [162] reported the tempered upper bainite structure, which consisted of the bainite ferrite laths with fine needle-shaped carbides of Mo_2C, precipitated during the tempering. Between the ferrite laths the aggregates of the particles of cementite of two shape types could be found: the long rods or the spheres. The length of the rods was dependent of the carbon content as it was formed by the ejection of its particles from the enriched surrounding ferrite lath during the end of bainite transformation [158], [162]. Although it is a very common description of the SA508 grade 3 microstructure it was recently questioned [4], [35], [163]. The material is a mix of martensite, allotriomorphic ferrite, Widmanstätten ferrite and pearlite, the amount of which depends on the chemical composition, the austenite grain size and the cooling rate. Additionally, during casting of the low-alloy steels the relatively high manganese content strongly increases the segregation tendency. Segregation causes the depletion of the alloying elements from some areas simultaneously with enrichment of others. These local variations in chemical composition result in local changes in transformation start temperature and introduce differences in the mechanical properties. The consequences are various and can occur even at the macroscopic distances, such as the type A-segregates (*Figure 95*, *Figure 96*), which are the canals of enriched areas, roughly antiparallel to gravity. During the solidification the interdendritic liquid of the high alloy content moves up through the mushy zone towards the centre of the ingot, due to the thermo-solutal convection, driven by the temperature and composition differences. During such 'climbing' it re-melts the nearby area and leaves alloying element enriched 'trails' inside the material, harder and with less toughness than the surrounding bulk, which due to the scale on which it occurs, cannot be removed by the heat treatment process [35], [163].

The one of the main problems of the large-size elements heat treatment is lack of certainty that the cooling rate at the middle-wall within the element during the quenching process is sufficient to ensure the expected microstructure evolution. The discussion about possible transformation progression was presented by Pickering et al. [35] [163]. His observations were made on samples cut from a 200t casting prepared with the usual RPV's elements treatment and then austenitised at 940°C for 30 min and quenched. A cooling rate 0.1°C/s was chosen as such a value is in the range of the values measured at the middle-wall of thick section of large forgings. During the quenching, when the cooling starts the austenite decomposition begins. The first transformation to occur is the allotriomorphic ferrite at the

temperature range of 700 – 650°C, which forms at the areas slightly depleted in solute due to the segregation, following the nucleation at the grain boundaries. These regions are former-dendrite arms centers, where material was segregated during the solidification. Allotriomorphic ferrite consists around 0.1 – 0.15% of the microstructure, but the higher the start temperature the more of this type of ferrite forms. Then, around 550°C most of the bulk of the material transforms into coarse laths, identified as Widmanstätten ferrite. Pickering indicates that this phase has been incorrectly recognized as upper bainite in the vast majority of previous work, demonstrated by the lack of carbide precipitations when examined in the SEM, which are present in upper bainite. At the dilatometric curve the Widmanstätten ferrite transformation was two-stage, where the highest strain peaks was observed until 500°C and the smaller strains were observed to 400°C. The growth of allotriomorphic and Widmanstätten ferrite cause the rejection of the excess carbon to the untransformed austenite, which lies between them. Such enriched microstructure is then transformed into lower bainite, which can be recognized by the coarse elongated particles of cementite. In the areas of the A-segregates the high alloy enrichment increases the hardenability and deterring Widmanstätten ferrite development, which favors development of the lower bainite interspersed with bright-etched austenite/martensite islands. Allotriomorphic ferrite was not found here at all. At the last stages of the cooling process the remaining austenite is likely to transform into the finer bainite or the martensite or can last as the martensite/austenite island, which were observed between ferrite grains. The end structure can be described as the mix of Widmanstätten ferrite with bands of the allotriomorphic ferrite and lower bainite between them, together with the islands of retained austenite beside the martensite.

The formation of such microstructure is highly connected with the local enrichment in A-segregated areas due to the segregation. Pickering [35], [163] reports that the three important substructures could be distinguished: Widmanstätten ferrite, which had the largest share within the element, characterized by coarse, clean laths; the bands of allotriomorphic ferrite, which formed at the slightly depleted from solute, compared to the Widmanstätten ferrite; and the fine and dark etched A-segregates, which were enriched in alloying elements and consisted of mix of the various phases like finer lower bainite, partially twinned martensite and retained austenite. As the A-segregates are the after-effects of the 'climbing route' of the segregated area within the solidifying material, it can goes even for a hundreds of μm. The carbides precipitation can be found inside their grains, which are uneven in size, but finer in comparison to the Widmanstätten ferrite, which often lays aside, together with the allotriomorphic ferrite, creating

some kind of transition channel within the bulk. The carbides precipitation inside the allotriomorphic ferrite grains had a very similar look to the one found in the Widmanstätten ferrite, but with further investigations were identified as part of the lower-bainite microstructure. The characteristic form for the A-segregates are the bright etched blocks of the austenite/martensite, which can be also founded in the rest of the microstructure, but in the significantly smaller amounts. Electron microscopy revealed that these blocks contain elements like nickel or molybdenum and can be found decomposed into very fine bainite, visible at higher resolution. Also, it should be noted that the circle shaped MnS and mixed oxide inclusions of various, sometimes relatively big, sizes, were reported within the whole specimens.

The tempering process has a significant impact on the microstructure of the RPV elements. Tempering causes a decrease in dislocation density and carbide coarsening, especially in areas, where the carbides amount is high, like in between the allotriomorphic and Widmanstätten ferrites. This leads to a reduction in toughness. There is also a loss in strength due to the blocks of austenite/martensite being decomposed into ferrite and cementite. Tempering causes coarsening of cementite during longer tempering, particularly in A-segregates, where there is a higher tendency to carbides formation due to the manganese, nickel and molybdenum presence.

The formation of channels with different microstructure leads to a reduction in mechanical properties such as decreased toughness. Pickering suggests that, based on the similarity to the wrought steels case, the cooling rate after heat treatment should be kept in the range 0.2 – 0.4°C/s. Such values are sufficient to achieve a finer microstructure, free of allotriomorphic ferrite, with more austenite/martensite islands. Although it seems reasonable, maintaining of high enough cooling rates within the thick sections of the SA508 grade 3 elements is the primary problem [35], [163].

A quite detailed description of the welded microstructure is presented in the literature related. This is because the welding process is critical to the designing of RPVs components. During welding the hot joint metal raises the temperature of the material around the weld to transform it to austenite. On subsequent cooling, the cooling rate of the weld and the surrounding material depends on the distance from the weld. On transformation from austenite a whole spectrum of phases are formed in the Heat Affected Zone (HAZ). The common approach is to use the dilatometric test on the various sample with different cooling rate to predict the microstructure changes, which is the same approach as used here.

During cooling after welding different microstructural areas can be distinguished in the HAZ in order from the lowest to highest temperature experienced, namely: the intercritical or partially austenitised (IC); the fine grained (FG); the coarse grained (CG); and the fusion zone [97], [99], [102], [105], [157]. All of these locations are presented in Figure 97, which was obtained from [97] as an example of SA508 gr. 3 microstructure investigations. In [97] the residual stress due to the welding process applied on the SA508 gr. 3 steel was investigated. The samples were subjected to stress relief heat treatment before welding (Figure 97b). In Figure 97c the microstructure of the intercritical region is presented, which constituents a white, weaker etched regions of untransformed ferrite, which was not austenitised during the thermal welding cycle, and the stronger etched dark regions, which are believed to be pearlite, bainite or mix of martensite and austenite. During the thermal welding cycle the austenitisation of these regions caused enrichment in carbon, which increased their hardenability. The intercritical zone represents the boundary of the HAZ and the rest of the material.
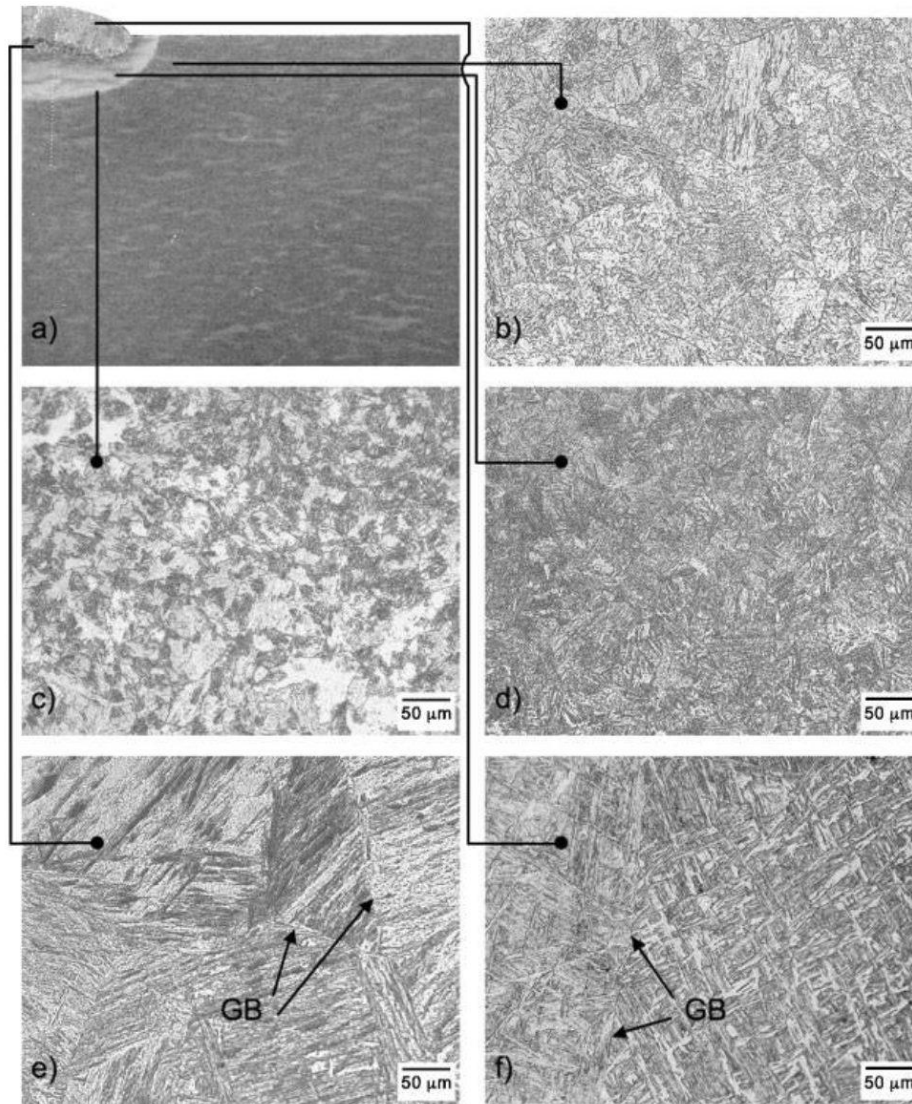
Figure 97 Microstructures of the HAZ due to the welding process in SA508 gr. 3 steel. a) the whole sample, b) typical stress-relieved area, c) ICHAZ, d) FGHAZ, e) CGHAZ, f) fusion zone. GB – former grain boundaries of austenite [97].

In the fine grained and coarse grained zones the temperature was high enough to cause the full austenitisation (Figure 97d and e), and subsequent cooling results in a mix of the bainite and martensite, with the former being preferred. In Figure 97e the weaker etched regions are believed to be martensite or retained austenite and the stronger etched are plates of bainite with carbon rich regions [97]. According to [99] the carbides precipitate mostly along prior austenite grain boundaries. In both zones the peak temperature is high enough to cause the growth of the grains, but only in CGHAZ is it sufficient to dissolve the carbides, which inhibit grain growth, what results in the difference in the grains size. According to Mark et al. [105] approximate temperatures corresponding to the zones CGHAZ, FGHAZ and ICHAZ during the welding are

in range 1500°C – 1100°C, 1100°C – 790°C and 790°C – 670°C, respectively. These values correspond to the temperatures at which AlC precipitates are believed to dissolve, according to Pous-Romero [4]. Kim et al. in [99] reported the presence of rod-type intergranular particles, which were identified by SEM investigations. Figure 97f shows the fusion zone, where the intragranular nucleated acicular ferrite can be identified from the typical interwoven microstructure of elongated ferrite grains. In Figure 97e and Figure 97f the former austenite grain boundaries are highlighted [97], [99], [105], [157].

This microstructural evolution of the SA508 grade 3 steel was used to describe and analyze the optical micrographs obtained from dilatometric samples in this work. All seven dilatometric samples cooled with various cooling rates were sorted into groups related to their cooling rates, which were shown on the CCT diagram in Figure 94. The following microstructural analysis describes the curves by these groups. The data used for the microstructure description are taken from the CCT diagram (Figure 94), the dilatometric cooling curves together with their 1st derivatives (Figure 91, Figure 92, Figure 93), the micrographs (Figure 95, Figure 96) and the hardness values (Table 37). However, these considerations are based on optical microscopy and electron microscopy would have been required to give definitive statements, but this was not possible during the pandemic.

The curves cooled with CR=0.05°C/s and CR=0.1°C/s, Figure 94, created mix of phases that should contain ferrite, pearlite and bainite. The pearlite and ferrite transformations should start around 700 – 650°C and bainite around 550°C due to the diagram. Some typical structures were seen for CR=0.05°C/s such as allotriomorphic and Widmanstätten ferrite and pearlite, visible in Figure 95b). The structure that appears to arise from A-segregation is highlighted in Figure 95a). This region is darker, probably arising from the high enrichment in elements, resulting in finer grains. These could be the bainite structures, which form inside the A-segregates channels separating them from the bulk of Widmanstätten ferrite. Figure 95c) and d) presents the optical micrographs of the CR=0.1°C/s sample. On the lower magnification (Figure 95c) the clear A-segregate channel of fine grains with coarse carbides are visible, where the finer structure is probably allotriomorphic ferrite and the coarse structure at the bottom is Widmanstätten ferrite, clearly visible in Figure 97d).

The first strain peak on the CR=0.05°C/s dilatometric curve (Figure 91) can be related to pearlite transformation, due to CCT diagram, but it is also the temperature of the allotriomorphic ferrite, which is component of the A-Segregates. It starts around 730°C and

ends around 600°C. The second dilatometric peak on the same curve starts around 550°C, which correspond with the formation of Widmanstätten ferrite, indicated by Pickering [35], [163]. The characteristic two-staged shape can be visible, with the 'break' around 500°C. As the transformation extends to very low temperatures, around 370°C, there is probability that the bainite could form at the last stages.

The first large dilatometric peak of the phase transformation on the CR=0.1°C/s sample dilatometric curve appears at the temperature of 540°C and it consists of two disturbances, around 460°C and 435°C (Figure 91). These values correspond again with Widmanstätten transformation. It is puzzling that there is only transformation event on the curve, where on the micrographs (Figure 95) there can be seen a very large inhomogeneity of the microstructure, which is a mix of many phases. On the other hand, the peak is very deep, which suggest overlapping of the different transformation peaks, which could be observed on the micrographs.

The difference between the hardness of these samples at different cooling rates, Table 37, is relatively small (HV=300.1 and HV=330.6). The sample with higher cooling rate (CR=0.1°C/s) has higher hardness value, which is probably a result of the lower amount of the pearlite or the greater amount of the bainite.

The next sample was cooled down with the CR=0.5°C/s (Figure 91). This sample differs from the others as it was obtained from the sample 'Points', which was heated to 1200°C and held for 2h. Such a high temperature, together with the relatively long holding time, caused the drastic lowering of the hardness value. This is probably caused by the dissolution of the AlN particles and extensive grain growth. Although the large grain size decreases the yield strength of the SA508 gr. 3 [3] due to the Hall-Petch relation (4) [164], [165], it provides higher creep resistance [166], which can be crucial for the components that work for a very long time under high stress and at high temperatures. To prevent excessive grain growth, time and temperature of the heating stage have to be precisely controlled. The expected characteristic temperature points are typical (Figure 94). However, at 790°C there is a large strain peak, probably allotriomorphic transformation, which ends around 700°C. The next peak was probably due to the Widmanstätten ferrite formation, and lasts from 700°C – 400°C, so probably overlapped the bainitic transformation.

The CCT diagram suggests the sample cooled down with CR=1°C/s should contain ferrite, bainite and martensite. The ferrite transformation should start around 700 − 600°C, the bainite transformation around 550°C, which confirmed by Francis in [66]. The cooling rate

could be high enough to start the martensite transformation around 400°, which also indicates the relatively high hardness value. In this sample the highest fluctuations of the microstructure hardness test results can be observed, probably caused by the presence of a mixture of many phases, grouped in relatively large to the bulk of the sample, clusters. The highest difference between the hardest and softest location is reaching even up to HV=109.9. The 1st derivative curve calculated from the dilatometric curve indicates the transformations at the temperature are around 700°C and from 650°C to almost 200°C. Also, the curve cannot be described as flat until the end of the cooling. Figure 95e) and f) present the microstructure of the sample with lower and higher magnification obtained by optical microscopy, which shows that the microstructure is far from homogeneous. Coarse carbides inside the laths indicate upper bainite or Widmanstätten ferrite. The segregation channels, as it can be seen in Figure 95e) take rather complicated routes, where the allotriomorphic ferrite seems to be in much lower amount.

The CCT (*Figure 94*) indicates that in the samples of CR=5°C/s and CR=10°C/s (Figure 96) bainite and martensite should be present, while in the last sample, cooled down with the highest cooling rate CR=100°C/s, only the martensite should be present. The microstructure of the CR=5°C/s sample in Figure 96a) and b) showed many white areas scattered within the field. They are also visible in significantly lower number in the microstructure of the CR=10°C/s sample and in the CR=100°C/s, but the hue is darker. These could be the M/A regions as this structure appears at the higher cooling rates in Figure 96c) – f). The bulk is probably the mix of Widmanstätten ferrite and lower bainite, but with significant presence of the martensite, but until the highest cooling rate the presence of the segregation effects can be seen. The A-segregates are characterised by the high enrichment in alloy elements, which increase hardenability. This could indicate that the sheaf of darker material highlighted in Figure 96e) – f) is martensitic. There can be observed some kind of transformation for the sample CR=5°C/s at the temperature range of 540 – 390°C. There is no evidence of such transformation on the dilatometric curve of the samples with higher cooling rate, like CR=10°C/s and CR=100°C/s. Looking at the dilatometric curves in Figure 92 the relatively high hardness values of these samples and the low temperature values of the phase transformation together with the similar microstructures indicate the fully martensite presence.

4.3. Model validation

The main purpose of this part of the work is to present the experimental results which were used to develop the numerical model able to predict the differences in local dimensions resulting from the transient temperature field and the phase transformation occurring in the forged part under the specific heat treatment conditions. The model was applied to estimate the differences in local volumes of the material, where the calculations were based on the differences in cooling rates at the nodes, during the heat treatment process. In the first part of the work the transient temperature field of the forging during cooling process was calculated. The temperature values from the reference points were compared with the corresponding experimental results obtained by Al-Bermani et al. [167]. The results from the modelling were in good agreement with the experimental ones, which shows that the model is able to predict the transient temperature field under conditions similar to those observed in the industrial process. The calculated cooling rates at certain points within the model were then compared with the results obtained from the model developed in [167]. The results were presented in the text and discussed. In the second part of the work the changes of the dimensions of the forging resulted from the phase transformation during cooling process were calculated using the developed code. The results were compared with the dimensions of the forging obtained from the industrial process [167]. The obtained results were presented and discussed. The accuracy of the prediction abilities of the model were then evaluated.

For the modelling, the experiment described in [167] was used. The forged 95-tonne disc shaped part was subjected to the defined heat treatment cycle. The steel used was SA508 gr. 3. The dimensions of the part are presented in Figure 99. The temperature was measured using four thermocouples embedded in the surfaces of the forging (two at the top and two at the bottom surface) and four additional thermocouples embedded below the surfaces at 75 mm depth, at the locations shown in Figure 98. Surface thermocouples were positioned at 0°, 90°, 180° and 270° clock positions, at the periphery of the disc shaped forging. From these four values, the average was calculated and used as the input temperature in the developed finite element (FE) model. The data acquired from the subsurface thermocouples were compared with the temperature obtained from the corresponding points in the numerical model. The obtained experimental and modelling results have shown good agreement indicating both the correct

formulation of the numerical problem and good predictive abilities of the model for calculation of the transient temperature fields.
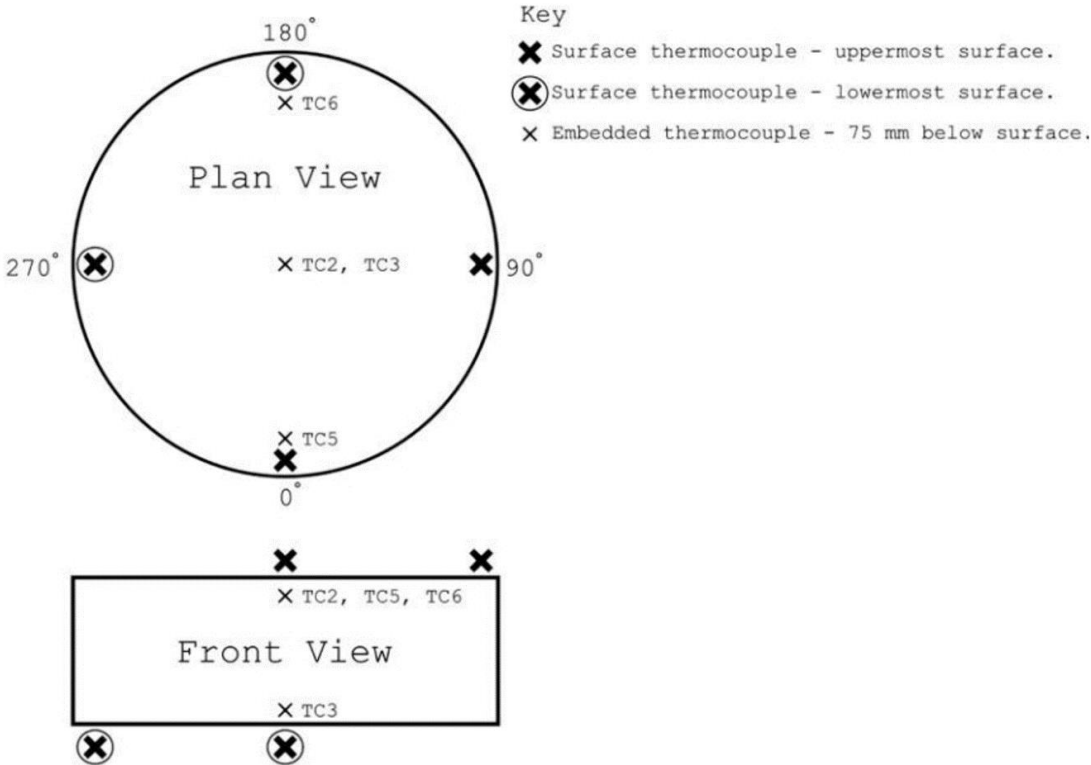
Figure 98 Schematic representation of the thermocouple locations during the heat treatment, namely on and under the surface at 75 mm depth. Peripheral subsurface thermocouples have been offset inboard for clarity [167].

Additionally, the thermal history of the forging was obtained from the following reference points: first, at the quarter thickness depth from the top of the surface and second, at the mid-wall depth of the forging. Both points were located on the y-axis in the middle of the forging (Figure 100). For these points the cooling rates were determined in specific range, from 800°C to 600°C (labelled as t_{86} cooling rate). These cooling rates were further used in [167] as input boundary conditions in the performed experiment. The presented results were used for comparison between the numerical ones obtained from the described model.

The specific geometry was applied in the model, reflecting the rectilinear 2D profile machined out of the forging before the heat treatment (Figure 99). In this profile all of the angles between faces were 90° (ignoring the radii of the fillets in the corners). After the heat treatment these angles were changed as a result of stresses induced during the heat treatment. In the second part of this work, the values of the angles obtained after the heat treatment in the real industrial

172

conditions were compared with the corresponding results obtained using the developed numerical model. The level of the disagreement between both sets of the angles were used as the quality determinant for the prediction ability of the developed model.

4.4. Numerical modelling

A half of the axisymmetric section, shown in Figure 99, represents the 2D geometry of the forged part, which was subjected to rapid cooling, from 890°C to ~10°C during 26580 seconds (7h 23min). The material parameters for steel SA508 gr. 3 were used and the dependence of high temperatures was included according to [168]. The dimensions of the forging were presented in Figure 99.
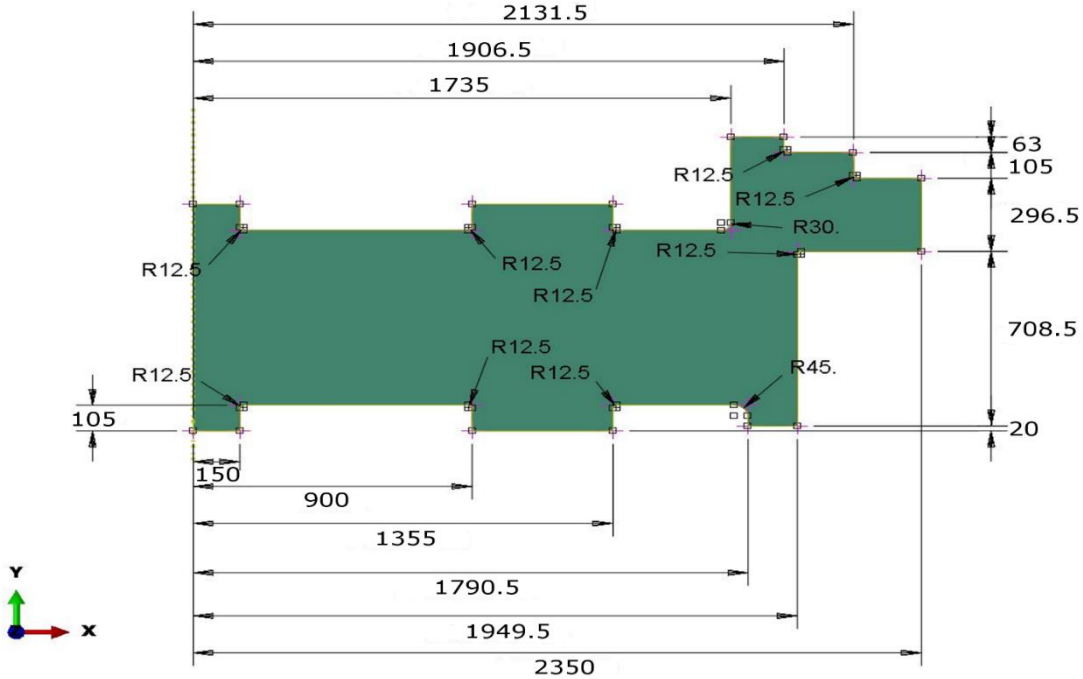
Figure 99 Geometry of the half of section of the forging.

The austenitisation temperature in the model at the beginning of the cooling process was assumed to be 890°C. The cooling was described as a change of the temperature in time at the outer edges of the model. The exact temperature was an average value of the temperatures of four thermocouples attached to the surfaces of the forging obtained by Al-Bermani et al. [167].

The x-axis symmetry was assumed due to the relatively large dimensions of the forging. One node of the FE model was constrained in y direction (U2=0). All the described boundary conditions were schematically presented in Figure 100. The linear quadrilateral and linear triangular finite elements were used. Two types of mesh with different density of the elements were applied for the calculations.

4.5. Results and discussion

4.5.1. Transient temperature field
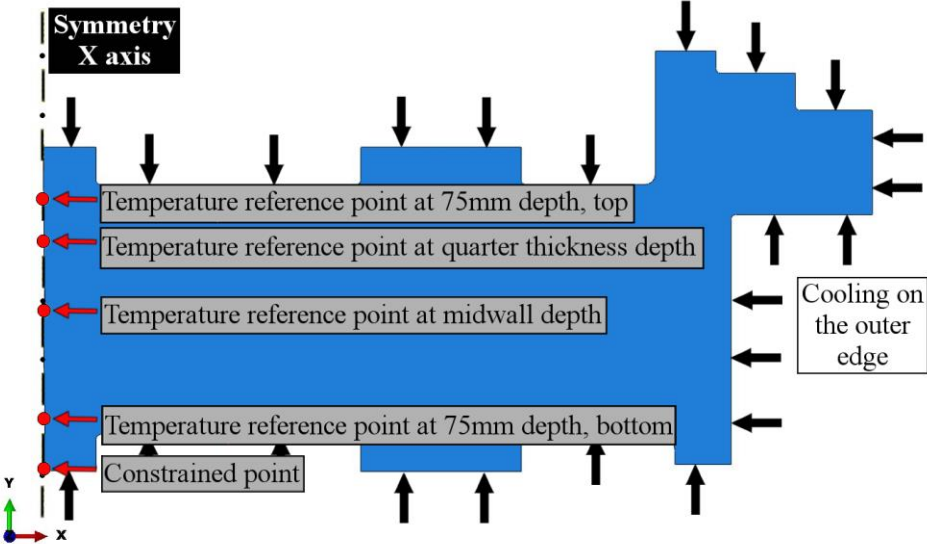
Figure 100 Boundary conditions in the developed model.

As the calculations of the changes in local material volume during the heat treatment were based on the cooling rate at the nodes, the prediction of the transient temperature field within the model was crucial for further analysis. In the modelling, a temperature drop from 890°C to approximately 10°C at a given time had been applied at the edges. The calculated temperatures located at the reference points placed at 75 mm depth under the top and bottom surfaces at the symmetry x axis are presented in Figure 101 along with the experimental results taken from [167] for comparison.

174

a) Temperature at near the top surface b) Temperature at near the bottom surface
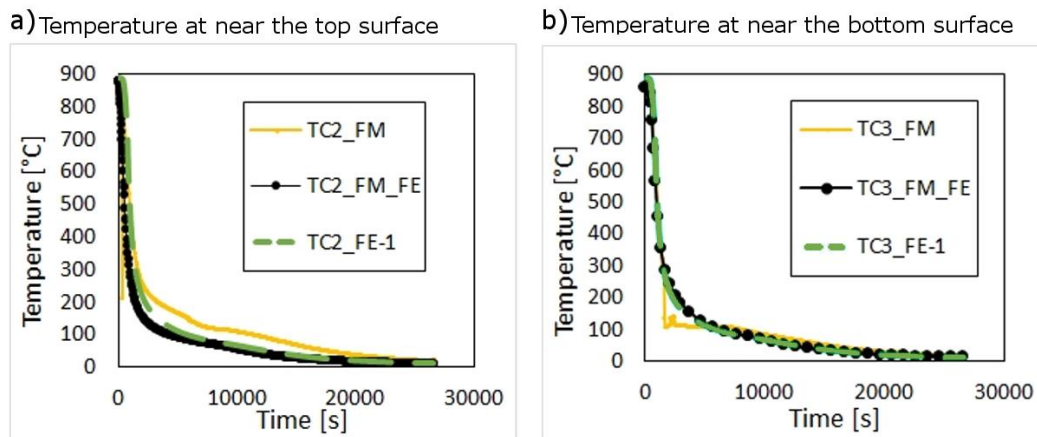
Figure 101 The changing in time temperature recorded during the experiment at the 75 mm depth, TC_FM and the corresponding temperatures predicted using both FE models developed in [1], TC_FM_FE, and in this work, TC_FE-1, are shown for the following areas of the following areas of the forging: a) TC2 – the top area and b) TC3 – the bottom area.

The yellow lines, labelled as TCx FM, are the temperatures during cooling registered with thermocouples embedded at the subsurface of the forging at the 75 mm depth from the surface. The black dotted lines, labelled as TCx_FM_FE, are the temperatures at the same positions calculated using the numerical model developed in [167]. The green dashed lines, labelled as TCx_FE-1, are the temperatures calculated using the numerical model developed in this work. It can be seen that the temperatures predicted by the author are slightly closer to the temperature recorded in the industrial process in both cases, at the top and at the bottom of the model geometry (Figure 101a and Figure 101b respectively), compared to the results obtained in the model in [167].

The transient temperature fields for the different stages of the process were presented in Figure 102. It can be seen that due to the large dimensions of the model, after relatively long period of time (>20min), around 90% of the whole element has a temperature still near to the initial one (Figure 102a). In such a situation, stresses between cooled and the regions that are still hot can easily rise to the yield stress. These areas are located typically between the fast cooled edges and the middle of the forging. The most rapid temperature change occurred in the relatively short time compared to the time of the whole process. As it can be seen in Figure 102b, after one quarter time of the process, there is no near-initial temperature areas. Although the flange is already cooled at that time, most of the regions have temperature values around

500°C, while the small hot core was ~700°C. After a similar amount further time, at around half of a process (Figure 102c), the edges of the part were completely cooled down and the core of the forging was at approximately 200°C. During the rest of a process, the temperature dropped from 200°C to ~10°C.
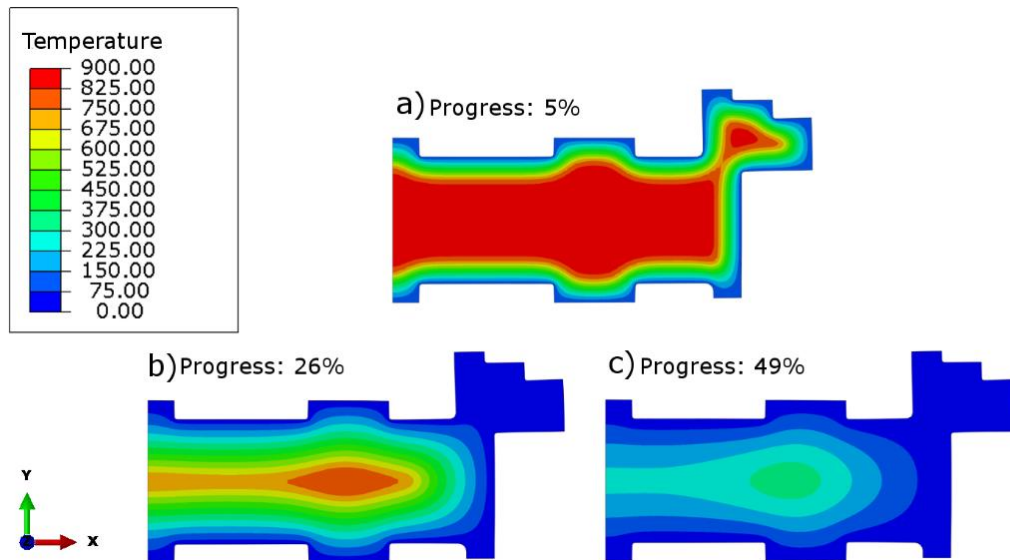
Figure 102 The transient temperature field predicted for the different time moments from the beginning of the process: a) 1350s; b) 7000s and c) 13000s.

The predicted cooling rates at the reference points in the mid-wall and at the quarter thickness of the forging were compared with numerical results from [167] in Figure 103. According to [167], the details of austenitisation process were commercially sensitive, although the predicted thermal profiles at these reference points can give sufficient insight into the process. The cooling rates calculated for various areas of the model were crucial for the prediction of the microstructure evolution during the heat treatment.

The predicted cooling rates from [167] were calculated as 3.5 and 5.8 °C min^{-1} for the mid-wall and quarter thickness positions respectively. The corresponding values predicted using the model developed in this work were 6.2 and 14.1°C min^{-1} for the same positions. It can be seen that the cooling rates predicted in this work were approximately 2 times higher than those predicted in [167]. This can be related to the temperature differences presented in Figure 101, which suggests that the transient temperature field within the whole part can vary from that calculated in [167]. In [167], the obtained cooling rates and the temperature values were used as the input for cooling of two samples cut from the same forging during machining. Then, their microstructures were compared with the samples cut from the reference areas in the forging.
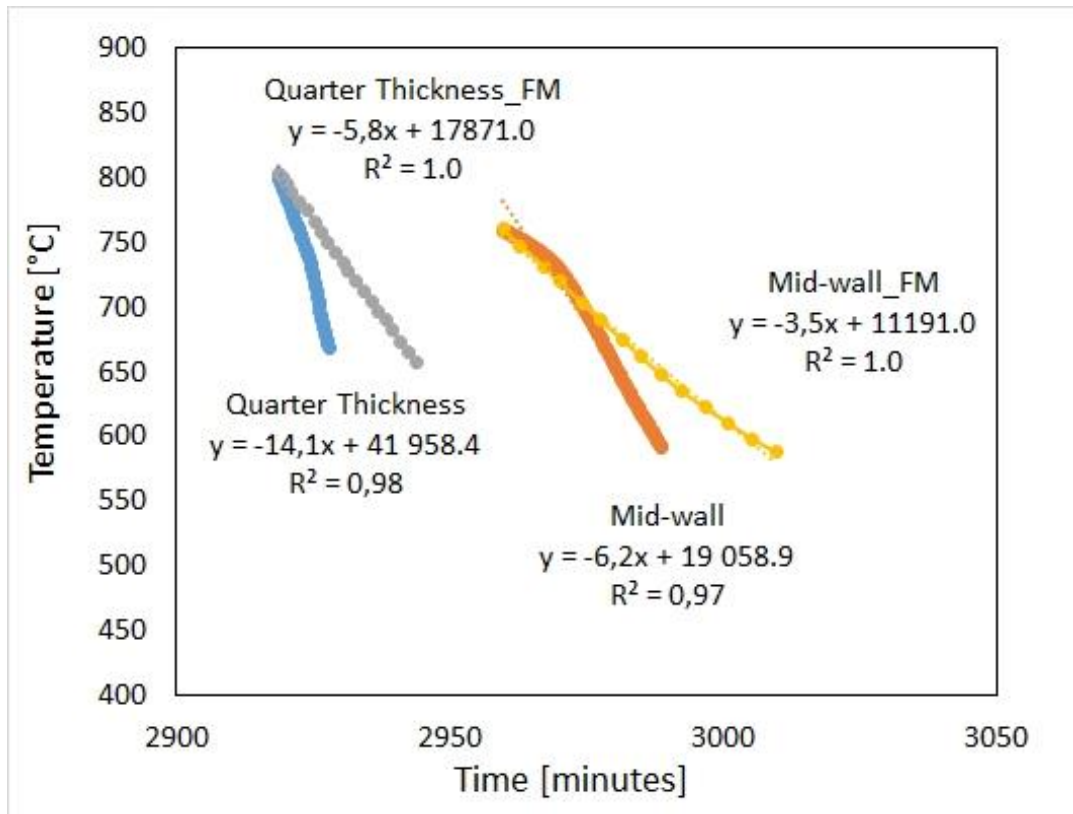
Figure 103 Predicted t_{86} cooling rates located on y-axis of the forging, at quarter thickness and mid-wall positions; curves calculated in model from [167], grey and yellow, are marked 'FM'; curves calculated in the developed in this work model are blue and orange. Equations and R^2 values for linear trend lines adjacent to each cooling curve.

4.5.2. Mesh shapes

Due to the large dimensions of the model the different types of meshing were tested. Among many the following two were presented in Figure 104.
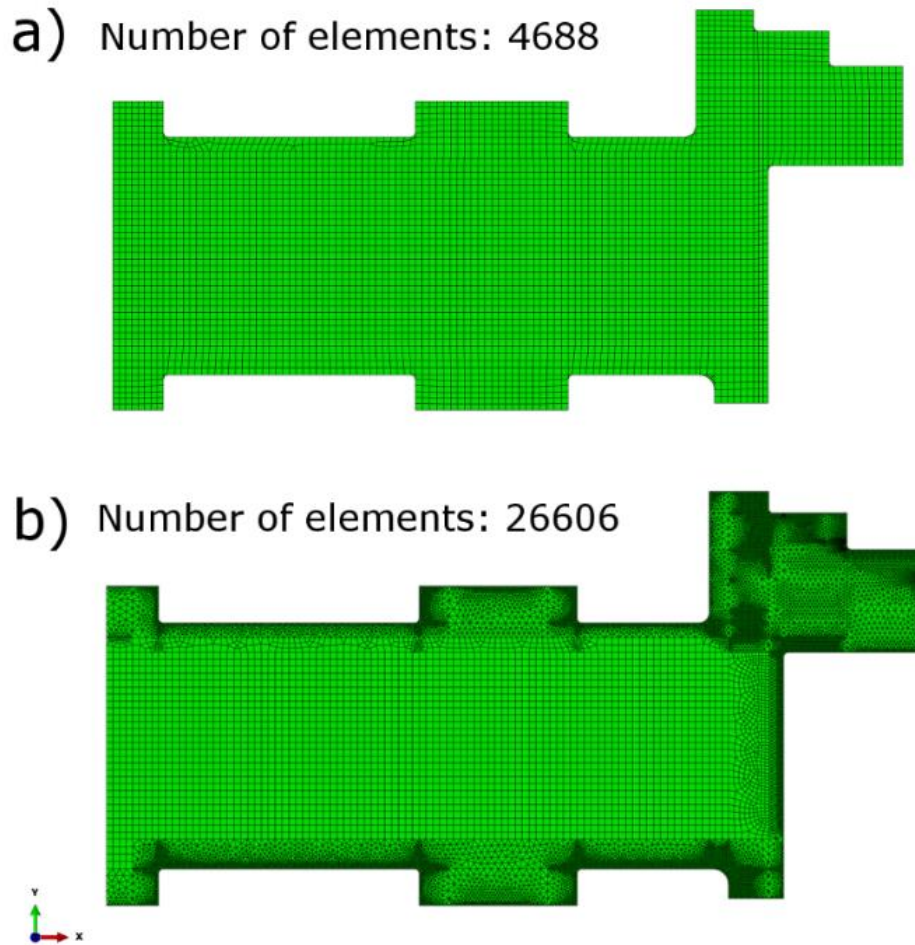
Figure 104 Different types of meshes tested in the model.

The element types used were a 4-node axisymmetric thermally coupled quadrilateral and 3-node thermally coupled axisymmetric triangle. The coarse mesh shown in Figure 104a is characterized by a very few triangle elements in the region of interests and general domination of the quadrilateral elements within the rest of the model. In the second case (Figure 104b), the finer mesh built from triangle elements was imposed at the vicinity of the areas near the edges, where the temperature boundary conditions were applied, and also near the corners, where the measurements of angles were performed further in the work.

The impact of the mesh complexity was investigated during calculations of the temperature, stress and strain intensity distributions. Although the significant differences between the consecutive stages of the process were observed in the stress distribution (Figure 105), it can be seen that the dependence of the obtained results on the mesh complexity is relatively low for the number of the used elements.
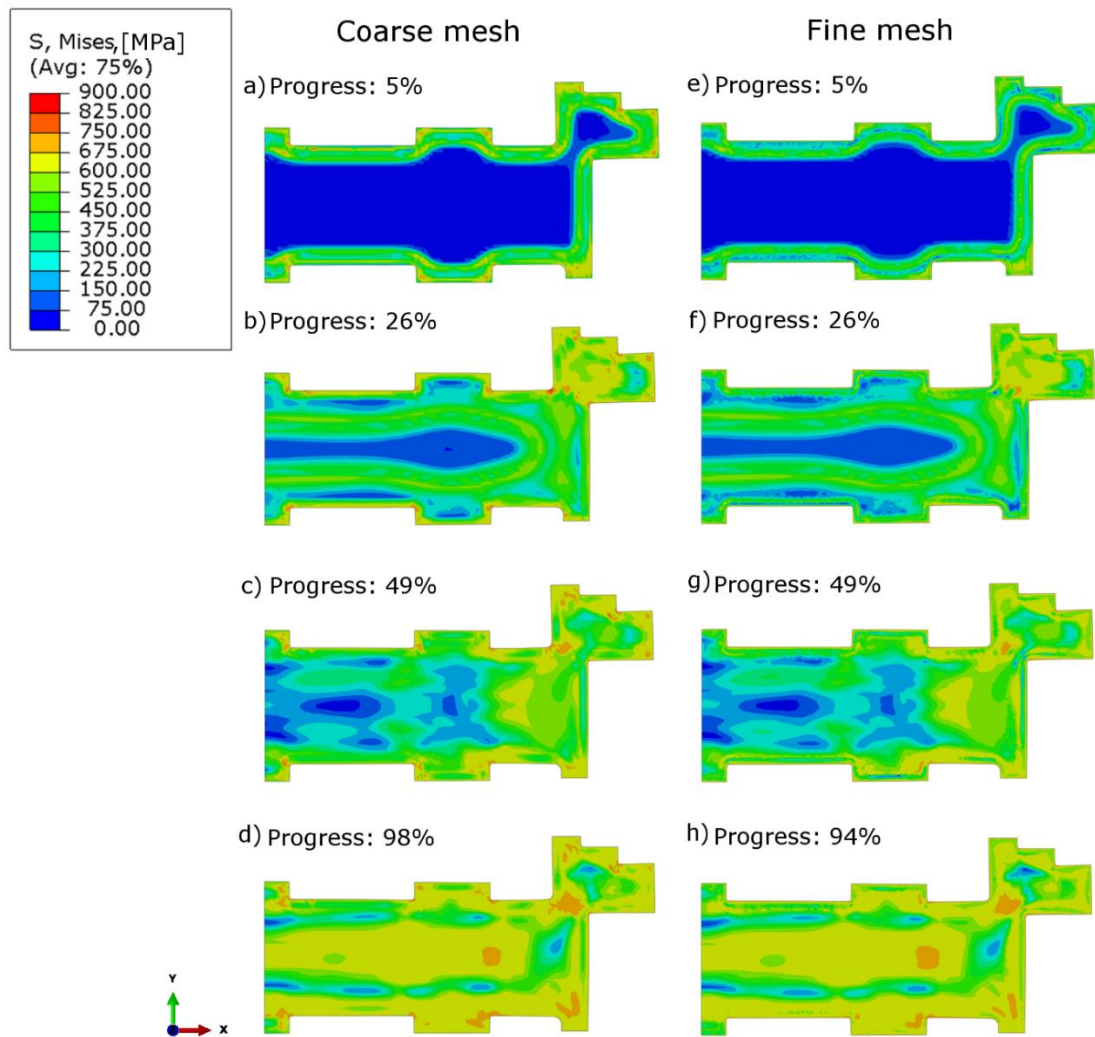
Figure 105 The stress distribution obtained from the numerical analysis using the coarse mesh [a), b), c), d)] and using the fine mesh [e), f), g), h)] for the various stages of the cooling process.

Although the level of stress is not large in the scale of the whole part, the higher values mostly occurred in the areas near the surface and in the corners, which are critical. These regions were often a border between areas of a relatively large temperature differences and could influence the angles values which measurement were performed and presented further in the text. It could be seen that the highest stresses occurred at the end of the process, as shown in Figure 105d and Figure 105h. Although the highest values of the stress were calculated in the corners applying the model with coarse mesh, the finer mesh in these regions seemed to scatter these concentrated strains. Diversion of the mesh size for the same boundary conditions in the process allows calculation time to be saved and for better quality of the results in the regions of interest, as the finer mesh indicates the higher resolution of the stress distribution.

The strain intensity distribution was presented in Figure 106.
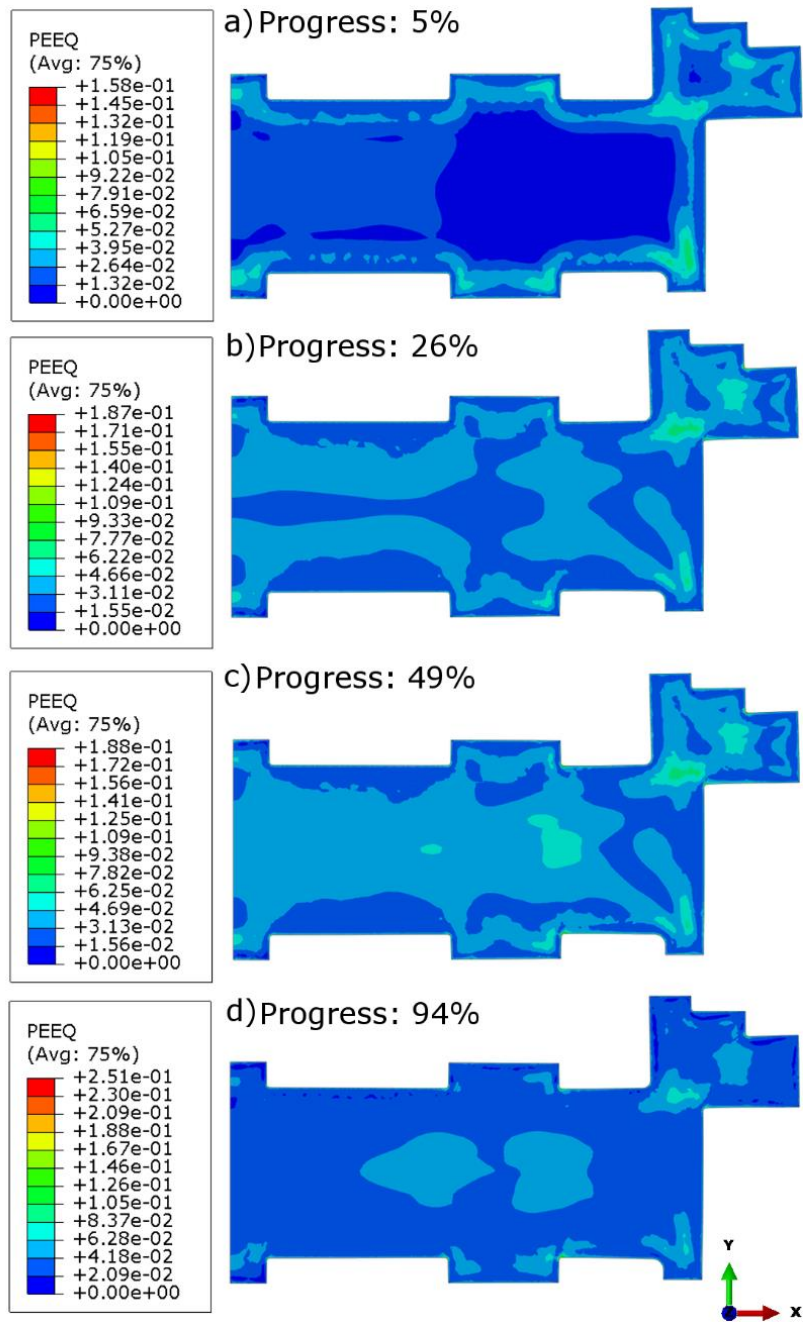
Figure 106 The strain intensity distribution in the model with the fine mesh for the various stages of the cooling process.

The border minimal and maximum values on the legend were user-defined for every presented step for stronger emphasis of the differences appearing between the particular stages of the cooling process. The highest strains are present at the very end of the process and were probably caused by the progressing shrinkage of the volume, which was caused by local thermal expansion difference between the areas of a different temperature within the model. This region

was in the neck between the greatest bulk of the forging and the outer flange. The higher values of strain intensity are also present near the edges and corners, which were the areas of interests due to the angular measurements in these positions, presented further in the text.

4.5.3. Phase transformation model

The main purpose of this part of the work was to develop the model which could be able to predict the changes in material volume due to the transient temperature field and locally occurring phase transformation. The developed model calculates the heat exchange between the set temperature change in time at its edges and between its insides, estimating the cooling rates at every node in the model, at every moment. Based on the temperature and the cooling rate, the model sets the relevant temporary thermal expansion coefficient, obtained through the previously performed dilatometric experiments. These experiments were conducted to investigate the behaviour of the material during cooling under specific conditions to obtain the dilatometric curve. The dilatometric tests were performed with the following cooling rates: 0.05°C/s, 0.1°C/s, 0.5°C/s, 1°C/s, 5°C/s, 10°C/s and 100°C/s. The obtained curves were translated to sets of thermal expansion coefficients, related to the temperature and cooling rate. Such an approach allows for prediction of the change in the volume at the small areas with the similar temperature and cooling rate and takes into account the dilatometric shape phenomena, which occur due to the phase transformation.

To validate the model predictive abilities the author used the conditions of the industry process, described in detail in [167]. The mentioned earlier rectilinear machined profile has been subjected to quenching and tempering cycle, known collectively as a quality heat treatment cycle. All of the angles between flat and cylindrical faces in the profile were machined out to be 90°. After the heat treatment the distortions caused by the stress increased due to the uneven transient temperature field and phase transformation, which changed the dimensions of the angles. The developed model was set up under conditions similar to those presented in [167] to calculate dimensions after the cooling process of the forging.

For clarity, the angles were numbered as shown in Figure 107.
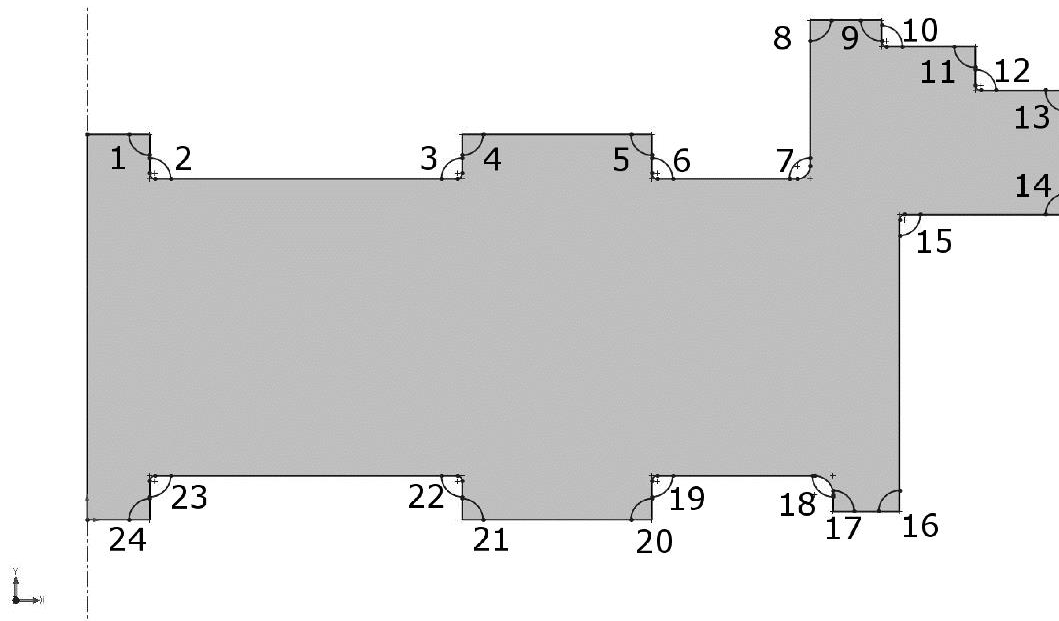
Figure 107 The ordinal numbers assigned to the angles in the profile.
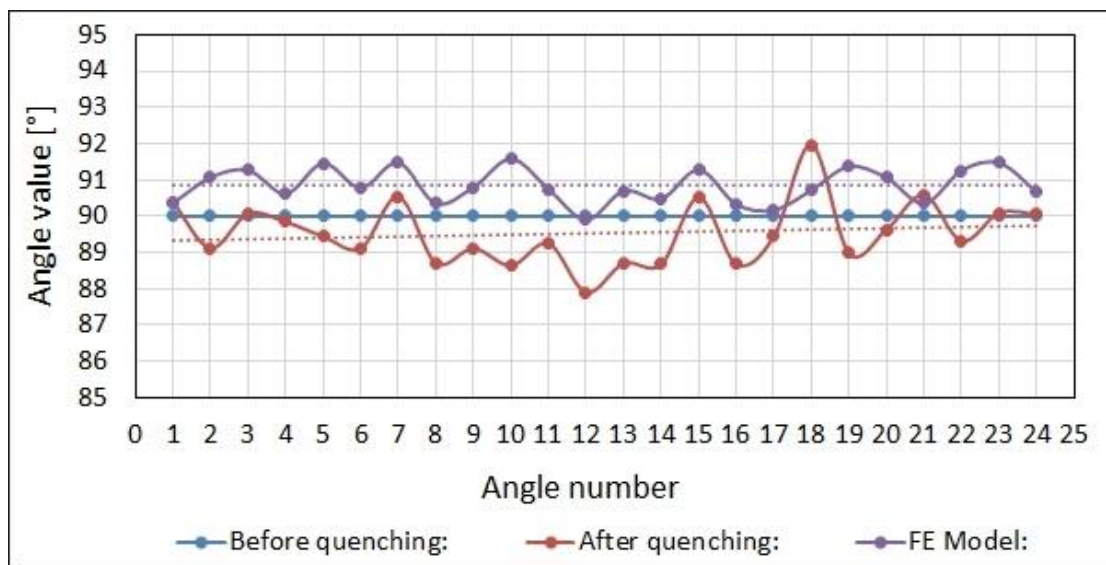
Figure 108 The angles' values measured from the model with the coarse mesh. For angles number reference see Figure 107.

The measurements of the angles were performed using free software for image processing and analysis, ImageJ. The set of close-up pictures were taken from both of the models, with the coarse and the fine mesh. The results were presented below.
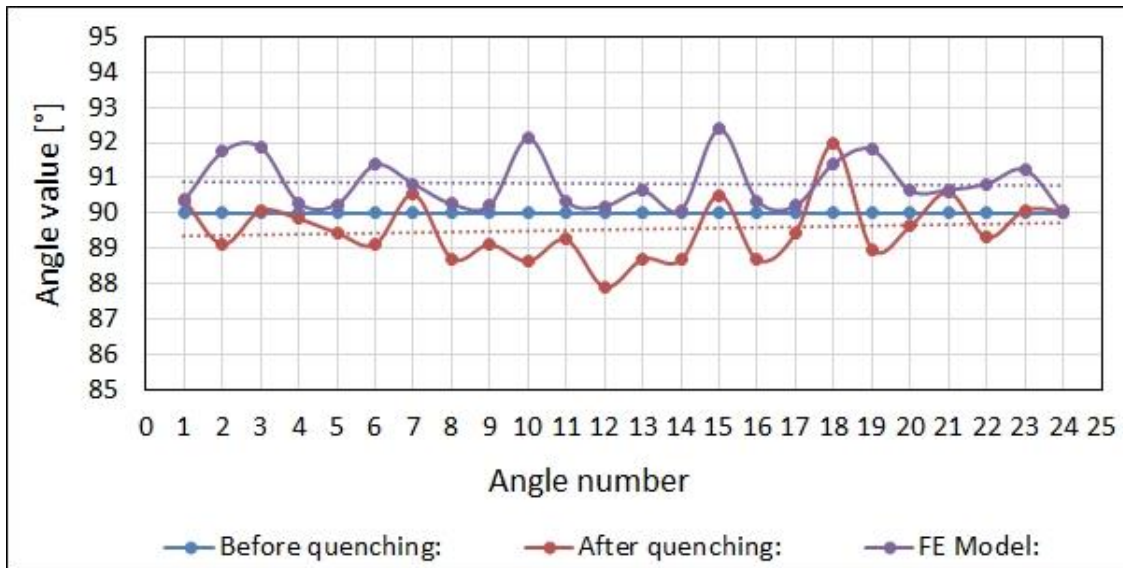
Figure 109 The angles' values measured from the model with the fine mesh. For angles number reference see Figure 107.

Table 38 The measured angles' values from model with coarse and fine mesh.

Angle no.:	Before quenching:	After quenching:	FE model (the coarse mesh):	FE model (the fine mesh):
1	90°	90.38°	90.36°	90.34°
2	90°	89.12°	91.07°	91.74°
3	90°	90.07°	91.27°	91.87°
4	90°	89.84°	90.62°	90.29°
5	90°	89.44°	91.46°	90.25°
6	90°	89.12°	90.78°	91.37°
7	90°	90.54°	91.48°	90.83°
8	90°	88.71°	90.35°	90.26°
9	90°	89.11°	90.80°	90.23°
10	90°	88.64°	91.58°	92.12°

11	90°	89.25°	90.75°	90.34°
12	90°	87.90°	89.90°	90.20°
13	90°	88.70°	90.70°	90.63°
14	90°	88.67°	90.48°	90.09°
15	90°	90.52°	91.28°	92.38°
16	90°	88.67°	90.33°	90.35°
17	90°	89.44°	90.17°	90.21°
18	90°	91.97°	90.72°	91.42°
19	90°	88.98°	91.37°	91.80°
20	90°	89.63°	91.06°	90.64°
21	90°	90.59°	90.35°	90.66°
22	90°	89.31°	91.26°	90.83°
23	90°	90.09°	91.47°	91.23°
24	90°	90.06°	90.67°	90.00°

Considering the data presented in Figure 108, Figure 109 and Table 38, it can be seen that the predicted angles obtained from the developed FE model were close to the measured ones, obtained from the industrial process. In the model with the simpler mesh, the values were nearly exactly the same at the angles 1, 17 and 21. In the model with finer mesh, the smallest differences between the calculated and measured values were observed at the angles 1, 4, 7, 17, 18, 21 and 24, which is nearly 30% of all angles. The results obtained using the model with coarse mesh were more uniform. It can be seen in Figure 108 that there were no high peaks or lows that could significantly deviate from the average. A different situation was found in the second model, where the angles numbered as 2, 3, 10, 15 and 19 were much greater than the rest, where the angles have values generally lower than the average from the first model. These phenomena may be related to the location of these angles (Figure 107) and may be caused by

the specific position of the outer flange. Similar peaks were observed at angles 7, 15, 18 and 21 during the industrial process. It indicates that the simpler mesh can still provide sufficiently good results overall, the finer mesh, which causes calculation very time-consuming, could be more desired, whenever the higher level of the accuracy within the expected results is required.

The objections about the model predictive abilities could be associated with the direction of the angles' growth. Only one measurement, the angle numbered 12 in the model of the coarse mesh, showed the negative sign of the growth, from 90.00° to 89.90°, while all of the measurements of the angles in model of the fine mesh showed positive signs of the growth. In the industrial process the positive angle growth was recorded at the angles numbered 1, 2, 7, 15, 18, 21, 23 and 24, which is around 33% of all angles, while the rest of them dropped below the initial 90°. This could be related to the amount of the implemented dilatometric data. Each of the dilatometric curves obtained at specific cooling rates was put into the model as the table of the thermal expansion coefficients related to the small temperature intervals. Such a procedure increases the accuracy of the prediction of material contraction/expansion resulting from the phase transformation. The number of implemented dilatometric curves is strongly related to the prediction accuracy of the material microstructure during the heat treatment process. The final results obtained using the developed model were sufficient assuming the amount of the implemented input data.

The absolute differences between the angles before and after the heat treatment were calculated and the one average value was extracted for every set of values (measured after the quenching in the industrial process, calculated from simple mesh model and calculated from fine mesh model). These average absolute values of all of the angles were calculated to present the average differences between the results from the industrial process, the results calculated from the model with simple mesh and the results calculated from the model with fine mesh, together with the standard deviations. All of the data were presented in Table 39.

Table 39 Differences between the average absolute angles with standard deviations: between the values from before and after the heat treatment, and between the values measured and the calculated from both models.

	After quenching:	Simple mesh:	Fine mesh:
Difference between before and after quenching average absolute angles' values:	0.82°	0.85°	0.84°
Standard deviation:	0.55°	0.45°	0.70°
Difference between the measured after quenching and the calculated from the models average absolute angles' values:		0.66°	0.70°
Standard deviation:		0.48°	0.55°

It can be seen that the differences between the measured and calculated angles are 0.03° and 0.02° for the simple and fine mesh respectively, which is nearly the same. The standard deviation value of the results calculated from the model with simplified mesh is only 0.1° smaller, while the one calculated from the model with finer mesh is 0.15° greater compared to that calculated from the measured angles values after quenching in industrial process. All of the calculated differences between the models and industrial data are within the range of standard deviation. The absolute differences calculated between the numerical results and the industrial process data were respectively 0.66° and 0.70°. The results confirm the relatively low sensitivity of the FE model to the mesh within the chosen range of the elements.

5. Study case – simulation of welding process

5.1. Introduction

The modern nuclear reactor pressure vessels are massive constructions of complicated shape, which consist of number of minor connected elements, made of the same and the different materials. Over the decades effort was put in improving the design in a way of replacing as many of the smaller elements with a bigger ones as possible. Although, it is impossible to completely avoid the joining the parts, to connect the elements the various kinds of welding process is widely applied [169]. The welding is a quite invasive process, as it introduces additional stresses into a material through the high local heat input, what creates the inhomogeneous temperature field around the weld and changes the microstructure. The gradient of the properties due to the various heat affected zones in the two joined material creates the different mechanical respond of the thermal expansion coefficient, which follows the mismatch of the local volume and stresses arise.

As the SA508 grade 3 steels are one of the major material used for RPVs constructions the welding process of this steel is one of the most often discussed problem in the literature, as it is impacting the material parameters, like fracture toughness [98]. Many of them use numerical simulation to map the residual stresses within the investigated material, like for example [98], [169]–[172], among the many.

In order to validate the developed in this work final model, the simplified welding process is numerically recreated. It has to be highlighted that the welding process itself is not a concern of this work, although due to the importance of such, this topic cannot be omitted during the consideration of modelling of the residual stress origins in SA508 grade 3 steels.

5.2. Methods

In order to sufficiently reflect all aspect of the problem without going into the unimportant details, six models were constructed. Their brief description is included in Table 42. The first three present the development of the heat transfer process during the subsequent deposition of the weld beads on the surface, with the different positions of the weld path. The fourth and fifth models are connected with the subroutine with Fortran code, which described the developed transformation model and predicts the stress field. The sixth model combines all of the previously tested techniques and additionally uses the most complicated geometry.

Table 40 Material properties of the SA508 grade 3 steel used in this chapter, assigned to the table surface [170]:

SA508gr3						
Temperature (∘C)	Density (t/mm3)	Specific Heat (mJ/(t*K))	Thermal Conductivity (mW/mm/∘C)	Coefficient of Thermal Expansion ×10-6 (mm/mm/∘C)	Young's Modulus (MPa)	Poisson's Ratio
25	7.85E-09	450E-06	41.00	12.50	210900	0.29
100	7.83E-09	481E-06	41.80	12.70	207100	0.29
200	7.80E-09	520E-06	41.70	13.10	201800	0.30
300	7.77E-09	564E-06	40.50	13.50	193900	0.30
400	7.73E-09	618E-06	38.60	13.80	184100	0.30
500	7.70E-09	688E-06	36.30	14.20	172300	0.31
600	7.66E-09	786E-06	34.00	14.60	159100	0.31
700	7.64E-09	113.1E-06	29.80	13.80	142200	0.32
800	7.66E-09	594E-06	26.00	11.00	127500	0.34
900	7.60E-09	609E-06	27.30	12.50	117700	0.35
1000	7.55E-09	624E-06	28.50	13.80	107700	0.35
1100	7.50E-09	640E-06	29.70	14.90	97600	0.36
1200	7.44E-09	655E-06	31.00	15.60	87400	0.36
1300	7.39E-09	671E-06	32.20	16.40	77000	0.37

Plastic Strain (%)	0	0.04	0.08	0.12	0.16	0.20	0.24	0.28
Temperature (∘C)	True Stress (MPa)							
25	361	637	726	784	828	864	894	920
200	277	545	637	698	745	784	816	845
500	240	476	556	609	650	684	713	739
700	229	407	407	406	405	402	399	396
900	92	92	92	92	92	92	91	90
1100	25	25	25	25	25	25	24	24
1300	8	8	8	8	8	8	8	8
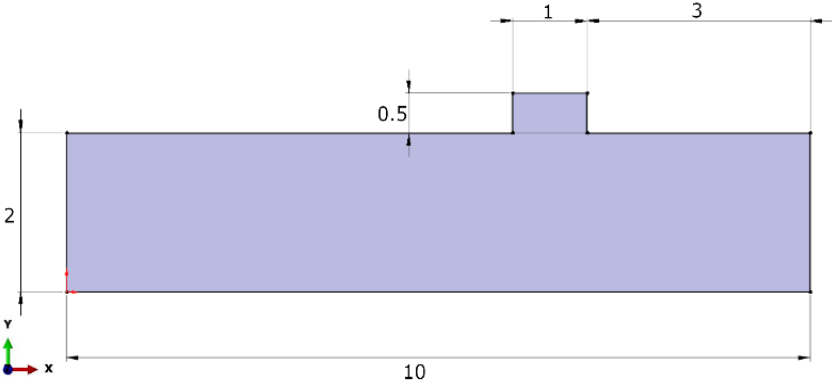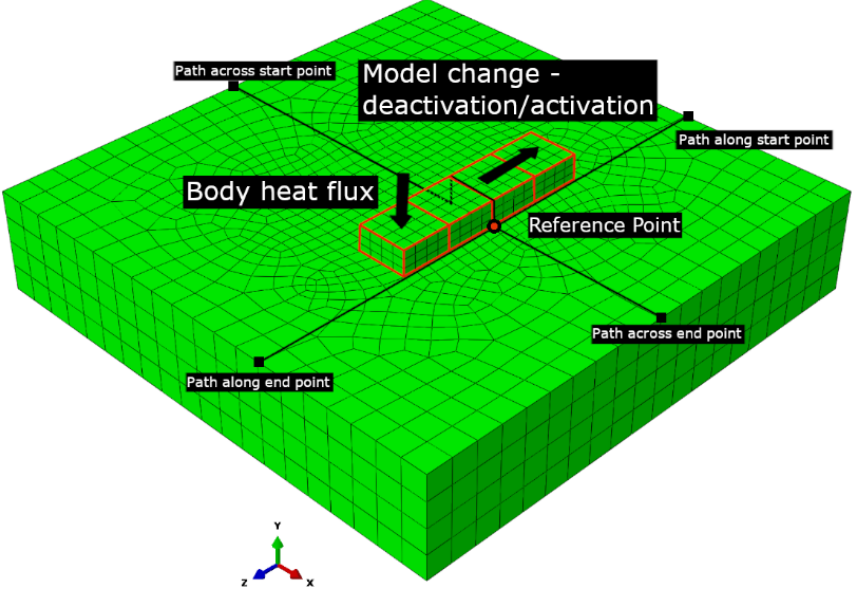
Table 41 Material properties of the Inconel52M used in this chapter, assigned to the weld [170]:

INCONEL52M						
Temperature (°C)	Density (t/mm3)	Specific Heat (mJ/(t*K))	Thermal Conductivity (mW/mm/°C)	Coefficient of Thermal Expansion ×10-6 (mm/mm/°C)	Young's Modulus (MPa)	Poisson's Ratio
25	8.19E-09	435E+06	13.03	12.35	214300	0.31
100	8.17E-09	452E+06	14.34	12.68	209500	0.31
200	8.14E-09	470E+06	16.07	13.14	202800	0.32
300	8.1E-09	488E+06	17.79	13.60	195800	0.32
400	8.07E-09	505E+06	19.49	14.06	188600	0.32
500	8.03E-09	522E+06	21.17	14.51	181200	0.33
600	7.99E-09	666E+06	22.84	14.96	173500	0.33
700	7.94E-09	708E+06	23.23	15.83	162700	0.33
800	7.89E-09	581E+06	23.98	16.68	152000	0.33
900	7.84E-09	604E+06	25.54	17.15	143600	0.34
1000	7.79E-09	629E+06	27.09	17.64	134800	0.34
1100	7.74E-09	644E+06	28.64	18.13	125800	0.34
1200	7.69E-09	668E+06	30.20	18.62	116700	0.35
1300	7.64E-09	693E+06	31.76	19.11	107400	0.35

Plastic Strain (%)	0	0.04	0.08	0.12	0.16	0.20	0.24	0.28
Temperature (°C)	True Stress (MPa)							
25	420	625	685	723	751	773	792	809
200	301	459	506	535	557	575	590	603
500	244	376	415	440	459	474	487	498
700	220	335	369	390	406	411	405	399
900	56	70	70	70	69	69	68	68
1100	26	26	26	26	26	26	26	25
1400	6	6	6	6	6	6	6	6

The models used the material properties typical for the SA508 grade 3 steel assigned to the surface and the material properties of the INCONEL52M assigned to the weld (Table 40 and Table 41). The material properties and the final geometry are based roughly on Zhang et al.'s work [170]. The predefined temperature is used in the models, usually different for the surface and for the weld. The temperature-displacement coupled models (4, 5 and 6) are fixed in the numerical space by blocking the moves of the reference nodes (#2, #3, #4 and #5). The mesh elements used are from the standard element library with linear geometric order. The hexahedral elements were chosen, the DC3D8 type for the heat transfer models and the C3D8T for the coupled temperature-displacement models. The elements number was different for each model and in range 4000 – 20 000. All the details are presented in the Table 42.

Table 42 The set of key properties of the welding process models set:

Case 1: Heat transfer problem.
 	
Total time: 180.8s
 	
Predefined fields:
 	
- geometry's temperature: 20°C
 	
Interaction:
 	
- surface film condition:
   - film coefficient: 0.05 [W/m^{2}K]
   - sink temperature: 20°C
- elements deactivation and activation
 	
Load case:
 	
- body heat flux (subroutine DFLUX)
 	
Mesh:
 	
- nodes (5393)
- DC3D8 elements (4196)

Case 2: Heat transfer problem. Total time: 41s	

<ins>Predefined fields:</ins> - table's temperature: 300°C - weld's temperature: 20°C <ins>Interaction:</ins> - elements deactivation and activation <ins>Load case:</ins> - body heat flux (subroutine DFLUX) <ins>Mesh:</ins> - nodes (3380) - DC3D8 elements (2540)	
<ins>Case 3: Heat transfer problem.</ins>	
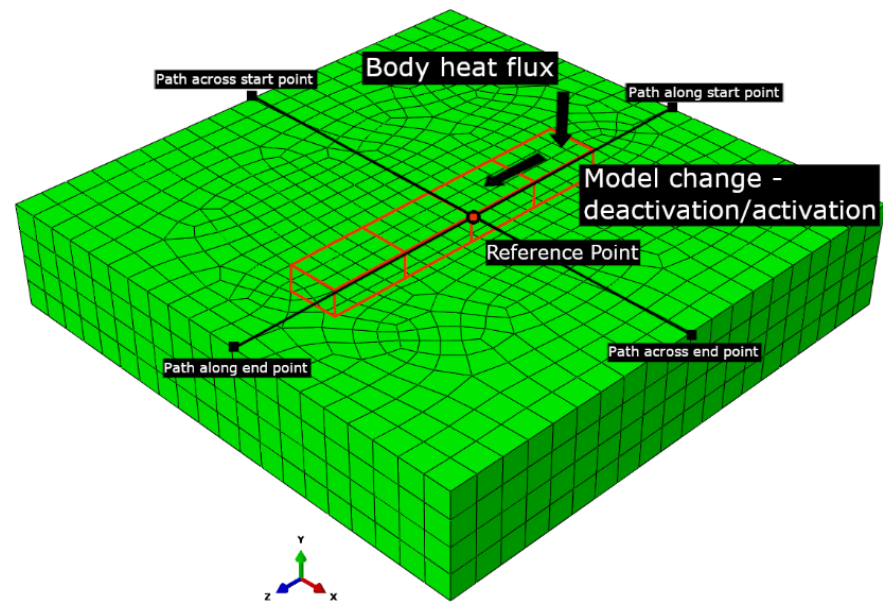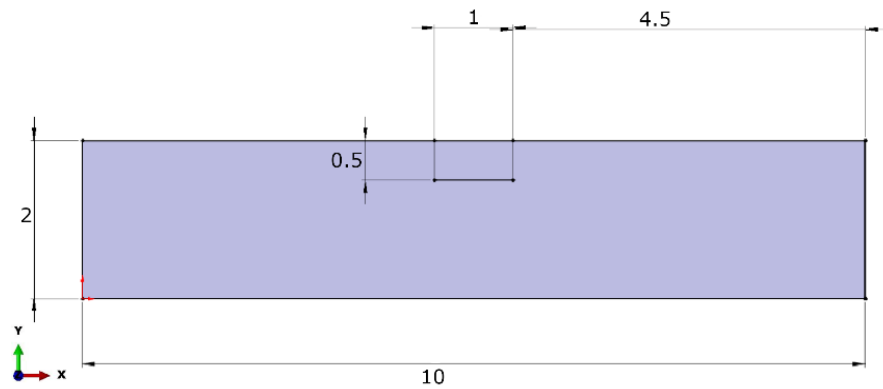
Total time: 41s
 	
Predefined fields:
 	
- table's temperature: 300°C
- weld's temperature: 20°C
 	
Interaction:
 	
- surface film condition:
  - film coefficient: 0.05 [W/m^{2}K]
  - sink temperature: 20°C
- elements deactivation and activation
 	
Load case:
 	
- body heat flux (subroutine DFLUX)
 	
Mesh:
 	
- nodes (4965)
- DC3D8 elements (3800)	
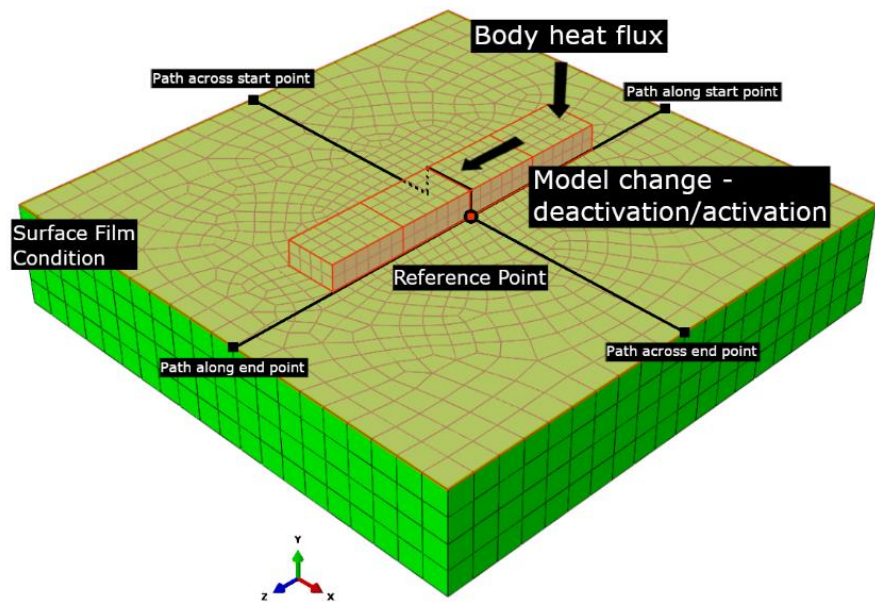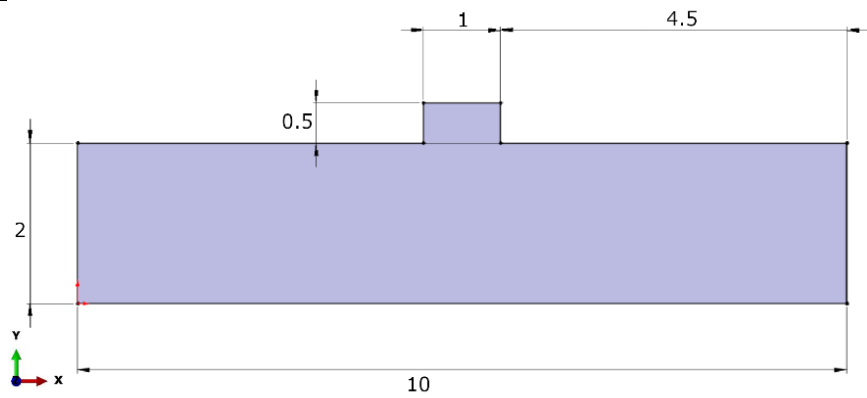
Case 4: Coupled temperature - displacement problem. Total time: 50s	

Cooling time: 40s
 	
Predefined fields:
 	
- geometry's temperature: 20°C
 	
Interaction:
 	
- surface film condition:
   - film coefficient: 0.2 [W/m^{2}K]
   - sink temperature: 20°C
- elements deactivation and activation
 	
BC:
 	
- fix: Encastre (U1 = U2 = U3 = UR1 = UR2 = UR3 = 0) at ref. points
 	
Load case:
 	
- body heat flux: 4 load cases for each weld element (9000 [mW/mm^2]
 	
Mesh:
 	
- nodes (5412)
- C3D8T elements (4384)	
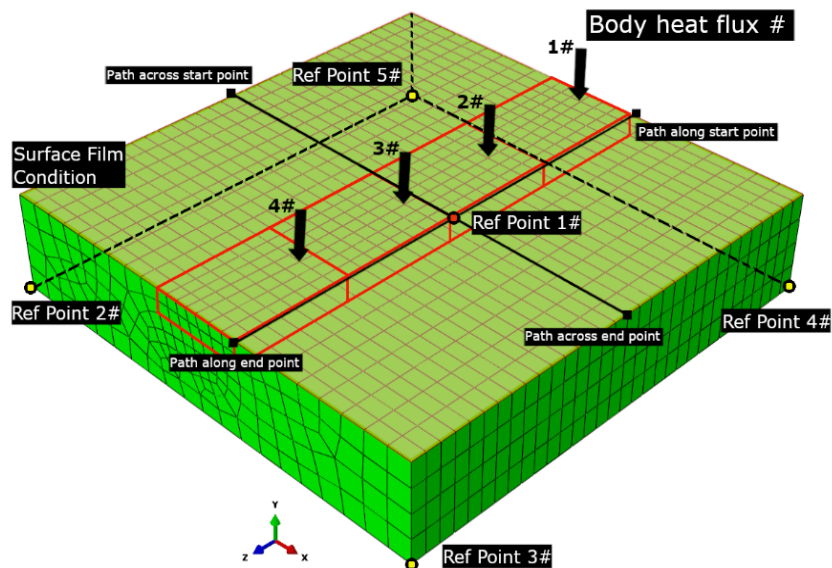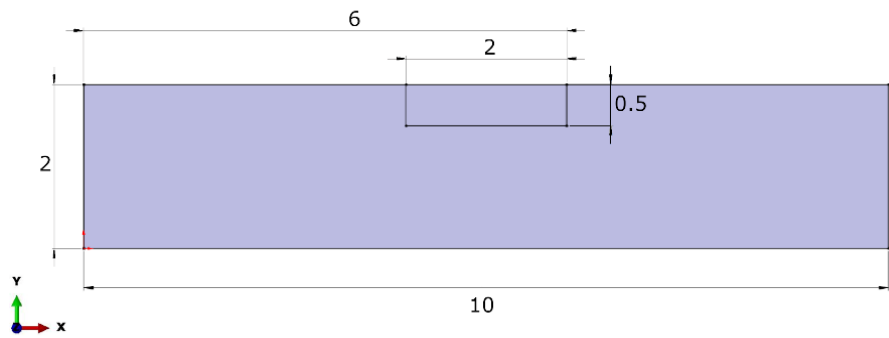
Case 5: Coupled temperature - displacement problem.

Total time: 30.8s

Cooling time: 30s

Predefined fields:

- table's temperature: 300°C
- weld's temperature: 20°C

Interaction:

- surface film condition:
  - film coefficient: 0.1 [W/m^{2}K]
  - sink temperature: 20°C
- elements deactivation and activation

BC:

- fix: Encastre (U1 = U2 = U3 = UR1 = UR2 = UR3 = 0) at ref. points

Load case:

- body heat flux (subroutine DFLUX)

Mesh:

- nodes (17872)
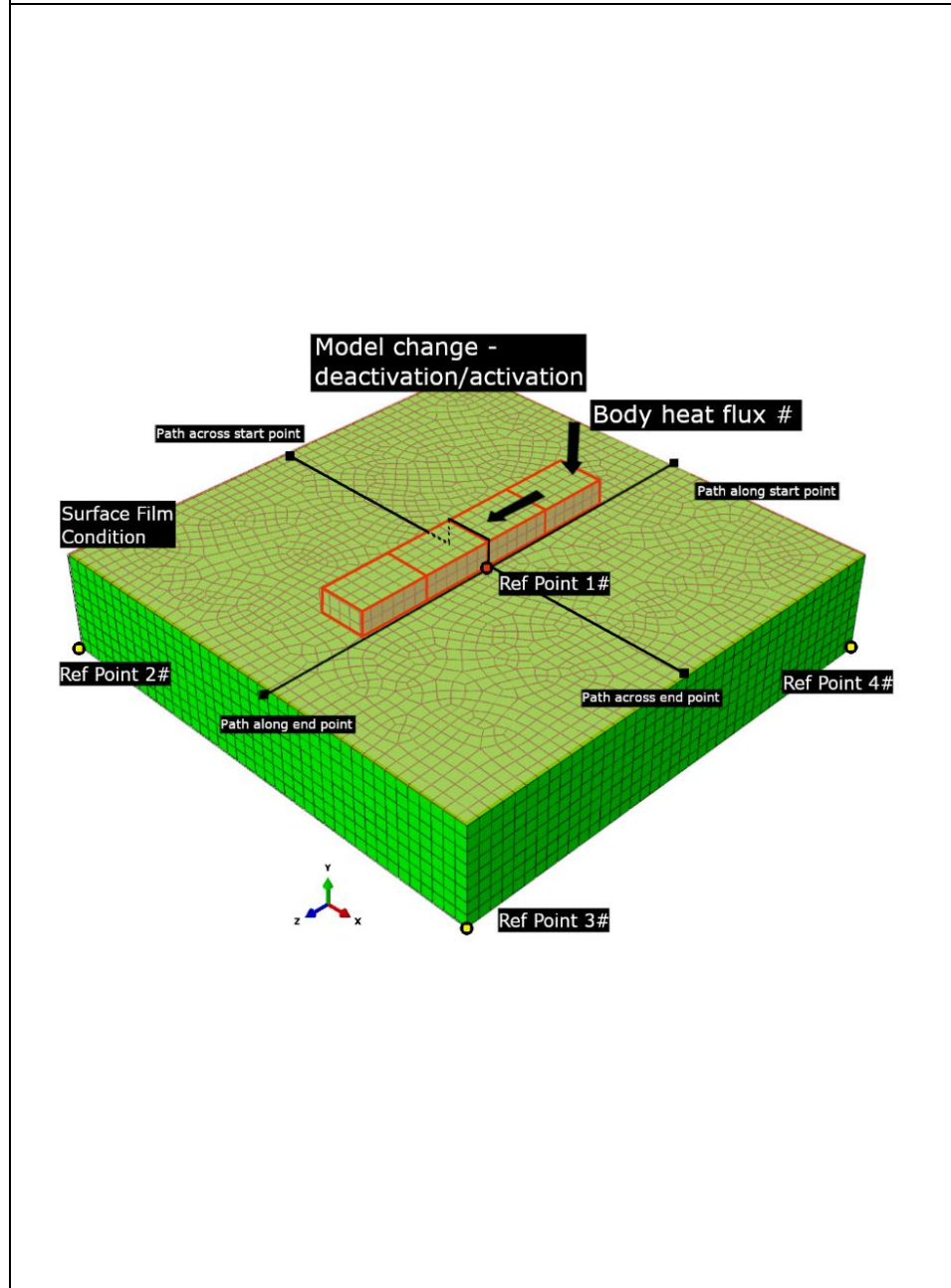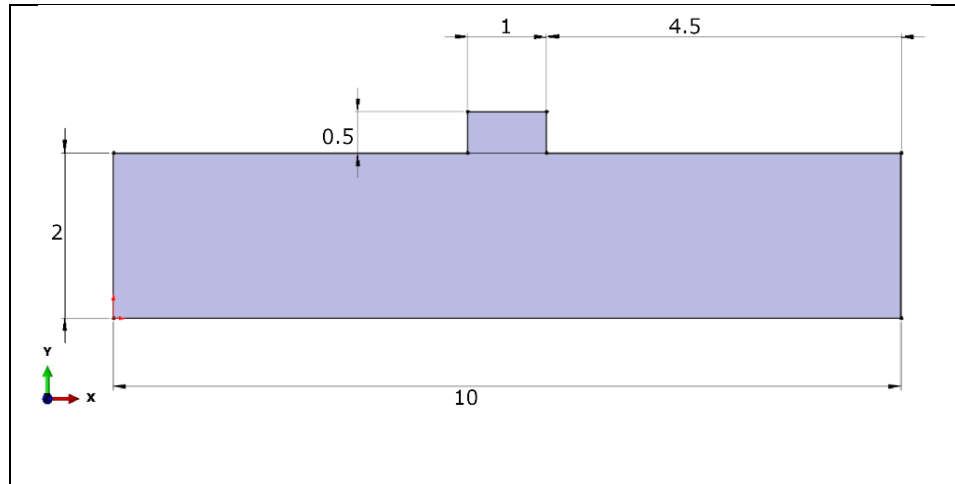
- C3D8T elements (15208)	

Case 6: Coupled temperature - displacement problem.
 	
Total time: 88s
 	
Cooling time: 80s
 	
Predefined fields:
 	
- table's temperature: 150°C
- weld's temperature: 20°C
 	
Interaction:
 	
- surface film condition:
    - film coefficient: 0.35 [W/m²K]
    - sink temperature: 20°C
- elements deactivation and activation
 	
BC:
 	
- fix: Encastre (U1 = U2 = U3 = UR1 = UR2 = UR3 = 0) at ref. points
- symmetry of XY plane (ZSYMM (U3 = UR1 = UR2 = 0)

- symmetry of YZ plane (XSYMM (U1 = UR2 = UR3 = 0) - symmetry of ZX plane (YSYMM (U2 = UR1 = UR3 = 0) <u>Load case:</u> - body heat flux (subroutine DFLUX) <u>Mesh:</u> - nodes (23030) - C3D8T elements (20064)	

The welding process is recreated numerically by coupling the moving volumetric heat source (load), described by another Fortran code in subroutine DFLUX, with the Deactivation/Activation of the geometry (interaction). The idea was based on the model of laser cladding, described in detail by Bajda et al. in [173], which is in turn defined as a volumetric heat source to be absorbed in a volume of a green body. The heat source energy was described by a Gaussian distribution in the radial direction and exponential decay in the depth direction due to the equation (24):

$$Q(r,y) = Q exp\left(\frac{-2r^2}{R_0^2}\right) exp(-\alpha Y) \tag{24}$$

where $Q(r,y)$ is the heat flux at point (r,y), Q_0 is the peak flux, R0 is $1/e^2$ radius of the heat source beam on the top surface and α is the absorption coefficient of the green body. The peak flux Q_0 is represented by the equation (25):

$$Q = \left(\frac{Q_L}{\pi R_0^2 d}\right) \tag{25}$$

where Q_L is the weld beam power and d is the heat penetration depth. The movement of the heat source is described by the equation of the position in the space (26):

$$R = \sqrt{X^2 + Y^2 + \left(Z + Z_f\right)^2}$$
(26)

where R is the actual position of the heat source, X, Y, Z are the space coordinates, and Z_f is the update of the position in Z direction. Table 43 presents the parameters, which were used in each of the models.

Table 43 Heat source parameters described in the subroutine DFLUX, using Fortran code:

Subroutine: DFLUX						
Case	Heat source power Q_L [mW]	Beam Radius R_0 [mm]	Absorptivity of the surface α	Penetration depth d [mm]	Body flux Q [mW/mm^3]	Heat source velocity V [mm/s]
1	120000	0.6	1	0.5	212207	5
2	300000	0.8	1	0.5	298416	7.5
3	120000	0.8	1	0.5	119366	8
4	40000	0.8	1	0.5	39789	12.5
5	22000	0.8	1	0.7	15631	8.5
6	80000	0.8	1	0.7	56841	12.5

In the set of the constructed models the development of the numerical representation of the welding process was presented. First, the different geometries and temperature conditions of the welding process were tested to calculate the transient temperature field and then, the developed in this thesis model, which predicts the residual stresses in SA508 gr. 3 steel, is applied. The results are presented in the form of temperature, displacement and stress charts obtained from the reference points highlighted on the model schemes in the Table 42. Also, the

temperature differences before and after cooling process obtained at the certain time points from the path of the nodes are presented and discussed (Table 42). The used subroutines are attached in the Appendix A. Such formulated numerical model is sufficient enough as a simplification of the welding process to present the use of the developed transformation model for the SA508 grade 3 steel.

5.3. Results and discussion:

The developed set of models allowed the presentation of the various numerical approaches in the case of the SA508 gr. 3 steel welding. The temperature, displacement and stress results obtained from the various points and set of points through the process time from the models are presented below, together with the model's graphics. The chosen are presented from the variety of the results.
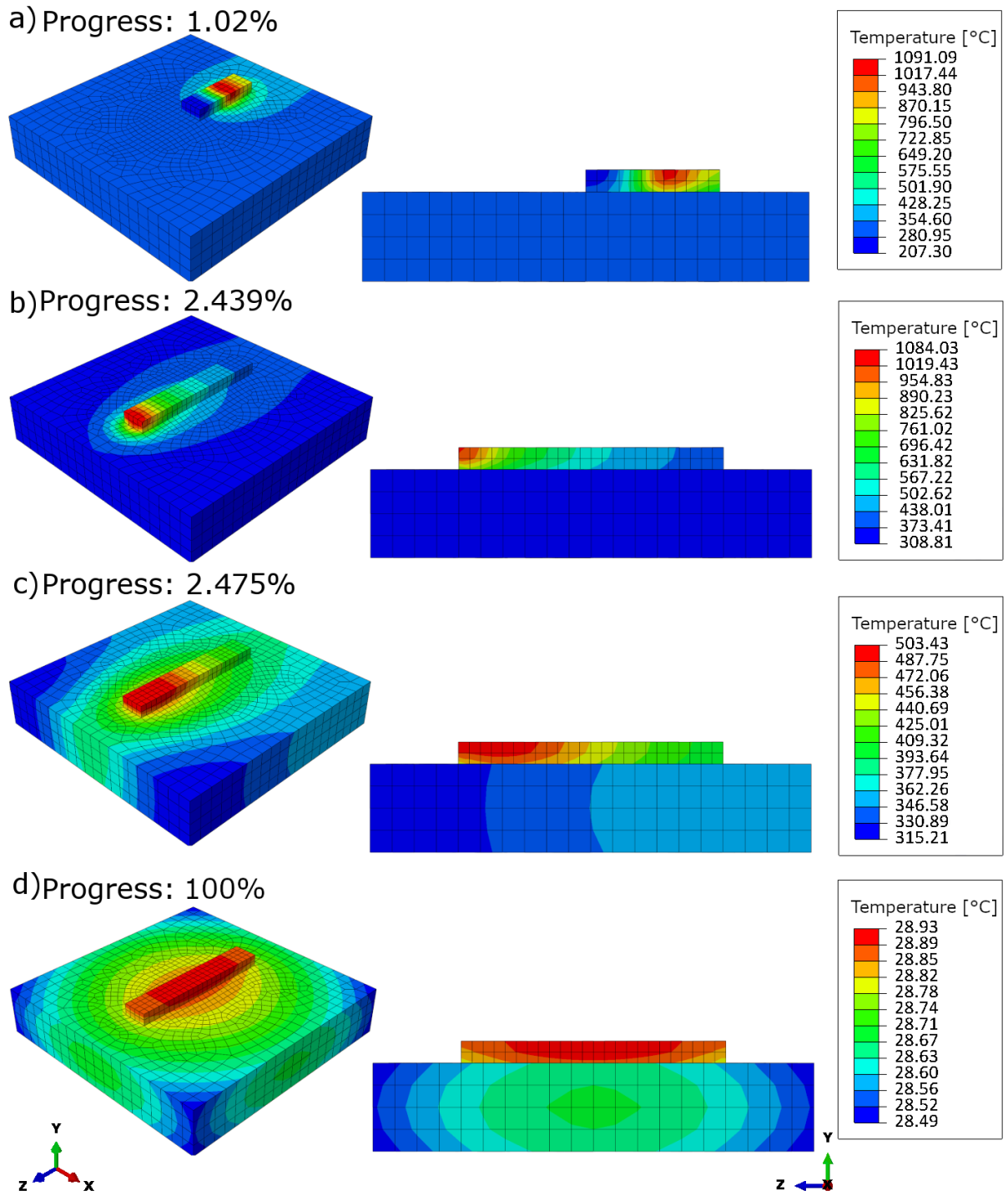
Figure 110 The temperature distribution at the different time points (a, b, c and d) of the welding process of the heat transfer model of the case 3.

The distribution of the transient temperature field during the third heat transfer case (see Table 42) is presented in *Figure 110*. The geometry of that case is such that the four weld beads are subsequently placed upon the initially heated surface of the SA508 gr. 3 steel. At the same time the heat source is directed on the volume of the each bead, consequently moving with the

time in the direction of their appearance. The length of the table is the same in all the models and is equal to 10mm, while the single bead in this case is 1.5 mm long. The initial temperature of the surface is set to 300°C, while the temperature of the activated/showing up bead is set to 20°C and is nearly instantaneously increased by the heat source. The surface of the steel is subjected to the air cooling during the whole process. After the welding, which takes 1s, 40s of cooling is applied, which in this case bases on the air cooling, which means the heat exchange between the surface and the ambient by the prescribed earlier surface film coefficient. As can be seen in *Figure 110*a) the temperature at the beginning of the welding is very high at the weld bead, above 1100°C, and already dropped from the initial value at the steel surface, from 300°C to 200°C. Due to the small dimensions of the geometry, the process is very rapid. After ~ 2.5s (*Figure 110*b) the adding of the elements is finished, and the cooling process is about to start. It can be seen that the high temperature of the weld bead, increased by the heat source, maintains its level, but the surface's temperature, despite being constantly cooled down through the contact with the ambient, increased above the initial temperature. This is caused by the vicinity of the hot weld beads. It can be noticed that the temperature of the beads is held only by the heat source, as the temperature rapidly drops about twice, when it is surpassed (*Figure 110*c), with the negligible increase of the temperature of the steel surface. After the end of the cooling in the air process, the temperature is close to the ambient value (20°C) through the whole model. *Figure 110* represents the temperature results obtained from all of the heat transfer problems. The relations between the temperatures field of the other heat transfer cases are included in the summary charts in *Figure 111*.
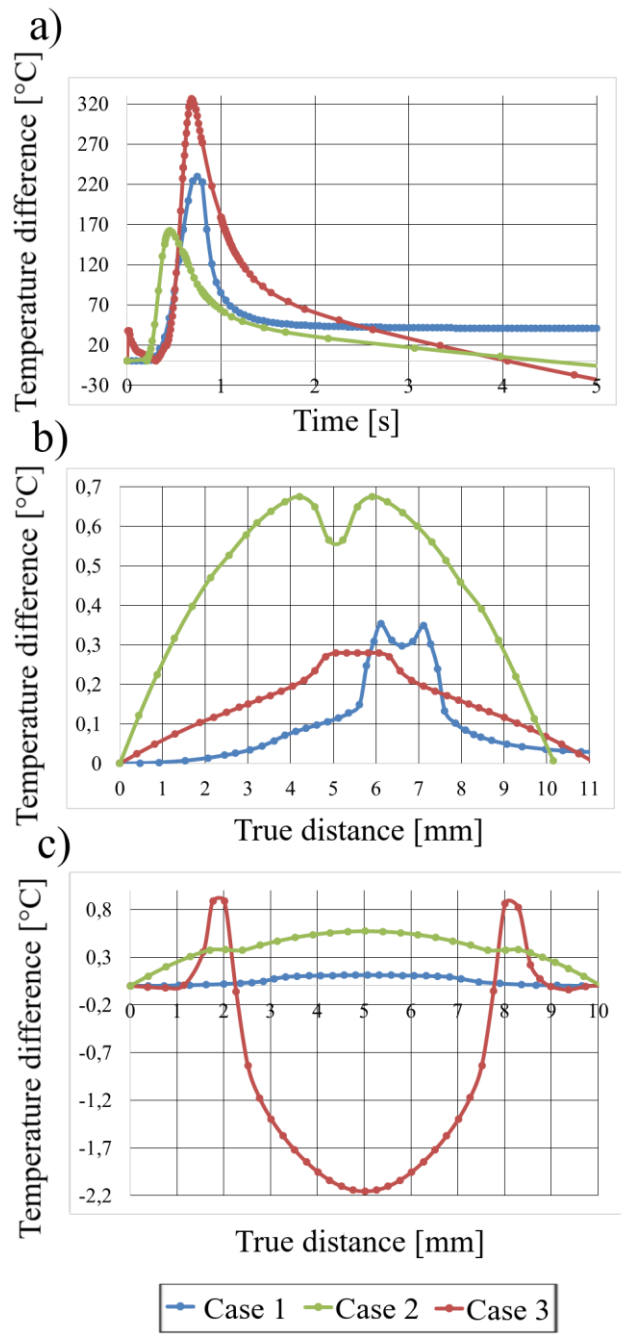
Figure 111 The differences of the temperature from the beginning of the process of each heat transfer cases from the various places of the geometry: a) from the reference node b) from the path of nodes across the weld c) from the path of nodes along with the weld.

The temperature changes since the beginning of the process, obtained from the different nodes from all of the heat transfer cases, are presented in *Figure 111*. *Figure 111*a) presents the temperature registered at the certain reference points (see Table 42), which are placed on the

steel surface, next to the weld. It can be seen that the highest temperature increase occurs for case 3, where the weld is at the centre of the steel table, on the surface. Although the value of body flux is the lowest (Table 43) this case is very similar to the case 1. The biggest difference between them is the higher beam radius, heat source velocity and the length of the beads (1 mm vs 1.5 mm) in the case 3.

In *Figure 111*b) the highest temperature difference values are for the case 2. The path of the nodes is leading across the table and the weld. As in the second case the weld is poured into the groove in the material, there is a larger contact surface and the surroundings are heating faster. The peak of the case 1 is moved to right, as in this case the weld is not placed symmetrically on the table.

In *Figure 111*c) the case 2, which has the highest value of body flux maintains the high values of the temperature to the end of the process, which is not really affected by the time passed for cooling. Also, due to the mentioned large contact surface with the steel table, it not affected so much by the heat exchange. The case 1, which has the shortest weld path also maintains small temperature differences at the end of the process. The case 3 however deals with the highest temperature peaks at steel table surface, where the weld is heating it. Also, it can be seen that due to the applied film coefficient interaction, which controls the heat exchange with the ambient conditions, the weld, which is larger than in the case 1, is cooled much faster.

These models present the base of the heat transfer models, which is then connected with the coupled temperature-displacement model described below, used to calculate the temperature related strain and stress states.
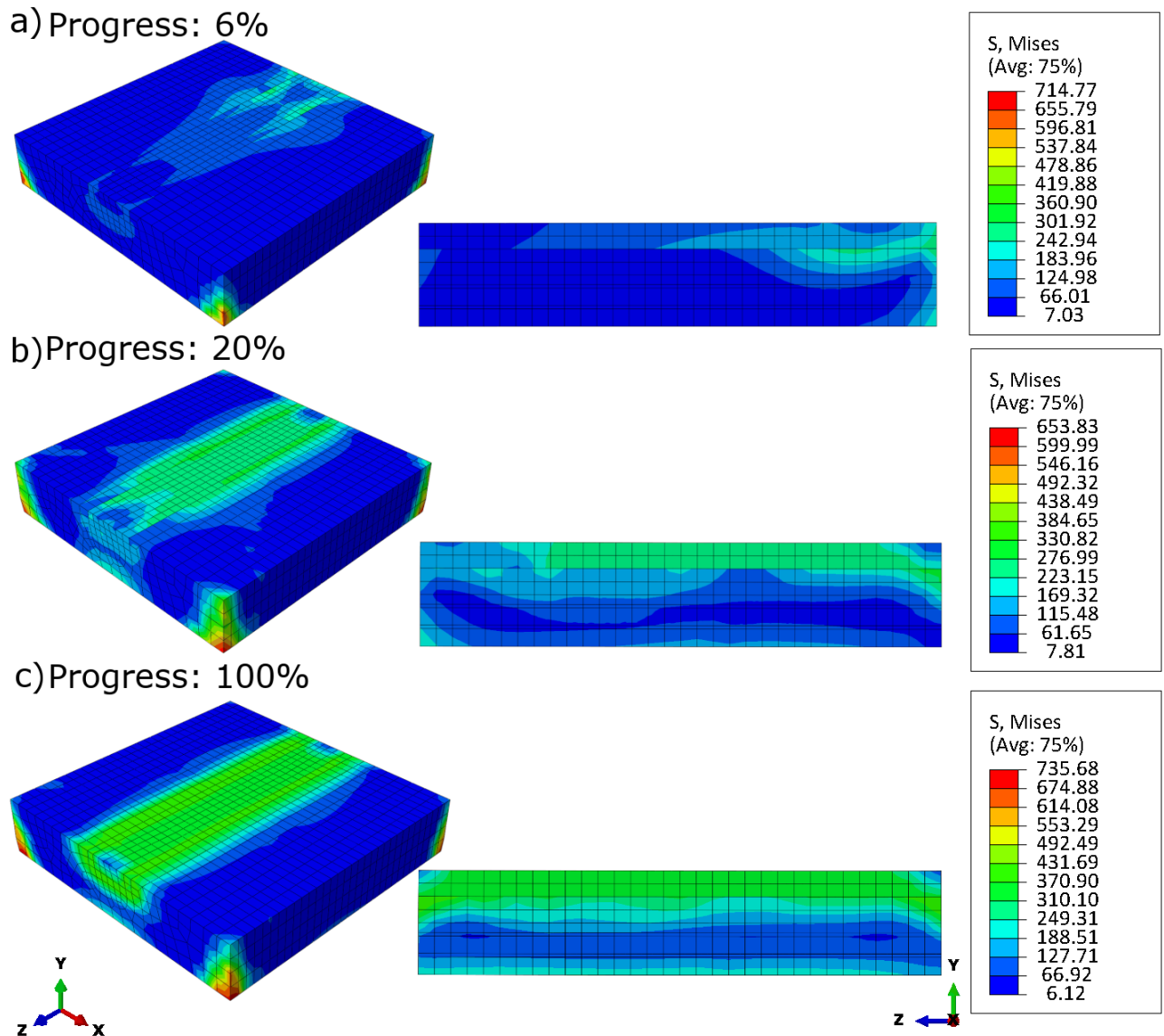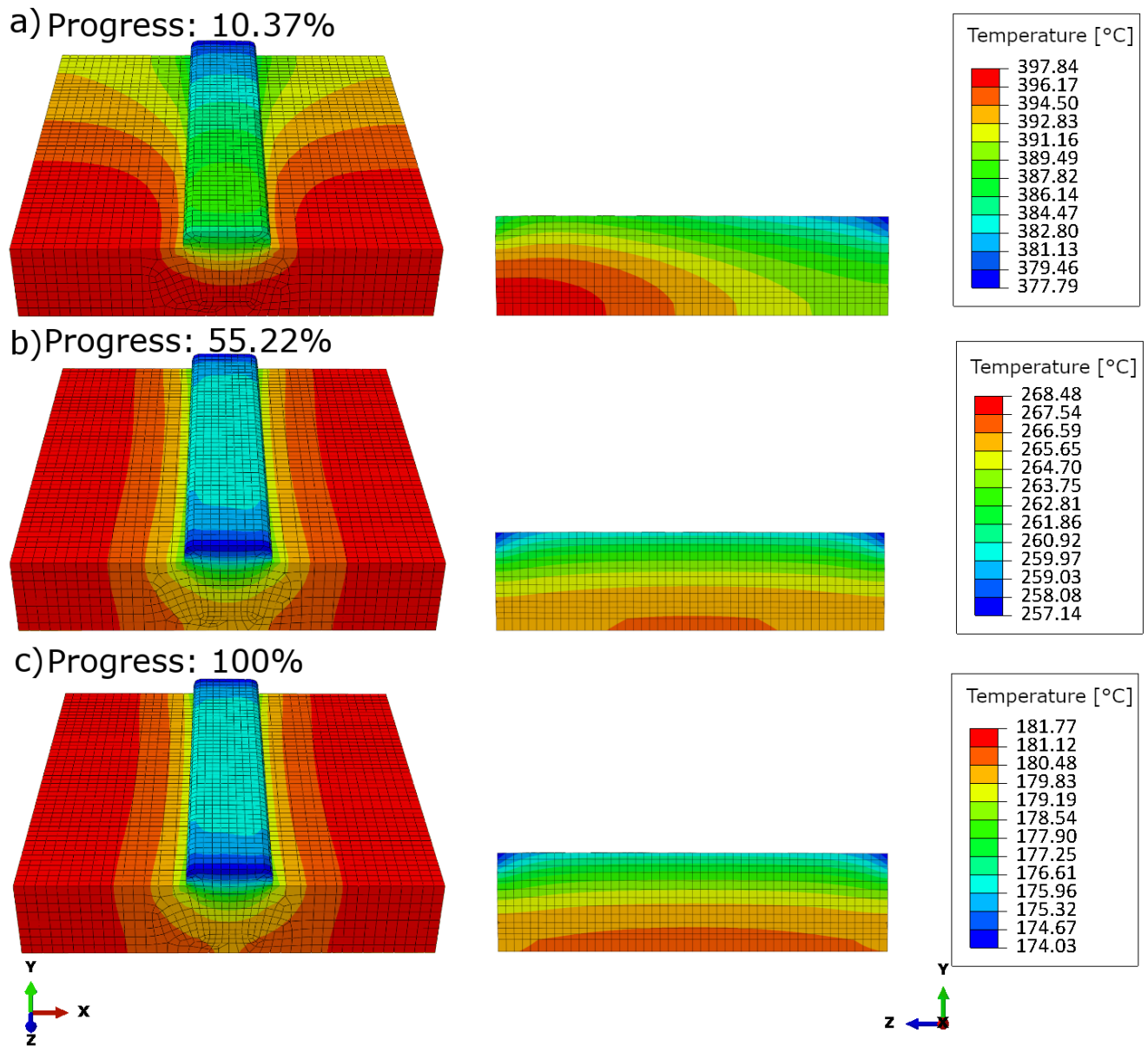
Figure 112 The stress distribution at the different time points (a, b, and c) of the welding process of the coupled temperature-displacement model of the case 4.

In Figure 112 the stress distribution of the second coupled temperature-displacement model, named case 5, is presented. This model is based on the idea the geometry of the case 2, where the weld beads are poured into the shallow groove of the steel base material. The size of beads is larger than in other cases (*Table 42*). This model does not use the subroutine code to control the heat source. Instead the four load cases are created, each one for each of the bead. Each of them describes the heat load of 90 000 mW/mm^3, where the control of its movement is performed by the prescribed amplitude. The time of the welding is also longer, it takes 2.5s per bead, which gives 10s for welding process and 40s for cooling. The cooling process is described by applying the surface film coefficient of 0.2 W/m^{2}K.

It can be seen in the models, where the beads are hidden inside the material, like case 2, 4 and partially 6, that there are high values of the stress in region of the contact area between the weld and the material. Comparing the temperature expansion coefficient values in the both used materials (The *Table 40* and *Table 41*) it can be noticed that the weld material Inconel52M has the higher values of this coefficient, with the difference going even up to 5×10^{-6} mm/mm°C in the higher temperatures like 700°C – 900°C. It causes the increase of the stress value even during the cooling process, due to the fact that the bulk of the steel table cools slower than the weld, which causes the differences in the local sizes. It shows that the cooling process must be performed during the proper period of time, allowing the temperature and in turn the volume of the materials to adjust to each other.
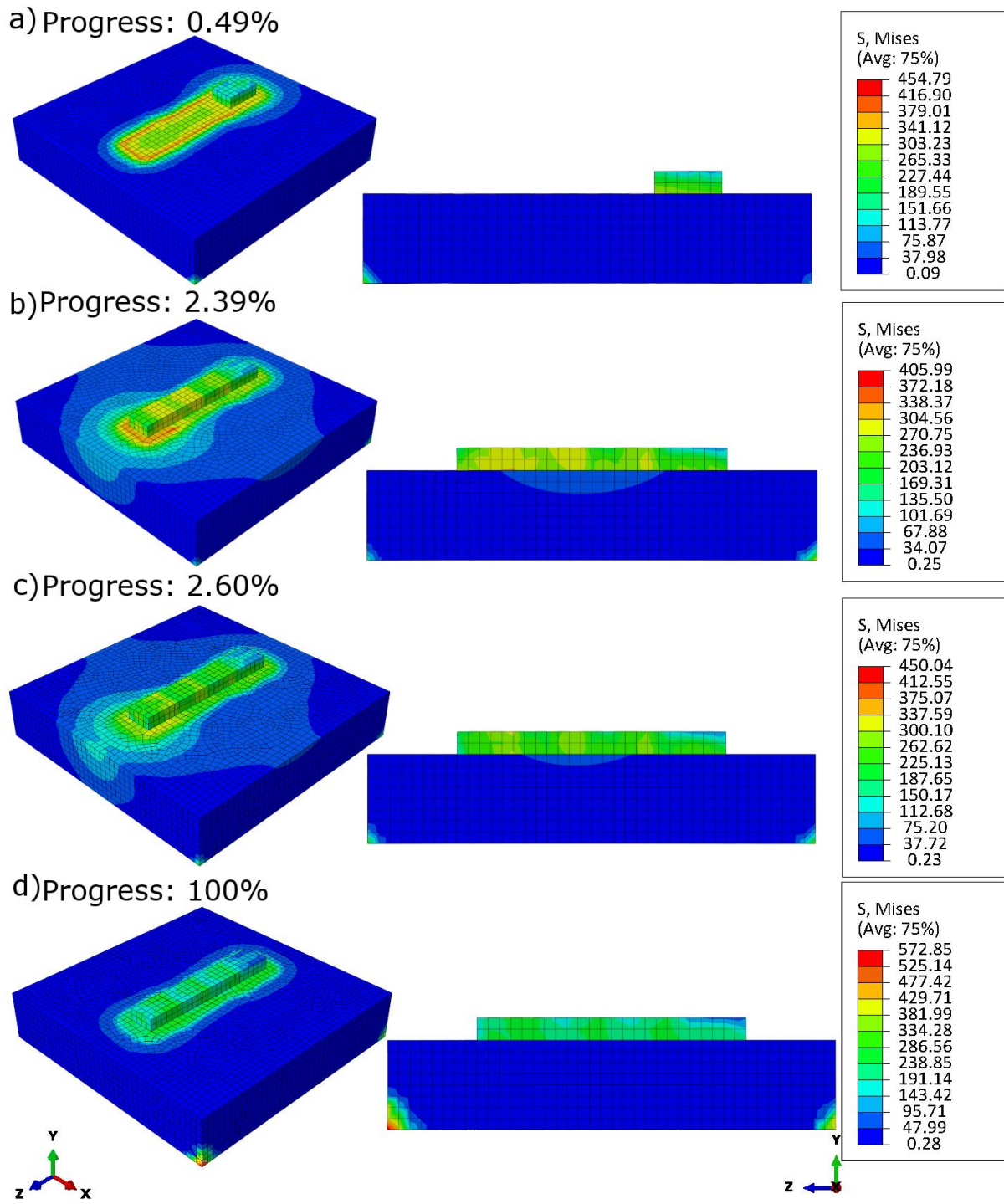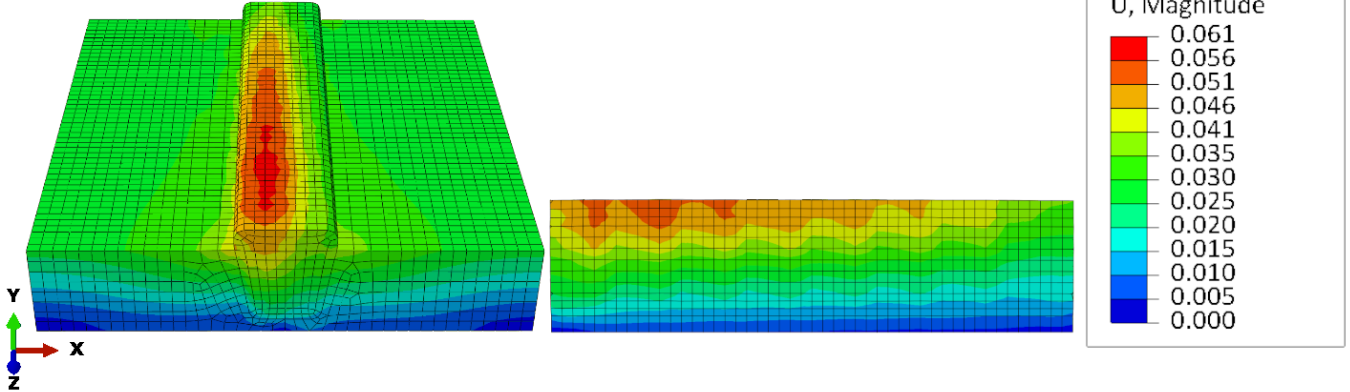
Figure 113 The stress distribution at the different time points (a, b, c and d) of the welding process of the coupled temperature-displacement model of the case 5.

In Figure 113 the stress distribution of the second coupled temperature-displacement model, named case 5, is presented. This model is based on the geometry of the case 3. In Figure 113a) it can be seen the very beginning of the welding process. As in this case the surface film coefficient is applied only to steel surface, the weld path is not affected by the described

coefficient control. It means that the steel table, whose temperature is predefined to 300°C at the beginning of the process, cools down very quickly to the ambient temperature of 20°C, excluding the weld path surface. It creates the temperature difference and causes the increase of the stresses in the region, where the weld path will be placed.

Like before, the placing of the weld elements upon the steel surface takes a very short time and after 1-2s the cooling process starts (Figure 113b). The appearance of the weld elements decreases the stress values in just aforementioned region that suggests the smoother distribution of the heat exchange due to presence of the contact surface of the weld.

In Figure 113c) the beginning of the cooling process is presented. The highest values of the stresses are present in the corners of the steel table. The stresses, which occurs within the weld and in its surroundings are decreasing. They are temperature-dependent, as it can be clearly seen that the first weld beads, which are cooled faster than the last ones, faster reach the stress on the level of 0.23 − 100MPa (progressively darker blue colours in Figure 113c) and Figure 113d). The highest peaks of the stress values in the corners of the steel table are caused by the trials of the geometry to move due to the arising stresses, which affects it mostly in the fixing region. Such phenomenon is common during numerical calculations, but is irrelevant to the results and can be neglected. It can be seen in *Figure 113*d that the overall stress values in the weld and in the table surface are decreasing from around 300MPa before the cooling to around 200MPa after.
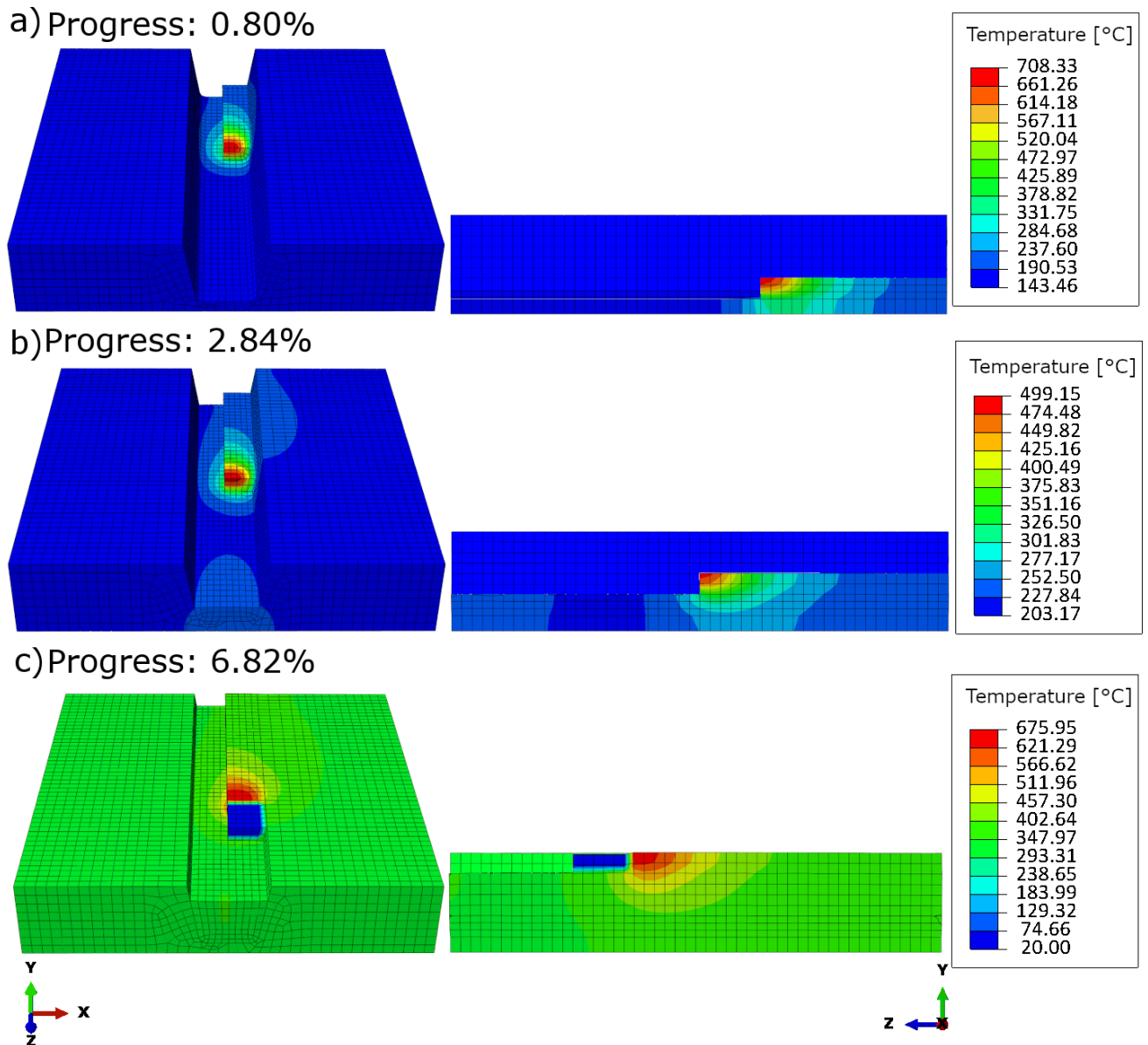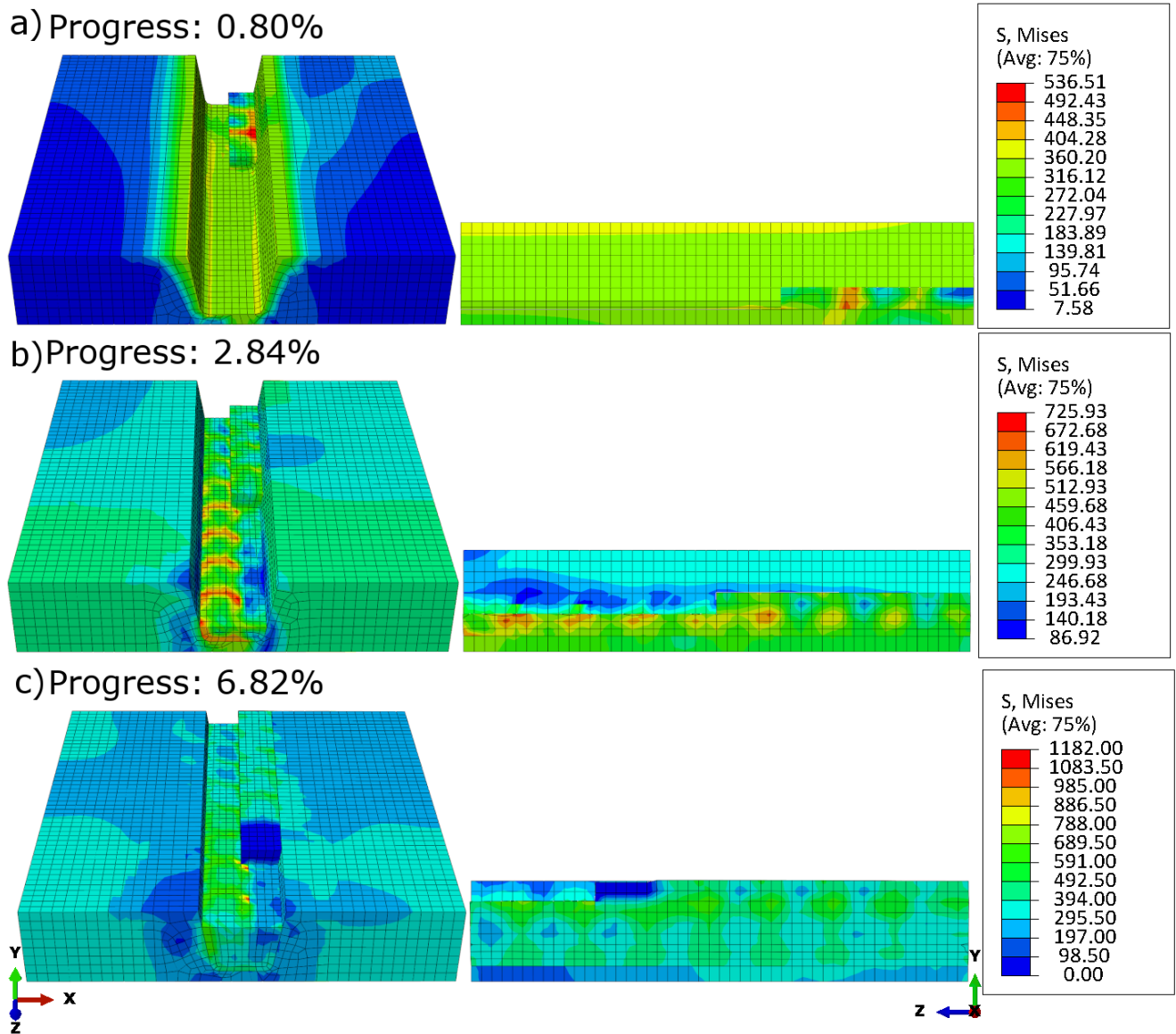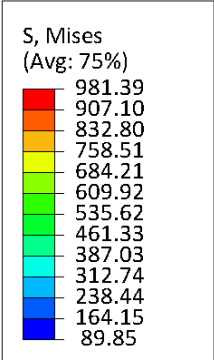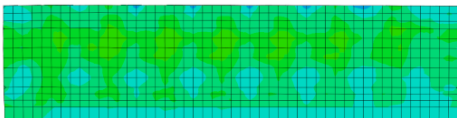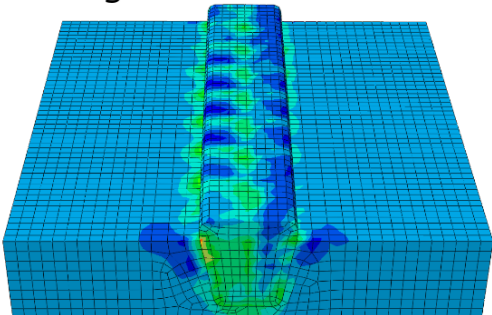
Figure 114 The temperature distribution at the different time points (a, b and c) at the beginning of the welding process of the coupled temperature-displacement model of the Case 6.
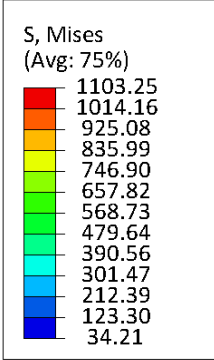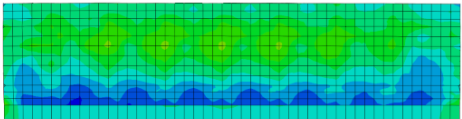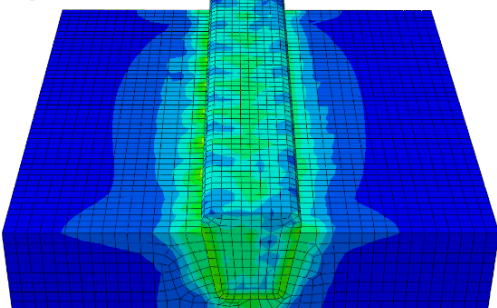
In *Figure 114* the temperature distribution at the beginning of the welding process of the case 6 is presented. Compared to the other cases, this model uses a quite complicated geometry, which is considered to be close to the case from the Zhang et al. [170]. There are 80 weld beads stacked in 5 layers of two rows of 8 beads per layer. The first four layers are hidden inside the deep groove and the last layer is placed upon the previous, the fourth one, above the steel table. The element number is the greatest among the other cases, and it is 20 064 with the 30 030 nodes. Additionally, the symmetry conditions in all of the three directions on the steel

table surfaces are applied (*Table 42*), which helped to avoid the high values of the stress at the fixed corners.

In *Figure 114*a) shows that at the beginning the predefined temperature of the weld table decreased only a little, around 7°C. The temperature at the bead is quite high, despite the low body flux value, deep penetration and large beam radius, comparing to the other cases (*Table 43*). The film coefficient is also higher than usual (*Table 42*). The larger temperature inertia can be caused by the symmetry condition, which creates the dimensions of the table larger that slows down the cooling and also, the fact that new beads are placed upon each other can create the cumulative effect. In *Figure 114*b) it can be seen that the temperature at the bead is lower than in *Figure 114*a), but the temperature of the weld table increased by about 50°C, which suggests that the part of the heat is used for the heating of the table. In *Figure 114*c) the table temperature is already high, around, 240°C – 400°C. The new bead has the temperature of 20°C, because when it appears, which takes around $1x10^{-7}$s, the heat source is still positioned at the old bead and would not move forward yet at this time.

As this case is longer and more complicated than the previous ones, the only welding process was presented here, the cooling was reported further in the text.
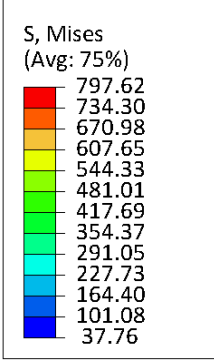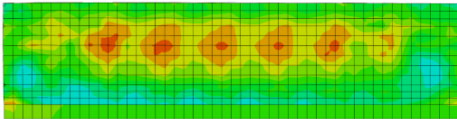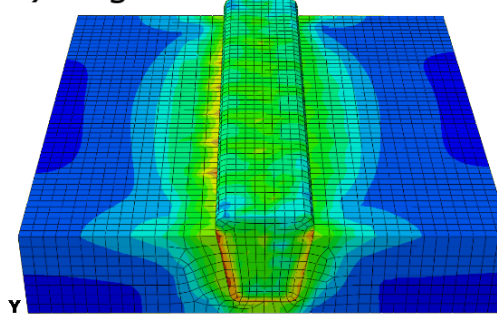
Figure 115 The temperature distribution at the different time points (a, b and c) at the cooling of the welding process of the coupled temperature-displacement model of the Case 6.

In *Figure 115* the temperature distribution during the cooling process of the case 6 is presented. The welding process in this case is 8s long, where every bead is placed upon the material in 0.1s. After that, the cooling process proceeded, which lasted 80s. During this time, as it can be seen in *Figure 115* the temperature drops from nearly 400°C in the hottest areas to the almost evenly distributed 170°C – 180°C within the cross section.

It can be seen in *Figure 115*a) that there is almost 20°C difference at the temperature at the front of the table compared to the back, in correlation with the heat source movement path. After around 40s, after the middle of the cooling process the temperature field is stabilised and

212

did not change greatly until the end, what can be seen during comparison of *Figure 115*b) and *Figure 115*c). As the driving force of the cooling is dependent on the temperature difference between the objects, in which the heat exchange occurs, the fastest temperature change occurs at the beginning of the cooling in air or water, because the temperature difference is the highest.

As it is expected, cooling rate is the highest in the layer of the weld elements, which is not embedded within the surface. The contact with such a quickly cooled object drives cooling more quickly than the rest of the table, despite the surface film coefficient applied to the table weld surface.
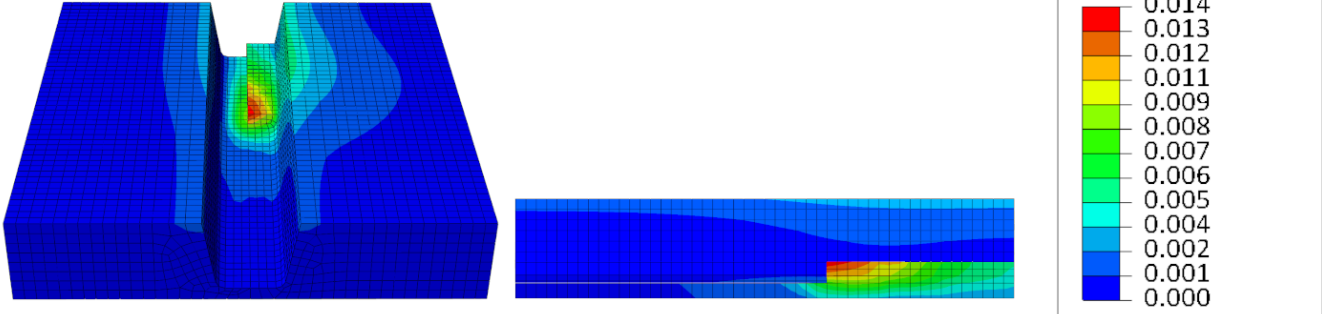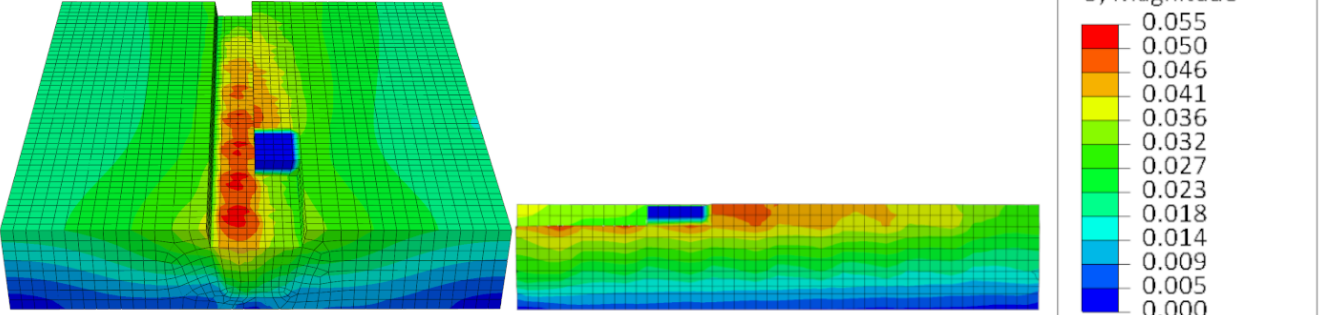
Figure 116 The displacement distribution at the different time points (a, b and c) of the welding process of the coupled temperature-displacement model of the Case 6.

In *Figure 116* the displacement from the original position during the case 6 is presented. It can be seen in *Figure 116*a) the area of the nodes, which are displaced during the whole process, is related to the temperature field (*Figure 114*) more than to the stress field (*Figure 117*). The interesting phenomenon can be seen in *Figure 116*b) and c) where the displacement is marked as the consecutive red 'stains' on the path of the moving heat source. This cannot be seen in the temperature field in *Figure 115* unless the temperature range on the legend is changed. In *Figure 116*c) there can be seen that this concentrated displacement is not much affected by the cooling and the visible on the cross section 'waves' on the couple last beads are visible until the end of the cooling process.

Also, the surface of the weld table is much more displaced than the bottom due to the heating from the heat source. This effect is strengthened in the middle of the model at the bottom, where there is the vicinity of the hot weld, although it is visible at this time point probably due to the fact that the temperature does not reach the ambient value completely.

Figure 117 The stress distribution at the different time points (a, b and c) at the beginning of the welding process of the coupled temperature-displacement model of the Case 6.

In *Figure 117* the stress values at the certain time points during the welding process of the case 6 are presented. It can be seen that such formulated welding process introduces high values of the stresses on the contact surface between the just-placed weld bead, the internal wall and floor of the groove within the steel table and the contact surface between the welds. It can be seen in *Figure 117*b) the characteristic red waves of the higher stresses, which are localised in the aforementioned regions. These places fade with the process time, what creates the complicated chessboard look-like within the material, with the region of higher and lower stress values, arranged alternately. The stress distribution, which can be seen on all of the images in *Figure 117*(a, b and c) within the steel table is inhomogeneous. It is very dependent from the

current place of the heat source and it slowly arising together with time. It can be also seen that with the stress values, which arise in each of the newly-imposed weld, are higher than the previous one and it is not seems to lowering with the progress of the process time.

Figure 118 The stress distribution at the different time points (a, b and c) at the cooling of the welding process of the coupled temperature-displacement model of the Case 6.

In *Figure 118* the stress values at the certain time points during the cooling after the welding process of the case 6 are presented. It can be seen that in contradiction to the other variable, the stress path is very complicated during the cooling part of the process. In *Figure 118*a) the characteristic alternating regions due to the higher stresses at the contact surfaces can be seen. It can be also seen that the highest values of the stress are within the model geometry, probably at the weld-steel boundary. The right row of the weld beads in the outer layer has

lower stresses than the on the right, as it was longer cooled down, because it was created first. The stress values are within the plastic range except for the max values.

In *Figure 118*b) around the middle of the cooling process time is presented, where it can be seen that the stresses within the steel table are much lower than at the beginning of the process, around 100°C – 200°C. Although the stresses within the weld continue to increase, especially the maximum values, which can be related to the large temperature change at the beginning of the cooling process and with the phase transformation model, which is activated during the cooling. It can be also seen on the image of the cross section on the right that the very low stresses are present at the bottom of the weld, which can be related to the symmetry condition in this region, creating the relatively thin layer of the steel in vicinity of the weld, which prevents the introduction of stress.

In *Figure 118*c) the end of the cooling process is shown, and the stresses within the geometry are lower. The maximum stress values decreased, which allowed for the regions of the lower stresses to be visible, like the contact surfaces between the weld and the table. Although their colour is changed to brighter red, comparing the legend of *Figure 118*b) and c) the values are increased only slightly. Also, there can be visible the pattern of the 6 bright red regions on the cross section, and that at the end of the cooling the stress values within the table increased again. These differences are probably introduced by the ongoing phase transformation, and additionally by the mismatch of the local volume due to the various values of the heat expansion coefficients of the weld and the steel material, which causes the compressing of the weld by the steel surrounding.
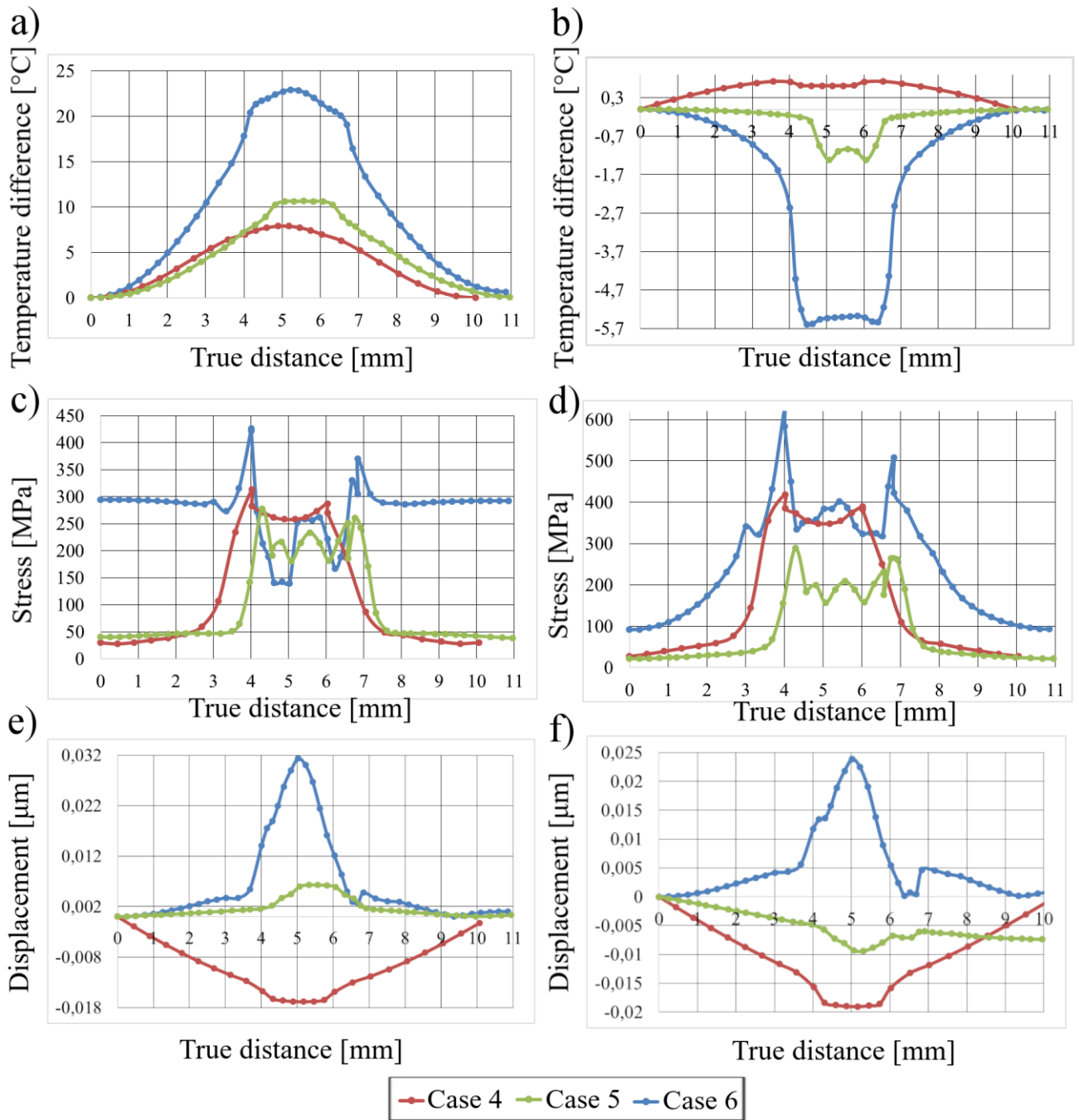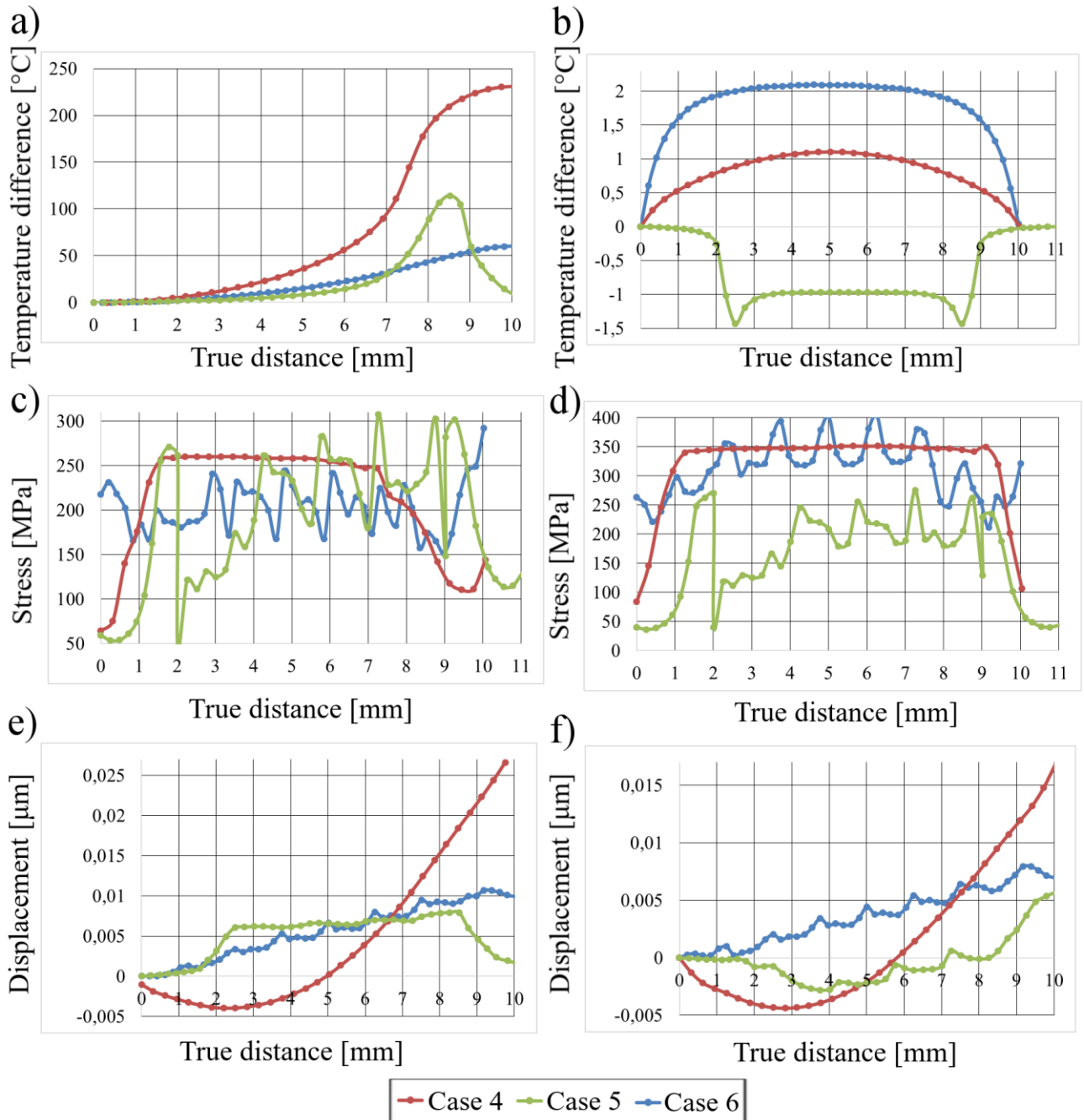
Figure 119 The temperature differences [°C] (a, b), stress [MPa] (c, d) and displacement [mm] (e, f) of the coupled temperature-displacement cases (4, 5, 6) obtained from the path of the nodes across the table and the weld before the cooling (a, c, e) and after cooling process (b, d, f).

Figure 119 presents the results obtained from the coupled temperature-displacement cases from the path of the nodes situated across the table and the weld. The results present the temperature differences [°C], stress [MPa] and displacement [mm] before and after the cooling

process. The highest temperature differences are present, in descending order in case 6, 5 and 4 (*Figure 119*a). It is characteristic that this order is not changed after the cooling process (*Figure 119*b). In the case 4 it can be seen that despite the smallest temperature differences at the path after the welding process, the cooling does not change the sign of the changes. It means that in this case the temperature of the weld is still higher than in the surroundings, which can be caused by the geometry of this model, with the larger contact with (the bigger than in the other cases) weld beads. Case 5 presents a quite typical response, where there is not a very high difference between the table surrounding the weld, and the weld, around 10°C. After the cooling the temperature of the weld drops faster than in the bulk material of the steel table, with characteristic 'horns', as the corners of the weld cool faster because of the much greater contact surface with the ambient. Case 6 presents the highest values of the temperature differences, both before and after the cooling, which is connected with the greater amount of the weld material.

*Figure 119*c and d present the stress distribution across the table and the weld, before and after the cooling process for each of the coupled temperature-displacement cases. It can be seen that the stress values in the first two cases are similar, not much above zero at both ends of the steel table, and rises towards the weld, where it reaches its peak, and then diminishes symmetrically. In the case 6 there is high stress introduced by the welding, around 300MPa, in the whole cross section area of the table, what can be caused by the complicated multi-layered welding path. In all three cases it can be seen that the corners of the weld are accumulating stress. In the case 4, where the beads are 'hidden' in the welding groove, there is lack of three consecutive peaks on the weld, visible in the other cases. These peaks are connected with the weld geometry, which include the corners between the steel table and the weld that creates additional stress-accumulating regions.

Although the stress values in the case 6's weld are lower than in the steel table after the cooling process this is the case, where the values increased the most, from a range 150 MPa – 250 MPa to 350 MPa – 600 MPa, which was expected to have been caused by the phase transformation process. The stress of the case 4 increased not much from a range 250 MPa – 300 MPa to 350 MPa – 400 MPa, and in the case 5 they widened from the 200 MPa – 270 MPa to 150 MPa – 300 MPa. The stresses in the steel table in the case 6 decreased to the 100 MPa level.

*Figure 119*e and f presents the displacement from the original position of the nodes since the beginning of the simulation. The change of the sign in case 4 is a result of the results being obtained after the welding process and the displacement is recorded from the beginning of the process. It means that in the case 4 the temperature of the surface, from which the path of nodes were obtained, cooled down below its predefined temperature, which moved the nodes from its original position according with the shrinkage due to the cooling. It can be seen that there is a little difference in this case between the after welding state and after the cooling state. It is slightly different in the case of case 5 and case 6, in which the differences are greater, and also the peaks connected with the phase transformations are visible after the cooling.

Figure 120 The temperature differences [°C] (a, b), stress [MPa] (c, d) and displacement [mm] (e, f) of the coupled temperature-displacement cases (4, 5, 6) obtained from the path of the nodes along the table and the weld before the cooling (a, c, e) and after cooling process (b, d, f).

Figure 120 presents the results obtained from the coupled temperature-displacement case 6 from the path of the nodes situated along with the table and the weld. The results present the temperature differences [°C], stress [MPa] and displacement [mm] before and after the

cooling process. It can be seen in *Figure 120*a that there is a characteristic trend of ascending temperature with the path, a result of the results being obtained in the direction of the welding path. It means that the temperature of the weld beads at the end of the path is higher than at the beginning, as it is still under the influence of the heat source, which is deactivated at the end of the welding part. It can be seen that the higher temperature differences values are in the case 4, what can be connected with the way of defining the heat source as the embedded value with movement controlled by the amplitude method, instead of the subroutine Fortran code, like in the other cases. The difference is large, about 250°C. In the case 5 there is a visible peak which occurred due since the weld material ends and the steel table, with the different parameters, is included into the results. The lowest temperature difference values, about 50°C, are recorded in the case 6, which is a result of the heat source speed being higher than in the other cases and the larger bulk of welding material keep high temperature values at the beginning of the path, making the differences lower. *Figure 120*b gives values after the cooling part. It can be seen that in the cases 4 and 6 the temperature of the weld is still higher than the steel table. This is because in these cases the steel table is not included in the node path, unlike in the case 5, which also presents the characteristic 'horns' of cooled faster corners of the weld. The change of sign in case 5 means that the weld is cooler compared to the steel table can be connected with the smaller amount of the material, with the large surface with contact to the ambient, relatively to the other cases.

*Figure 120*c and d show the stress distribution. It can be seen that in the case 4 the line of the stress is very straight, without many peaks, like in the case of the other cases, in both parts, before and after the cooling. The decreasing stress in *Figure 120*c can be connected with uneven movement speed due to the amplitude method control. The peaks small peaks that can be observed in the other cases are certainly connected with the consequential adding of the new weld beads. The stress values in case 5 are lowered by the cooling for about 50 MPa, the peaks are smoothed out. This is similar to case 6 where the stress distribution is also smoother, but in this case the stresses are higher after the cooling, which can be connected with the multi-layered weld path which is much larger than in other cases.

In *Figure 120*e and f the displacement from the original position of the nodes since the beginning of the simulation alongside to the weld is presented. It can be seen that in the case 4 the displacement is connected with the stress curve from *Figure 120*c, as the change of the stress curve, around 5-6 mm is related to the change of the sign of the node movement in *Figure 120*e. In the cases 5 and 6 there can be seen the characteristic peaks, which correspond with the aforementioned stress peaks. It is interesting that the cooling created the inverted movement of

the node in case 5, which can be connected with the cooling of the weld, *Figure 120*b. Also, it can be seen that the cooling process lowered the displacement values in all of the cases. Although in this case the phase transformation peaks cannot be clearly distinguished, the overall changes in the material response is obvious.

The results obtained allowed detailed stress investigations for all three coupled temperature-displacements models were performed with respect to every direction. In the first model in the x direction the compression stresses are present under the weld (-460 MPa), where the extraction of the weld with the tensile stress within +400 MPa are influencing the bottom of the steel table. The lower tensile stresses are also observed within the steel table (+260 MPa). In the y direction the compression stresses are present in the steel table at the contact surface with weld (-350 MPa), which are compressed by the extraction of the weld (+380 MPa). In the z direction there are compression stresses present in the both places from the previous directions: contact surface walls (-250 MPa) and under the weld (-400 MPa) within the steel table. Inside the central region of the weld there are tensile stresses present (+300 MPa), which increase towards the contact surfaces (+600 MPa).

In the second model in the x direction the compression stresses are present within the steel table: in close vicinity of the weld and across the table (up to -300 MPa). The tensile stresses are present across the table in the region before and after the weld (+70 MPa) and under the weld (+100MPa). Within the weld the compressive and tensile stresses appear alternately. In the y direction the tensile stresses occur in the regions between the weld beads (+80 MPa) and the tensile stresses are present within all the steel table at a low level (-30 MPa), increasing towards the surface (up to -150 MPa). The maximum tensile stresses are present under the weld (+116 MPa), and the maximum compressive stresses are present between the particular weld beads (-230 MPa). In the z direction the low tensile stresses (up to +50 MPa) are present within the steel table, increasing towards the weld (up to +100 MPa) except the regions before and after the weld, across the table, where there are tensile stresses (-50 MPa). In the close vicinity and within the weld the tensile stresses achieve high values (-300 and -175 MPa).

In the third model in the x direction there are tensile stresses within the steel table surface (+100 MPa). The highest values are at the surface around the weld in the middle of the model (+250 MPa – +350 MPa). The higher stresses are on the side, where the second row of the welding material was poured, which was limited from both sides by the steel table and the already poured first weld row of the layer. The tensile stresses are also present around (up to +350 MPa) and within the weld also, arising from the weld bottom (up to +250 MPa). The compressive stresses are present below the weld in the steel table (up to -400 MPa), and in its

layer, which is above the steel table surface line (up to -250 MPa). In the y direction the tensile stresses are present under the weld and in its lower layers (+250 MPa). The highest values are at the surface with the steel table (+600 MPa). The compressive stresses are at the steel table surface (-100 MPa) and the region of contact with the weld surface (-350 – -400 MPa). Within the weld there are tensile forces (-100 MPa) in the layers above the steel table surface line. In the z direction there are tensile stresses inside the weld below the steel table surface line (+400 – +650 MPa), when above that line these values are little lower (+200 – +400 MPa). The tensile stresses are present within the steel table, especially around the weld region (-315 MPa).

5.4. Summary

As various kinds of welding processes are widely used to connect the component parts in the RPV's construction, a model was developed to predict the results for welding of SA508 gr. 3 steel, such as the temperature, the stress and the displacement. The model was simplified to demonstrate the developed approach, but the results generally were satisfying enough and in good correlation with the literature [169]–[172]. The distribution of the temperature achieved the characteristic M-shape, and there was a visible mechanical response corresponding with the before and after cooling state, related to the material extraction/contraction and the dilatometric effect. Although the obtained stress results are strongly related to the specific conditions of each case, there are usually tensile stresses present in the weld, with especially higher values located in the lower layers and at the contact surfaces. The compressive stresses within the welds are present between the weld beads, represented by the separate sets of elements. The tensile stresses in the steel table are in some cases under the weld and in the centre of the part, but mostly the compressive stresses are present at the contact walls and within the whole geometry, where the values are a bit of lower.

6. Conclusions and future work

6.1. Conclusions

The aim of this project was to perform a complex analysis of the residual stresses that arise during the heat treatment of heavy and large forgings. The investigations were performed by constructing detailed numerical analyses, based on the finite elements method (MES) and supported by experimental tests. The results allowed for the development of the numerical model, which was using the data obtained from the dilatometric and mechanical tests along with the micrographs from the optical microscope (LM) and the data collected from the manufacturing process at Sheffield Forgemasters International Ltd. The model was validated by the calculating the temperature, stress and strains fields in the large-size heat-treated forging, basing on the industrial case, and was used to calculate similar results for the numerical case, which was based on the simplified welding process, typical for the SA508 gr. 3 steel. The model is based on the new approach, which allows for predicting, controlling and adjustment of the cooling rates within the cross section to manage the residual stress, which arise during the heat treatment of the large-size forgings.

In the first stage of this project a simplified 3D thermo-mechanically coupled numerical model based on the finite element method was developed, capable of taking into account changes in the specific volume during both austenite-ferrite transformation and the local thermal contraction during cooling from austenite temperature region. The model can be coupled with any of the available phase transformation models allowing simulation of the inhomogeneous metal part contraction due to both thermal contraction and the phase transformation connected dilatometric effect. The model can also be used as a direct model during inverse calculations for identification of phase transformation model parameters on the basis of measurement of the dilatometric effect. The following two commercial FE codes, such as MSC Marc 2013.1.0 and Abaqus/Standard 6.12, were used for solving the non-steady state 3D problem of the metal expansion/contraction during cooling from the austenite region. The numerical calculations have been performed for illustration of the predictive capabilities of the developed thermal-mechanical finite element model. For this purpose, it was combined with the simplified phase transformation model.

It has been shown that a discrete random distribution of the appearing ferritic phase within the sample cross section results in more gentle changes of the section contraction with time during cooling than that in the case of the conventional (homogeneous) approach. The difference is quite small, about 5-15 μm, but it is large with respect to the small dimensions of the sample. This indicates that during the microstructural evolution investigations into the phase transformation, the origins of the phase transformation within the cross section of the sample should not be ignored. Most of the literature is focused on the volume of the particular phases, but ignore important factors that transformation has on the outcome. This result shows that these phenomena are worthy of closer investigations.

More numerical experiments were performed that showed that by including the changes in the order in which the new phase appears during modelling the shape of the strain curve can be controlled. This means that one is able to change the shape of the transformation peak on the strain curve without changing the boundary conditions of the process. This discovery should turn the attention that perhaps the phase transformation origins present within the material could determine its growth and then, its final volume.

The temperature distribution within the volume of the small cross sections of the material, like in the case of the tested cube 10x10x10mm, can be assumed as homogeneous for the low cooling rates, such as 5°C/s. However, the temperature gradients within the volume are increased and influence the results of prediction at high cooling rates, 80 and 163°C/s even for such small dimensions. The differences could take up even to 150°C. It has to be remembered that the boundary conditions of the process have to be adjusted to the conductivity parameters of the material.

It has been shown that additional refinement of the finite element mesh can affect the model prediction and also has to be taken into account. The reported difference in the strain results were even up to 5 μm for the small dimension model (cube 10x10x10mm) between 125 elements per model to 1000 elements, and the same 5 μm in the dilatometric model, between 3778 elements and 52058. The change of the mesh element number influenced the final results because of the more shredded distribution of the new phase during the phase transformation. The new phases had slightly expanded volumes relative to the remaining austenite elements. The element number in the model is necessary to be taken into consideration when the optimum mesh size is chosen for the direct model.

After further development of the model the phenomenon related to the phase transformation and the transient temperature field due to the cooling during the dilatometric test was simulated. The model was able to predict the local values of the cooling rate at the depth

of the material during cooling. It was shown that the differences between temperature values measured at the same point in a material are greater for higher values of the cooling rates, which can cause the higher values of residual stress. The differences between the temperatures achieved on the particular nodes from the node path directed inside to the material were as follow: 2°C, 5°C, 7.5°C, 10°C, 11°C (±0.5°C) between the highest tested cooling rate (100°C) and the rest of them. The deviation of 0.5°C is the range of the temperature differences on the nodes between the rests of the cooling rates. These results confirms that the residual stresses are created at the depth of the material, where the differences with the cooling rates follow the different thermal expansion within the regions.

It was also shown that the highest values of the local cooling rates appears at the beginning of the cooling process at the surface. Although, the differences were noticeable for a very short time (up to 200ms), which was related with the small dimensions of the simulated dilatometric sample, it has to be noted that these values increase in the large-size elements.

The change in the cooling rate value caused a delay of the transformation start temperature. It was related to the different transformation ratio between austenite and ferrite elements in time periods of the phase transformation. This means that for the different cooling ratio there was a different amount of the transformed phase, which corresponded with the volume fractions for the characteristic temperatures.

The hardness tests on the material that is typically used in construction of large-size elements in nuclear reactor pressure vessels, SA508 gr. 3 steel, were performed on the samples of raw material and after the dilatometric tests with the different cooling rates of 0.05°C/s, 0.1°C/s, 0.5°C/s, 1°C/s, 5°C/s, 10°C/s and 100°C/s. The results are, correspondingly: 300.1 HV, 330.6 HV, 245.1 HV, 464.1 HV, 470.7 HV, 656.9 HV, 563.7 HV. Together with the micrographs they allow for the identification of the phases and structures within the material, which were a typical for the SA508 gr.3 steel mix of martensite, allotriomorphic ferrite, Widmanstätten ferrite, pearlite and tempered upper and lower bainite. Also, austenite/martensite islands, Mo_2C carbides and cementite were observed. Very characteristic A-segregates were also clearly visible. The cooling rates values used are in range which can be met during the heat treatment of the RPVs forgings. These findings confirm that the microstructure of such elements can be highly heterogeneous.

Two of the samples were also heated to 890°C and 1100°C held for 30 minutes and then quenched in water for carbide identification. Light microscopy and Vickers hardness tests were performed on the dilatometer samples. The microstructure of mixed Widmannstäten

ferrite, allotriomorphic ferrite, martensite and bainite was observed, consistent with the published CCT diagram for this steel.

In the case of the quenched samples there were no visible presence of carbides, what can suggest that they dissolved in both cases, at the temperature 1100°C and 890°C, or that they were too fine to resolve by optical microscopy. The microstructures of both the quenched samples, I and II, were very similar but it can be seen that sample II, which was quenched from the higher temperature had a smaller grain size. The quenched samples had a homogenous martensitic structure characterized by high hardness values. The grain size was quite similar in both case, about 300μm, and the hardness was similar, which was around 432 HV, was relatively small and could be related to the segregation during the cooling.

The final 2D model was constructed to predict the mechanical behaviour of the material subjected to cooling based on the change of a local volume due to the temperature change and phase transformation. The model was used for calculation of the stress distribution in the industrial case of heat treatment of the forging. The obtained results were satisfying and closer to the measured ones than those predicted from the developed in literature model, which had up to 100°C at the largest difference.

The model was used to calculate the cooling rates at the quarter thickness location and in the mid-wall of the model geometry. The calculated cooling rates were about two times higher inside the part than those presented in literature. The calculated transient temperature field allowed for estimation of the cooling rate at every node in the model at every moment during the process. These data were used to assign the thermal expansions coefficients obtained from the dilatometric test to the model. This allowed the prediction of the alteration of the local volume due to the temperature change and phase transformation.

The changes in the values of the angles between cylindrical and flat surfaces in the rectilinear model geometry reflecting the cross section of the treated forging were calculated for two kind of meshes, simple and fine and were compared to the values registered during the industrial process. The absolute differences between the angles before and after the heat treatment were calculated and one average value was extracted for every set of values (measured after the quenching in the industrial process, calculated from simple mesh model and calculated from fine mesh model). These average absolute values of all the angles were calculated to present the average differences between the results from the industrial process, the results calculated from the model with simple mesh and the results calculated from the model with fine mesh, together with the standard deviations.

228

The stress and strain intensity within the model during the cooling process were also presented. The highest values of the tensile stress were present at near the surface regions, up to 75mm depth. They were usually around 60 – 200 MPa, arising in the small regions like inner corners or tops between the edges even to +500 MPa. The compressive stresses were reported mostly inside the model in the range of 0 – 150 MPa, arising even up to -500 MPa at the edges. The results of the strain intensity had their highest values in the external flange, from 0.105 at the beginning of the process to around 0.0837 at its end. The differences between the coarse and the fine mesh were not large in this case.

The differences between the measured and calculated angles were 0.03° and 0.02° for the simple and fine mesh respectively, which is nearly the same. The standard deviation value of the results calculated from the model with simplified mesh was only 0.1° smaller, while the one calculated from the model with finer mesh was 0.15° greater compared with that calculated from the measured angles values after quenching in the industrial process. All of the calculated differences between the models and industrial data were within the range of standard deviation. The absolute differences calculated between the numerical results and the industrial process data were 0.66° and 0.70° respectively. The results confirm the relatively low sensitivity of the FE model to the mesh within the chosen range of the elements.

The developed model was validated in the last section of the work, where it was used to calculate the transient temperature field, stress distribution and the node displacement in the simplified welding case. The case was based on the approach where the weld material was placed on the steel table and then it is heated by the moving heat source. After that it is cooled down. The three thermal models were developed to calculate the transient temperature field and then three coupled temperature-displacement models for stress/strain calculations. It was reported that the temperature field is strongly connected with the geometry, the place of the weld and the heat source parameters. Although the temperature of the weld was nearly 1100°C, the steel table was only heated by the contact with the hot weld, which causes its temperature drop at the beginning of the process. The highest temperature rise in the steel table, about 320°C, was reported in the model where the large weld beads were placed at the center of the table. In this model the highest temperature difference between the weld and the steel table after cooling s was also reported, about 2.2°C in respect to the 0.3 and 0.25 in the two other thermal models.

There were three coupled temperature-displacement models developed: with the weld groove inside the material, with the weld placed upon the material, and with the complicated geometry, closest to the real one and widely used in the literature. After applying the cooling

conditions the residual stress values in the first case were observed within the whole weld and within the steel table in close to the weld regions. The temperature distribution presented in a form of temperature differences on the surface, measured in both directions, across and alongside, presented the characteristic M-shape. The mechanical response corresponding with the before and after cooling state, related to the material extraction/contraction and the dilatometric effect of the phase transformation could be also observed. It was indicated that the particular cases geometry strongly influenced the results. Beside this observation, the stress results showed that a tensile stresses arose in the weld, with especially higher values located in the lower layers, interacting on the bottom of the steel table and at the contact surfaces located at the walls. The compressive stresses within the welds are present between the weld beads, represented by the separate sets of elements, which were expanding and contracting due to its temperature, impacting on each other. The tensile stresses in the steel table are in some cases under the weld and in the center of the part, but mostly the compressive stresses are present at the contact walls and within the whole geometry, where the values are a bit of lower. Taking into the account the necessary simplifications which had to be applied, the obtained results range from -460 MPa to +650 MPa, strongly related to the measuring direction, conditions and geometry of the particular case, which are in good agreement with the results from the cited literature.

6.2. Future work

As the numerical modelling of the phase transformations through the control of the heat expansion coefficient of the material is recognized in the thesis as the powerful tool in predicting the material stress/strain response during the processing it needs to be further explored. Due to the limitations, there were a number of simplifications that had to be made in order to obtain the satisfying results. The several aspects which are worthy of further exploration were omitted like the effects related to transformation induced plasticity and stress induced transformation. The influence of the individual physical phenomena on the stress management should be accessed during further stages of the topic investigations assuming particular geometries, the variations of technological parameters, chemical content and structural features of the processing parts. Also, it is recognized that the predictive powers of the models are dependent on the material data, so it is worth increasing the base of the

dilatometric tests as an input to the analysis. This will give more information on the transformations start temperatures, the volume phases calculations and the better adjustment of the Avrami-based equations. As the particular thermal expansion coefficient values are crucial for the developed approach, the recognition of the process-parameters-dependent correlations of the TEC of specific phases of the used material would enhance the model.

One of the most common topics in the related with the SA508 steel topic is the correlations between the grain size and the material response. Including of such aspect in the developed model would also be a profitable path to follow.

As the welding process is still very popular way of processing the SA508 steels, further development of the model in the direct welding approach would also be a beneficial.

As all mentioned factors may impact the outcomes they should be undertaken in further analysis.

7. References

[1]   G. Maltese, "Particles of man (part I)," *Lett. Mat.*, vol. 1, no. 3, pp. 145–154, 2013.

[2]   U.S. Department of Energy, "The History of Nuclear Energy," vol. 17, no. 1, pp. 83–85, 1984.

[3]   A. A. Kiely, "Characterisation and interpretation of austenite grain growth kinetics in an advanced nuclear pressure vessel steel," University of Cambridge, 2016.

[4]   H. Pous-Romero, "Quantitative basis for the structure and properties of a critically-important pressure vessel steel," University of Cambridge, 2014.

[5]   E. Fermi, E. Amaldi, E. Segre, O. D'Agostino, and F. Rasetti, "Artificial radioactivity produced by neutron bombardment," *Proc. R. Soc. London. Ser. A, Contain. Pap. a Math. Phys. Character*, vol. 146, no. 857, pp. 483–500, 1934.

[6]   R. Jacobs, "Born violent: The origins of nuclear power," *Asian J. Peacebuilding*, vol. 7, no. 1, pp. 9–30, 2019.

[7]   A. Einstein, "The principle of conservation of motion of the center of gravity and the inertia of energy," *Ann. Phys.*, vol. 20, pp. 627–633, 1906.

[8]   "National Institute of Standards and Technology," *U.S. Department of Commerce*. [Online]. Available: https://physics.nist.gov/cgi-bin/cuu/Value?mn%7Csearch_for=neutron+mass. [Accessed: 23-Jan-2019].

[9]   E. De Sanctis, S. Monti, and M. Ripani, *Energy from Nuclear Fission. An Introduction.* Springer, 2016.

[10]   N. Mukunda, "Enrico Fermi. Life, Personality and Accomplishments," *Resonance*, vol. 19, no. 1, pp. 8–17, 2014.

[11]   G. Jezierski, *Energia jądrowa wczoraj i dziś*. Warszawa: Wydawnictwo Naukowo-Techniczne, 2014.

[12]   A. Roy, "Enrico Fermi — The complete physicist," *Resonance*, vol. 19, no. 8, pp. 684–703, 2014.

[13] "Nuclear Regulatory Commision (NRC) website." [Online]. Available: https://www.nrc.gov/. [Accessed: 14-Feb-2020].

[14] K. L. Murty, *Materials' ageing and degradation in light water reactors : mechanisms and management*. Woodhead Publishing, 2013.

[15] J. Kubowski, *Elektrownie jądrowe*, IInd. Warszawa: Wydawnictwo Naukowo-Techniczne, 2014.

[16] R. Duffey and I. Pioro, "Ensuring the future of nuclear power," *Mech. Eng.*, vol. 141, no. 11, pp. 30–35, 2019.

[17] E. R. Masterson, *Introduction to nuclear reactor physics*. CRC Press. Taylor & Francis Group, 2018.

[18] WNA, "Plans For New Reactors Worldwide." [Online]. Available: https://www.world-nuclear.org/information-library/current-and-future-generation/plans-for-new-reactors-worldwide.aspx. [Accessed: 18-Feb-2020].

[19] S. Kawaguchi, H. Moritani, H. Tsukada, K. Suzuki, E. Murai, and I. Sato, "Current forging technology for integrated type steel forgings for nuclear steam supply system components," *Nucl. Eng. Des.*, vol. 81, no. 2, pp. 219–229, 1984.

[20] C. J. Duffy, "Modelling the Electron Beam Welding of Nuclear Reactor Pressure Vessel Steel," University of Cambridge, 2014.

[21] K. Suzuki, I. Kurihara, T. Sasaki, Y. Koyoma, and Y. Tanaka, "Application of high strength MnMoNi steel to pressure vessels for nuclear power plant," *Nucl. Eng. Des.*, vol. 206, no. 2–3, pp. 261–277, 2001.

[22] B. S. Lee, M. C. Kim, J. H. Yoon, and J. H. Hong, "Characterization of high strength and high toughness Ni-Mo-Cr low alloy steels for nuclear application," *Int. J. Press. Vessel. Pip.*, vol. 87, no. 1, pp. 74–80, 2010.

[23] H. Pous-Romero and H. K. D. H. Bhadeshia, "Continuous Cooling Transformations in Nuclear Pressure Vessel Steels," *Metall. Mater. Trans. A*, vol. 45A, no. 11, pp. 4897–4906, 2014.

[24] K. Suzuki, "Neutron irradiation embrittlement of ASME SA508, C1.3 steel," *J. Nucl.*

Mater., vol. 108–109, no. C, pp. 443–450, 1982.

[25] P. Bocquet, A. Cheviet, and R. Dumont, "Examples of the evolution of materials for nuclear applications: metallurgical improvement of 16MND5 steel and new technologies for manufacturing heavy components," *Nucl. Eng. Des.*, vol. 151, no. 2–3, pp. 503–511, 1994.

[26] Y. Tanaka and I. Sato, "Development of high purity large forgings for nuclear power plants," in *Journal of Nuclear Materials*, 2011, vol. 417, no. 1–3, pp. 854–859.

[27] M. Erve, F. Papouschek, K. Fischer, and C. Maidorn, "State of the art in the manufacture of heavy forgings for reactor components in the Federal Republic of Germany," *Nucl. Eng. Des.*, vol. 108, no. 3, pp. 485–495, 1988.

[28] S. H. Chi and G. E. Lucas, "Differences in mechanical properties and microstructure of SA508 Cl. 3 reactor pressure vessel steels manufactured by different steel refining process," *Trans. 15th Int. Conf. Struct. Mech. React. Technol.*, pp. 223–230, 1999.

[29] J. Kim, H. K. Kwon, H. S. Chang, and Y. W. Park, "Improvement of impact toughness of the SA 508 class 3 steel for nuclear pressure vessel through steel-making and heat-treatment practices," *Nucl. Eng. Des.*, vol. 174, no. 1, pp. 51–58, 1997.

[30] Praca zbiorowa pod redakcją Jana Sińczaka, *Podstawy Procesów Przeróbki Plastycznej*. Kraków: Wydawnictwo Naukowe Akapit, 2010.

[31] P. Skubisz, J. Sińczak, A. Łukaszek-Sołek, and S. Bednarek, *Kucie swobodne i półswobodne*. Kraków: ARBOR, 2011.

[32] J. Talamantes-Silva, P. Bates, S. Al-Bermani, P. Davies, A. Hambleton, and D. Bunney, "New Challenges in the Production of Ultra Large Forgings for the Manufacturing of Pressure Vessels," in *Proceedings of the ASME 2013 Pressure Vessels and Piping Conference July 14-18*, 2013, pp. 1–9.

[33] D. J. Cogswell, "Statistical Modelling of the Transition Toughness Properties of Low Alloy Pressure Vessel Steels Volume 1 : Main Body," *Eng Dr. Thesis*, vol. 1, no. July, 2010.

[34] H. Pous-Romero, I. Lonardelli, D. Cogswell, and H. K. D. H. Bhadeshia, "Austenite grain growth in a nuclear pressure vessel steel," *Mater. Sci. Eng. A*, vol. 567, pp. 72–

79, 2013.

[35] E. J. Pickering and H. K. D. H. Bhadeshia, "The Consequences of Macroscopic Segregation on the Transformation Behavior of a Pressure-Vessel Steel," *J. Press. Vessel Technol.*, vol. 136, no. 3, p. 31403, 2014.

[36] J. Sroka, J. Talamantes-Silva, M. Krzyzanowski, and W. M. Rainforth, "Modelling of transient temperature field and phase transformation change : a way for residual stress management in large size forgings."

[37] I. Sato and K. Suzuki, "Manufacturing and material properties of forgings for the reactor pressure vessel of the high temperature engineering test reactor," *Nucl. Eng. Des.*, vol. 171, pp. 45–56, 1997.

[38] Y. Tanaka and I. Sato, "Development of high purity large forgings for nuclear power plants," *J. Nucl. Mater.*, vol. 417, no. 1–3, pp. 854–859, 2011.

[39] H. Pous-Romero and H. Bhadeshia, "Coalesced Martensite in Pressure Vessel Steels," *J. Press. Vessel Technol.*, vol. 136, no. 3, pp. 031402-1-031402–6, 2014.

[40] L. A. Dobrzanski, *Metaloznawstwo z podstawami nauki o materiałach*. Warszawa: Wydawnictwo Naukowo-Techniczne, 1996.

[41] M. C. Draper and S. Ankem, "Hydrogen Embrittlement Mitigation Techniques in High Strength Steel Manufacture," in *20th International Forgemasters Meeting IFM 2017*, 2017, pp. 418–427.

[42] E. I. S. Garza, "Mechanical Properties and Microstructure of Large Steel Forgings for Applications in the Energy Sector," The University of Sheffield, 2017.

[43] K. Przybylowicz, *Metaloznawstwo*, 7th ed. Warszawa: Wydawnictwo Naukowo-Techniczne, 2003.

[44] "ASME, SA508 - SPECIFICATION FOR QUENCHED AND TEMPERED VACUUM-TREATED CARBON AND ALLOY STEEL FORGINGS FOR PRESSURE VESSELS," *Sect. II A - Ferr. Mater. Specif. ASME Boil. Press. Vessel Code.*, 2000.

[45] S. Bajda, "Badania układów wielowarstwowych zbudowanych z materiałów

ultradrobnoziarnistych utleniających się powierzchniowo," 2019.

[46] S. J. Lee and Y. K. Lee, "Prediction of austenite grain growth during austenitization of low alloy steels," *Mater. Des.*, vol. 29, no. 9, pp. 1840–1844, 2008.

[47] L. M. Fu, H. R. Wang, W. Wang, and A. D. Shan, "Austenite grain growth prediction coupling with drag and pinning effects in low carbon Nb microalloyed steels," *Mater. Sci. Technol.*, vol. 27, no. 6, pp. 996–1001, 2011.

[48] M. E. Liu and Q. Yu, "Effects of Alloying Elements on Mechanical and Electrical Properties of Al-Fe-Cu-RE-Zr Alloy," *Zhuzao/Foundry*, vol. 68, no. 8, pp. 880–884, 2019.

[49] J. Majta, *Odkształcanie i własności. Stale mikrostopowe. Wybrane zagadnienia.* Kraków: Uczelniane Wydawnictwa Naukowo-dydaktyczne AGH, 2008.

[50] S. Kawaguchi, H. Tsukada, K. Suzuki, I. Sato, M. Kusuhashi, and S. Onodera, "Application of 20 MnMoNi 5 5 steel with lowered Si content to heavy thick steam generator tube sheet forgings," *Nucl. Eng. Des.*, vol. 87, no. C, pp. 249–257, 1985.

[51] K. Suzuki, I. Sato, M. Kusuhashi, and H. Tsukada, "Current steel forgings and their properties for steam generator of nuclear power plant," *Nucl. Eng. Des.*, vol. 198, no. 1, pp. 15–23, 2000.

[52] H. K. D. H. Bhadeshia, "Some phase transformations in steels," vol. 15, no. January, pp. 22–29, 1999.

[53] J. W. Christian, *Theory of Transformations in Metals and Alloys*. Oxford: Pergamon Press, 1965.

[54] K. Suzuki, "Neutron irradiation embrittlement of ASME SA508, C1.3 steel," *J. Nucl. Mater.*, vol. 108–109, no. C, pp. 443–450, Jul. 1982.

[55] H. K. D. H. Bhadeshia and R. W. K. Honeycombe, *Steels: Microstructure and Properties*, 3rd ed. Butterworth-Heinmann, 2006.

[56] H. K. D. H. Bhadeshia, "Metals & Alloys (year 3 lectures)." [Online]. Available: https://www.phase-trans.msm.cam.ac.uk/teaching.html. [Accessed: 22-May-2020].

[57] A. D. King and T. Bell, "Morphology and Crystallography of Widmanstätten

Proeutectoid Ferrite," *Met. Sci.*, vol. 8, no. 1, pp. 253–260, 1974.

[58]   J. D. Watson and P. G. McDougall, "The crystallography of widmanstätten ferrite," *Acta Metall.*, vol. 21, no. 7, pp. 961–973, 1973.

[59]   H. K. D. H. Bhadeshia and L. E. Svensson, *Modelling the Evolution of Microstructure in Steel Weld Metal*. London, 1993.

[60]   H. K. D. H. Bhadeshia, "Diffusional Formation of Ferrite in Iron and its alloys," *Prog. Mater. Sci.*, vol. 29, pp. 321–386, 1985.

[61]   H. K. D. H. Bhadeshia, *Bainite in Steels*. Maney Publishing, 2019.

[62]   H. K. D. H. Bhadeshia, "Carbon in Bainite," *University of Cambridge Materials*. [Online]. Available: https://www.phase-trans.msm.cam.ac.uk/bainitee.html. [Accessed: 10-Jun-2020].

[63]   H. K. D. H. Bhadeshia, "Martensite in Steels. Materials Science and Metalurgy," 2002. [Online]. Available: https://www.phase-trans.msm.cam.ac.uk/2000/C9/lectures45.pdf. [Accessed: 22-Jun-2020].

[64]   P. J. Withers and H. K. D. H. Bhadeshia, "Residual stress. Part 1– Measurement techniques," *Mater. Sci. Technol.*, vol. 17, no. 4, pp. 366–375, 2001.

[65]   A. Kulawik and J. Wróbel, "Wyznaczanie odkształceń towarzyszących hartowaniu powierzchniowym wielościegowym źródłem ciepła," *Model. Inżynierskie*, vol. 47, pp. 1896–771, 2013.

[66]   J. A. Francis, H. K. D. H. Bhadeshia, and P. J. Withers, "Welding residual stresses in ferritic power plant steels," *Mater. Sci. Technol.*, vol. 23, no. 9, pp. 1009–1020, 2007.

[67]   J. Sroka, J. Talamantes-Silva, M. Krzyzanowski, and W. M. Rainforth, "Modelling of transient temperature field and phase transformation change: A way for residual stress management in large size forgings," *Comput. Methods Mater. Sci.*, vol. 16, no. 2, 2016.

[68]   D. Senczyk and S. Moryksiewicz, "Naprężenia własne – pojęcia i klasyfikacja.," *Serwis Badania nieniszczące (Nondstructive testing)*, 2007. [Online]. Available: http://www.badania-nieniszczace.info/Badania-Nieniszczace-Nr-01-03-2007/pdf/senczyk_naprezenia_wlasne.pdf. [Accessed: 15-Feb-2020].

[69]   P. J. Withers and H. K. D. H. Bhadeshia, "Residual stress. Part 2– Nature and origins," *Mater. Sci. Technol.*, vol. 17, no. 4, pp. 366–369, 2001.

[70]   B. Pawłowski, "'Obrobka cieplna i cieplno-chemiczna stali.' - Learning materials of Department of Physical and Powder Metallurgy at The University of Science and Technology in Cracow, Poland." [Online]. Available: http://www.kmimp.agh.edu.pl/pliki/oc.pdf. [Accessed: 25-Jun-2020].

[71]   J. Sińczak, A. Łukaszek-Sołek, and K. Sołek, *Leksykon Kuźnictwa i Metaloplastyki.* Kraków: Wydawnictwo Naukowe Akapit, 2007.

[72]   D. Halliday, R. Resnick, and J. Walker, *Podstawy fizyki. Tom 2*, 2nd ed. Warszawa: Wydawnictwo Naukowe PWN, 2016.

[73]   S. Woźniak, "Drgania." University of Poznań . Department of Physics. Faculty of Nonlinear Optics., Poznań, p. 135, 2015.

[74]   "The Chemistry Library. Part of the LibreTexts Project. Physical and Theoretical Chemistry: Anharmonic Oscillator." [Online]. Available: https://chem.libretexts.org/Bookshelves/Physical_and_Theoretical_Chemistry_Textboo k_Maps/Supplemental_Modules_(Physical_and_Theoretical_Chemistry)/Quantum_Me chanics/06._One_Dimensional_Harmonic_Oscillator/Anharmonic_Oscillator. [Accessed: 09-Jul-2020].

[75]   K. Tosha, "Influence of Residual Stresses on the Hardness Number in the Affected Layer Produced by Shot Peening," *Second Asia–Pacific Forum Precis. Surf. Finish. Deburring Technol.*, pp. 48–54, 2002.

[76]   T. Croucher, "Minimizing machining distortion in aluminum alloys through successful application of uphill quenching - A process overview," *ASTM Spec. Tech. Publ.*, vol. 1523 STP, no. 7, pp. 332–351, 2010.

[77]   A. Maurotto, Y. Gu, D. Tsivoulas, and M. G. Burke, "Surface Integrity of SA508 Gr 3 Subjected to Abusive Milling Conditions," *Procedia CIRP*, vol. 45, pp. 279–282, 2016.

[78]   W. S. Mattos, G. E. Totten, and L. C. F. Canale, "Uphill quenching of aluminum alloys," *Mater. Perform. Charact.*, vol. 6, no. 5, pp. 894–903, 2017.

[79]   A. Bokota and L. Sowa, "Naprężenia w hartowanym elemencie stalowym chłodzonym

z różną intensywnością. Symulacje numeryczne.," vol. 3, no. 9, pp. 3–8, 2003.

[80] A. Kulawik and J. Wróbel, "Wyznaczanie odkształceń towarzyszących hartowaniu powierzchniowym wielościegowym źrółem ciepła.," *Model. Inżynierskie*, no. 47, pp. 123–128, 2013.

[81] M. M. Araújo, A. Lauria, M. B. M. Mendes, A. P. R. A. Claro, C. A. de A. Claro, and R. W. F. Moreira, "Analysis of residual stress and hardness in regions of pre-manufactured and manual bends in fixation plates for maxillary advancement," *Oral Maxillofac. Surg.*, vol. 19, no. 4, pp. 369–373, 2015.

[82] T. Croucher, "Controlling Residual Stress in High Strength Aluminum Alloys - One Engineer 's History , Approach and Opinions.," no. February, pp. 1–28, 2011.

[83] K. Suzuki, I. Sato, and H. Tsukada, "Manufacturing and material properties of ultralarge size forgings for advanced BWRPV," *Nucl. Eng. Des.*, vol. 151, no. 2–3, pp. 513–522, 1994.

[84] S. Onodera, S. Kawaguchi, H. Tsukada, H. Moritani, K. Suzuki, and I. Sato, "Manufacturing of ultra-large diameter 20 MnMoNi 5 5 steel forgings for reactor pressure vessels and their properties," *Nucl. Eng. Des.*, vol. 84, no. 2, pp. 261–272, 1985.

[85] "Sheffield Forgemasters Ltd. website." [Online]. Available: https://www.sheffieldforgemasters.com/.

[86] P. Carlone and G. S. Palazzo, "Development and validation of a thermo-mechanical finite element model of the steel quenching process including solid-solid phase changes," *Int. Appl. Mech.*, vol. 46, no. 8, pp. 955–971, 2011.

[87] P. Carlone, G. S. Palazzo, and R. Pasquino, "Finite element analysis of the steel quenching process: Temperature field and solid-solid phase change," *Comput. Math. with Appl.*, vol. 59, no. 1, pp. 585–594, 2010.

[88] A. Kulawik and J. Wróbel, "Influence of the rate of immersion on stress state during hardening of steel element.," *Model. Inżynierskie*, vol. 43, pp. 137–144, 2012.

[89] X. Wang, F. Li, Q. Yang, and A. He, "FEM analysis for residual stress prediction in hot rolled steel strip during the run-out table cooling," *Appl. Math. Model.*, vol. 37, no.

1–2, pp. 586–609, 2013.

[90] A. Kulawik, "Model of hardening process of the axisymmetric element with the movement of coolant.," *Model. Inżynierskie*, vol. 41, 2011.

[91] T. Croucher, "Using polyalkylene glycol quenchants to effectively control distortion and residual stresses in heat treated aluminum alloys," *ASTM Spec. Tech. Publ.*, vol. 1523 STP, no. 10, pp. 309–331, 2010.

[92] J. Babeł and A. Kulawk, "Modelowanie odkształceń strukturalnych procesu obróbki cieplnej.," *Model. Inżynierskie*, vol. 42, pp. 11–18, 2011.

[93] Y. Kim, J. Cho, and W. Bae, "Efficient forging process to improve the closing effect of the inner void on an ultra-large ingot," *J. Mater. Process. Technol.*, vol. 211, no. 6, pp. 1005–1013, 2011.

[94] X. X. Zhang, Z. S. Cui, W. Chen, and Y. Li, "A criterion for void closure in large ingots during hot forging," *J. Mater. Process. Technol.*, vol. 209, no. 4, pp. 1950–1959, 2009.

[95] D. Dye, B. A. Roder, S. Tin, M. A. Rist, J. A. James, and M. R. Daymond, "Modeling and Measurement of Residual Stresses in a Forged IN718 Superalloy Disc," *Superalloys 2004 (Tenth Int. Symp.*, pp. 315–322, 2004.

[96] Z. Zhou, P. F. Thomson, Y. Lam, and D. D. W. Yuen, "Numerical analysis of residual stress in hot-rolled steel strip on the run-out table," *J. Mater. Process. Technol.*, vol. 132, no. 1–3, pp. 184–197, 2003.

[97] J. A. Francis, M. Turski, and P. J. Withers, "Measured residual stress distributions for low and high heat input single weld beads deposited on to SA508 steel," *Mater. Sci. Technol.*, vol. 25, no. 3, pp. 325–334, 2009.

[98] H. Dai, J. A. Francis, and P. J. Withers, "Prediction of residual stress distributions for single weld beads deposited on to SA508 steel including phase transformation effects," *Mater. Sci. Technol.*, vol. 26, no. 8, pp. 940–949, 2010.

[99] S. Kim, S. Lee, Y.-R. Im, H.-C. Lee, Y. J. Oh, and J. Hong, "Effects of alloying elements on mechanical and fracture properties of base metals and simulated heat-affected zones of SA 508 steels," *Metall. Mater. Trans. A*, vol. 32, no. APRIL, pp.

903–911, 2001.

[100] H. Ming, Z. Zhang, J. Wang, E. H. Han, and W. Ke, "Microstructural characterization of an SA508-309L/308L-316L domestic dissimilar metal welded safe-end joint," *Mater. Charact.*, vol. 97, pp. 101–115, 2014.

[101] K. H. Lee, M. J. Jhung, M. C. Kim, and B. S. Lee, "Effects of tempering and PWHT on microstructures and mechanical properties of SA508 GR.4N steel," *Nucl. Eng. Technol.*, vol. 46, no. 3, pp. 413–422, 2014.

[102] G. Obasi *et al.*, "Measurement and Prediction of Phase Transformation Kinetics in a Nuclear Steel During Rapid Thermal Cycles," *Metall. Mater. Trans. A Phys. Metall. Mater. Sci.*, vol. 50, no. 4, pp. 1715–1731, 2019.

[103] J. a. Francis, R. J. Moat, H. Abdolvand, and A. Forsey, "An Assessment of the Mechanisms of Transformation Plasticity in SA508 Grade 3 Steel during Simulated Welding Thermal Cycles," *Mater. Sci. Forum*, vol. 777, pp. 188–193, 2014.

[104] K. L. Murty, P. Q. Miraglia, M. D. Mathew, V. N. Shah, and F. M. Haggag, "Characterization of gradients in mechanical properties of SA-533B steel welds using ball indentation," *Int. J. Press. Vessel. Pip.*, vol. 76, no. 6, pp. 361–369, 1999.

[105] A. F. Mark *et al.*, "On the evolution of local material properties and residual stress in a three-pass SA508 steel weld," *Acta Mater.*, vol. 60, no. 8, pp. 3268–3278, 2012.

[106] T. S. Byun, J. H. Hong, F. M. Haggag, K. Farrell, and E. H. Lee, "Measurement of through-the-thickness variations of mechanical properties in SA508 Gr.3 pressure vessel steels using ball indentation test technique," *Int. J. Press. Vessel. Pip.*, vol. 74, no. 3, pp. 231–238, 1997.

[107] C. García De Andrés, F. G. Caballero, C. Capdevila, and L. F. Álvarez, "Application of dilatometric analysis to the study of solid-solid phase transformations in steels," *Mater. Charact.*, vol. 48, no. 1, pp. 101–111, 2002.

[108] E. J. Pickering, J. Collins, A. Stark, L. D. Connor, A. A. Kiely, and H. J. Stone, "In situ observations of continuous cooling transformations in low alloy steels," *Mater. Charact.*, vol. 165, no. March, p. 110355, 2020.

[109] I. I. . Boyadjiev, P. F. . Thomson, and Y. C. . Lam, "Computation of the diffusional

transformation of continuously cooled austenite for predicting the coefficient of thermal expansion in the numerical analysis of thermal stress," *ISIJ Int.*, vol. 36, no. 11, pp. 1413–1419, 1996.

[110] A. Milenin, T. Rec, W. Walczyk, and M. Pietrzyk, "Model of Curvature of Crankshaft Blank during Heat Treatment, Accounting for Phase Transformations," *Steel Res. Int.*, vol. 87, no. 4, pp. 519–528, 2016.

[111] Q. Rong, Y. Yang, L. Meng, J. Lin, Y. Li, and J. Lin, "Experimental studies and constitutive modelling of AA6082 in age forming conditions Experimental studies and constitutive modelling of AA6082 in age conditions," *Procedia Eng.*, vol. 207, pp. 293–298, 2017.

[112] F. Lyu, Y. Li, Z. Shi, X. Huang, Y. Zeng, and J. Lin, "Stress and temperature dependence of stress relaxation ageing behaviour of an Al – Zn – Mg alloy," *Mater. Sci. Eng. A*, vol. 773, p. 138859, 2020.

[113] Y. Li, Z. Shi, J. Lin, Y. Yang, P. Saillard, and R. Said, "Effect of machining-induced residual stress on springback of creep age formed AA2050 plates with asymmetric creep-ageing behaviour," *Int. J. Mach. Tools Manuf.*, vol. 132, no. December 2017, pp. 113–122, 2018.

[114] R. P. Garrett, J. Lin, and T. A. Dean, "An investigation of the effects of solution heat treatment on mechanical properties for AA 6xxx alloys : experimentation and modelling," vol. 21, pp. 1640–1657, 2005.

[115] J. Liu *et al.*, "Journal of Materials Processing Technology Size-dependent mechanical properties in AA6082 tailor welded specimens," *J. Mater. Process. Tech.*, vol. 224, pp. 169–180, 2015.

[116] J. Zheng, J. Lin, J. Lee, R. Pan, C. Li, and C. M. Davies, "A novel constitutive model for multi-step stress relaxation ageing of a pre-strained 7xxx series alloy," *Int. J. Plast.*, vol. 106, no. February, pp. 31–47, 2018.

[117] J. Lin and Y. Liu, "A set of unified constitutive equations for modelling microstructure evolution in hot deformation," vol. 144, pp. 281–285, 2003.

[118] K. Zheng, D. J. Politis, L. Wang, and J. Lin, "A review on forming techniques for

manufacturing lightweight complex d shaped aluminium panel components," *Int. J. Light. Mater. Manuf.*, vol. 1, no. 2, pp. 55–80, 2018.

[119] J. Zheng, R. Pan, R. C. Wimpory, J. Lin, C. Li, and C. M. Davies, "A novel manufacturing process and validated predictive model for high- strength and low- residual stresses in extra-large 7xxx panels," *Mater. Des.*, vol. 173, p. 107767, 2019.

[120] T. A. Deiters and I. Mudawar, "Optimization of spray quenching for aluminum extrusion, forging, or continuous casting," *J. Heat Treat.*, vol. 7, no. 1, pp. 9–18, 1989.

[121] A. C. L. Lam, Z. Shi, J. Lin, and X. Huang, "Influences of residual stresses and initial distortion on springback prediction of 7B04-T651 aluminium plates in creep-age forming," *Int. J. Mech. Sci.*, vol. 103, pp. 115–126, 2015.

[122] Q. Rong *et al.*, "A Experimental investigations of stress-relaxation ageing behaviour of AA6082," *Mater. Sci. Eng. A*, vol. 750, no. February, pp. 108–116, 2019.

[123] R. Pan, T. Pirling, J. Zheng, J. Lin, and C. M. Davies, "Quantification of thermal residual stresses relaxation in AA7xxx aluminium alloy through cold rolling," *J. Mater. Process. Tech.*, vol. 264, no. February 2018, pp. 454–468, 2019.

[124] R. Pan, C. M. Davies, W. Zhang, Z. Shi, T. Pirling, and J. G. Lin, "The Effectiveness of Cold Rolling for Residual Stress Reduction in Quenched 7050 Aluminium Alloy Forgings," vol. 716, pp. 521–527, 2016.

[125] J. Zheng, C. M. Davies, J. Lin, R. Pan, and C. Li, "Constitutive modelling of a T74 multi-step creep ageing behaviour of AA7050 and its application to stress relaxation ageing in age formed aluminium components," *Procedia Eng.*, vol. 207, pp. 281–286, 2017.

[126] Q. Rong, Z. Shi, Y. Li, and J. Lin, "Constitutive modelling and its application to stress-relaxation age forming of AA6082 with elastic and plastic loadings," *J. Mater. Process. Tech.*, vol. 295, no. March, p. 117168, 2021.

[127] I. Milenin, M. Pernach, and M. Pietrzyk, "Application of the control theory to modelling austenite-ferrite phase transformation in steels," *Comput. Methods Mater. Sci.*, vol. 15, no. 2, pp. 327–335, 2015.

[128] K. T. Kuziak R., Pietrzyk M., "Identification of parameters of phase transformation

models for steels," *Steel Grips*, vol. 1, pp. 59–66, 2003.

[129] M. Pietrzyk, R. Kuziak, and T. Kondek, "Physical and Numerical Modelling of Plastic Deformation of Steels in Two-Phase Region," in *Materials Science and Technology*, 2003.

[130] M. Burdek, J. Marcisz, J. Stępień, and M. Adamczyk, "Optimisation of ageing parameters cold strain of maraging steel and investigation of dynamic mechanical properties of steel for bodies manufactured by flow forming," *Res. Proj. Financ. by State Budg. Funds assigned Statut. Act.*, vol. 4, 2010.

[131] P. Kongsuwan, G. Brandal, and Y. Lawrence Yao, "Laser Induced Porosity and Crystallinity Modification of a Bioactive Glass Coating on Titanium Substrates," *J. Manuf. Sci. Eng.*, vol. 137, no. 3, p. 031004, 2015.

[132] P. Krüger, "On the relation between non-isothermal and isothermal Kolmogorov-Johnson-Mehl-Avrami crystallization kinetics," *J. Phys. Chem. Solids*, vol. 54, no. 11, pp. 1549–1555, 1993.

[133] M. Suehiro, T. Senuma, H. Yada, and K. Sato, "Application of Mathematical Model for Predicting Microstructural Evolution to High Carbon Steels," *ISIJ Int.*, vol. 32, no. 3, pp. 433–439, 1992.

[134] M. P. Roman Kuziak, "Finite-element modeling of accelerated cooling of rods after hot rolling," in *Proceedings of the 41st MWSP Conf., ISS.*, 1999, pp. 405–414.

[135] P. C. Campbell, E. B. Hawbolt, and J. K. Brimacombe, "Microstructural engineering applied to the controlled cooling of steel wire rod: Part III. Mathematical model-formulation and predictions," *Metall. Trans. A*, vol. 22, no. 11, pp. 2791–2805, Nov. 1991.

[136] A. Roosz, Z. Gacsi, and E. G. Fuchs, "Isothermal formation of austenite in eutectoid plain carbon steel," *Acta Metall.*, vol. 31, no. 4, pp. 509–517, 1983.

[137] M. Gómez, S. F. Medina, and G. Caruana, "Modelling of Phase Transformation Kinetics by Correction of Dilatometry Results for a Ferritic Nb-microalloyed Steel," *ISIJ Int.*, vol. 43, no. 8, pp. 1228–1237, 2003.

[138] M. Krzyzanowski, J. H. Beynon, R. Kuziak, and M. Pietrzyk, "Development of

technique for identification of phase transformation model parameters on the basis of measurement of dilatometric effect - Direct problem," *ISIJ Int.*, vol. 46, no. 1, pp. 147–154, 2006.

[139] K. H. Lee, M. C. Kim, B. S. Lee, and D. M. Wee, "Master curve characterization of the fracture toughness behavior in SA508 Gr.4N low alloy steels," *J. Nucl. Mater.*, vol. 403, no. 1–3, pp. 68–74, 2010.

[140] M. Sun, L. Hao, S. Li, D. Li, and Y. Li, "Modeling flow stress constitutive behavior of SA508-3 steel for nuclear reactor pressure vessels," *J. Nucl. Mater.*, vol. 418, no. 1–3, pp. 269–280, 2011.

[141] B. S. Lee, J. H. Hong, W. J. Yang, M. Y. Huh, and S. H. Chi, "Master curve characterization of the fracture toughness in unirradiated and irradiated RPV steels using full- and 1/3-size pre-cracked Charpy specimens," *Int. J. Press. Vessel. Pip.*, vol. 77, no. 10, pp. 599–604, 2000.

[142] J. Jung, S. M. An, K. H. Soon, and H. Yeol Kim, "Evaluation of heat-flux distribution at the inner and outer reactor vessel walls under the in-vessel retention through external reactor vessel cooling condition," *Nucl. Eng. Technol.*, vol. 47, pp. 66–73, 2015.

[143] K. H. Lee, S. G. Park, M. C. Kim, and B. S. Lee, "Cleavage fracture toughness of tempered martensitic Ni-Cr-Mo low alloy steel with different martensite fraction," *Mater. Sci. Eng. A*, vol. 534, pp. 75–82, 2012.

[144] C. M. Sellars, "Computer modelling of hot-working processes," *Mater. Sci. Technol.*, vol. 1, no. April, pp. 325–332, 1985.

[145] M. Pietrzyk, T. Kondek, and J. Majta, "Method of identification of the phase transformation model for steels," *Math. Model. Met. Process. Manuf.*, vol. 35, no. 19, 2000.

[146] L. Trębacz, "Identyfikacja kryteriów pękania plastycznego w oparciu o wyniki badań doświadczalnych." Kraków, p. 123, 2011.

[147] D. Szeliga, J. Gawad, and M. Pietrzyk, "Parameters Identification of Material Models Based on the Inverse Analysis," *Int. J. Appl. Math. Comput. Sci.*, vol. 14, no. 4, pp.

549–556, 2004.

[148] D. Szeliga, J. Gawad, and M. Pietrzyk, "Inverse analysis for identification of rheological and friction models in metal forming," *Comput. Methods Appl. Mech. Eng.*, vol. 195, no. 48–49, pp. 6778–6798, 2006.

[149] N. Kim and H. Choi, "The prediction of deformation behavior and interfacial friction under hot working conditions using inverse analysis," *J. Mater. Process. Technol.*, vol. 208, no. 1–3, pp. 211–221, 2008.

[150] H. Pous-Romero, I. Lonardelli, D. Cogswell, and H. K. D. H. Bhadeshia, "Austenite grain growth in a nuclear pressure vessel steel," *Mater. Sci. Eng. A*, vol. 567, pp. 72–79, 2013.

[151] A. Gavrus, E. Massoni, and J. L. Chenot, "An inverse analysis using a finite element model for identification of rheological parameters," *J. Mater. Process. Technol.*, vol. 60, no. 1–4, pp. 447–454, 1996.

[152] H. Cho and T. Altan, "Determination of flow stress and interface friction at elevated temperatures by inverse analysis technique," *J. Mater. Process. Technol.*, vol. 170, no. 1–2, pp. 64–70, 2005.

[153] H. Cho, G. Ngalle, and T. Altan, "Simultaneous Determination of Flow Stress and Interface Friction by Finite Element Based Inverse Analysis Technique," *CIRP Ann.*, vol. 52, no. 1, pp. 221–224, 2003.

[154] B. Pawłowski, P. Bała, and R. Dziurka, "Improper interpretation of dilatometric data for cooling transformation in steels," *Arch. Metall. Mater.*, vol. 59, no. 3, pp. 1159–1161, 2014.

[155] B.-J. Lee, H.-D. Kim, and J.-H. Hong, "Calculation of α/γ equilibria in SA508 grade 3 steels for intercritical heat treatment," *Metall. Mater. Trans. A*, vol. 29, no. 5, pp. 1441–1447, 1998.

[156] X. Wu and I. Kim, "Effects of strain rate and temperature on tensile behavior of hydrogen-charged SA508 Cl. 3 pressure vessel steel," *Mater. Sci. Eng. A*, vol. 348, no. 1–2, pp. 309–318, 2003.

[157] W. Guo, S. Dong, J. a. Francis, and L. Li, "Microstructure and mechanical

characteristics of a laser welded joint in SA508 nuclear pressure vessel steel," *Mater. Sci. Eng. A*, vol. 625, pp. 65–80, 2015.

[158] Y. R. Im, Y. J. Oh, B. J. Lee, J. H. Hong, and H. C. Lee, "Effects of carbide precipitation on the strength and Charpy impact properties of low carbon Mn-Ni-Mo bainitic steels," *J. Nucl. Mater.*, vol. 297, no. 2, pp. 138–148, 2001.

[159] Y. R. Im, B. J. Lee, Y. J. Oh, J. H. Hong, and H. C. Lee, "Effect of microstructure on the cleavage fracture strength of low carbon Mn-Ni-Mo bainitic steels," *J. Nucl. Mater.*, vol. 324, no. 1, pp. 33–40, 2004.

[160] K. H. Lee, M. C. Kim, W. J. Yang, and B. S. Lee, "Evaluation of microstructural parameters controlling cleavage fracture toughness in Mn-Mo-Ni low alloy steels," *Mater. Sci. Eng. A*, vol. 565, pp. 158–164, 2013.

[161] D. XIA *et al.*, "Mechanical Properties and Corrosion Resistance of SA508-4 Low Carbon Alloy Steel," *Electrochemistry*, vol. 81, no. 4, pp. 262–268, 2013.

[162] K. H. Lee, M. C. Kim, W. J. Yang, and B. S. Lee, "Evaluation of microstructural parameters controlling cleavage fracture toughness in Mn-Mo-Ni low alloy steels," *Mater. Sci. Eng. A*, vol. 565, pp. 158–164, 2013.

[163] E. J. Pickering and H. K. D. H. Bhadeshia, "Macrosegregation and microstructural evolution in a pressure-vessel steel," *Metall. Mater. Trans. A Phys. Metall. Mater. Sci.*, vol. 45, no. 7, pp. 2983–2997, 2014.

[164] E. O. Hall, "The Deformation and Ageing of Mild Steel: III Discussion of Results," *Proc. Phys. Soc. Sect. B*, vol. 64, no. 9, pp. 747–753, Sep. 1951.

[165] N. J. Petch, "The cleveage strength of polycrystals.," *J. Iron Steel Inst.*, 1953.

[166] N. S. Stoloff, "Nickel-base superalloys," in *Microstructure and Properties of Materials*, 1996, pp. 51–106.

[167] S. S. Al-Bermani, P. S. Davies, C. Chesman, B. P. Wynne, and J. Talamantes-Silva, "Use of controlled heat treatment to predict mechanical properties in steel components," *Ironmak. Steelmak.*, vol. 43, no. 5, pp. 351–357, 2015.

[168] "BS EN1993-1-2. Eurocode 3: Design of steel structures - Part 1-2: General rules -

Structural fire design. Annex C [informative] Stainless Steel," 2011.

[169] A. N. Vasileiou, M. C. Smith, J. A. Francis, D. W. Rathod, J. Balakrishnan, and N. M. Irvine, "Residual stresses in arc and electron-beam welds in 130 mm thick SA508 steel: Part 2 –measurements," *Int. J. Press. Vessel. Pip.*, vol. 172, no. September 2018, pp. 379–390, 2019.

[170] S. Zhang *et al.*, "Experimental characterisation and numerical modelling of residual stresses in a nuclear safe-end dissimilar metal weld joint," *Metals (Basel).*, vol. 11, no. 8, 2021.

[171] A. N. Vasileiou *et al.*, "Development of microstructure and residual stress in electron beam welds in low alloy pressure vessel steels," *Mater. Des.*, vol. 209, p. 109924, 2021.

[172] J. Balakrishnan *et al.*, "Residual stress distributions in arc, laser and electron-beam welds in 30 mm thick SA508 steel: A cross-process comparison," *Int. J. Press. Vessel. Pip.*, vol. 162, no. July 2017, pp. 59–70, 2018.

[173] S. Bajda *et al.*, "Laser cladding of bioactive glass coating on pure titanium substrate with highly refined grain structure," *J. Mech. Behav. Biomed. Mater.*, vol. 119, no. February, p. 104519, 2021.

8. List of figures

9. List of tables

10. List of author's publications

1. J. Sroka, S. Bajda, M. Krzyżanowski, W. M. Rainforth, „Identification of scale failure parameters for low carbon steel oxides essential for hot rolling", STEELSIM 2015, 6th International conference on Modelling and simulation of metallurgical process in steelmaking, Bardolino, Garda Lake, Italy, 23 – 25, September 2015, ISBN: 97888898990054.

2. J. Sroka, J. Talamantes-Silva, M. Krzyżanowski, W. M. Rainforth, "Modelling of transient temperature field and phase transformation change: a way for residual stress management in large size forgings", Computer Methods in Material Science, AGH, ISSN: 1641-8581, 2016, vol. 16, no. 2, p. 87 – 96.

3. J. Sroka, M. Krzyżanowski, "Naprężenia własne w odkuwkach wielkogabarytowych [Residual stresses in Large size forgings]", Pomiędzy Naukami: VIth Nationwide Polish Conference, 15 September 2017, Chorzów, Poland, ISBN: 978-83-62408-21-4, p. 97

11.   Appendix A

Subroutines

Initial models: Asb_UEXPAN_New – Model 2, random distribution, rough mesh.

```fortran
subroutine uexpan(expan,dexpandt,temp,time,dtime,predef,dpred,
        statev,cmname,nstatv,noel)
    include 'aba_param.inc'
    character*80 cmname
    DIMENSION EXPAN(*),DEXPANDT(*),TEMP(2),TIME(2),PREDEF(*)
    integer lol,lil
    common/lporz/weklilos(125),iflg,lasttemp,wekliprz(125)
    common/lporz2/ kkl,jkl,ikl
    if (iflg.eq.0) then
    do i=1, 125
998 call random_seed(j)
    R=j
    call RANDOM_NUMBER(r)
    K=INT(126*r)
    If (K.eq.0) then
    K=K+1
    endif
    do j=1, 125
    if(K.eq.weklilos(j)) goto 998
    enddo
    if(ikl.le.124)then
    ikl=ikl+1
    endif
    weklilos(ikl)=K
    enddo
    iflg=1
    kkl=1
    jkl=1
    do i=1, 125
    wekliprz(i)=0
    enddo
    endif
    lol=0
    lil=0
c-----Cooling rate and Transformation Start temperature-------------------------
    corate=5
    alfa=1.5e-5
    Tf=825-27.6*corate
c      Tf=600
c-----total number of elements to be transformed at the given temperature--------
    If (temp(1).lt.Tf.and.temp(1).gt.500) then
    if (temp(1).ne.lasttemp) then
    const1=2
    xalfa=1.-exp((-log(const1))*(((Tf-temp(1))/corate)/10.5)**2.08)
    navram=Int(125*xalfa)
    endif
    do i=1, navram
    if (noel.eq.weklilos(i)) then
```

```
      lol=1
      endif
      enddo
      if (lol.eq.1) then
      do i=1, 3
      expan(i) = -alfa*temp(2)
      enddo
      jkl=jkl+1
      endif
      lasttemp=temp(1)
      endif
C-------------------------------------------------------------------------
2     format('kkl=',i5.0,x,'m(1)=',i3.0,x,'lol=',i3.0,x,
      'lil=',i3.0,x,'t(1)=',f7.3)
      return
      end
```

Initial models: Proba - Model 2, table of HTC, finer mesh.

```
      SUBROUTINE UEXPAN(EXPAN,DEXPANDT,TEMP,TIME,DTIME,PREDEF,
      DPRED,STATEV,CMNAME,NSTATV,NOEL)
      INCLUDE 'ABA_PARAM.INC'
      CHARACTER*80 CMNAME
      DIMENSION EXPAN(*),DEXPANDT(*),TEMP(2),TIME(2),PREDEF(*),
      DPRED(*),STATEV(NSTATV)
      common/pl/weklilos(125),iflg,lasttemp,wekliprz(4000)
      common/p2/ jkl,ikl
      open (unit=7,file='path \parametry.txt', status='old')
      if (iflg.eq.0) then
      do i=1, 125
      do z=1, 125
      call random_seed(j)
      R=j
      call RANDOM_NUMBER(r)
      K=INT(126*r)
      If (K.eq.0) then
      K=K+1
      endif
      do j=1, 125
      if(K.eq.weklilos(j)) then
      iflg2=1
      endif
      enddo
      if (iflg2.ne.1) exit
      enddo
            if(ikl.le.124)then
      ikl=ikl+1
      endif
      weklilos(i)=i
      enddo
      iflg=1
      kkl=1
      jkl=1
      do i=1, 125
```

```fortran
      wekliprz(i)=0
      enddo
      write (7,*) weklilos
      endif
c-----------Table guarantying change of the heat expansion coefficient-----------
(…)
c----------------End of the table--------------------------------------------------
      lol=0
      lil=0
      corate=5
      Tf=825-27.6*corate
c-----total number of elements to be transformed at the given temperature--------
      If (temp(1).lt.Tf.and.temp(1).gt.500) then
      if (temp(1).ne.lasttemp) then
      const1=2
      xalfa=1.-exp((-log(const1))*(((Tf-temp(1))/corate)/10.5)**2.08)
      navram=Int(125*xalfa)
      endif
      do i=1, navram
      if (noel.eq.weklilos(i)) then
      lol=1
      endif
      enddo
      if (lol.eq.1) then
      do i=1, 125
      if (noel.eq.wekliprz(i)) then
      lil=1
      endif
      enddo
      endif
      if (lil.ne.1) then
       alfa=1.5e-5
      do i=1, 3
      expan(i) = -1.6*alfa*temp(2)
      enddo
      wekliprz(jkl)=noel
      write (7,*) noel, jkl
      jkl=jkl+1
      if (jkl.eq.4001) then
      jkl=1
      endif
      endif
      lasttemp=temp(1)
      endif
      RETURN
      END
```

Initial models: Asb_UEXPAN_1 – simple transformation, Model 3

```fortran
      subroutine uexpan(expan,dexpandt,temp,time,dtime,predef,dpred,
     *    statev,cmname,nstatv,noel)
      include 'aba_param.inc'
      character*80 cmname
      dimension expan(*),dexpandt(*),temp(2),time(2),predef(*),
```

```fortran
      dpred(*),statev(nstatv)
 alpha = 1.0d-05
 If (temp(1) .lt. 750d0 .and. temp(1) .gt. 500d0) then
       alpha = 1.44d-05
 else if (temp(1) .lt. 500d0) then
     alpha = 9.8d-06
 endif
       expan(1) = alpha*temp(2)
 return
 end
```

Dilatometric models: Table of HTC, Model 5.

```fortran
      SUBROUTINE UEXPAN(EXPAN,DEXPANDT,TEMP,TIME,DTIME,PREDEF,
     DPRED,STATEV,CMNAME,NSTATV,NOEL)
      INCLUDE 'ABA_PARAM.INC'
      CHARACTER*80 CMNAME
      DIMENSION EXPAN(*),DEXPANDT(*),TEMP(2),TIME(2),PREDEF(*),
     DPRED(*),STATEV(NSTATV)
      common/pl/cokolwiek
c-----------Table of thermal expansion temperature-dependence-------
c     ----SA508 gr.3 steel data-------
      If (temp(1).le.1200.and.temp(1).gt.790) then
      alfa=16.86e-5
      do i=1, 3
      expan(i) = alfa*temp(2)
      enddo
      endif
      If (temp(1).le.900.and.temp(1).gt.790) then
      alfa=18.86e-5
      do i=1, 3
      expan(i) = alfa*temp(2)
      enddo
      endif
      If (temp(1).le.750.and.temp(1).gt.680) then
      alfa=22e-5
      do i=1, 3
      expan(i) = alfa*temp(2)
      enddo
      endif
      If (temp(1).le.680.and.temp(1).gt.620) then
      alfa=15.9e-5
      do i=1, 3
      expan(i) = alfa*temp(2)
      enddo
      endif
      If (temp(1).le.620.and.temp(1).gt.550) then
      alfa=15.3e-5
      do i=1, 3
      expan(i) = alfa*temp(2)
      enddo
      endif
      If (temp(1).le.550.and.temp(1).gt.500) then
      alfa=14.8e-5
      do i=1, 3
      expan(i) = alfa*temp(2)
      enddo
      endif
      If (temp(1).le.500.and.temp(1).gt.450) then
      alfa=14.5e-5
      do i=1, 3
      expan(i) = alfa*temp(2)
      enddo
```

```fortran
      endif
      If (temp(1).le.450.and.temp(1).gt.400) then
      alfa=14.2e-5
      do i=1, 3
      expan(i) = alfa*temp(2)
      enddo
      endif
      If (temp(1).le.400.and.temp(1).gt.371) then
      alfa=14e-5
      do i=1, 3
      expan(i) = alfa*temp(2)
      enddo
      endif
      If (temp(1).le.371.and.temp(1).gt.315) then
      alfa=13.8e-5
      do i=1, 3
      expan(i) = alfa*temp(2)
      enddo
      endif
      If (temp(1).le.315.and.temp(1).gt.260) then
      alfa=13.41e-5
      do i=1, 3
      expan(i) = alfa*temp(2)
      enddo
      endif
      If (temp(1).le.260.and.temp(1).gt.204) then
      alfa=13.05e-5
      do i=1, 3
      expan(i) = alfa*temp(2)
      enddo
      endif
      If (temp(1).le.204.and.temp(1).gt.149) then
      alfa=12.69e-5
      do i=1, 3
      expan(i) = alfa*temp(2)
      enddo
      endif
      If (temp(1).le.149.and.temp(1).gt.93) then
      alfa=12.24e-5
      do i=1, 3
      expan(i) = alfa*temp(2)
      enddo
      endif
      If (temp(1).le.93.and.temp(1).gt.38) then
      alfa=10.17e-5
      do i=1, 3
      expan(i) = alfa*temp(2)
      enddo
      endif
      If (temp(1).le.38.and.temp(1).gt.0) then
      alfa=10.08e-5
      do i=1, 3
      expan(i) = alfa*temp(2)
      enddo
      endif
      RETURN
      END
```

Dilatometric models: Transformation without DEPVAR option – model 6.

```fortran
      SUBROUTINE UEXPAN(EXPAN,DEXPANDT,TEMP,TIME,DTIME,PREDEF,
     DPRED,STATEV,CMNAME,NSTATV,NOEL)
      INCLUDE 'ABA_PARAM.INC'
      CHARACTER*80 CMNAME
      DIMENSION EXPAN(*),DEXPANDT(*),TEMP(2),TIME(2),PREDEF(*),
     DPRED(*),STATEV(NSTATV)
c        common/pl/iwekliex(634),iwekliprz(634),atemp(634),lasttemp
c up for seed=0.5
c        common/pl/iwekliex(1451),iwekliprz(1451),atemp(1451),lasttemp
c up for seed=0.35
      common/pl/iwekliex(3778),iwekliprz(3778),atemp(3778),lasttemp
c up for seed=0.25
c        common/pl/iwekliex(52058),iwekliprz(52058),atemp(52058),lasttemp
c up for seed=0.1
c     iwekliex – vector of elements, which finished transformation.
c     634x16 – number of elements x two calling of calculations x 8 per node
c     iwekliprz – number of transformed elements.
c     atemp – start temperature of transformation vector.
c     lasttemp – temprerature value from the last calculations.
      common/p2/ jkl,j,lil,lal,navram
      common/p3/xdtem1,xdist,xdist2
      open(unit=9,file='path\1.txt', status='old')
      open(unit=10,file=path\2.txt', status='old')
      open(unit=11,file=path\3.txt', status='old')
c-----------Table of thermal expansion temperature-dependence-------
c       ----SA508 gr.3 steel data--------

      If (temp(1).le.1200.and.temp(1).gt.600) then
      alfa=18.86e-6
      do i=1, 3
      expan(i) = 2*1.285*alfa*temp(2)
      enddo
      endif

      If (temp(1).le.600.and.temp(1).gt.0) then
c-----average from Tabela.for subrutine of 11 values above 500°C---
      alfa=11.65e-6
      do i=1, 3
      expan(i) =2*1.222*alfa*temp(2)
      enddo
      endif
c---------------End of the table------------------------------------------------
c     Code control parameters
      lol=0
      lul=0
      Tf=652
      corate=0.08
      xdtem1=0.00001
      xdist2=55
c-----Transformation------------------------------------------------
      If (temp(1).lt.Tf.and.temp(1).gt.420) then
c-----total number of elements to be transformed at the given temperature--------
            const1=1.00043
            cxdwa=12.5
            cxtrzy=1.95
      xalfa=1.-exp((-log(const1))*(((Tf-temp(1))/corate)/cxdwa)**cxtrzy)
       xalfa=xalfa**2
c              navram=Int(634*xalfa)
c              navram=Int(1451*xalfa)
            navram=Int(3778*xalfa)
```

```fortran
c              navram=Int(52058*xalfa)
c--------checking, if element is already transformed----------------------------
c          do i=1, 634
c          do i=1, 1451
         do i=1, 3778
c          do i=1, 52058
            if (noel.eq.iwekliprz(i)) then
            lol=1
            endif
         enddo
C-------Continuing of transformation for element already in transformation------
         if (lol.eq.1) then
            alfa=-18.86e-6
            do i=1, 3
               expan(i) =2*1.6*alfa*temp(2)
            enddo
c-------End of transformed elements transformation-------------------------------
c-------New elements transformation----------------------------------------------
         else if(jkl.le.navram)then
            alfa=-18.86e-6
            do i=1, 3
               expan(i) =2*1.6*alfa*temp(2)
            enddo
            jkl=jkl+1
            iwekliprz(jkl)=noel
            atemp(jkl)=temp(1)
           write(9,*)noel,xalfa,navram,jkl,temp(1)
         endif
c---Control parameters for possible number of element transformed----------------
         xdist=temp(1)
         lasttemp=temp(1)
c---checking, if the element finished transformation, if so – HTC for ferrite----
c          do i=1, 634
c          do i=1, 1451
         do i=1, 3778
c          do i=1, 52058
            if (noel.eq.iwekliex(i)) then
               alfa=11.65e-6
               do kl=1, 3
                  expan(kl) =2*1.222*alfa*temp(2)
               enddo
               lul=1
            endif
         enddo
C-----Element quit from the transformation--------------------------------------
         if (temp(1).le.580.and.lul.eq.0) then
            if (lal.eq.0) then
               if (j.eq.0) then
               j=1
               lal=1
               endif
            endif
c          do k=1, 634
c          do k=1, 1451
         do k=1, 3778
c           do k=1, 52058
         if (noel.eq.iwekliprz(k)) then
         lel=1
         endif
         enddo
         if (lel.eq.1) then
            a=atemp(j)-temp(1)
```

270

```fortran
            if (a.gt.xdist2) then
```
```fortran
                  alfa=11.65e-6
                     do i=1, 3
                        expan(i) =2*1.222*alfa*temp(2)
                     enddo
                  iwekliex(j)=noel
                  j=j+1
               endif
            endif
            endif
         endif
```
```fortran
C-----checking the vector content-------------------------------------------
         if (temp(1).le.200.and.lil.eq.0) then
         write (10,*) atemp,iwekliprz,iwekliex
         write (11,*) iwekliex
         lil=1
         endif
c----End of the transformation-----------------------------------------------
      RETURN
      END
```

Dilatometric models: using of the DEPVAR option, model 6.

```fortran
      SUBROUTINE UEXPAN(EXPAN,DEXPANDT,TEMP,TIME,DTIME,PREDEF,
       DPRED,STATEV,CMNAME,NSTATV,NOEL)
      INCLUDE 'ABA_PARAM.INC'
      CHARACTER*80 CMNAME
      DIMENSION EXPAN(*),DEXPANDT(*),TEMP(2),TIME(2),PREDEF(*),
       DPRED(*),STATEV(NSTATV)
c----COMMON BLOCKS – vectors dependent of numer of elements--------------------
c      common/pl/iwekliex(634),iwekliprz(634),atemp(634),lasttemp
c up for seed=0.5
c      common/pl/iwekliex(1451),iwekliprz(1451),atemp(1451),lasttemp
c up for seed=0.35
      common/pl/iwekliex(3778),iwekliprz(3778),atemp(3778),lasttemp
c up for seed=0.25
c      common/pl/iwekliex(52058),iwekliprz(52058),atemp(52058),lasttemp
c up for seed=0.1
c-----Description------------------------------------------------------------
c     iwekliex – vector of elements, which finished transformation.
c     634x16 - number of elements x two calling of calculations x 8 per node
c     iwekliprz - number of transformed elements.
c     atemp - start temperature of transformation vector.
c     lasttemp - temperature value from the last calculations.
c---COMMON BLOCKS------------------------------------------------------------
      common/p2/ jkl,j,lil,lal,navram,iii,x
      common/p3/xdtem1,xdist,xdist2
c-----------Table of thermal expansion temperature-dependence-----------------
c-----------SA508 gr.3 steel data--------------------------------------------
      If (temp(1).le.1200.and.temp(1).gt.460) then
      alfa=24.2351e-6
      do i=1, 3
      expan(i) = 2*alfa*temp(2)
      enddo
      endif
```

```fortran
      If (temp(1).le.460.and.temp(1).gt.0) then
      alfa=14.2363e-6
c-----average from Tabela.for subroutine of 11 values above 500°C---
      do i=1, 3
      expan(i) =2*alfa*temp(2)
      enddo
      endif
c----------------End of the table----------------------------------------------------
c-----TRANSFORMATION START TEMPERATURE---------------------------------------------
c      ----------
c       Koryg1=-170.792
c       corate=0.08
c       Tf=652 (745)
c      Tooks around 40min
c      ----------
c       Koryg1=-283.62
c       corate=0.05
c       Tf=540 (645)
c      Tooks around 1h
c      ----------
c       Koryg1=-310.24
c       corate=0.1
c       Tf=512   (573)
c      Tooks around 30-35min.
c      ----------
      Koryg1=-302.4
      corate=1
c       Tf=495
c      Tooks around -10min.
c      ----------
c       Koryg1=-315
c       Koryg1=-357
c       corate=5
c       Tf=380 (430-372)
c      Tooks around 7-10min.
c      ----------
c       Koryg1=-228
c       corate=10
c       Tf=321
c      Tooks around 7-10min.
c      ----------
c       Koryg1=2276
c       corate=100
c       Tf=341 (355-341)
c      Tooks around 7-10min.
c      ----------
      Tf=(825-27.6*corate)+Koryg1
c--------------------------------------------------------------------------------------
------------------------------------------
c     Code control parameters
      lol=0
      lul=0
      xdtem1=0.00001
      xdist2=55
c-------------COOLING RATE---------------------------------------------------------
c     Averege cooling rate--------------
      open(unit=11,file=path\statevy.txt', status='old')
40    format('noel=',i4,x,'temp(1)=',f9.4,x,'time(2)=',f9.4,x,'statev(2)
     =',f9.4,x,'temp(2)=',f9.4,x,'Dtime=',f9.4,x,'statev(3)=',f9.4)
      if (time(2).gt.x) then
      statev(2)=(1200-temp(1))/time(2)
c     Local cooling rate--------------
```

```fortran
      statev(3)=(temp(2)/time(1))
      write(11,40)  noel,temp(1),time(2),statev(2),temp(2),dtime,statev(
      3)
      x=x+1
      endif
c-----Transformation----------------------------------------------------------
c-----Start of transformation-------------------------------------------------
      if (temp(1).lt.Tf) then
      statev(1)=1
      endif
      if(temp(1).lt.250) then
      statev(1)=0
      endif
      If (statev(1).eq.1) then
c-----total number of elements to be transformed at the given temperature-------
c---------Discretizing--------------------------------------------------------
            const1=1.00043
            cxdwa=12.5
            cxtrzy=1.95
      xalfa=1.-exp((-log(const1))*(((Tf-temp(1))/corate)/cxdwa)**cxtrzy)
       xalfa=xalfa**2
c             navram=Int(634*xalfa)
c             navram=Int(1451*xalfa)
            navram=Int(3778*xalfa)
c             navram=Int(52058*xalfa)
c--------checking, if element is already during transformation------------------
c          do i=1, 634
c          do i=1, 1451
          do i=1, 3778
c          do i=1, 52058
            if (noel.eq.iwekliprz(i)) then
            lol=1
            endif
          enddo
C-------Continuing of transformation for element already in transformation------
          if (lol.eq.1) then
            alfa=-18.86e-6
            do i=1, 3
               expan(i) =2*1.6*alfa*temp(2)
            enddo
c-------End of transformed elements transformation-----------------------------
c-------New elements transformation--------------------------------------------
          else if(jkl.le.navram)then
            alfa=-18.86e-6
            do i=1, 3
               expan(i) =2*1.6*alfa*temp(2)
            enddo
            jkl=jkl+1
            iwekliprz(jkl)=noel
            atemp(jkl)=temp(1)
c          write(9,*)noel,xalfa,navram,jkl,temp(1)
          endif
c---Control parameters for possible number of element transformed--------------
          xdist=temp(1)
          lasttemp=temp(1)
c---checking, if the element finished transformation, if so - HTC for ferrite----
c          do i=1, 634
c          do i=1, 1451
          do i=1, 3778
c          do i=1, 52058
            if (noel.eq.iwekliex(i)) then
               alfa=11.65e-6
```

```fortran
                  do kl=1, 3
                      expan(kl) =2*1.222*alfa*temp(2)
                  enddo
                  lul=1
              endif
          enddo
C-----Element quit from the transformation--------------------------------------
          if (temp(1).le.580.and.lul.eq.0) then
              if (lal.eq.0) then
                  if (j.eq.0) then
                  j=1
                  lal=1
                  endif
              endif
c         do k=1, 634
c         do k=1, 1451
          do k=1, 3778
c         do k=1, 52058
          if (noel.eq.iwekliprz(k)) then
          lel=1
          endif
          enddo
          if (lel.eq.1) then
              a=atemp(j)-temp(1)
              if (a.gt.xdist2) then
c-----average, like before---------------------------------------------------
                  alfa=11.65e-6
                      do i=1, 3
                          expan(i) =2*1.222*alfa*temp(2)
                      enddo
                  iwekliex(j)=noel
                  j=j+1
              endif
          endif
          endif
      endif
C-----checking the vector content-----------------------------------------------
          if (temp(1).le.200.and.lil.eq.0) then
c          write (10,*) atemp,iwekliprz,iwekliex
c          write (11,*) iwekliex
          lil=1
          endif
c----End of the transformation---------------------------------------------------
      RETURN
      END
```

Dilatometric models: Tabela_AlfaPunktyAuto – model 6, cooling rates

```fortran
      SUBROUTINE UEXPAN(EXPAN,DEXPANDT,TEMP,TIME,DTIME,PREDEF,
      DPRED,STATEV,CMNAME,NSTATV,NOEL)
      INCLUDE 'ABA_PARAM.INC'
      CHARACTER*80 CMNAME
      DIMENSION EXPAN(*),DEXPANDT(*),TEMP(2),TIME(2),PREDEF(*),
      DPRED(*),STATEV(NSTATV)
      common/ble/ lol, alfa(117),i,T1,T2,T3
c----------Table--------------------------------------------------------------
      alfa    (      1     )=     2.37992E-05
      (…)
      alfa    (      117    )=     1.14087E-05
```

I	II	III	IV	V	VI	VII	VIII
2,38E-05	2,39E-05	2,36E-05	2,43E-05	-2,06E-05	1,51E-05	1,75E-05	1,19E-05
2,30E-05	2,35E-05	2,33E-05	2,38E-05	-2,04E-05	1,42E-05	1,53E-05	1,25E-05
2,49E-05	2,34E-05	2,34E-05	2,56E-05	-1,63E-05	1,58E-05	1,53E-05	1,20E-05
2,45E-05	2,42E-05	2,33E-05	2,53E-05	-9,11E-06	1,63E-05	1,48E-05	1,15E-05
2,39E-05	2,30E-05	2,28E-05	2,45E-05	-2,75E-06	1,56E-05	1,54E-05	1,14E-05
2,51E-05	2,37E-05	2,34E-05	2,35E-05	1,73E-06	1,59E-05	1,42E-05	
2,42E-05	2,38E-05	2,30E-05	2,18E-05	5,60E-06	1,63E-05	1,42E-05	
2,51E-05	2,36E-05	2,40E-05	2,15E-05	8,24E-06	1,65E-05	1,39E-05	
2,48E-05	2,28E-05	2,36E-05	1,99E-05	9,36E-06	1,54E-05	1,34E-05	
2,41E-05	2,38E-05	2,32E-05	1,70E-05	1,09E-05	1,57E-05	1,38E-05	
2,42E-05	2,39E-05	2,80E-05	1,42E-05	1,24E-05	1,60E-05	1,36E-05	
2,42E-05	2,33E-05	2,84E-05	1,08E-05	1,19E-05	1,53E-05	1,33E-05	
2,32E-05	2,29E-05	2,62E-05	7,29E-06	1,41E-05	1,62E-05	1,30E-05	
2,34E-05	2,35E-05	2,19E-05	2,00E-06	1,34E-05	1,52E-05	1,29E-05	
2,45E-05	2,27E-05	1,98E-05	-7,30E-06	1,46E-05	1,60E-05	1,38E-05	
2,42E-05	2,32E-05	2,15E-05	-1,86E-05	1,43E-05	1,77E-05	1,30E-05	

```
if (lol.eq.0) then
T1=1200
T2=T1-10
T3=T1
lol=1
i=1
endif
If (temp(1).le.T2) then
T1=T3-10
T3=T1
T2=T1-10
i=i+1
endif
          If (temp(1).le.T1.and.temp(1).gt.T2) then
alfa=alfa(i)
      endif
do j=1, 3
expan(j)=2*alfa(i)*temp(2)
enddo
RETURN
END
```

Dilatometric models: Tabela_Przem1 – model 8, cooling rates

Also: Inverse – model 7

```fortran
      SUBROUTINE UEXPAN(EXPAN,DEXPANDT,TEMP,TIME,DTIME,PREDEF,
     DPRED,STATEV,CMNAME,NSTATV,NOEL)
      INCLUDE 'ABA_PARAM.INC'
      CHARACTER*80 CMNAME
      DIMENSION EXPAN(*),DEXPANDT(*),TEMP(2),TIME(2),PREDEF(*),
     DPRED(*),STATEV(NSTATV)
c      common/pl/iwekliex(634),iwekliprz(634),atemp(634),lasttemp
c up for seed=0.5
c      common/pl/iwekliex(1451),iwekliprz(1451),atemp(1451),lasttemp
c up for seed=0.35
      common/pl/iwekliex(3778),iwekliprz(3778),atemp(3778),lasttemp
c up for seed=0.25
c      common/pl/iwekliex(52058),iwekliprz(52058),atemp(52058),lasttemp
c up for seed=0.1
c     iwekliex – vector of elements, which finished transformation.
c     634x16 - number of elements x two calling of calculations x 8 per node
c     iwekliprz - number of transformed elements.
c     atemp - start temperature of transformation vector.
c     lasttemp - temperature value from the last calculations.
      common/p2/ jkl,j,lil,lal,navram
      common/p3/xdtem1,xdist,xdist2
      open(unit=9,file='path\1.txt', status='old')
      open(unit=10,file=path\2.txt', status='old')
      open(unit=11,file='path\3.txt', status='old')
      If (temp(1).le.1200.and.temp(1).gt.600) then
      alfa=18.86e-6
      do i=1, 3
c     expan(i) = 2*1.285*alfa*temp(2)
      expan(i) = 2*1.345*alfa*temp(2)
      enddo
      endif
      If (temp(1).le.600.and.temp(1).gt.0) then
c-----average from Tabela.for subroutine of 11 values above 500°C---
      alfa=11.65e-6
      do kl=1, 3
                  expan(kl)=2*1.12*alfa*temp(2)
      enddo
      endif
c     Code control parameters

      lol=0
      lul=0
      Tf=652
      corate=0.08
      xdtem1=0.00001
      xdist2=55
c-----Transformation----------------------------------------------------------
      If (temp(1).lt.Tf.and.temp(1).gt.420) then
c-----total number of elements to be transformed at the given temperature--------
            const1=1.00039
            cxdwa=10.5
            cxtrzy=1.8
      xalfa=1-exp((-log(const1))*(((Tf-temp(1))/corate)/cxdwa)**cxtrzy)
      xalfa=xalfa**2
c            navram=Int(634*xalfa)
c            navram=Int(1451*xalfa)
            navram=Int(3778*xalfa)
c            navram=Int(52058*xalfa)
c--------checking, if element is already during transformation------------------
c         do i=1, 634
```

```fortran
c            do i=1, 1451
             do i=1, 3778
c            do i=1, 52058
                 if (noel.eq.iwekliprz(i)) then
                 lol=1
                 endif
             enddo
C-------Continuing of transformation for element already in transformation------
             if (lol.eq.1) then
                 alfa=-18.86e-6
                 do i=1, 3
                     expan(i) =2*1.9*alfa*temp(2)
                 enddo
c-------End of transformed elements transformation-------------------------------
c-------New elements transformation----------------------------------------------
             else if(jkl.le.navram)then
                 alfa=-18.86e-6
                 do i=1, 3
                     expan(i) =2*1.9*alfa*temp(2)
                 enddo
                 jkl=jkl+1
                 iwekliprz(jkl)=noel
                 atemp(jkl)=temp(1)
             write(9,*)noel,xalfa,navram,jkl,temp(1)
             endif
c---Control parameters for possible number of element transformed----------------
             xdist=temp(1)
             lasttemp=temp(1)
c---checking, if the element finished transformation, if so – HTC for ferrite----
c            do i=1, 634
c            do i=1, 1451
             do i=1, 3778
c            do i=1, 52058
                 if (noel.eq.iwekliex(i)) then
                     alfa=11.65e-6
                     do kl=1, 3
c                        expan(kl) =2*1.222*alfa*temp(2)
                         expan(kl) =2*1.12*alfa*temp(2)
                     enddo
                     lul=1
                 endif
             enddo
C-----Element quit from the transformation--------------------------------------
if (temp(1).le.580.and.lul.eq.0) then
                 if (lal.eq.0) then
                     if (j.eq.0) then
                     j=1
                     lal=1
                     endif
                 endif
c            do k=1, 634
c            do k=1, 1451
             do k=1, 3778
c            do k=1, 52058
             if (noel.eq.iwekliprz(k)) then
             lel=1
             endif
             enddo
             if (lel.eq.1) then
                 a=atemp(j)-temp(1)
                 if (a.gt.xdist2) then
c-----average, like before---------------------------------------------
```

```fortran
                  alfa=11.65e-6
                      do i=1, 3
                      expan(kl) =2*1.12*alfa*temp(2)
                      enddo
                  iwekliex(j)=noel
                  j=j+1
              endif
          endif
          endif
      endif
C-----checking the vector content----------------------------------------------------
          if (temp(1).le.200.and.lil.eq.0) then
          write (10,*) atemp,iwekliprz,iwekliex
          write (11,*) iwekliex
          lil=1
          endif
c----End of the transformation-------------------------------------------------------
      RETURN
      END
```

Comprehensive models: Model 10 – ModelTemp_flange, model 11 Axi_ModTemp

```fortran
      SUBROUTINE UEXPAN(EXPAN,DEXPANDT,TEMP,TIME,DTIME,PREDEF,
     DPRED,STATEV,CMNAME,NSTATV,NOEL)
      INCLUDE 'ABA_PARAM.INC'
      CHARACTER*80 CMNAME
      DIMENSION EXPAN(*),DEXPANDT(*),TEMP(2),TIME(2),PREDEF(*),
     DPRED(*),STATEV(NSTATV)
      common/nowe/x,alfyall(6,89)
      common/alf/jakikolwiek,i,j
c      abaqus j=cooling.inp user=ModTempDEPV_1.for interactive
c      statev(1)   - switch on every node, assigning beginning temperature values,
controlling assigning of alpha value.
c      statev(2)   - ACR - average cooling rate at the node, counted from previous
step
c      statev(3)   - LCR - local cooling rate at the node, counted from previous step
c      statev(4)   - The upper end of the range for the given alpha value
c      statev(5)   - The lower end of the range for the given alpha value
c      statev(6)   - Temperature of statev(4) for replacing
c      statev(7)   - Summ ACRów.
c      statev(8)   - Number of CR
c      statev(9)   - Average of ACR
c      statev(10)  - Previous time
c      statev(11)  - Previous noel
c      statev(12)  - indicator of column in Table of alphas, dependent from CR.

      if (jakikolwiek.eq.0)then
      alfyall(    1    ,    1   )=    1.1627E-05
      alfyall(    1    ,    2   )=    1.1627E-05
      alfyall(    7    ,    88  )=    2.0054E-05
(…)
      alfyall(    7    ,    89  )=    2.3122E-05
```

0,05	0,1	0,5	1	5	10	100
1,16E-05	1,10E-05	2,32E-05	8,74E-06	9,10E-06	5,79E-06	1,08E-05

1,16E-05	1,10E-05	2,32E-05	8,74E-06	9,10E-06	5,79E-06	1,08E-05
1,16E-05	1,10E-05	2,32E-05	8,74E-06	9,10E-06	5,79E-06	1,08E-05
1,16E-05	1,10E-05	2,32E-05	8,74E-06	9,10E-06	5,79E-06	1,08E-05
1,22E-05	1,16E-05	2,36E-05	9,06E-06	9,49E-06	7,19E-06	1,17E-05
1,19E-05	1,14E-05	2,33E-05	9,38E-06	9,99E-06	6,95E-06	9,58E-06
1,21E-05	1,17E-05	2,34E-05	1,06E-05	1,02E-05	8,42E-06	1,17E-05
1,28E-05	1,19E-05	2,33E-05	1,05E-05	1,08E-05	6,74E-06	9,56E-06
1,28E-05	1,21E-05	2,28E-05	1,15E-05	1,13E-05	8,99E-06	1,08E-05
1,26E-05	1,22E-05	2,34E-05	1,14E-05	1,11E-05	7,42E-06	1,08E-05
1,28E-05	1,24E-05	2,30E-05	1,17E-05	1,18E-05	7,15E-06	1,02E-05
1,28E-05	1,22E-05	2,40E-05	1,20E-05	1,11E-05	7,65E-06	1,04E-05
1,29E-05	1,33E-05	2,36E-05	1,15E-05	1,13E-05	6,91E-06	9,76E-06
1,29E-05	1,31E-05	2,32E-05	1,22E-05	1,25E-05	6,91E-06	9,30E-06
1,41E-05	1,36E-05	2,80E-05	1,23E-05	1,19E-05	6,08E-06	9,18E-06
1,34E-05	1,34E-05	2,84E-05	1,24E-05	1,12E-05	5,25E-06	9,67E-06
1,39E-05	1,39E-05	2,62E-05	1,27E-05	1,26E-05	4,69E-06	7,66E-06
1,33E-05	1,40E-05	2,19E-05	1,24E-05	1,11E-05	3,48E-06	7,12E-06
1,38E-05	1,42E-05	1,98E-05	1,35E-05	1,10E-05	1,77E-06	6,50E-06
1,38E-05	1,44E-05	2,15E-05	1,28E-05	1,08E-05	1,62E-07	4,48E-06
1,45E-05	1,50E-05	2,43E-05	1,20E-05	9,75E-06	-3,42E-06	3,48E-06
1,48E-05	1,53E-05	2,38E-05	1,26E-05	8,90E-06	-6,67E-06	2,49E-07
1,39E-05	1,45E-05	2,56E-05	1,21E-05	7,18E-06	-1,21E-05	-2,56E-06
1,45E-05	1,57E-05	2,53E-05	1,20E-05	7,33E-06	-2,10E-05	-6,00E-06
1,40E-05	1,49E-05	2,45E-05	1,08E-05	4,58E-06	-3,01E-05	-1,11E-05
1,48E-05	1,54E-05	2,35E-05	1,11E-05	2,96E-06	-4,93E-05	-1,64E-05
1,47E-05	1,58E-05	2,18E-05	1,07E-05	1,30E-06	-5,70E-05	-2,53E-05
1,45E-05	1,52E-05	2,15E-05	1,11E-05	-1,67E-06	-6,28E-05	-4,46E-05
1,55E-05	1,52E-05	1,99E-05	1,29E-05	-5,26E-06	-6,03E-05	-9,08E-05
1,44E-05	1,49E-05	1,70E-05	1,38E-05	-1,21E-05	-1,48E-05	-1,26E-04
1,53E-05	1,54E-05	1,42E-05	1,27E-05	-2,71E-05	1,20E-05	-5,47E-05
1,52E-05	1,53E-05	1,08E-05	1,16E-05	-5,74E-05	1,71E-05	3,11E-06
1,50E-05	1,52E-05	7,29E-06	1,17E-05	-6,58E-05	2,30E-05	1,33E-05
1,54E-05	1,50E-05	2,00E-06	1,14E-05	-2,72E-05	2,13E-05	2,05E-05
1,47E-05	1,52E-05	-7,30E-06	1,11E-05	-5,31E-06	2,30E-05	2,31E-05
1,43E-05	1,41E-05	-1,86E-05	8,10E-06	2,53E-06	2,22E-05	2,50E-05
1,25E-05	1,33E-05	-2,06E-05	5,22E-06	7,63E-06	2,49E-05	2,58E-05
1,04E-05	1,33E-05	-2,04E-05	2,07E-06	9,37E-06	2,23E-05	2,36E-05
5,73E-06	1,14E-05	-1,63E-05	-2,28E-06	8,02E-06	2,47E-05	2,54E-05
1,17E-06	1,03E-05	-9,11E-06	-8,90E-06	9,17E-06	2,23E-05	2,48E-05
-4,72E-06	7,25E-06	-2,75E-06	-1,07E-05	8,88E-06	2,34E-05	2,46E-05
-7,10E-06	8,07E-07	1,73E-06	-1,55E-05	8,31E-06	2,35E-05	2,68E-05
-5,86E-06	-1,19E-05	5,60E-06	-1,72E-05	8,69E-06	2,39E-05	2,58E-05
-3,15E-06	-3,03E-05	8,24E-06	-1,63E-05	1,05E-05	2,27E-05	2,42E-05
-2,84E-06	-5,55E-05	9,36E-06	-1,08E-05	1,34E-05	2,61E-05	2,64E-05
-8,54E-06	-6,78E-05	1,09E-05	-3,23E-06	1,50E-05	2,38E-05	2,41E-05

-2,36E-05	-4,82E-05	1,24E-05	2,40E-06	1,82E-05	2,38E-05	2,22E-05
-4,70E-05	-1,71E-05	1,19E-05	6,11E-06	1,81E-05	2,33E-05	2,61E-05
-5,44E-05	-1,24E-06	1,41E-05	6,96E-06	1,93E-05	2,32E-05	2,43E-05
-1,68E-05	9,32E-06	1,34E-05	1,11E-05	2,04E-05	2,44E-05	2,31E-05
4,01E-06	1,54E-05	1,46E-05	1,19E-05	2,21E-05	2,30E-05	2,60E-05
1,17E-05	1,72E-05	1,43E-05	1,34E-05	2,11E-05	2,47E-05	2,39E-05
1,86E-05	2,02E-05	1,51E-05	1,41E-05	2,23E-05	2,37E-05	2,49E-05
2,03E-05	2,24E-05	1,42E-05	1,60E-05	2,28E-05	2,52E-05	2,40E-05
2,19E-05	2,20E-05	1,58E-05	1,74E-05	2,35E-05	2,22E-05	2,67E-05
2,10E-05	2,20E-05	1,63E-05	1,89E-05	2,32E-05	2,51E-05	2,47E-05
2,22E-05	2,17E-05	1,56E-05	2,13E-05	2,29E-05	2,35E-05	2,44E-05
2,17E-05	2,23E-05	1,59E-05	2,28E-05	2,44E-05	2,43E-05	2,54E-05
2,12E-05	2,17E-05	1,63E-05	2,39E-05	2,22E-05	2,43E-05	2,49E-05
2,22E-05	2,21E-05	1,65E-05	2,33E-05	2,44E-05	2,38E-05	2,31E-05
2,00E-05	2,25E-05	1,54E-05	2,44E-05	2,40E-05	2,44E-05	2,75E-05
2,02E-05	2,19E-05	1,57E-05	2,43E-05	2,31E-05	2,52E-05	2,54E-05
1,85E-05	2,19E-05	1,60E-05	2,26E-05	2,40E-05	2,44E-05	2,40E-05
1,79E-05	2,24E-05	1,53E-05	2,39E-05	2,28E-05	2,40E-05	2,40E-05
1,96E-05	2,14E-05	1,62E-05	2,26E-05	2,44E-05	2,41E-05	2,28E-05
2,01E-05	2,18E-05	1,52E-05	2,45E-05	2,31E-05	2,49E-05	2,52E-05
2,24E-05	2,16E-05	1,60E-05	2,22E-05	2,44E-05	2,30E-05	2,38E-05
2,46E-05	2,21E-05	1,77E-05	2,52E-05	2,36E-05	2,48E-05	2,51E-05
2,62E-05	2,17E-05	1,75E-05	2,26E-05	2,38E-05	2,35E-05	2,37E-05
2,94E-05	2,22E-05	1,53E-05	2,38E-05	2,29E-05	2,32E-05	2,33E-05
2,73E-05	2,22E-05	1,53E-05	2,40E-05	2,36E-05	2,31E-05	2,63E-05
2,39E-05	2,21E-05	1,48E-05	2,47E-05	2,46E-05	2,36E-05	2,28E-05
2,29E-05	2,25E-05	1,54E-05	2,35E-05	2,39E-05	2,35E-05	2,21E-05
2,30E-05	2,22E-05	1,42E-05	2,36E-05	2,32E-05	2,35E-05	2,33E-05
2,21E-05	2,22E-05	1,42E-05	2,30E-05	2,41E-05	1,96E-05	2,50E-05
2,21E-05	2,26E-05	1,39E-05	2,44E-05	2,17E-05	2,57E-05	2,31E-05
2,21E-05	2,25E-05	1,34E-05	2,34E-05	2,46E-05	2,36E-05	2,33E-05
2,36E-05	2,22E-05	1,38E-05	2,31E-05	2,20E-05	2,32E-05	2,27E-05
2,37E-05	2,22E-05	1,36E-05	2,35E-05	2,34E-05	2,33E-05	2,25E-05
2,37E-05	2,25E-05	1,33E-05	2,40E-05	2,37E-05	2,17E-05	2,33E-05
2,37E-05	2,19E-05	1,30E-05	2,37E-05	2,25E-05	2,34E-05	2,11E-05
2,26E-05	2,22E-05	1,29E-05	2,32E-05	2,31E-05	2,14E-05	2,29E-05
2,36E-05	2,24E-05	1,38E-05	2,35E-05	2,32E-05	2,33E-05	2,09E-05
2,46E-05	2,27E-05	1,30E-05	2,37E-05	2,28E-05	2,32E-05	2,33E-05
2,32E-05	2,23E-05	1,19E-05	2,41E-05	2,20E-05	2,24E-05	2,32E-05
2,43E-05	2,29E-05	1,25E-05	2,36E-05	2,41E-05	2,46E-05	2,32E-05
2,41E-05	2,27E-05	1,20E-05	2,34E-05	2,33E-05	2,11E-05	2,27E-05
2,23E-05	2,01E-05	1,15E-05	2,62E-05	2,06E-05	2,14E-05	2,01E-05
2,28E-05	2,21E-05	1,14E-05	2,36E-05	2,33E-05	2,32E-05	2,31E-05

```fortran
      ! CR=100_2    Vector of Alpha values, obtained from the experiment for every CR
and temp.
      iiii=1
      open(unit=12,file=path\alfyall.txt', status='old')
      do iii=1, 6
      do jjj=1, 89
        write(12,39) iiii,alfyall(iii,jjj)
39    format(i5,'=',es12.4)
      iiii=iiii+1
       enddo
      enddo
      jakikolwiek=1
      x=15
      endif

      if (statev(1).eq.0) then
      statev(4)=890
      statev(5)=statev(4)-10
      statev(6)=statev(4)
      statev(1)=1
      statev(8)=0
      endif
      If (temp(1).le.statev(5)) then
      statev(4)=statev(6)-10
      statev(6)=statev(4)
      statev(5)=statev(4)-10
      endif
      If (temp(1).le.statev(4).and.temp(1).gt.statev(5)) then
      iT10=INT(statev(4))
      j=iT10/10
          endif
c----- COOLING RATE----------------------------------------------------------
c------Average cooling rate--------------
      open(unit=9,file='path\statevy.txt', status='old')

      statev(2)=(890-temp(1))/time(2)
      statev(7)=statev(7)+statev(2)
      statev(8)=statev(8)+1
      a_stat8=statev(8)
      statev(9)=statev(7)/statev(8)
      statev(10)=time(1)
      statev(11)=noel

50    format('noel:',i4,x,' |s(11):',f5.0,x,' |s(2):',f7.4,x,' |s(7):',
      f11.4,x,' |s(8):',f5.0,x,' |s(9):',f7.4,x,' |time:',se11.4,
      ' |s(10):',se11.4)
c------Local cooling rate----------------------------------------------------
      statev(3)=(-1*temp(2))/time(1)
      open(unit=11,file='path\elementy.txt', status='old')
      if    (statev(2).gt.-100.and.statev(2).le.0.06) then
      alfa=alfyall(1,j)

      elseif (statev(2).gt.0.06.and.statev(2).le.0.085) then
      alfa=(alfyall(1,j)+alfyall(2,j))/2
      elseif (statev(2).gt.0.085.and.statev(2).le.0.2) then
      alfa=alfyall(2,j)
      elseif (statev(2).gt.0.2.and.statev(2).le.0.4) then
      alfa=(alfyall(2,j)+alfyall(3,j))/2
      elseif (statev(2).gt.0.4.and.statev(2).le.0.6) then
      alfa=alfyall(3,j)
      elseif (statev(2).gt.0.6.and.statev(2).le.0.85) then
```

```fortran
      alfa=(alfyall(3,j)+alfyall(4,j))/2
      elseif (statev(2).gt.0.85.and.statev(2).le.2) then
      alfa=alfyall(4,j)
      elseif (statev(2).gt.2.and.statev(2).le.4) then
      alfa=(alfyall(4,j)+alfyall(5,j))/2
      elseif (statev(2).gt.4.and.statev(2).le.6) then
      alfa=alfyall(5,j)
      elseif (statev(2).gt.6.and.statev(2).le.8.5) then
      alfa=(alfyall(5,j)+alfyall(6,j))/2
      elseif (statev(2).gt.8.5.and.statev(2).le.20) then
      alfa=alfyall(6,j)
      elseif (statev(2).gt.20.and.statev(2).le.75) then
      alfa=(alfyall(6,j)+alfyall(7,j))/2
      elseif (statev(2).gt.75.and.statev(2).le.1500) then
      alfa=alfyall(7,j)
      endif

      do ikierunki=1, 3
      expan(ikierunki)=2*alfa*temp(2)
      enddo
      RETURN
      END



--------------------------------------------------------------------------------



      SUBROUTINE SDVINI(STATEV,COORDS,NSTATV,NCRDS,NOEL,NPT,
     LAYER,KSPT)
      INCLUDE 'ABA_PARAM.INC'
      DIMENSION STATEV(NSTATV),COORDS(NCRDS)
      RETURN
      END
```

Welding model:

```fortran
      SUBROUTINE DFLUX(FLUX,SOL,KSTEP,KINC,TIME,NOEL,NPT,COORDS,
     1 JLTYP,TEMP,PRESS,SNAME)
C
      INCLUDE 'ABA_PARAM.INC'
C
      DIMENSION FLUX(2), TIME(2), COORDS(3)
      CHARACTER*80 SNAME

      QL=80000                                  !LASER POWER [mW]
      R0=0.8                                     !BEAM RADIUS [mm]
      alfa=1                                    !absorbivity of bioglass
      DEPTH=0.7                                  !PENETRATION DEPTH [mm]
      Q=(QL/(R0**2*3.1415926*DEPTH))             !BODY FLUX [mW/mm^3]
      V=12.5                                       !Laser velocity

      X=COORDS(1)
      Y=COORDS(2)
```

```fortran
      Z=COORDS(3)


c     1L
      IF (TIME(2) .GT. 0.0001 .AND. TIME(2) .LE. 0.8001) THEN
      R=SQRT((X-0.43)**2+(Y+1.0)**2+(Z-(V*TIME(2)+0))**2)
      FLUX(1)=Q*EXP(-2*R**2/R0**2)*EXP(-alfa*Y)
      ENDIF
c     1R
      IF (TIME(2) .GT. 0.8001 .AND. TIME(2) .LE. 1.6001) THEN
      R=SQRT((X+0.43)**2+(Y+1.0)**2+(Z-(V*TIME(2))+10)**2)
      FLUX(1)=Q*EXP(-2*R**2/R0**2)*EXP(-alfa*Y)
      ENDIF
c     2L
      IF (TIME(2) .GT. 1.6001 .AND. TIME(2) .LE. 2.4001) THEN
      R=SQRT((X-0.425)**2+(Y+0.42)**2+(Z-(V*TIME(2))+20)**2)
      FLUX(1)=Q*EXP(-2*R**2/R0**2)*EXP(-alfa*Y)
      ENDIF
c     2R
      IF (TIME(2) .GT. 2.4001 .AND. TIME(2) .LE. 3.2001) THEN
      R=SQRT((X+0.425)**2+(Y+0.42)**2+(Z-(V*TIME(2))+30)**2)
      FLUX(1)=Q*EXP(-2*R**2/R0**2)*EXP(-alfa*Y)
      ENDIF
c     3L
      IF (TIME(2) .GT. 3.2001 .AND. TIME(2) .LE. 4.0001) THEN
      R=SQRT((X-0.46)**2+(Y+0.42)**2+(Z-(V*TIME(2))+40)**2)
      FLUX(1)=Q*EXP(-2*R**2/R0**2)*EXP(-alfa*Y)
      ENDIF
c     3R
      IF (TIME(2) .GT. 4.0001 .AND. TIME(2) .LE. 4.8001) THEN
      R=SQRT((X+0.46)**2+(Y+0.43)**2+(Z-(V*TIME(2))+50)**2)
      FLUX(1)=Q*EXP(-2*R**2/R0**2)*EXP(-alfa*Y)
      ENDIF
c     4L
      IF (TIME(2) .GT. 4.8001 .AND. TIME(2) .LE. 5.6001) THEN
      R=SQRT((X-0.5)**2+(Y)**2+(Z-(V*TIME(2))+60)**2)
      FLUX(1)=Q*EXP(-2*R**2/R0**2)*EXP(-alfa*Y)
      ENDIF
c     4R
      IF (TIME(2) .GT. 5.6001 .AND. TIME(2) .LE. 6.4001) THEN
      R=SQRT((X+0.5)**2+(Y)**2+(Z-(V*TIME(2))+70)**2)
      FLUX(1)=Q*EXP(-2*R**2/R0**2)*EXP(-alfa*Y)
      ENDIF
c     5L
      IF (TIME(2) .GT. 6.4001 .AND. TIME(2) .LE. 7.2001) THEN
      R=SQRT((X-0.4)**2+(Y-0.5)**2+(Z-(V*TIME(2))+80)**2)
      FLUX(1)=Q*EXP(-2*R**2/R0**2)*EXP(-alfa*Y)
      ENDIF
c     5R
      IF (TIME(2) .GT. 7.2001 .AND. TIME(2) .LE. 8.0001) THEN
      R=SQRT((X+0.4)**2+(Y-0.5)**2+(Z-(V*TIME(2))+90)**2)
      FLUX(1)=Q*EXP(-2*R**2/R0**2)*EXP(-alfa*Y)
      ENDIF
      RETURN
      END



          SUBROUTINE SDVINI(STATEV,COORDS,NSTATV,NCRDS,NOEL,NPT,
     1 LAYER,KSPT)
      INCLUDE 'ABA_PARAM.INC'
      DIMENSION STATEV(NSTATV),COORDS(NCRDS)
```

```fortran
      RETURN
      END


      SUBROUTINE UEXPAN(EXPAN,DEXPANDT,TEMP,TIME,DTIME,PREDEF,
     1 DPRED,STATEV,CMNAME,NSTATV,NOEL)
      INCLUDE 'ABA_PARAM.INC'
      CHARACTER*80 CMNAME
      DIMENSION EXPAN(*),DEXPANDT(*),TEMP(2),TIME(2),PREDEF(*),
     1 DPRED(*),STATEV(NSTATV)
      common/nowe/x,alfyall(6,89)
      common/alf/jakikolwiek,i,j
c      abaqus j=HT.inp user=ModTempDEPV1.for interactive
c      statev(1)   - trigger, on every node, controls the beginning temperature values
for the alphas
c      statev(2)   - Average CR on the node, counted from the beginning of the process
(ACR - average cooling rate)
c      statev(3)   - Temporary CR on the node, counted from the previous step (LCR -
local cooling rate)
c      statev(4)   - top temperature in the particular alphas' range
c      statev(5)   - bottom temperature in the particular alphas' range
c      statev(6)   - Temperature statev(4) służąca do podmiany
c      statev(7)   - Sum of ACRs
c      statev(8)   - Parameter counting CRs
c      statev(9)   - Average ACR
c      statev(10)  - Previous czas
c      statev(11)  - Previous noel
c      statev(12)  - Identificator of the column in alpha's table, CR dependent
c      TEMP(1)     - Current temperature (at the end of the increment).
c      TEMP(2)     - Temperature increment.
c      TIME(1)     - Step time at the end of the increment.
c      TIME(2)     - Total time at the end of the increment.
c      DTIME       - Time increment.
c      PREDEF(*)   - Array containing the values of all the user-specified predefined
field variables at this point (initial values at the beginning of the analysis and
current values during the analysis).
c      DPRED(*)    - Array of increments of predefined field variables.
c      CMNAME      - User-specified material name or gasket behavior name, left
justified.
c      NSTATV      - Number of solution-dependent state variables associated with this
material or gasket behavior type (specified when space is allocated for the array; see
Allocating space).
c      NOEL        - User-defined element number.

c      T=50
      if      (temp(1).gt.-100.and.temp(1).le.50) then
      alfa=12.35E-06
c      T=100.00
      elseif (temp(1).gt.50.and.temp(1).le.150) then
      alfa=12.68E-06
c      T=200.00
      elseif (temp(1).gt.150.and.temp(1).le.250) then
      alfa=13.14E-06
c      T=300.00
      elseif (temp(1).gt.250.and.temp(1).le.350) then
      alfa=13.60E-06
c      T=400.00
      elseif (temp(1).gt.350.and.temp(1).le.450) then
      alfa=14.06E-06
c      T=500.00
      elseif (temp(1).gt.450.and.temp(1).le.550) then
      alfa=14.51E-06
```

```fortran
c       T=600.00
        elseif (temp(1).gt.550.and.temp(1).le.650) then
        alfa=14.96E-06
c       T=700.00
        elseif (temp(1).gt.650.and.temp(1).le.750) then
        alfa=15.83E-06
c       T=800.00
        elseif (temp(1).gt.750.and.temp(1).le.850) then
        alfa=16.68E-06
c       T=900.00
        elseif (temp(1).gt.850.and.temp(1).le.950) then
        alfa=17.15E-06
c       T=1000.00
        elseif (temp(1).gt.950.and.temp(1).le.1050) then
        alfa=17.64E-06
c       T=1100.00
        elseif (temp(1).gt.1050.and.temp(1).le.1150) then
        alfa=18.13E-06
c       T=1200.00
        elseif (temp(1).gt.1150.and.temp(1).le.1250) then
        alfa=18.62E-06
c       T=1300.00
        elseif (temp(1).gt.1250.and.temp(1).le.2350) then
        alfa=19.11E-06
        endif
        If (time(2).ge.8.0001.and.temp(1).le.890) then
c-----COOLING-------------------------------------------------------------------
         [Table consisting of alphas values]
         .
         .
         .
         alfyall(     7    ,     89     )=     2.3122E-05  ! CR = 100_2
        endif
        if (statev(1).eq.0) then
        statev(4)=890
        statev(5)=statev(4)-10
        statev(6)=statev(4)
        statev(1)=1
        statev(8)=0
        If (temp(1).le.statev(5)) then
        statev(4)=statev(6)-10
        statev(6)=statev(4)
        statev(5)=statev(4)-10
        endif
                 If (temp(1).le.statev(4).and.temp(1).gt.statev(5)) then
            iT10=INT(statev(4))
        j=iT10/10
            endif
        endif
c------COOLING RATE CALCULATIONS------------------------------------------------
c------Average cooling rate--------------
        statev(2)=(890-temp(1))/time(2)
        statev(7)=statev(7)+statev(2)
        statev(8)=statev(8)+1
        a_stat8=statev(8)
        statev(9)=statev(7)/statev(8)
        statev(10)=time(1)
        statev(11)=noel
c------Temporary cooling rate--------------
        statev(3)=(-1*temp(2))/time(1)
        if     (statev(2).gt.-100.and.statev(2).le.0.06) then
        alfa=alfyall(1,j)
```

285

```fortran
      elseif (statev(2).gt.0.06.and.statev(2).le.0.085) then
      alfa=(alfyall(1,j)+alfyall(2,j))/2
      elseif (statev(2).gt.0.085.and.statev(2).le.0.2) then
      alfa=alfyall(2,j)
      elseif (statev(2).gt.0.2.and.statev(2).le.0.4) then
      alfa=(alfyall(2,j)+alfyall(3,j))/2
      elseif (statev(2).gt.0.4.and.statev(2).le.0.6) then
      alfa=alfyall(3,j)
      elseif (statev(2).gt.0.6.and.statev(2).le.0.85) then
      alfa=(alfyall(3,j)+alfyall(4,j))/2
      elseif (statev(2).gt.0.85.and.statev(2).le.2) then
      alfa=alfyall(4,j)
      elseif (statev(2).gt.2.and.statev(2).le.4) then
      alfa=(alfyall(4,j)+alfyall(5,j))/2
      elseif (statev(2).gt.4.and.statev(2).le.6) then
      alfa=alfyall(5,j)
      elseif (statev(2).gt.6.and.statev(2).le.8.5) then
      alfa=(alfyall(5,j)+alfyall(6,j))/2
      elseif (statev(2).gt.8.5.and.statev(2).le.20) then
      alfa=alfyall(6,j)
      elseif (statev(2).gt.20.and.statev(2).le.75) then
      alfa=(alfyall(6,j)+alfyall(7,j))/2
      elseif (statev(2).gt.75.and.statev(2).le.1500) then
      alfa=alfyall(7,j)
      endif
      endif

      do ikierunki=1, 3
      expan(ikierunki)=2*alfa*temp(2)
      enddo
c-----COOLING--ENDS-------------------------------------------------------------
      RETURN
      END
```